UNIVERSITY OF OKLAHOMA

GRADUATE COLLEGE

SEISMIC ATTRIBUTE ANALYSIS OF DEPTH-MIGRATED DATA

A DISSERTATION

SUBMITTED TO THE GRADUATE FACULTY

in partial fulfillment of the requirements for the

Degree of

DOCTOR OF PHILOSOPHY

By

TENGFEI LIN
Norman, Oklahoma
2016

SEISMIC ATTRIBUTE ANALYSIS OF DEPTH-MIGRATED DATA

A DISSERTATION APPROVED FOR THE
CONOCOPHILLIPS SCHOOL OF GEOLOGY AND GEOPHYSICS

BY

_____

Dr. Kurt J. Marfurt, Chair

_____

Dr. Xingru Wu

_____

Dr. Roger M. Slatt

_____

Dr. Shankar Mitra

_____

Dr. Isaac Hall

To my beloved Fuling Zhang

ACKNOWLEDGMENTS

To earn a PhD in Geophysics was my ultimate goal when I arrived at the University of Oklahoma four years ago. I have reached this goal with the support and guidance of a lot of people.

Dr. Marfurt has been a super advisor of mine. I received a lot of guidance, knowledge and encouragement on my research from him. I think myself very lucky to be his student. He treated me as his own child and opened my mind in Geophysics systematically. He helped me to debug the code whenever I faced problems in the codes that I was unable to solve. He always modifies the grammar and structure patiently in the papers. He was never strict with me and always encouraged me to spend time with my family back in China and travel during the holidays. Dr. Marfurt is one of the most wonderful persons I have ever met in my life.

I also want to express my gratitude to Dr. Shankar Mitra who is one of my committee members, and was my committee member for my Master degree. He helped me to understand the structural geology in his class, and expressed his kindness and gave me much useful advice.

I would also like to express my sincere thanks to Dr. Roger Slatt, who is also one of my committee members for his important comments and feedback on my research. I learned a lot of reservoir characterization from his courses.

I also thank my other committee members Dr. Isaac Hall. He has been very helpful to me. He gave me some most important new ideas on the wavelet-based Radon transform and the separation of converted wave from the traditional seismic data, which is one of the important parts of my PhD research.

Dr. Xingru Wu, the outside committee member for my PhD degree, offers enormous patience and help on both my study and daily life. He advised me a lot in microseismic attribute characterization.

I would also like to thank Dr. Jamie Rich, who was my committee member for my Master's degree. He is always nice to me and encouraged my research.

I would like to thank the entire staff of ConocoPhillips School of Geology and Geophysics: Rebecca Fay, Ginny Gandy-Guedes, Ginger Leivas, Leah Moser, Amber Roberts, Donna S. Mullins, Nancy Leonard, Adrianne Fox, Teresa Hackney and Jocelyn Cook for their help and support.

I also want to thank the AASPI Consortium sponsors, all the student members at the AASPI consortium and my fellow graduate students at the ConocoPhillips School of Geology and Geophysics for their help and support. I thank my friends: Kui, Brad, Bo, Shiguang, Sumit, Alfredo, Oswaldo, Bin, Tao, Fangyu, Jie, Sean, Thang, who helped me in various ways in my research. I would also like to thank my close friends Li, Yuqi, Zonghu, Ting, who has been here since I came to OU, helped me in different ways. I would like to acknowledge the support of some of my other friends.

I will not be able to express in few words how the love, affections and support of my parents, my older sister and brother, and my niece and nephews. Constant prayer and never-ending love of them for me helped me to get success in my life.

I would also like to thank deeply my love *Fuling Zhang* for staying beside me and have faith in me always. We are going to endure everything together and hopefully we will be together in the coming years. Her sweet smile and love gives me constant encouragement for my work.

TABLE OF CONTENTS

LIST OF TABLES

LIST OF FIGURES

ABSTRACT

Most seismic attributes are originally designed and computed on time-migrated data. While some papers show the values of attribute analysis on depth-migrated data, few have compared the images to corresponding time-migrated volumes. I therefore use time- and depth-migrated volumes from Bohai Bay Basin, China, to show not only the values of depth-migration, but also the necessary data-conditioning, algorithmic modification, and interpretation of attributes computed from depth data.

Since one of the goals for depth migration is to image steep dips, depth migration also allows steeply dipping noise to overprint the image. I suppress this noise through careful structure-oriented filtering. Fault plane reflections are imaged well by depth migration, and give rise to dips that conflict with those of the underlying reflectors.

In depth-migrated data, spectral components are now measured in cycles per kilometer or cycles per kilofeet (wavenumber) rather than in cycles/s or Hertz (frequency). While smoothly varying velocity models used in Kirchhoff depth migration give rise to smoothly varying wavenumber stretch, discontinuous velocity models used in wave equation and reverse time migration will give rise to wavenumber artifacts straddling the velocity discontinuity boundary. Furthermore, imaging of steep dips results in a shift by $\cos\theta$ of true to lower apparent spectral components.

In order to quantitatively evaluate the coherence, I follow early work on the significance of events seen in semblance-based velocity spectra and use an F-statistic to quantify the significance of coherence measures at each voxel. The accuracy and resolution of such measures depend on the bandwidth of the data, the signal-to-noise ratio, and the size of the spatial and temporal analysis windows used in their numerical estimation. In 3D interpretation, low-coherence estimates not only seismic noise, but also geologic signal, such as fault planes and channel edges.

Ideally, vertical attribute analysis windows should be scaled by some fraction of the dominant wavelength. Unfortunately, the dominant wavelength increases with depth in time-migrated data due to attenuation. Moreover, since the size of the dominant wavelength changes as a function of velocity in depth-migrated data, a single fixed-sized window may be too large for shallower data and too small for deeper data. Therefore, I construct laterally and vertically smoothly varying analysis windows based on the spectral content of the data resulting in data-adaptive attribute computation.

I demonstrate the value of these algorithmic modifications to a survey acquired over the Bohai Bay Basin, China. The complex faulting gives rise to a laterally variable velocity, so that depth migration of the data is necessary. After data conditioning, I obtain a relatively clean, noise-free, well-focused depth-migrated image. Artifacts in the time-migrated data such as fault shadows give rise to false coherence anomalies, while velocity pull-up and pushdown give rise to false curvature

anomalies. These artifacts are minimized and a more accurate image of the fault network is constructed in the depth-migrated data. Finally, structural features such as folds and flexures are directly linked to the depth-structure of the data via the laterally variable velocity model.

Prestack data conditioning, including residual moveout correction, reduction of migration stretch, and suppression of coherent noise, is critical to subsequent prestack inversion and anisotropy analysis. The Radon transform is a powerful noise suppression tool, and is routinely used to suppress multiples. Traditional Radon transforms are often smeared in the transform domain, limiting the signal to noise separation. We prototype a Radon transform based on a matching pursuit method, to minimize smearing and suppress data stretch. Specifically, the algorithm will ask "which Ricker wavelet with which moveout, best represents the seismic gather". After each estimate, that event is removed from the data, forming a residual. The algorithm will iterate until all events are described. My hypothesis that the wavelet-based Radon transform will provide improved separation between primaries and multiples, which is proved through the application to a marine data volume acquired by KIGAM in the Jeju Basin, Korea.

CHAPTER 1

SPECTRAL ANALYSIS OF DEPTH-MIGRATED DATA

Tengfei Lin[1], Bo Zhang[2], Kurt Marfurt[1]

[1] University of Oklahoma, ConocoPhillips School of Geology and Geophysics,

[2] University of Alabama, Department of Geological Sciences.

ABSTRACT

Spectral decomposition is a powerful analysis tool that has been successful in delineating channels, fans, overbank deposits and other relative thin architectural elements in clastic and carbonate depositional environments. Because of its success in characterizing fluvial-deltaic and basin floor turbidite-fan systems, most publications on spectral decomposition discuss time-migrated data. Interpreting spectral components and spectral attributes such as peak frequency on depth-migrated data requires a slightly different perspective. First, the results are computed as cycles/km (or alternatively as cycles/1000 ft) rather than as cycles/s or Hertz, with the dominant wavenumber decreasing with increasing velocity at depth. Second, interpreters resort to depth migration when there are significant lateral velocity changes in the overburden and/or steep dips. All present-day implementations compute spectral components along vertical traces rather than perpendicular to the strata, giving rise to tuning and other anomalies at an apparent rather than at a true frequency or wavenumber.

We illustrate the interpretational differences of spectral decomposition between time- and depth-migrated data using a simple synthetic model and a modern 3D data volume. We show how one can approximately compensate for reflector dip by normalizing each spectral magnitude component by $1/\cos\theta$, where θ is the volumetric dip magnitude commonly computed in seismic attribute analysis. We demonstrate the

algorithm through application to two 3D surveys, which indicates the significance of dip compensation of spectral decomposition in seismic data, especially for the depth-migrated seismic volumes.

LIST OF KEYWORDS

Spectral decomposition, Dip compensation factor.

INTRODUCTION

Most published applications on seismic attributes have used time-migrated data. Interpreting seismic attributes such as coherence on depth-migrated data requires a slightly different perspective. First, the samples are in meters or feet rather than in milliseconds. Second, the Fourier Transform is commonly used during the estimation of seismic attributes, where spectral components are computed in cycles/km (or alternatively as cycles/1000 ft) rather than in cycles/s or Hertz, with the dominant wavenumber decreasing with increasing velocity at depth. Third, we typically use a constant user-defined window to calculate window-based attributes. Such a constant window size cannot adapt to the lateral and vertical variation in seismic resolution, giving suboptimum results. This becomes especially noticeable with depth-migrated data where the dominant wavelength increases with depth due both to attenuation and increasing velocity.

Seismic attributes have been applied to depth-migrated data since their inception. Because the dominant wavelength increases with increasing velocity, which in turn increases with depth, attributes such as coherence benefit by using shorter vertical analysis windows in the shallow section and longer vertical analysis windows in the deeper section. Since most coherence implementations require a fixed vertical analysis window, the interpreter simply runs the algorithm using an appropriate window for each zone to be analyzed. Curvature is naturally computed in the depth

domain, with most algorithms requiring a simple conversion velocity for time-migrated data. For more accurate results, the interpreter uses different conversion velocities for different target depths, or simply converts the entire volume to depth using well control. Both coherence and curvature are structurally driven attributes, with coherence computed along structural dip and curvature computed from structural dip.

Spectral decomposition is computed trace by trace, which implicitly ignores any dipping structures. One of the most common uses of spectral decomposition is to map fluvial (e.g. Partyka et al., 1999; Peyton et al., 1998) and deep-water (e.g. Bahorich et al., 2002) depositional systems. Key to interpreting these spectral components is the thin-bed tuning model. Widess (1973) used wedge model to quantify the detection of thin-bed anomalies. The maximum constructive interference occurs when the wedge thickness is the tuning thickness (one-half of the two-way travel-time period for the time-migrated data or one-quarter of the wavelength for the depth-migrated data). Using this model, Laughlin et al. (2002) showed that thicker channels exhibited a stronger response at lower frequencies, while the thinner flanks of the channel exhibited a stronger response at higher frequencies. Although this is the most common use of spectral decomposition, spectral components are currently the method of choice in spectral blanking, estimating attenuation ($1/Q$). Spectral components are also used in pore-pressure and seismic discontinuities prediction (Davagustto et al., 2013), as well as some implementations of seismic chronostratigraphy.

In this chapter, we show hot to correct the spectrum for dipping reflections. We begin with an overview of spectral decomposition and dip estimation. We then use the dip to correct the spectrum. We them show the value of this correction through application to a depth-migrated data volume from Bohai Bay Basin, P.R. China.

THEORETICAL ANALYSIS

Short-window Discrete Fourier Transform (SWDFT), Continuous Wavelet Transform, and Matching Pursuit Estimates of Spectral Components

There are currently three algorithms used to generate spectral components: short-window discrete Fourier transforms (SWDFT), continuous wavelet transforms, and matching pursuit. Leppard et al. (2010) found that matching pursuit provided greater vertical resolution and lesser vertical stratigraphic mixing than the other techniques. We suspect the fixed-window length least squares spectral analysis technique described by Puryear et al. (2008) provides similar spectral resolution to the (least squares) matching pursuit algorithm. While all of our examples here are generated using a matching pursuit algorithm described by Liu and Marfurt (2007), the concept of apparent vs. true frequency is perhaps easiest to understand using the fixed length analysis window used in the SWDFT. For time-migrated data, the window will be in seconds, such that the spectral components are measured in cycles/s or Hz. For depth-migrated data, the window will be in kilometers; such that the spectral components are measured in cycles/km. Significant care must be taken when loading the data into commercial software, where the SEGY standard stores the sample interval in microseconds. For everything to work correctly, a depth sample interval of 10 m will need to be stored as 10000 “microkilometers”. If the units are not stored in this manner, the numerical values of the data may appear to be in fractions of

cycles/m. Many commercial software packages will not operate for cycles/s (or cycles/km) that fall beyond a reasonable numerical range of 1-250. Once the data are loaded, the range of values will be different. If the time domain data range between 8-120 Hz, depth domain data will range between 2-30 cycles/km at a velocity of 4 km/s, such that anomalies will be shifted to lower "frequencies".

We create a wedge model using a 5-10-90-120 Ormsby wavelet and calculate the relevant peak frequency in Figure 1.1. White arrows indicate the top and bottom of the wedge. Peak frequency will increase with decreasing thickness.

Dip Compensation

If the dip angle is θ, and the real thickness h_r, then the apparent thickness $h_a = h_r / cos\,\theta$ (Figure 1.2). The tuning frequency (and tuning wavenumber) will therefore decrease with increasing values of θ. The shift to lower apparent frequency is familiar to those who examine data before and after time migration, where dipping events on unmigrated stacked data with moderate apparent frequency "migrate" laterally to steeper events with lower apparent frequency (Lin et al., 2013).

Since spectral decomposition is calculated trace by trace in the vertical direction, the results are accurate for perfectly flat horizon where $\theta = 0$. However, for dipping reflectors, spectral decomposition tuning effects will be in terms of the

vertical apparent thickness, which is always greater than the true thickness for dipping layers. According to tuning phenomenon and the schematic diagram in Figure 1.2:

$$h_a = \frac{\lambda_a}{4} = \frac{V_{pa} \cdot T_a}{4} = \frac{V_{pa}}{4 f_a}, \text{ and} \tag{1a}$$

$$h_r = \frac{\lambda_r}{4} = \frac{V_{pr} \cdot T_r}{4} = \frac{V_{pr}}{4 f_r}, \tag{1b}$$

where h_a is the apparent thickness along the vertical axis, h_r is the real thickness perpendicular to the thin layer, and θ is the dip angle of the thin layer. The relationship between f_a, the apparent tuning frequency in the vertical direction, and f_r, the real tuning frequency of the thin layer is

$$f_r \approx \frac{f_a}{\cos\theta}. \tag{2}$$

Figure 1.3a shows a synthetic example of a layer with a constant vertical thickness of 100 ft; the apparent tuning frequency should be 50 Hz for a velocity of 10000 ft/s. The apparent thickness is constant (gray line) across the model when measured vertically. The spectral analysis results in a constant value of f_{peak} = 50 Hz rather than the variable peak frequency indicated by the red line. Correcting the apparent thickness by 1/cosθ gives the correct result.

In Figure 1.3c, the real (perpendicular) thickness of the thin bed is 100 ft. In this example, the apparent tuning frequency will change laterally (gray line). In contrast, the dip-corrected tuning frequency of the real thickness would be constant (50 Hz, red line) across the model.

APPLICATION

Application to Time-Migrated Data from the US Gulf of Mexico

The Texas-Louisiana shelf of the Gulf of Mexico are characterized by salt domes and salt withdrawal basins resulting in both changes in thickness due to changes in accommodation space and changes in in apparent thickness due to post deposition changes in dip. Our objective is to use spectral components to map lateral changes in true dip vs. apparent dip. Figure 1.4a shows a horizon slice through apparent frequency co-rendered with coherence. Figure 14.b shows the dip magnitude, θ, with high dip magnitude at the edges of the minibasin. Moreover, Figure 1.4c indicates the dip compensation factor, with high values at the flanks of the minibasin.

In general, accommodation space decreases towards the flanks of the basin. However, Figure 1.4a indicates a decrease in tuning frequency, as increase in thickness towards the flanks. The decrease in tuning frequency is an artifact due to the dip. Figure 1.4d shows the same horizon slice after dip compensation, which now introduces thinning towards the edges of the minibasin. White arrow in Figure 1.5 indicates a channel, in which the peak frequency increases a lot after dip compensation due to the large dip magnitude.

Comparison of Time- vs. Depth-Migrated Data from East China

Figure 1.6 shows the time- and depth-migrated seismic profiles from an oilfield of East China, known to have multiple fault-controlled reservoirs. This phenomenon, along with the increase in wavelength and decrease in apparent resolution is a result of the increase of velocity with time (depth).

The sample increment for time-migrated data is Δt = 0.002 s, and for the depth-migrated data Δt = 0.01 km. Red dashed lines indicate three faults, which are much clearer in the depth-migrated data. The fault planes are also more continuous. Orange arrows indicate migration artifacts. In this case, the depth-migrated data suffer from more artifacts than the time-migrated data. The green arrow in the depth-migrated data indicates a lower frequency response compared to the time-migrated data. The blue arrow in the depth-migrated data shows a clear fault plane, which is poorly imaged in the time-migrated data. The frequency range is 4 – 40 Hz for the time-migrated data, while the wavenumber range is about 2 – 20 cycles/km for depth-migrated data (Figure 1.7). We find that the numerical value of the wavenumber for depth-migrated data is about half of the frequency for time-migrated data.

Figures 1.7a and b show the peak frequency co-rendered with seismic amplitude for both the time- and depth-migrated data. Both of images exhibit a similar peak frequency trends, even though the numerical values of peak wavenumber in depth-migrated data are nearly half of the peak frequency in the time-migrated data. Low peak frequency anomalies are lithogically bound (consistent with increasing velocity with age) along the horizon, except for the zone seriously blurred by the migration artifacts, indicated by white arrow in Figure 1.7b. The peak frequency tracks the horizons for the time-migrated data in Figure 1.7a. The steeper "depth" dip than time dip as well as some steeply dipping migration artifacts gives rise to the low frequency zones.

We filter the dip along structure to remove artifacts and compute dip compensation spectra and blend the results with seismic amplitude in Figures 1.9a and b where the dip in Figure 1.8 is zero (flat), the dip compensation factor is 1.0 and the peak frequency remains unchanged. When there is a steeply dipping reflector, the dip compensation factor is greater than one, shifting the result to a higher (true) peak frequency. The dip compensation factors follow faults and horizons. Because of the greater noise in the depth-migrated data, some of the dip estimates are erratic, giving rise to the erratic dip compensation values shown in Figure 1.9b.

Figures 1.10a and b show the real peak frequency of the time-migrated data and depth-migrated data. For the shallow part, the corrected peak frequency changes slightly, since the dip is small and the dip compensation factor is close one. For the steeply dipping deeper layers, the corrected peak frequency is significantly (~50%) higher than the original apparent peak frequency. The corrected peak frequency better correlates to the horizons than that in Figures 1.7a and b, especially for the depth-migrated data.

A dipping horizon A is picked (in Figure 1.11) in both time- and depth-migrated seismic volume. Red arrows indicate the main faults. Extracting the apparent peak frequency in Figure 1.12, we can found that the apparent peak frequency of the faulted zones indicated by white arrows is about 12 Hz for time-migrated data, and 10 cycles/km for the depth-migrated data. While the dip compensation makes them approach 14 Hz and 12 cycles/km, respective in Figure 1.13, which means the true thinning thickness of the faulted zones marked by white arrows should be smaller than the apparent one before dip compensation.

CONCLUSIONS

In the presence of strong lateral variations in velocity, time-migration fails to properly image the subsurface. To avoid such pitfalls, an interpreter needs to carefully calibrate the attribute anomalies to conventional vertical slices through the seismic amplitude volume. Accurate prestack depth migration removes most of these artifacts but presents its own unique challenges. First, coherent fault plane reflections will be indistinguishable from stratigraphic reflections by most attributes. Second, depth-migrated data are in general noisier than time-migrated data and may need to be conditioned using structure-oriented filtering prior to attribute computation. Third, because of the increase in velocity with depth, the change in wavelength from top to bottom of a survey in depth-migrated data is much greater than the change in period in time-migrated data. This longer wavelength will require different sized attribute analysis window to maintain a similar signal-to-noise ratio.

Depth migration is designed to handle complex structure which in many cases implies steep dips. In the presence of such steep dips, one need to correct spectral estimates made on vertical traces by $1/\cos\theta$ and then re-interpolates the spectrum. Spectral decomposition also provides the means to develop data-adaptive attribute analysis windows.

ACKNOWLEDGEMENTS

We thank BGP Inc., for the use of their Bohai Bay Basin data set. Numerical model was generated using Tesseral's Tesseral 2D software. Seismic displays were generated used Schlumberger's Petrel software. We also thank the sponsors of Attribute-Assisted Seismic Processing and Interpretation Consortium (AASPI) for their guidance and financial support.

CHAPTER 1 FIGURES

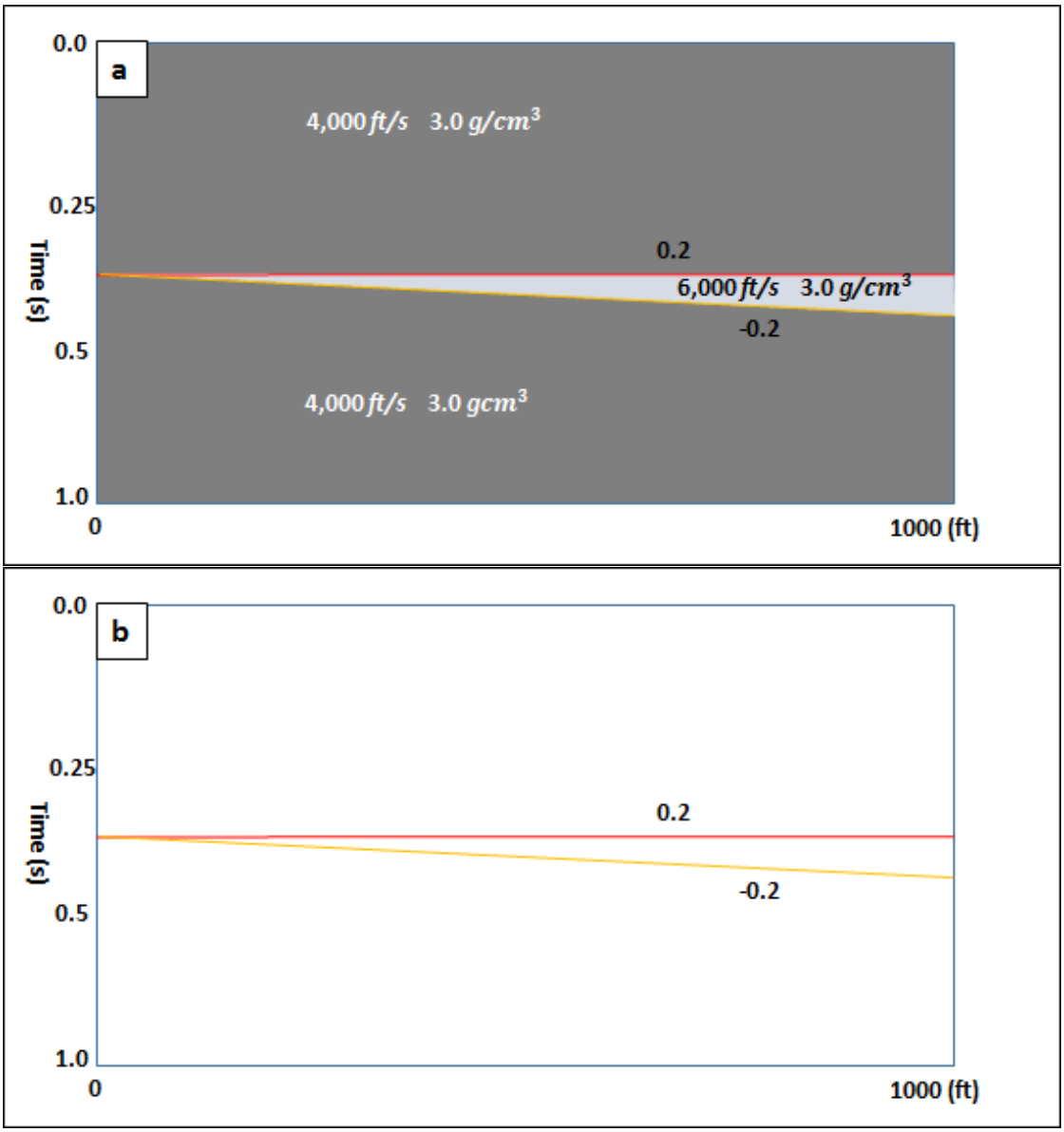

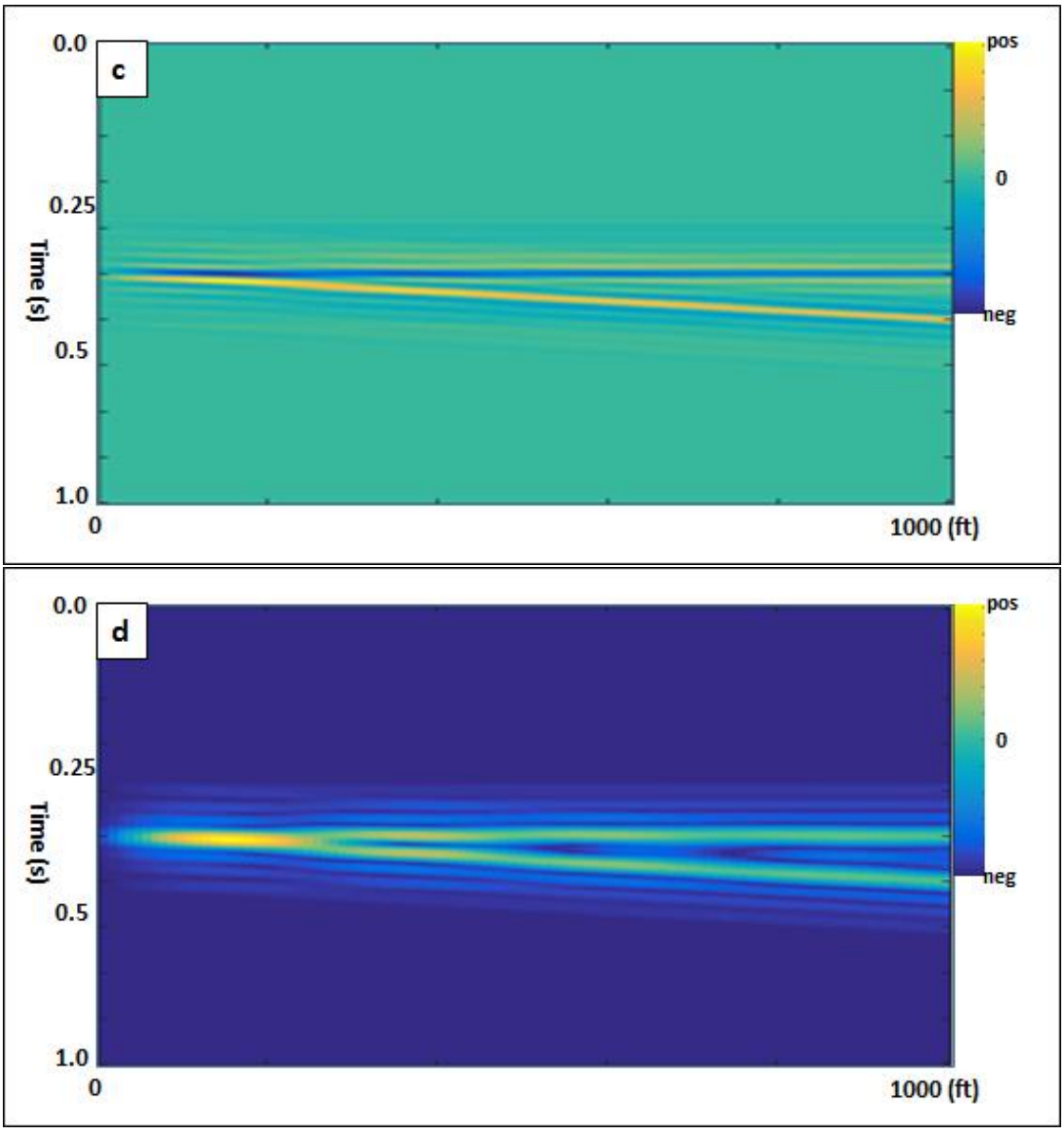

Figure 1.1. (a) The impedance, (b) reflectivity, (c) synthetic seismic amplitude with 5 percent random noise, and (d) envelope of the wedge model. The dominant frequency of the seismic wavelet is 40 Hz.

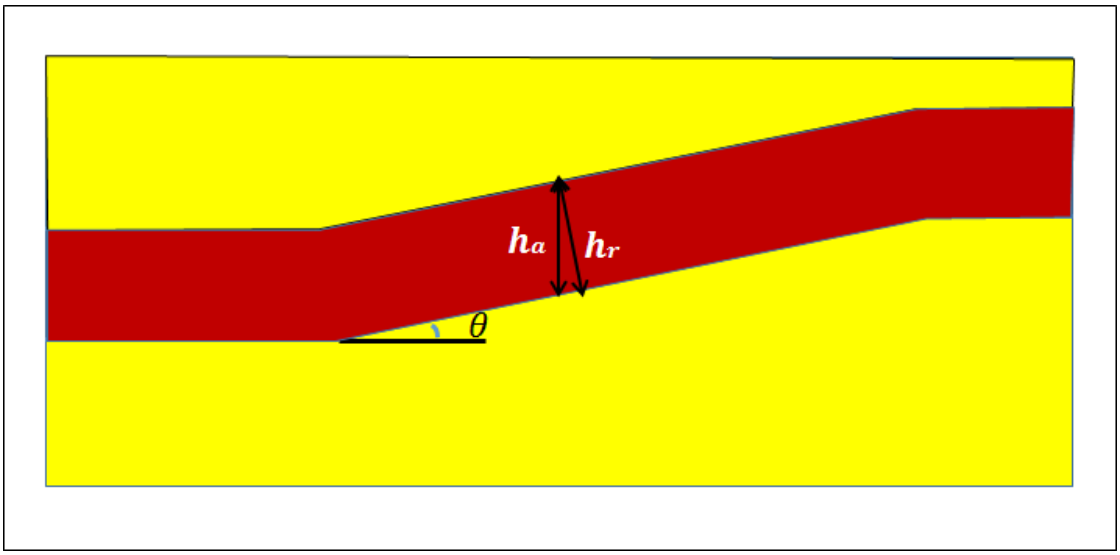

Figure 1.2. A schematic diagram showing differences between the apparent thickness h_a and the real thickness, h_r with respect to dip magnitude, θ.

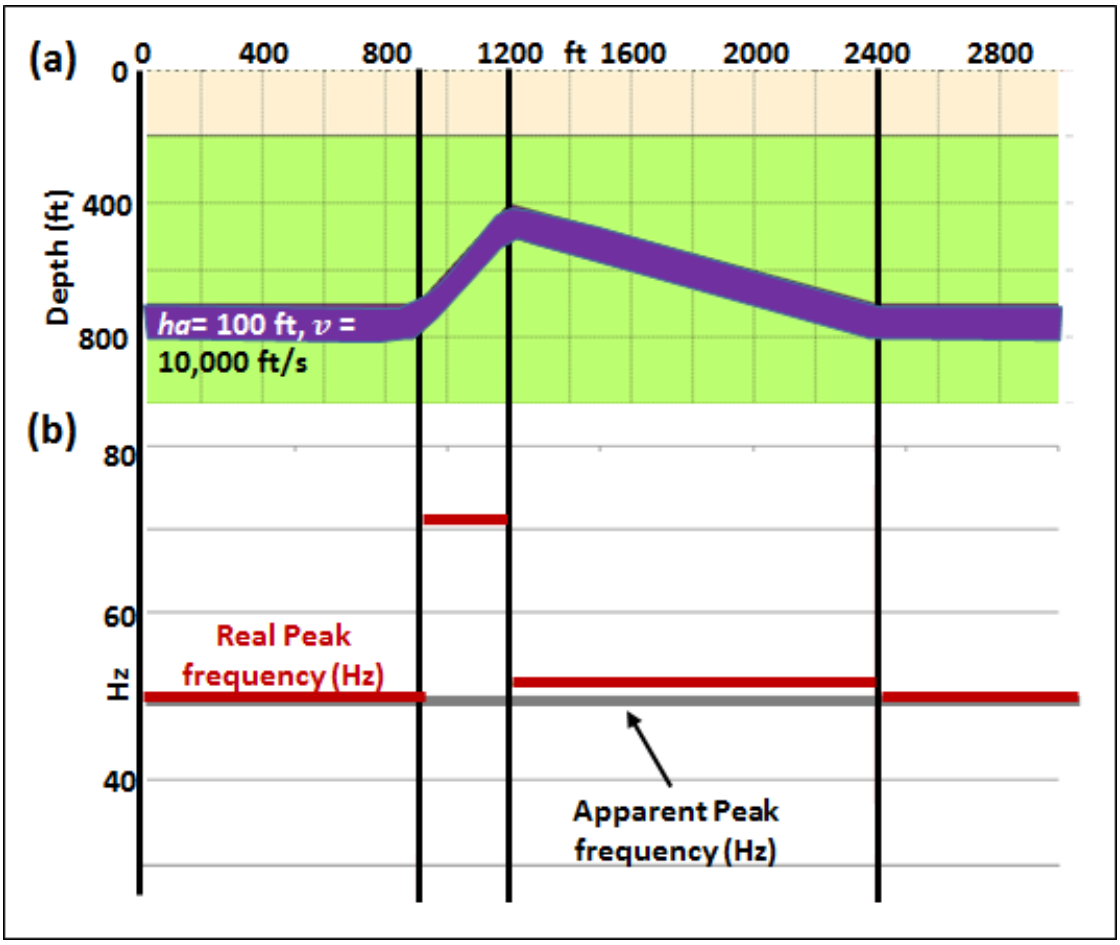
(a)
0
400
800
1200
ft
1600
2000
2400
2800
Depth (ft)
0
400
800
ha= 100 ft, v =
10,000 ft/s
(b)
80
60
40
Hz
Real Peak
frequency (Hz)
Apparent Peak
frequency (Hz)

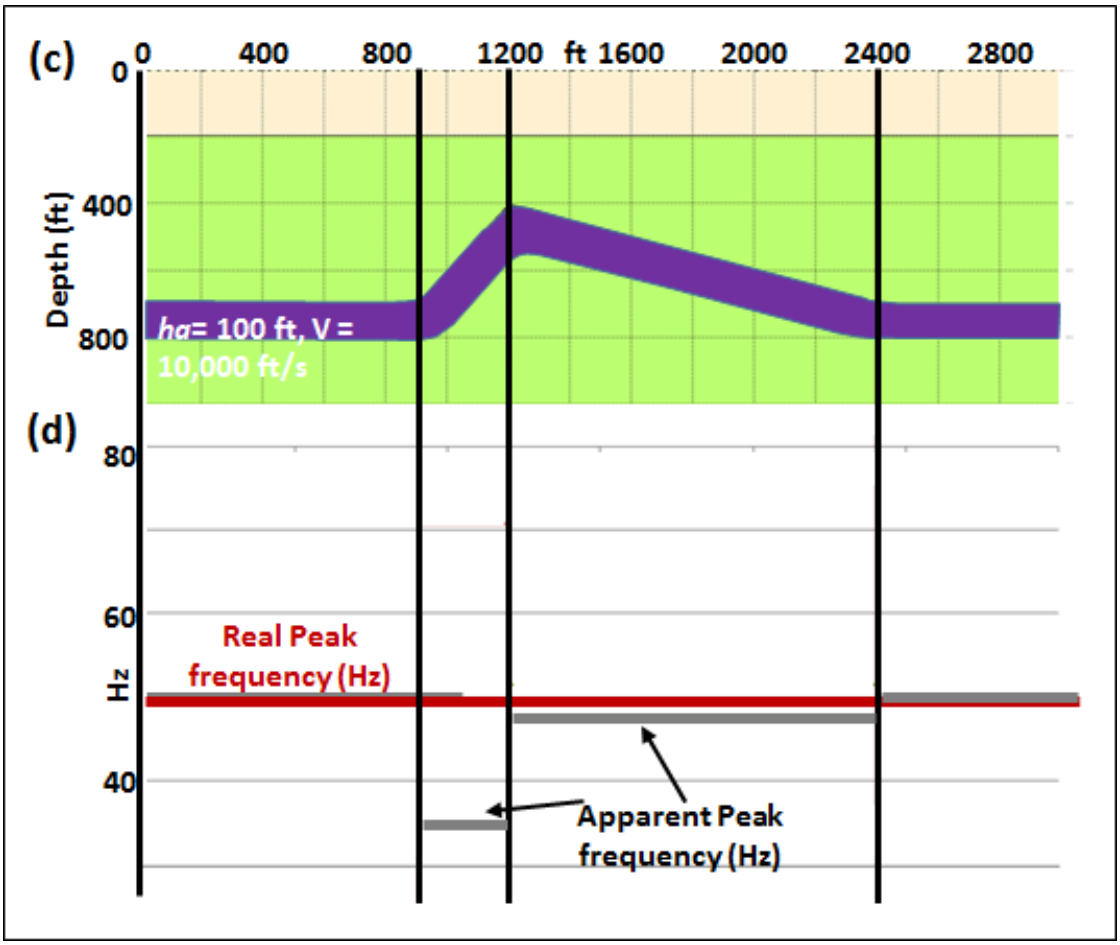

Figure 1.3. (a) A constant apparent thickness thin bed model showing a layer with flat dip, strong negative dip and moderate positive dip; (b) The real (marked by red line) tuning frequency (the apparent tuning frequency is 50 Hz) of the layer. (c) A constant real thickness thin bed model showing a layer with flat dip, strong negative dip and moderate positive dip; (d) The real (marked by red line) tuning frequency (the real tuning frequency is 50 Hz) of the layer.

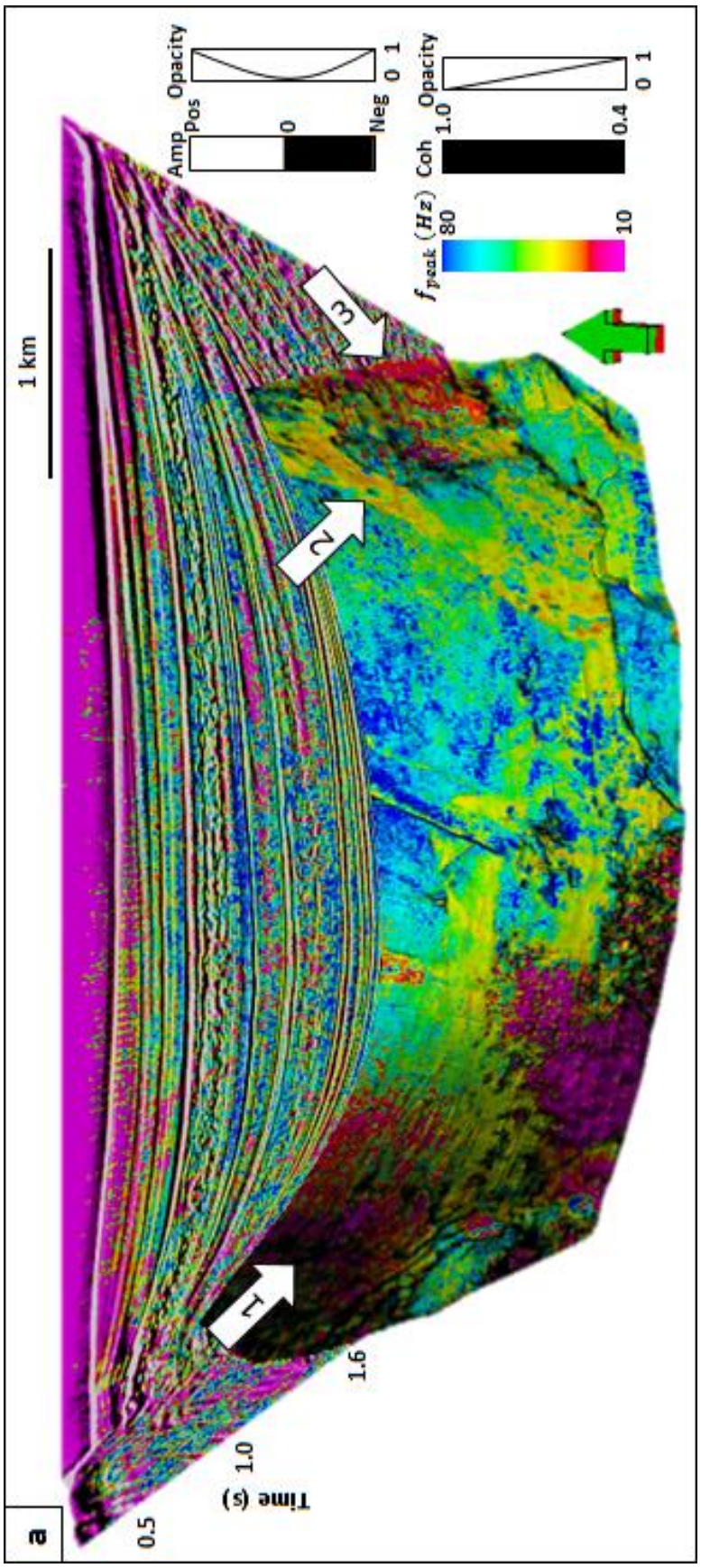
a
0.5
1.0
1.6
Time (s)
1 km
1
2
3
Amp
Pos
Neg
0
Opacity
0 1
Coh
1.0
0.4
Opacity
0 1
f_{peak} (Hz)
80
10

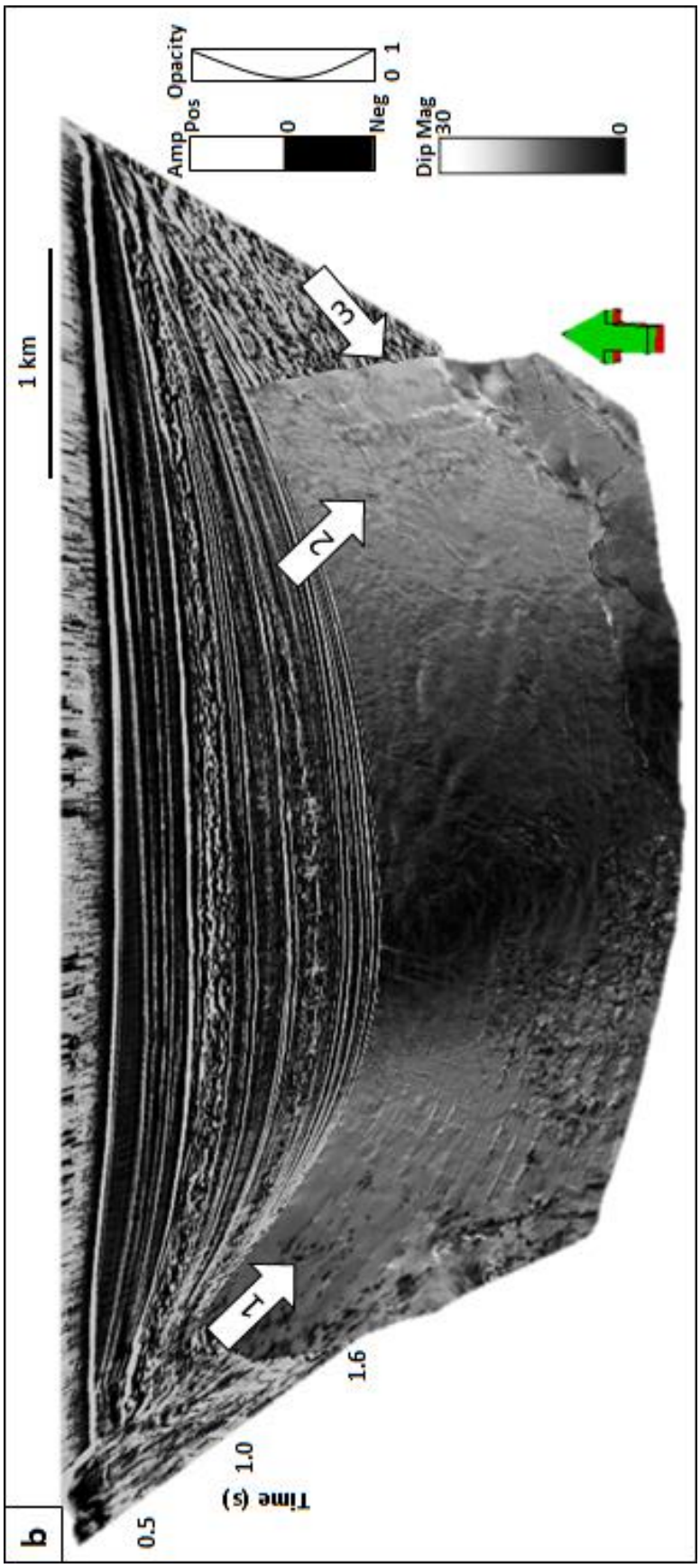
b
0.5
1.0
1.6
Time (s)
1 km
1
2
3
Amp
Pos
Neg
0
Opacity
0
1
Dip Mag
30
0

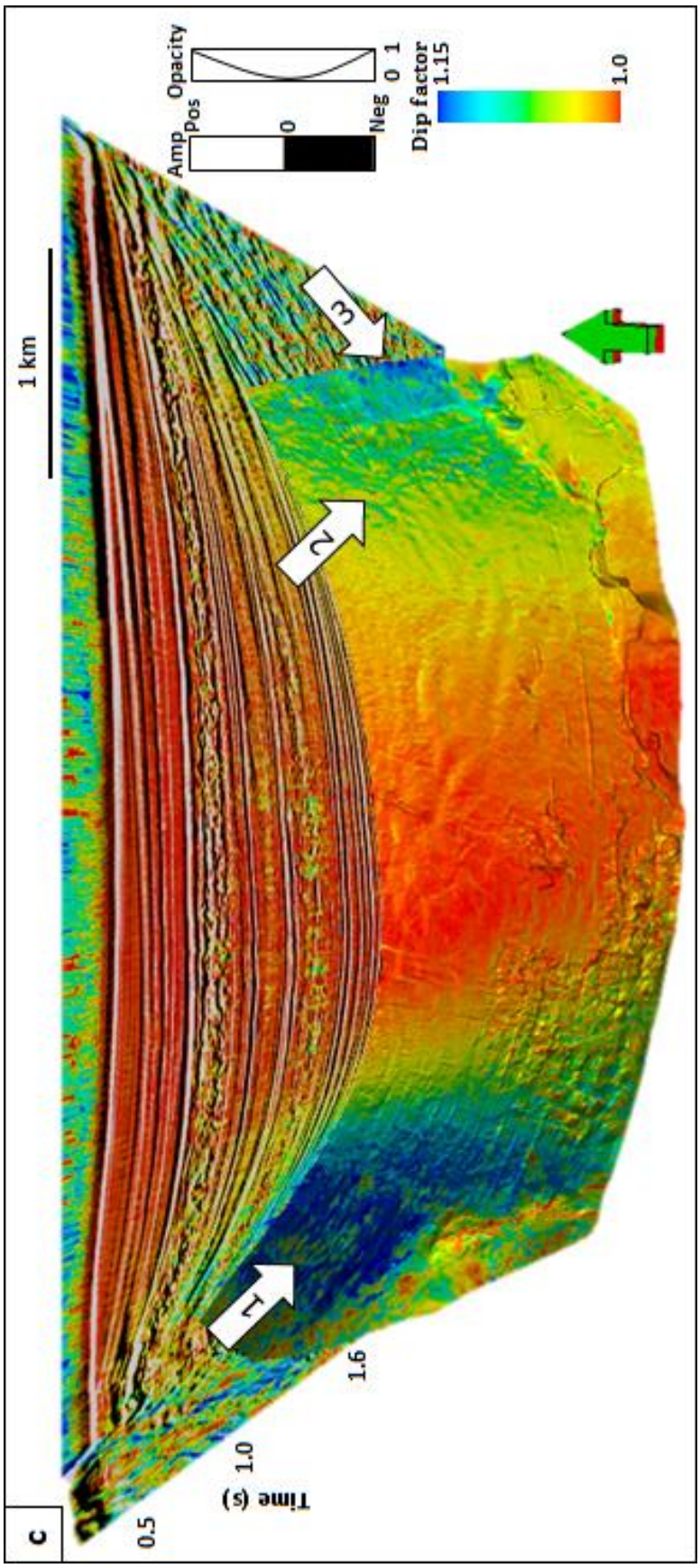
c
0.5
1.0
1.6
Time (s)
1 km
1
2
3
Amp
Pos
0
Neg
Opacity
0 1
Dip factor
1.15
1.0

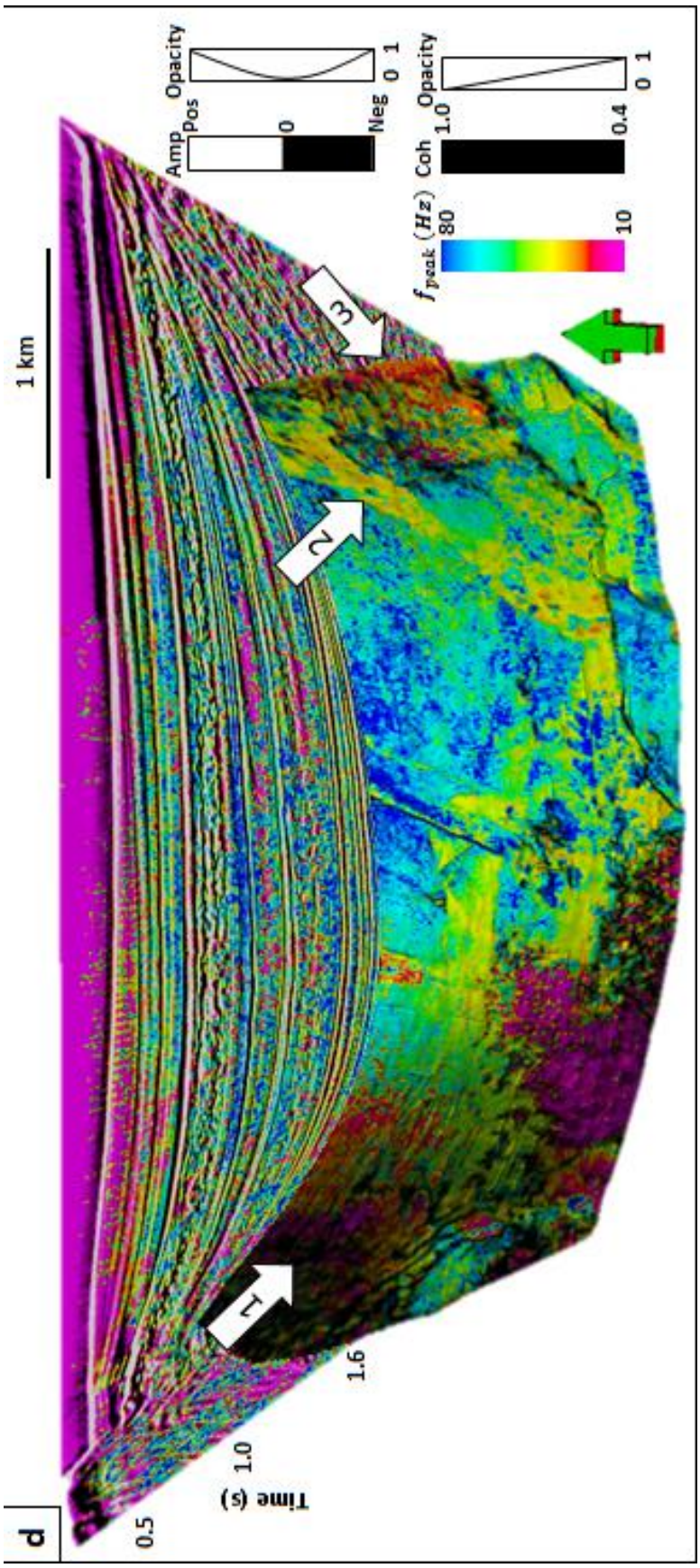
d
Time (s)
0.5
1.0
1.6
1 km
1
2
3
Amp
Pos
0
Neg
Opacity
0 1
Coh
1.0
0.4
Opacity
0 1
f_{peak} (Hz)
80
10

Figure 1.4. Vertical and horizon slice through (a) peak frequency, (b) dip magnitude, θ, (c) dip compensation factor and (d) corrected peak frequency. White arrows in (a) show a decrease in peak frequency indicating layer thickening towards the basin edges. After correction by $1/\cos\theta$ we see in (d) an increase in peak frequency indicating layer thinning towards the minibasin edges consistent with decreased accommodation space. (Data Courtesy of PGS).

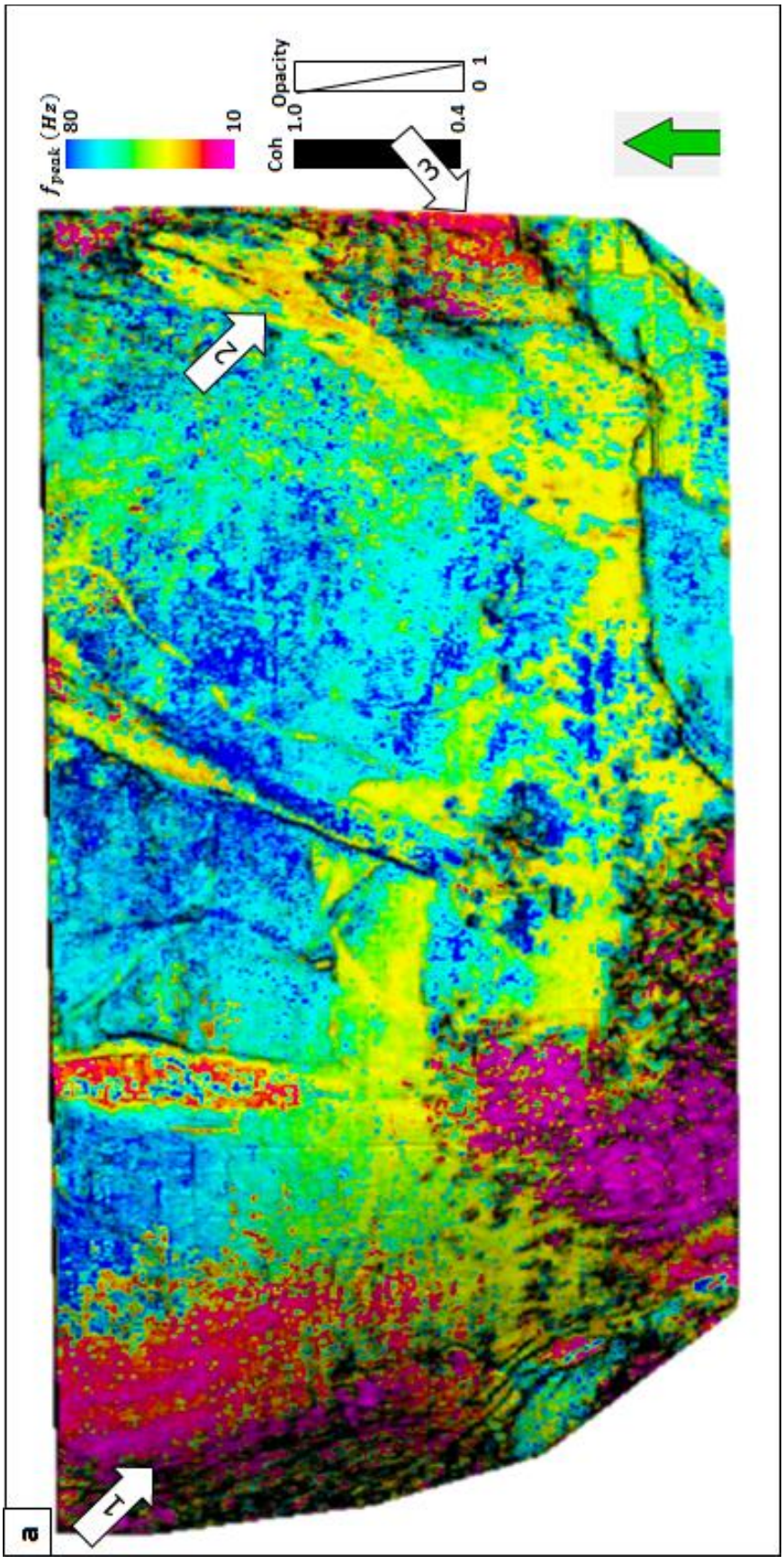
f_{peak} (Hz)
80
10
Coh
1.0
0.4
Opacity
0
1
1
2
3
a

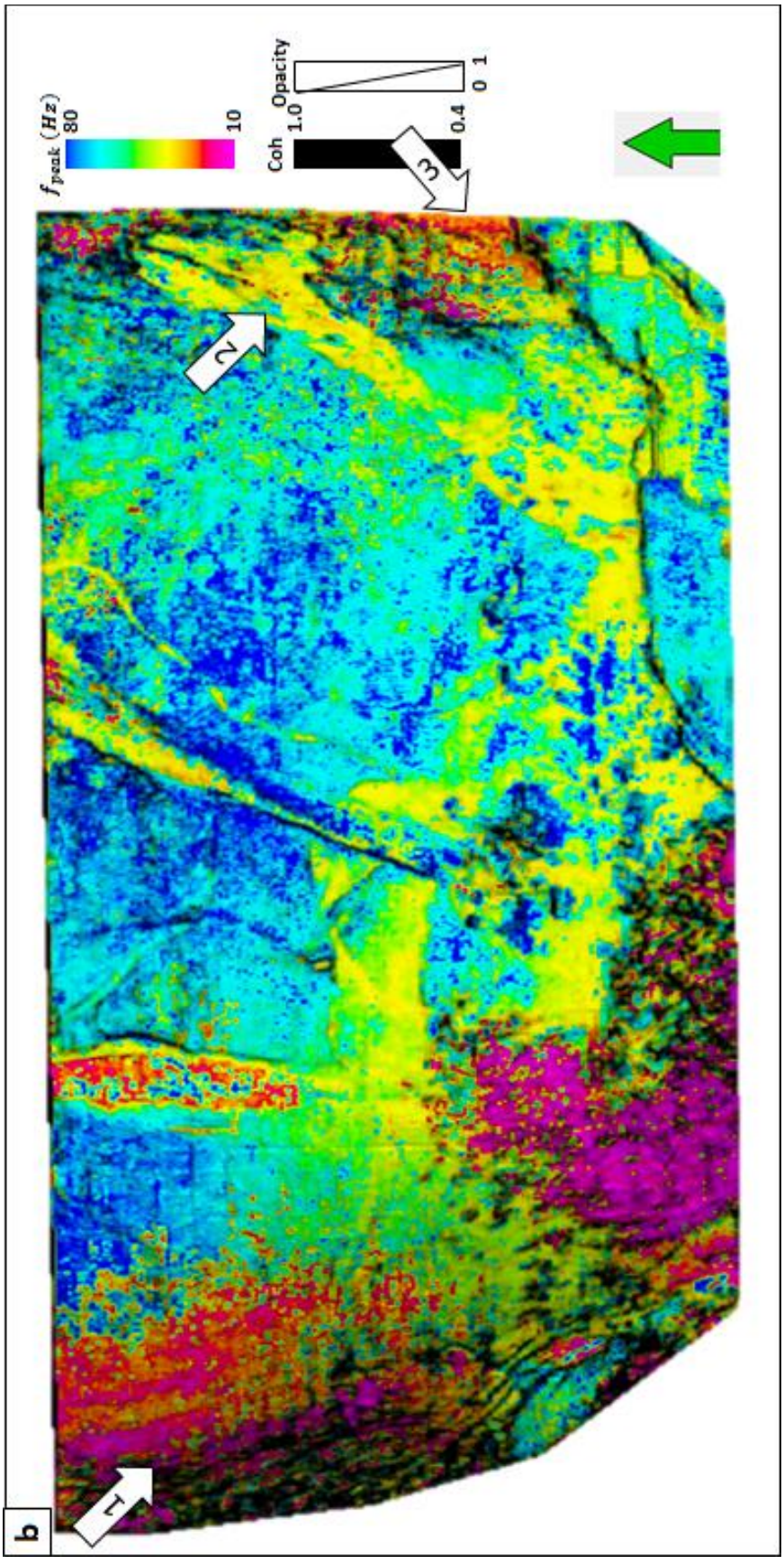
b
f_{peak} (Hz)
80
10
Coh
1.0
0.4
Opacity
0
1
1
2
3

Figure 1.5 Horizon slice through (a) peak frequency and (b) corrected peak frequency. White arrows in (a) show a decrease in peak frequency of the channel. After correction by $1/\cos\theta$ we see in (b) an increase in peak frequency indicating layer thinning towards the minibasin edges consistent with decreased accommodation space. (Data Courtesy of PGS).

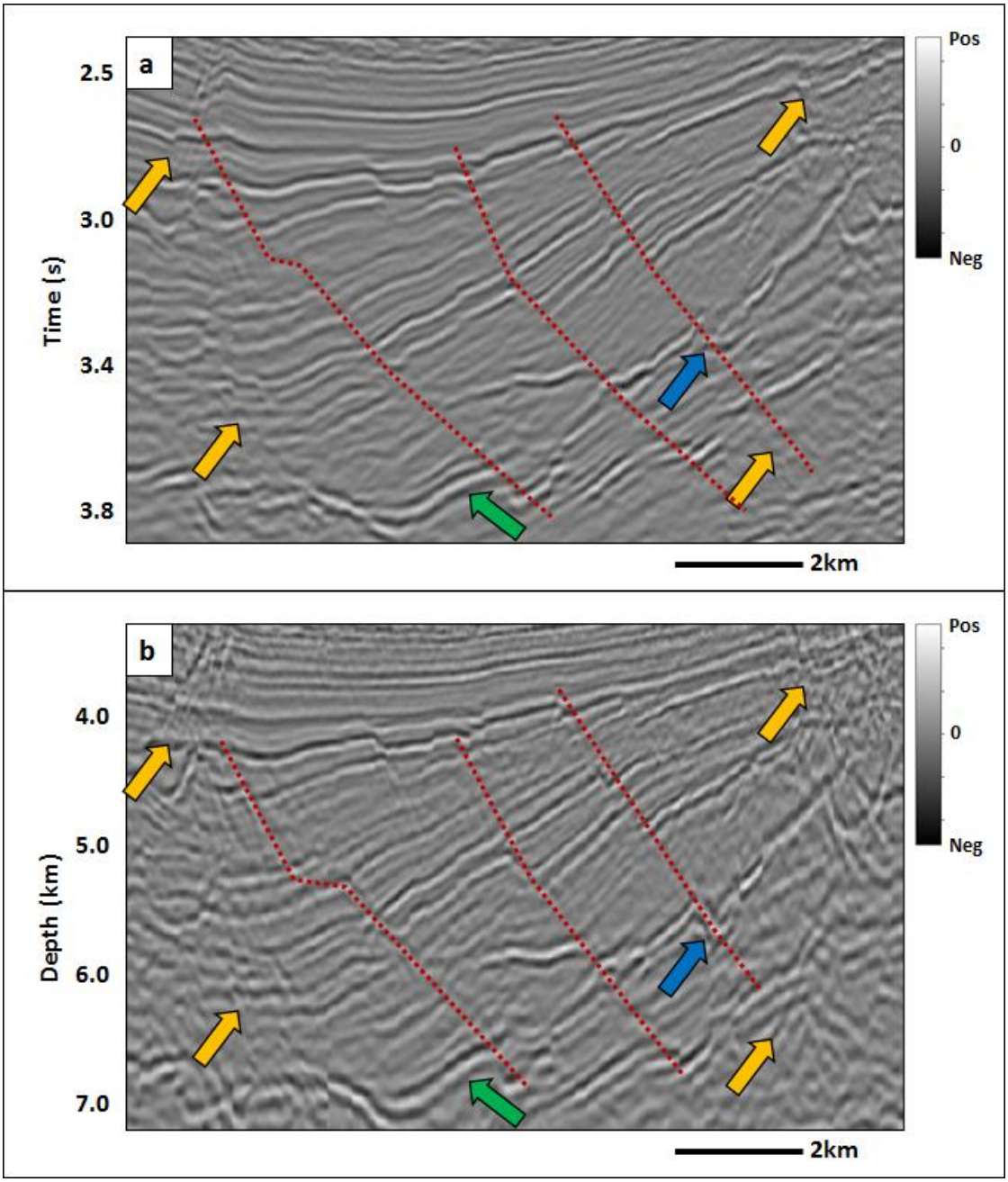

Figure 1.6. Vertical slice through (a) time- and (b) depth-migrated data.

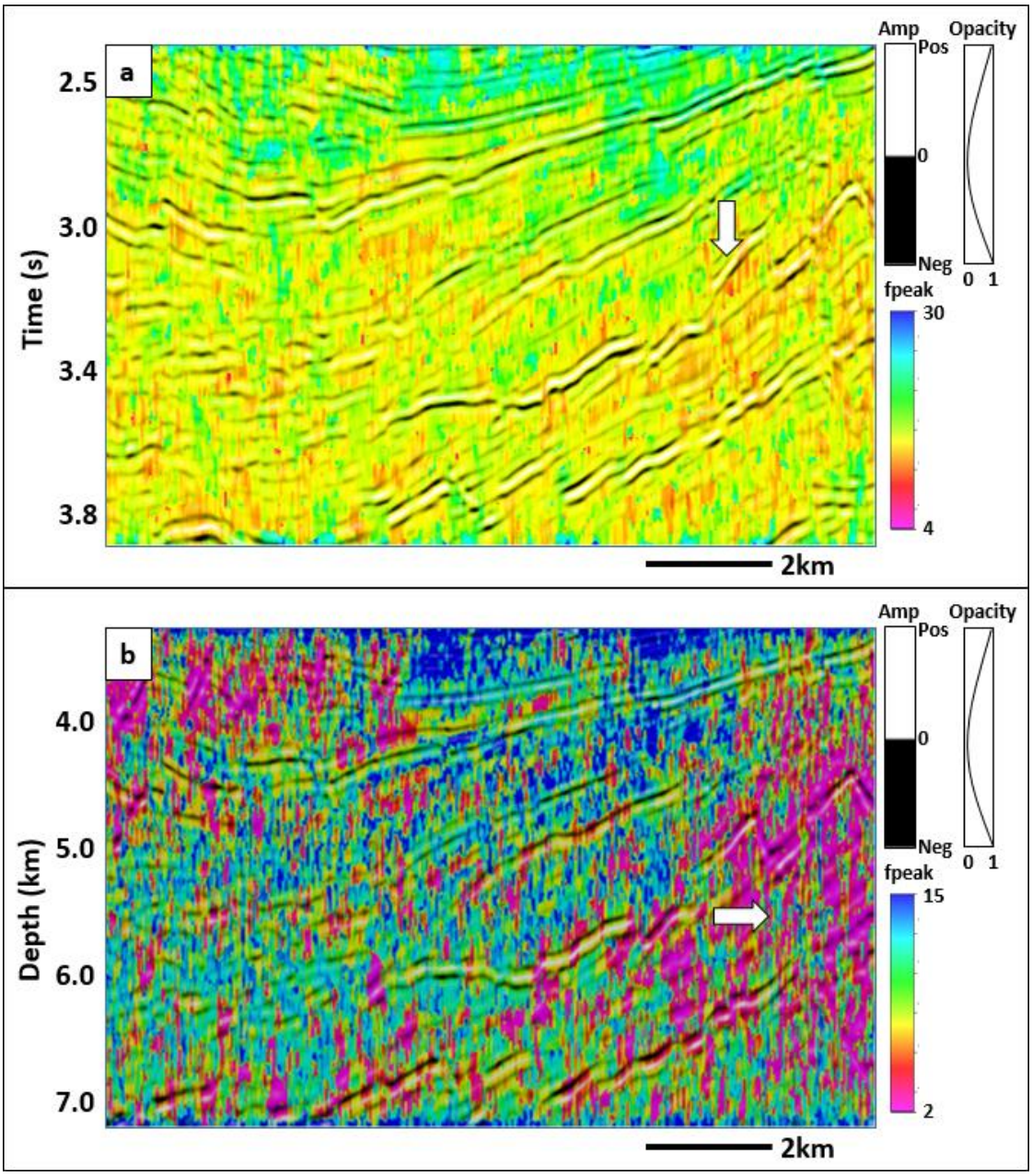

Figure 1.7. Apparent peak frequency blended with seismic amplitude of (a) time- and (b) depth-migrated data.

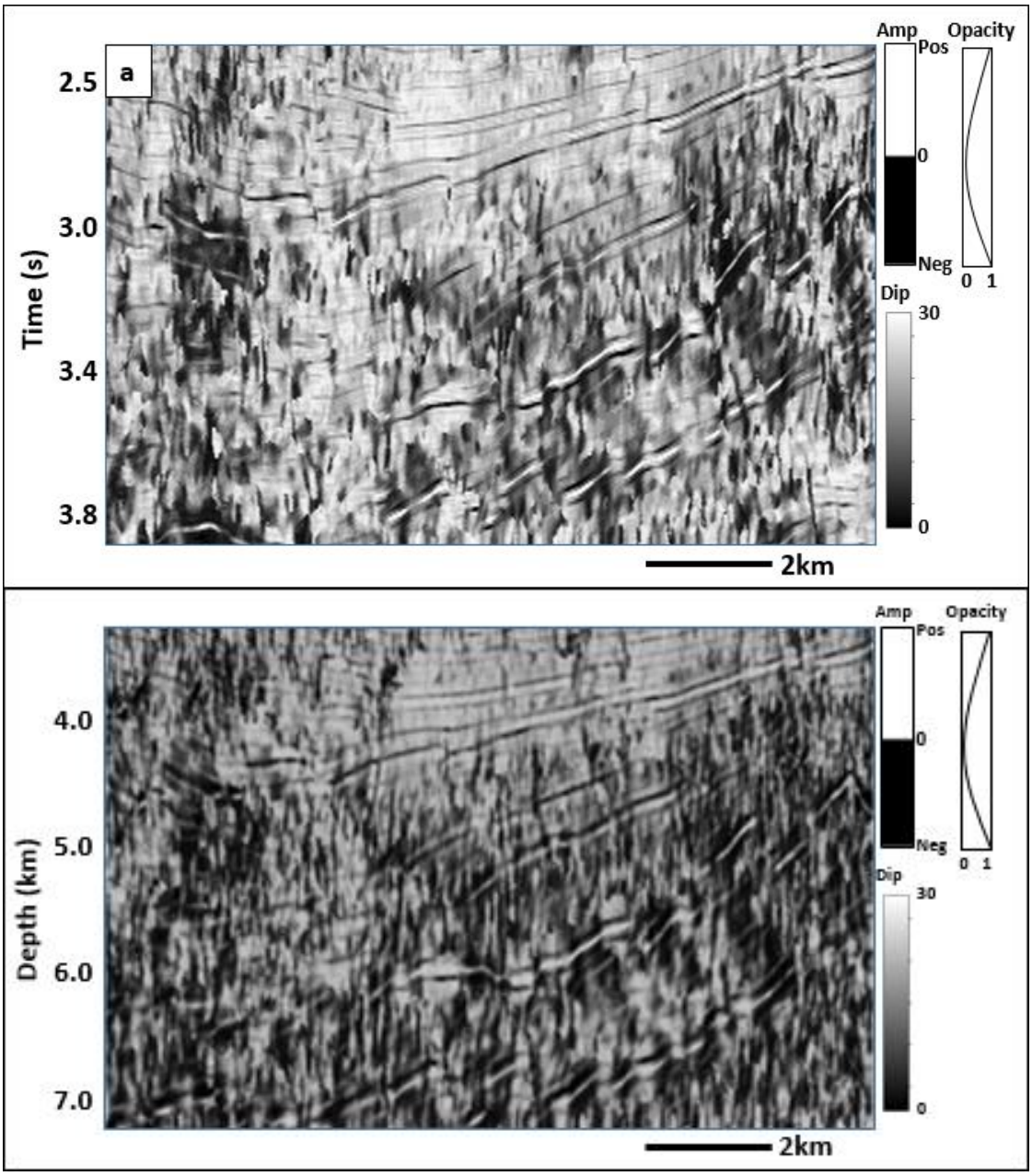

Figure 1.8. Dip magnitude ($1/\cos\theta$) blended with seismic amplitude of (a) time- and (b) depth-migrated data.

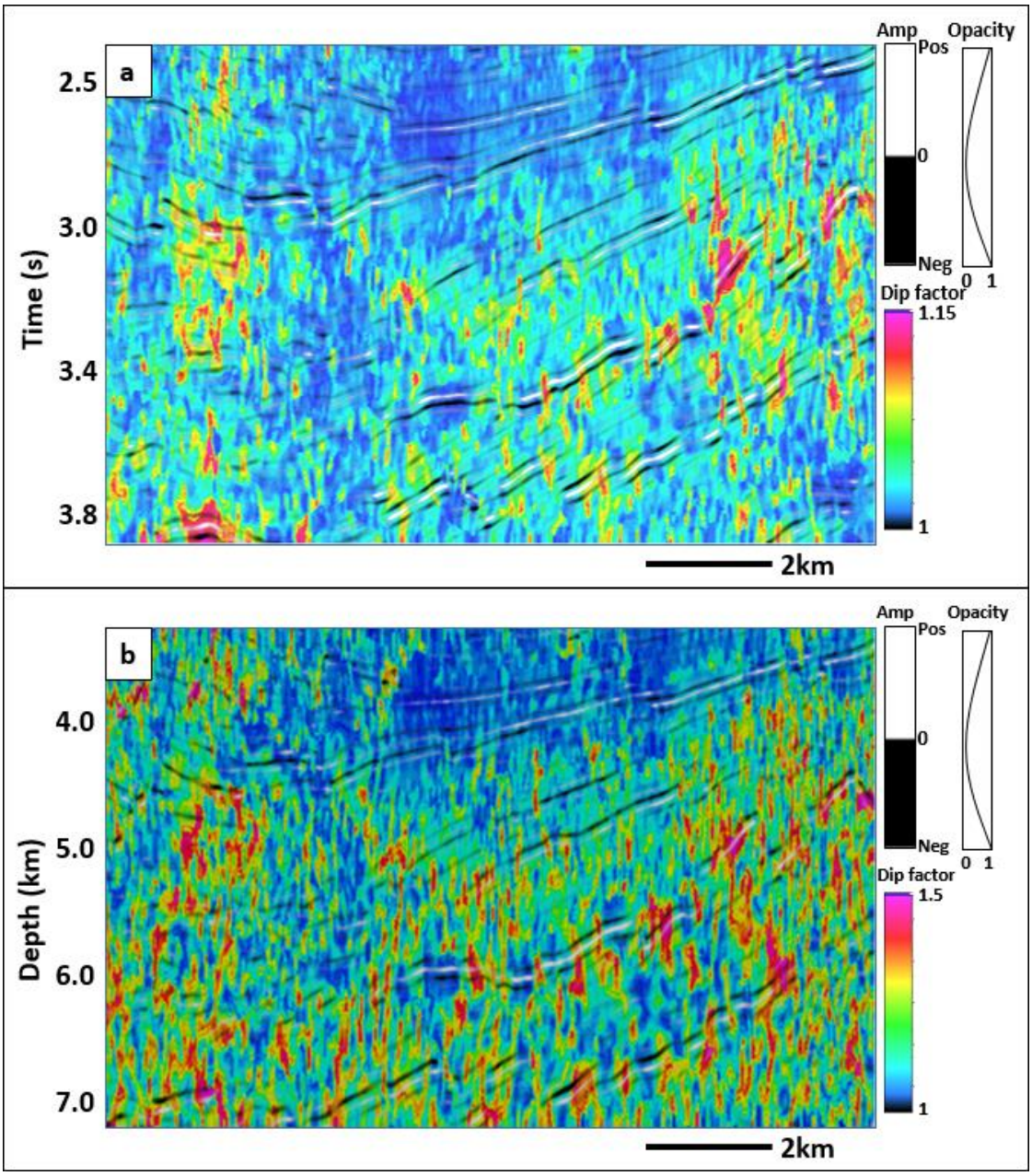

Figure 1.9. Dip compensation factor ($1/\cos\theta$) blended with seismic amplitude of (a) time- and (b) depth-migrated data.

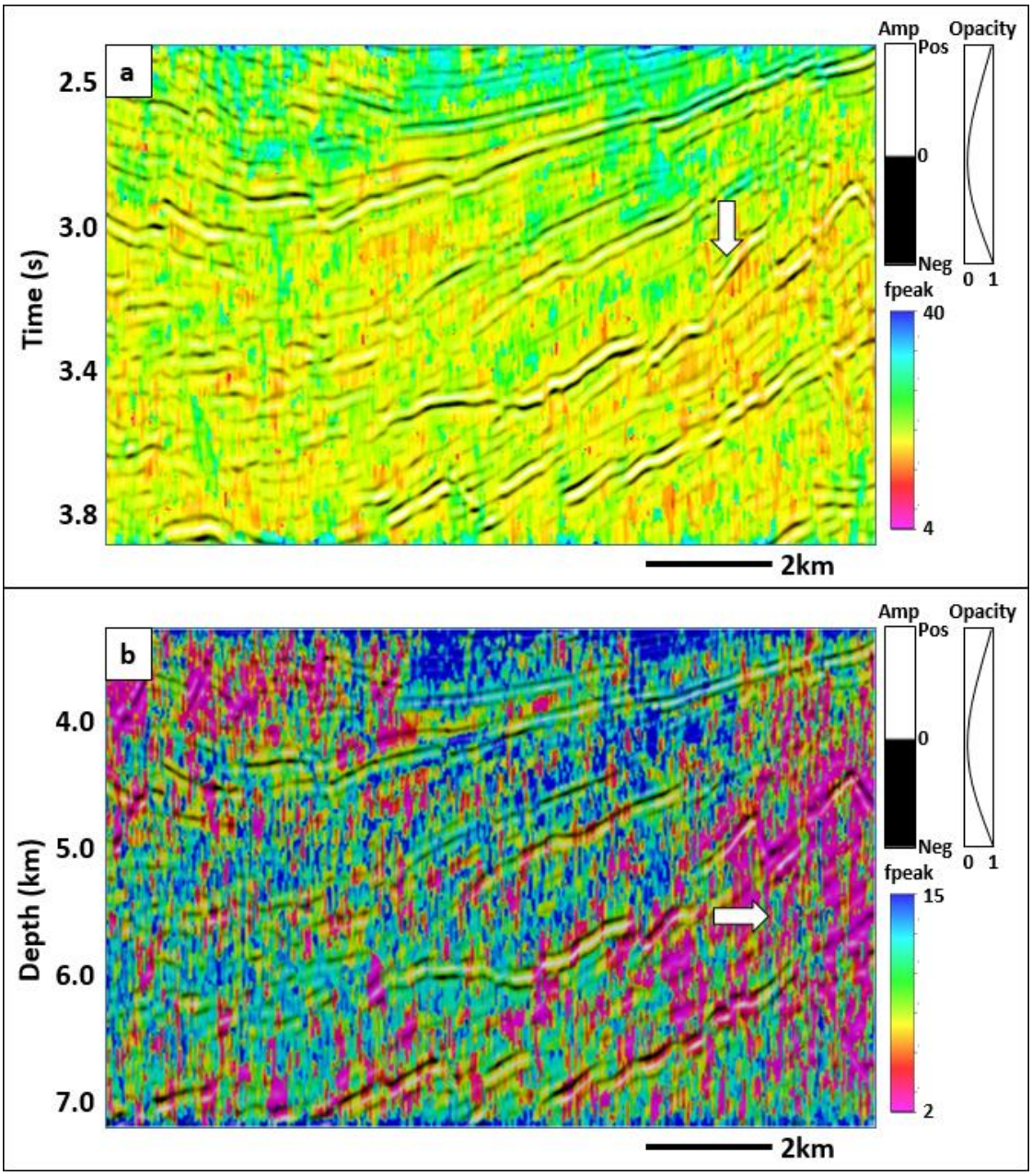

Figure 1.10. Dip-corrected peak frequency blended with seismic amplitude of (a) time- and (b) depth-migrated data.

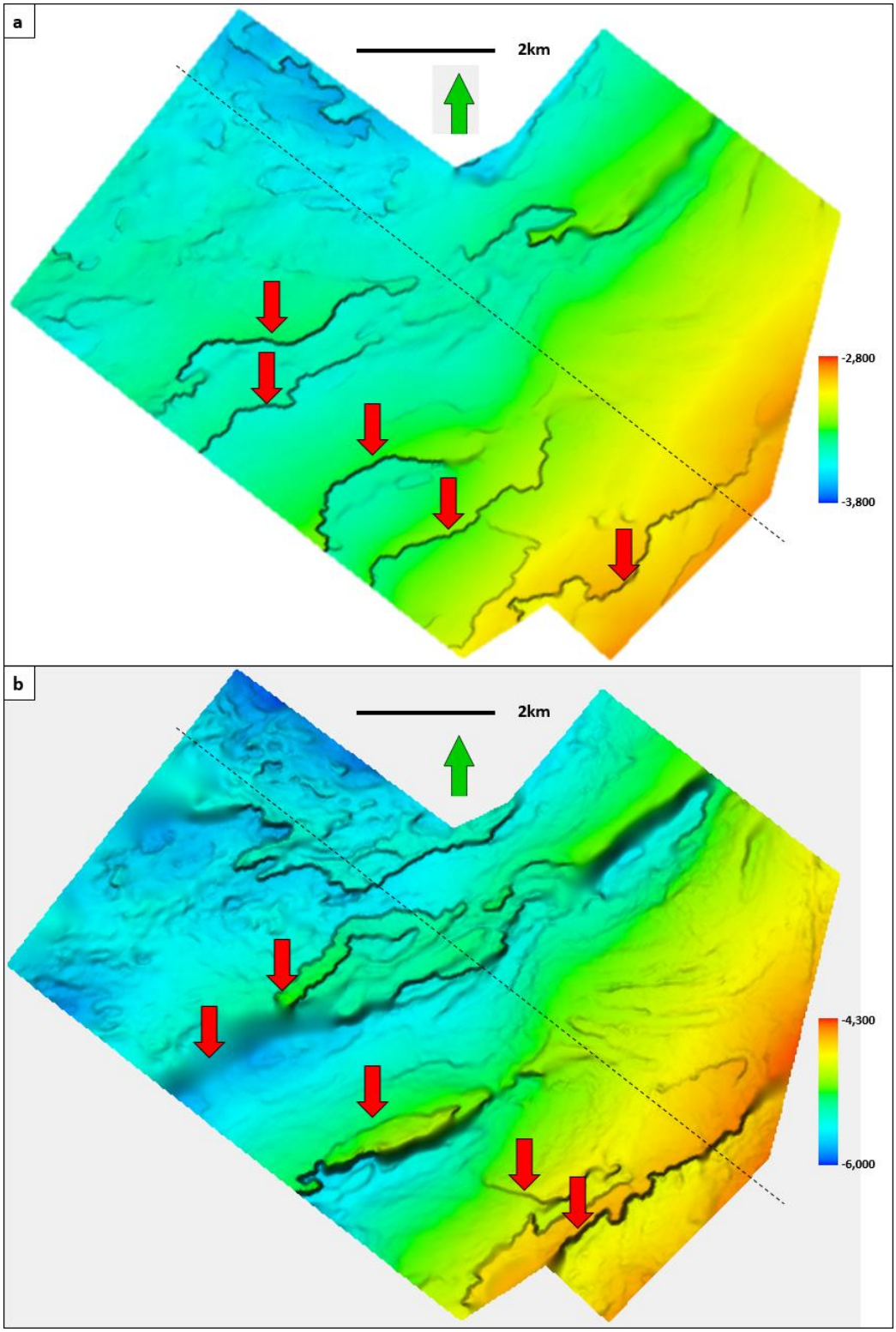

Figure 1.11. Time-structure map of Horizon A through (a) time- and (b) depth-migrated data.

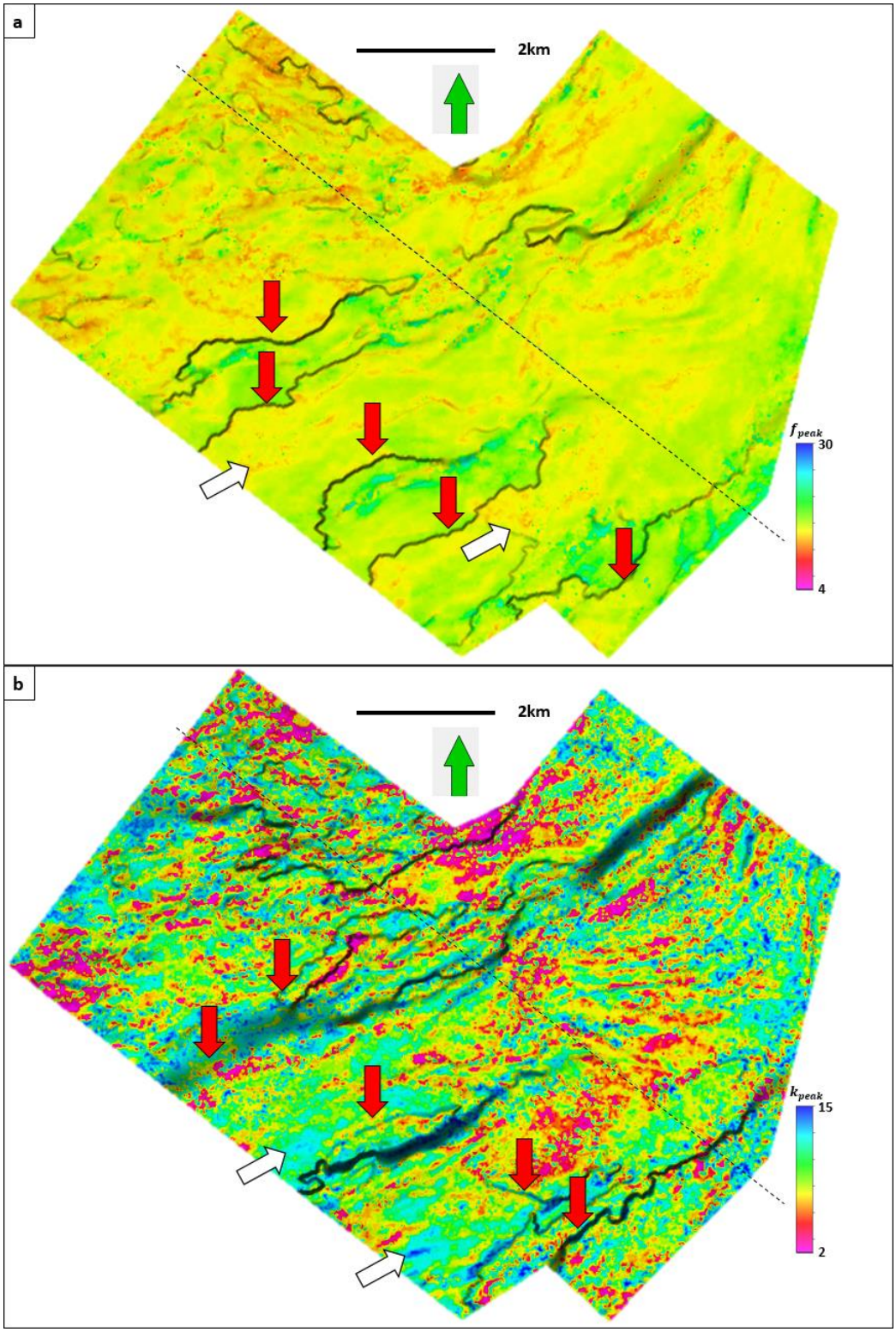

Figure 1.12. Apparent peak frequency along Horizon A of (a) time- and (b) depth-migrated data.

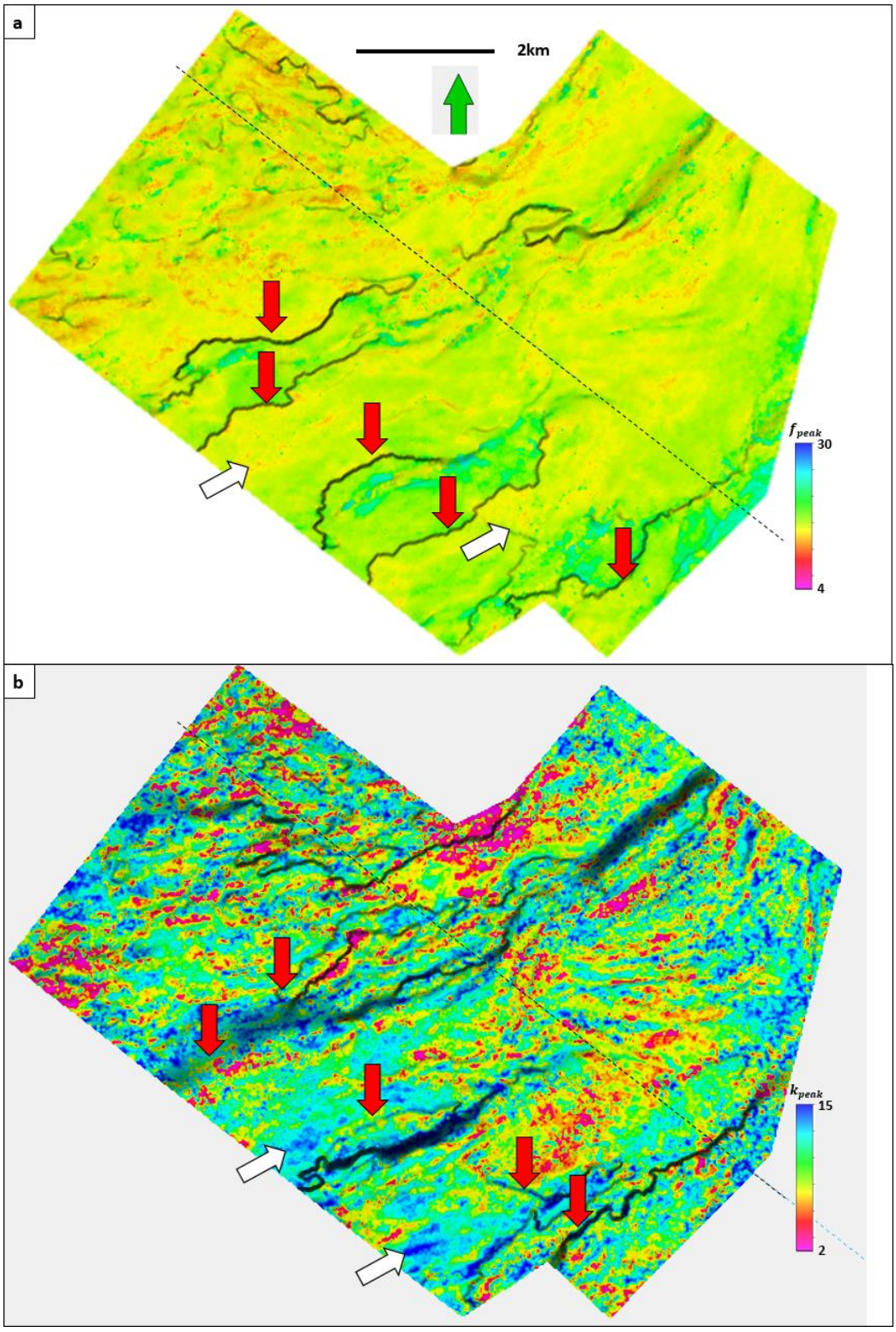

Figure 1.13. True peak frequency along Horizon A of (a) time- and (b) depth-migrated data

REFFERENCES

Bahorich, M., A. Motsch, K. Laughlin, and G. Partyka, 2002, Amplitude responses image reservoir: Hart's E&P, January, 59-61.

Davogustto D., MC de Matos, C Cabarcas, T Dao and K. J. Marfurt, 2013, Resolving subtle stratigraphic features using spectral ridges and phase residues: Interpretation, **1**(1), 93-108.

Leppard, C., A. Eckersley, and S. Purves, 2010, Quantifying the temporal and spatial extent of depositional and structural elements in 3D seismic data using spectral decomposition and multi-attribute RGB, in L. J. Wood, T. T. Simo, and N. C. Rosen, eds., Seismic imaging of depositional and geomorphic systems: 30th Annual GCSSEPM Foundation Bob F. Perkins Research Conference, 1-10.

Lin, T., 2013, Spectral decomposition of time- vs. depth-migrated data: 83th Annual International Meeting, SEG, Expanded Abstracts, 1384-1388.

Liu, J. L., and K. J. Marfurt, 2007, Multi-color display of spectral attributes: The Leading Edge, 268-271.

Partyka, G., J. Gridley, and J. A. Lopez, 1999, Interpretational applications of spectral decomposition in reservoir characterization: The Leading Edge, **18**, 353-360.

Peyton, L., R. Bottjer, and G. Partyka, 1998, Interpretation of incised valleys using new 3D seismic techniques: A case history using spectral decomposition and coherency: The Leading Edge, **17**, 1294-1298.

Puryear, C. I., S. Tai and J.P Castagna, 2008, Comparison of frequency attributes from CWT and MPD spectral decompositions of a complex turbidities channel model: 78th Annual International Meeting, SEG, Expanded Abstracts, 393– 396.

Widess, M. B., 1973, How thin is a thin bed? : Geophysics, **38**, 1176-1254.

CHAPTER 2

QUANTIFYING THE SIGNIFICANCE OF COHERENCE ANOMALIES

Tengfei Lin[1], Thang Ha[1], Kurt J. Marfurt [1] and Kevin L Deal[2]

[1]University of Oklahoma, ConocoPhillips School of Geology and Geophysics,

[2]Chevron Company.

This paper was published by the AAPG-SEG journal *Interpretation* in May 2016.

doi: 10.1190/INT-2015-0102.1

ABSTRACT

Semblance and other coherence measures are routinely used in seismic processing such as velocity spectra analysis, in seismic interpretation to estimate volumetric dip and to delineate geologic boundaries, and in poststack and prestack data conditioning such as edge-preserving structure-oriented filtering. While interpreters readily understand the significance of outliers for such measures as seismic amplitude being described by a Gaussian (or normal) distribution, and RMS amplitude by a log-normal distribution, the measurement significance of a given coherence of post stack seismic data is much more difficult to grasp.

We follow early work on the significance of events seen in semblance-based velocity spectra and use an F-statistic to quantify the significance of coherence measures at each voxel. The accuracy and resolution of such measures depend on the bandwidth of the data, the signal-to-noise ratio, and the size of the spatial and temporal analysis windows used in their numerical estimation. In 3D interpretation, low-coherence estimates not only seismic noise, but also geologic signal, such as fault planes and channel edges.

We therefore estimate the signal to noise ratio as the product of coherence and two alternative measures of randomness – the first being the disorder attribute and the second estimate based on eigenvalues of a window of coherence values. The disorder

attribute is fast and easy to compute while the eigenvalue calculation is computationally intensive and more accurate.

We demonstrate the value of this measure through application to two 3D surveys, where we modulate coherence measures by our F-statistic measure to show where discontinuities are significant and where they correspond to more chaotic features.

LIST OF KEYWORDS

Seismic Attributes, Significance, Coherence.

INTRODUCTION

Semblance and other coherence measures are routinely used in seismic processing such as velocity spectra analysis (Taner and Koehler, 1969; Neidell and Taner, 1971), seismic edge detection and volumetric dip estimation (Marfurt et al., 1998), and edge-preserving structure-oriented filtering (Hoecker and Fehmers, 2002; Marfurt, 2006). The application of seismic attributes to depth-migrated data where the wavelength extend by increasing velocity with depth justifies the use of data-adaptive analysis windows, where the window size is proportional to a percentile of the time- or time and space-varying spectra (Lin et al., 2014 and 2015).

In this paper, we reexamine the analysis by Douze and Laster (1979) on the significance of velocity-based semblance analysis in order to evaluate the significance of coherence anomalies within a noisy background, and the choice of parameters for structure-oriented filtering. These same concepts are readily generalized to eigen-structure type coherence estimates.

We begin with a summary of semblance and KL-filter (energy ratio) coherence algorithms as well as the use of the F-statistic. The F-statistic requires an estimate of the signal-to-noise ratio. We therefore evaluate Al-Dossary et al.'s (2014) disorder attribute and introduce a new signal-to-noise estimate based on the eigenvalues computed from a window of coherence. With these definitions in place, we apply our

new metric to a coherence volume computed from a survey acquired in China. We conclude with a discussion on how such estimates may be useful in risk analysis, differentiating different geologic features by their coherence expression, and for improved edge-preserving smoothing applications.

THEORETICAL ANALYSIS

Following Douze and Laster (1979) work, we generate a suite of figures to show the significance of typical windows used in edge detection and structure-oriented filtering. First, we define the significance of similarity (coherence) as the cumulative probability of a non-central F-distribution. A high value of significance means the calculation of similarity is more reliable. In contrast, a low value of significance always indicates an unreliable similarity value. The range of the significance is 0~1 (see Appendix).

Examining equation (22), we identify four basic parameters in computing significance: bandwidth, f_B, temporal analysis window size, $2K\Delta t$, spatial analysis window size, J, and the signal to noise ratio, S/N. With these values we can compute the significance of a given semblance estimate using the non-central F-distribution. The product of the bandwidth and the vertical analysis window $2K\Delta t f_B$ determines the first degree of freedom, the number of seismic traces, J, determines the second degree of freedom; while S/N determines the non-centrality parameter.

Douze and Laster (1979) demonstrate that the correlation between bandlimited experimental data and the theoretical cumulative probability distribution for broad band data is quite good, allowing us to use this formalism for not only their velocity anomalies, but also our coherence attribute and structure-oriented filtering application.

Meanwhile, considering the complex of the significance algorithms, the calculation takes five times longer than the coherence code for typical parameters.

APPLICATIONS

Example 1: A 2D Synthetic of a Normally Faulted Layers

Figure 2.2a shows a simple model used to generate a suite of 200 finite difference common shot gathers. These gathers were then prestack time-migrated to generate the image shown in Figure 2.2b. There are five main layers B, C, and D, each of which contains five sub-layers. To address the issue of signal to noise, we also added different levels of bandlimited incoherent noise in layers B and C. The white arrow indicates a fault plane reflection.

The images in Figure 2.3 form a matrix with vertical window sizes corresponding to 0, 10 and 20ms along column, and lateral window sizes of 5, 9 and 13 analysis points along rows, by blending the similarity and the significance of coherence to illustrate the influence of spatial (number of seismic traces) and temporal analysis window size on the significance of similarity. With the increase of temporal analysis window size, the significance value of similarity is higher, which indicates that the coherence value is more reliable. The increase in the number of seismic traces shows a similar phenomenon, but the resolution of the fault zone decreases.

Example 2: 3D Seismic Data over Bohai Bay Basin, China

We next compute the significance coherence computed from a 3D seismic volume acquired over Bohai Bay Basin, China that images a channel reservoir. Given the influence of d_1 (the vertical analysis window size) on significance, we introduce a self-adaptive window attribute calculation, defining the temporal window to be propotional to the average frequency of each time slice. Figure 2.4 shows time slices at t = 0.5 s through seismic amplitde, peak frequency and spectral bandwidth volumes using matching pursuit algorithm. The black arrow indicates a fault, the red arrow a channel, the blue arrow an oxbow which can be clearly seen in the coherence image shown in Figure 2.5.

Figure 2.5 shows slices at t = 0.5 s through coherence volumes computed using a self-adaptive temporal analysis window size, respectively. Black arrows indicate the main fault through the seismic slice. The inner bank of the oxbow lake can be indicated by the blue, and three distinguished channels by the red arrows.

Figure 2.6 shows the *S/N* corresponding to Figure 2.5 computed using equation (11). The temporal analysis window size not only affects the degrees of freedom, but also influences *S/N*, which indirectly controls the non-centrality parameter, ε.

Figure 2.7 shows the sensitivity of significance to temporal analysis window size and bandwidth. Black arrows indicate the faults characterized by low coherence and significance. Red arrows indicate channel deposition or sheet sand characterized

by high coherence and high significance. By computing the variable bandwidth and using a self-adaptive temporal analysis window size, we are able to improve the significance of coherence image, while maintaining the sharp contrast of faults and channel edges.

Example 3: Structure-Oriented Filtering Based on the Statistical Significance of Coherence

We now apply the significance analysis of coherence to a 3D seismic volume provided by Schlumberger. Figure 2.8 shows a time slice at t = 0.7 s through seismic amplitude, a white arrow indicates a meandering channel, orange arrows three main faults and red arrows North-South acquisition footprint noise.

Figure 2.9 shows the coherence slices corresponding to Figure 2.8 using different color bar, that aids in illustrating the interactive workflow of structure-oriented filtering used to define weights, w, for the similarity data volumes (Davogustto and Marfurt, 2011), using the color bar to choose appropriate color ramp values of s_{low} and s_{high}. Specifically, we set the color to be white if $s > s_{high}$, black if $s < s_{low}$ and shades of gray if $s_{low} < s < s_{high}$. The resulting image will be the weights applied to the filtered data on output such that all black discontinuities will be preserved and all white areas will be filtered.

By modifying the threshold values for s, we increase or decrease the smoothing weights thereby changing the aggressiveness of the filter. In Figure 2.9a (s_{high}=0.9, s_{low}=0.7), we adjust the color bar to enhance the footprint noise (red arrows) as well as structural and stratigraphic features (white and orange arrows). Figure 2.9b (s_{high}=0.99, s_{low}=0.97) indicates the preservation of structures indicated by green arrows, greater improvement of features indicated by blue arrows, and clearer suppression of the footprint noise in the significance of coherence slice. Furthermore, according to the definition of the significance of the coherence, it shows us the statistical conclusion, which holds physical meaning. By estimating the significance of coherence, we can easily suppress the footprint noise as well as other radom noise, because they can be seperated from structural anomlies compared with the ones in coherence. Consequently, more null hypothesis (no anomaly) are rejected in structure-oriented filtering using significance than statistical significance of coherence, which can be found the in Figure 2.10.

Figures 2.10a and b show the result of filtering the data in Figure 2.8 using structure-oriented filtering based on similarity and statistical significance of coherence. Red arrows in Figure 2.8 indicate footprint, the amplitude of the footprint Figure 2.10 is diminished while the sturctural features are sharpened. While there are still remnants of footprint noise visible in Figure 2.10a , it is almost removed in Figure 2.10b using the significance low threshold. Yellow arrows indicate residual footprint noise that can not be removed, this is because the values of the coherence and

significance of the artifacts are similar to those of the stratigraphic features. We have to keep the artifacts features in order to preserve the real features of coherence.

CONCLUSIONS

We have generalized analysis on the significance of velocity spectra to grantify the significance of coherence anomalies used in 3D interpretation and to control structure-oriented filtering. Four factors control the significance calculation: vertical window size, bandwidth, the number of seismic traces number and the *S/N*. The vertical window size is the most important of these four factors, and plays an important role in both the degrees of the freedom as well as the non-centrality parameter: ε. We estimate the signal to noise ratio using a dissimilarity calculation. This estimate is the data adaptive windows improve the significance. Besides, the estimation of significance is subjected to the calculation cost; while equally important, the use of significance helps determine parameters for edge-preserving structure oriented filtering. The footprint noise as well as other radom noise can be distinguished from structural anomalies contrast to the one as shown in coherence. Therefore, more null hypothesis (no anomaly) can be rejected in structure-oriented filtering using statistical significance of coherence than the one using statistical significance of coherence. In the future, we will keep our study in realizing the variable-horizontal window size.

ACKNOWLEDGEMENTS

We thank Schlumberger, for the use of the seismic data set in Westcam survey, and BGP Inc., for the use of their Bohai Bay Basin data set. Numerical model was generated using Tesseral's Tesseral 2D software. Seismic displays were generated used Schlumberger's Petrel software. We also thank the sponsors of Attribute-Assisted Seismic Processing and Interpretation Consortium (AASPI) for their guidance and financial support.

CHAPTER 2 FIGURES

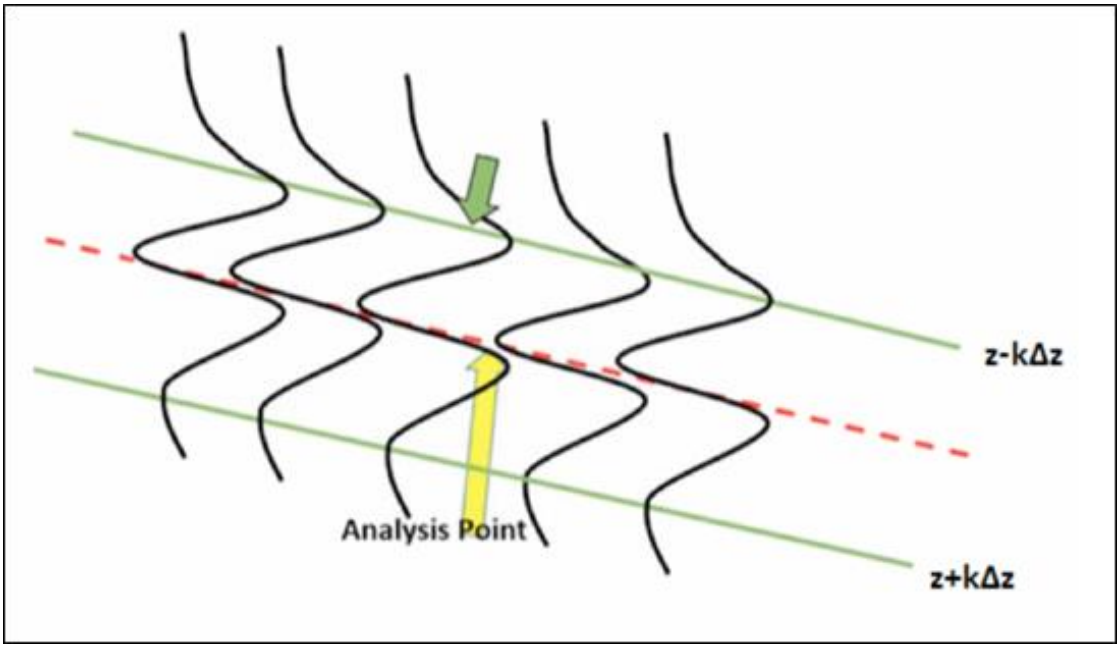

Figure 2.1. 2D diagram of similarity calculation.

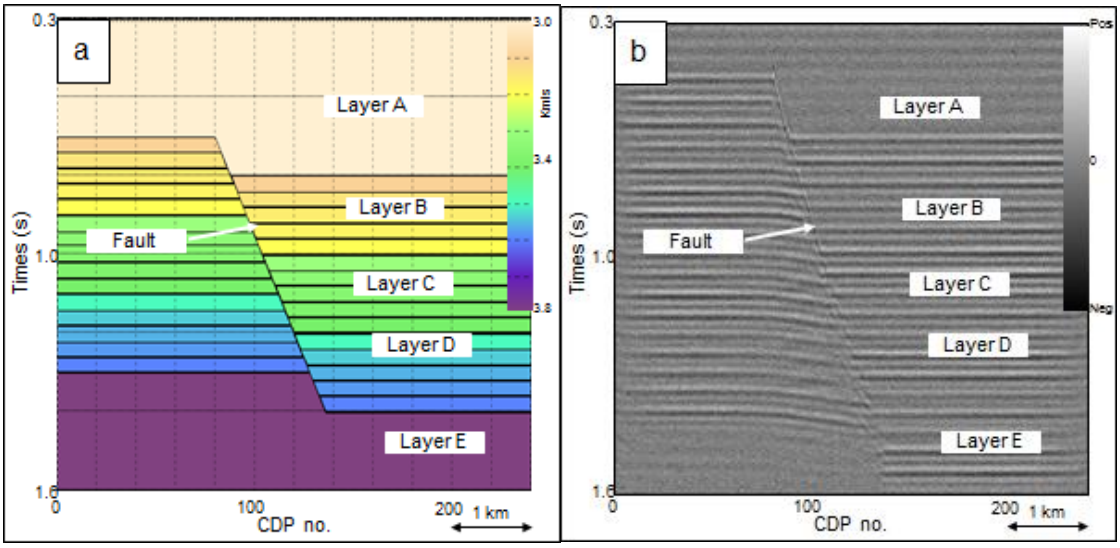

Figure 2.2. (a) The fault model and (b) the resulting image after forward modeling using a finite difference algorithm and prestack Kirchhoff time migration. Bandlimited random noise has been added resulting in P_S/P_N = 1.0.

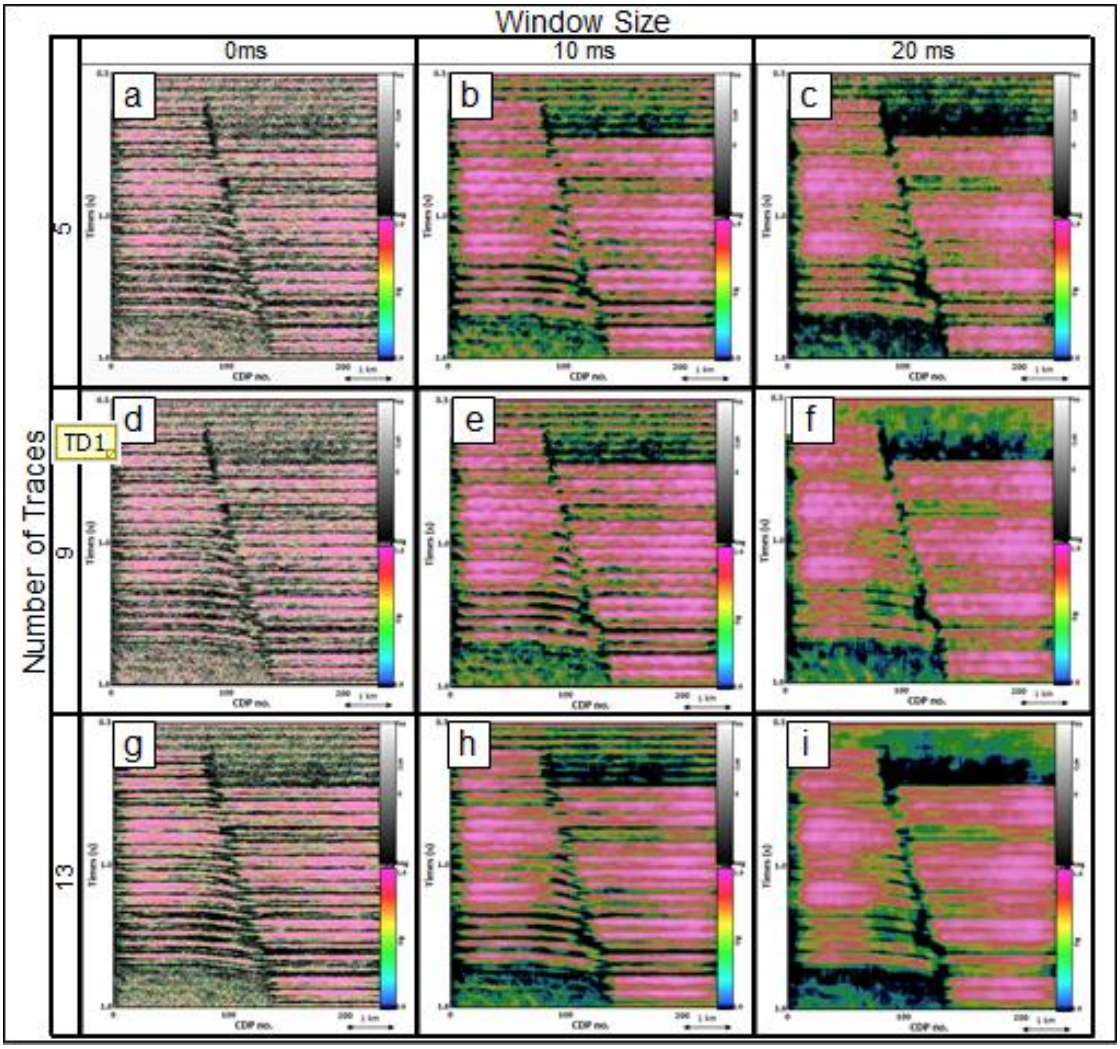

Figure 2.3. Vertical slices through similarity blended with significance of coherence computed from the seismic data shown in Figure 2.2b using a variable temporal analysis window size (0.0, 1.0, 2.0 of mean period) and variable number of trace (J = 5, J = 9 and J = 13).

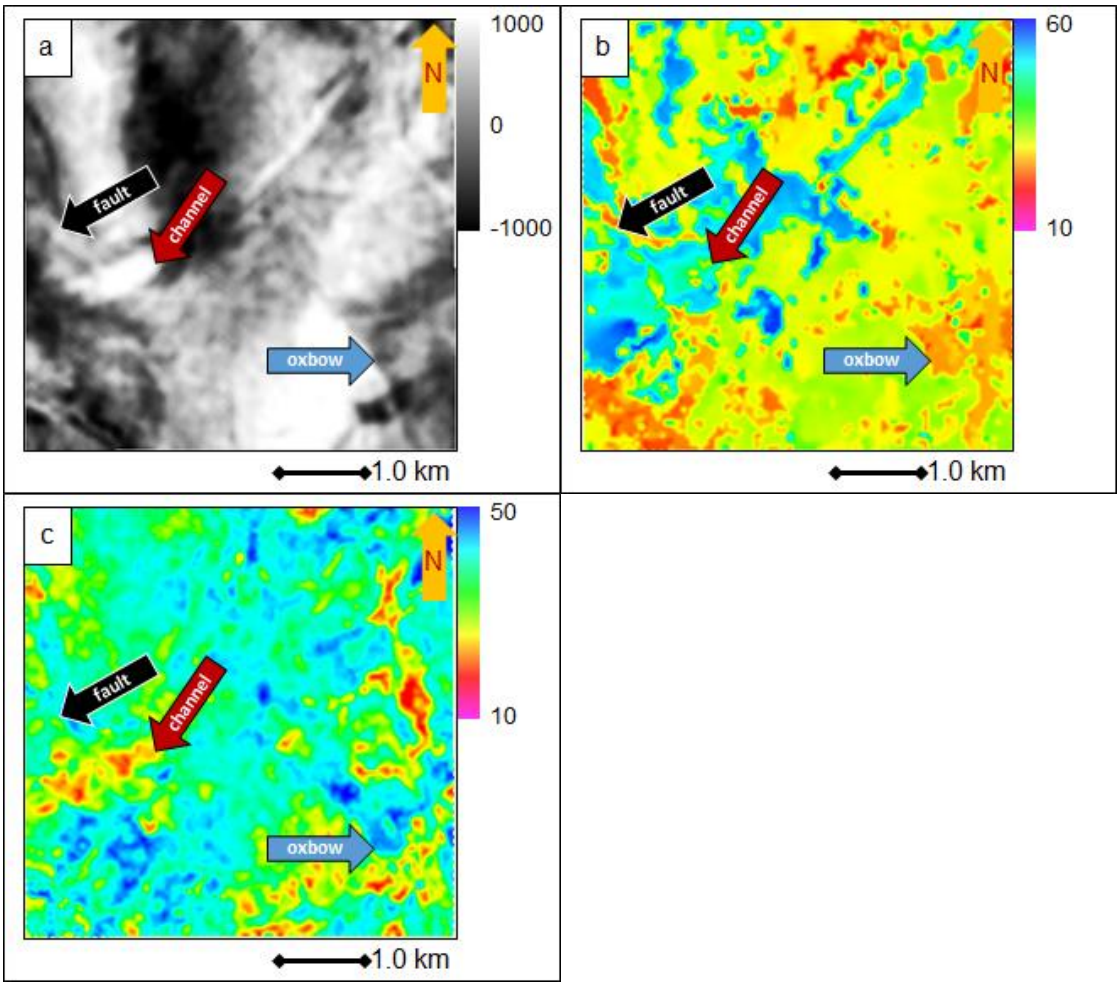

Figure 2.4. Time slices at t = 0.5 s through (a) seismic amplitude, (b) peak frequency and (c) bandwidth. The dominant frequency is approximately 25 Hz, corresponding to a period of 40 ms.

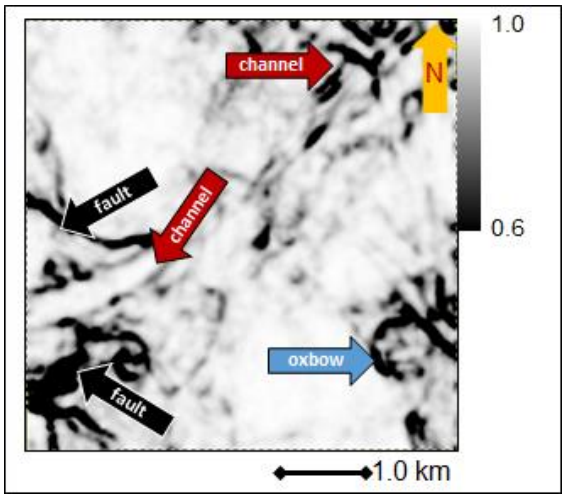

Figure 2.5. The coherence slice using self-adaptive (0.5~2.0 of the mean period of 20~80 ms) temporal analysis window size of seismic slice in Figure 2.4a.

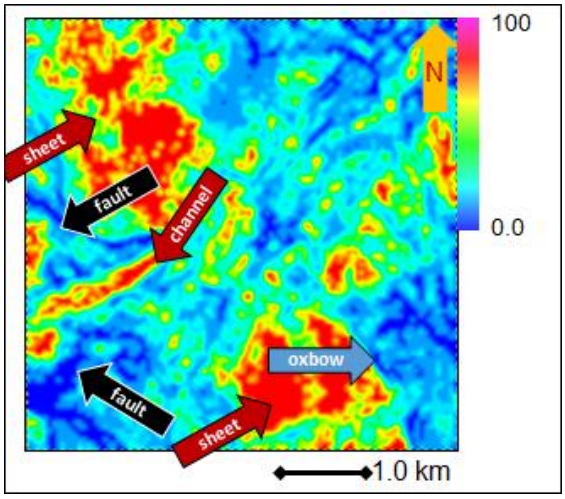

Figure 2.6. Time slice at t = 0.5 s through signal to noise ratio volumes computed using a self-adaptive temporal analysis window size (0.5~2.0 time of the mean period).

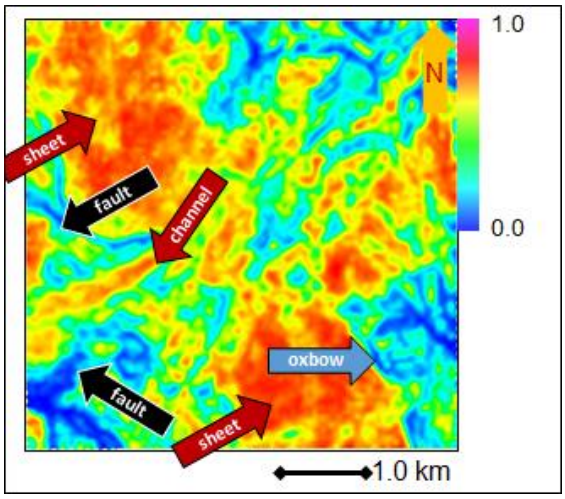

Figure 2.7. The significance slice using a self-adaptive temporal analysis window size 1.0 times the peak period corresponding to Figure 2.4b and variable bandwidth from Figure 2.4c.

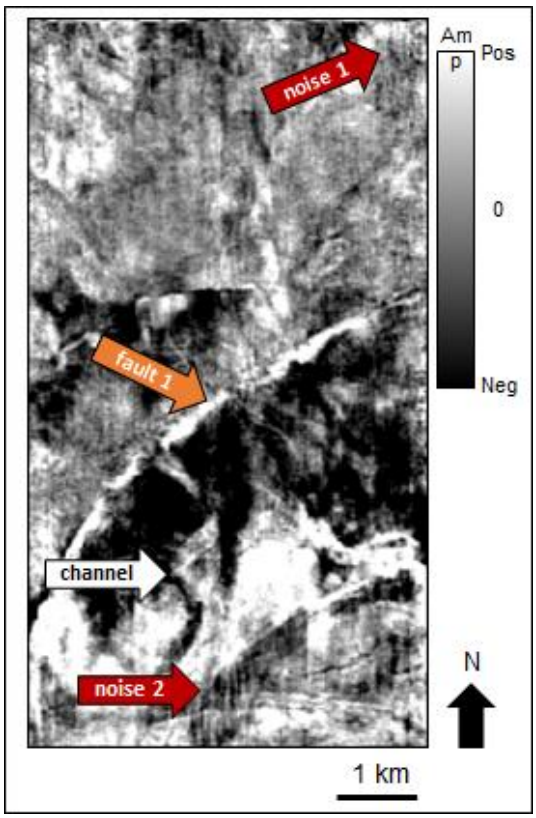

Figure 2.8. Time slice at t = 0.75s through seismic amplitude.

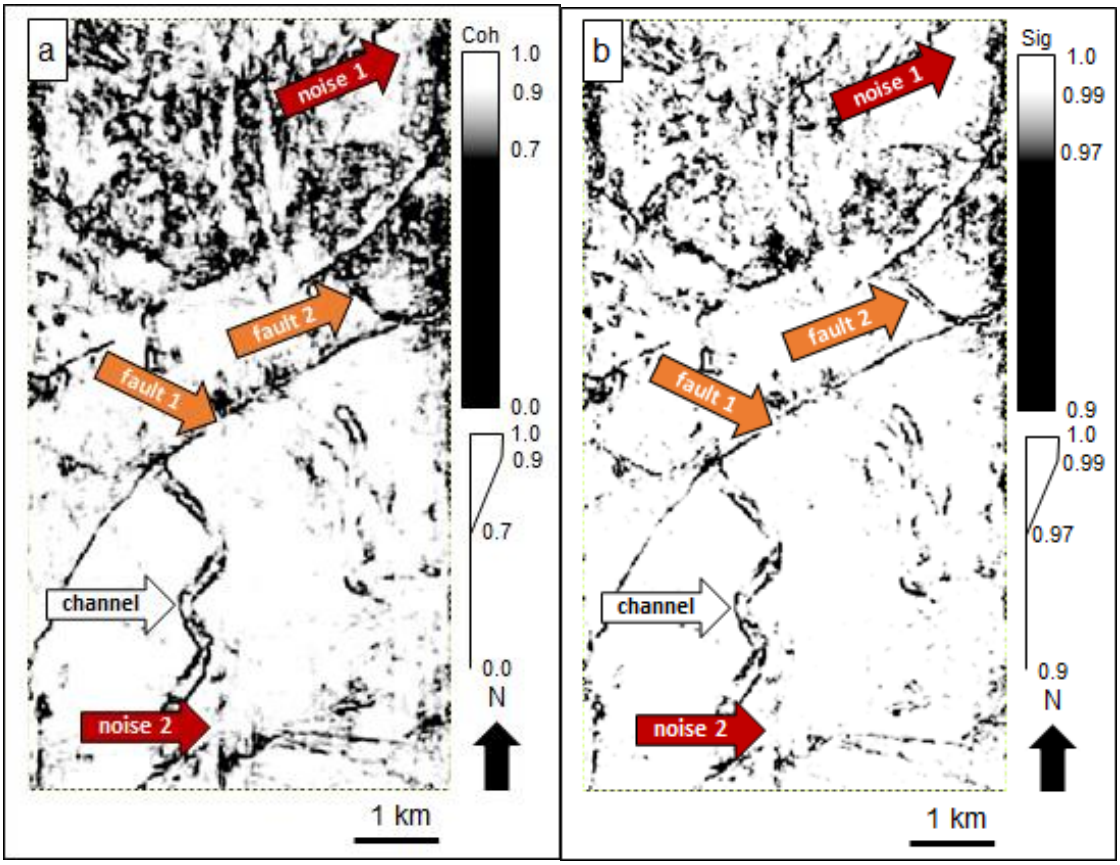

Figure 2.9. Time slices at t = 0.75s through (a), coherence using a self-adaptive temporal analysis window size and (b) significance of coherence of Figure 2.8.

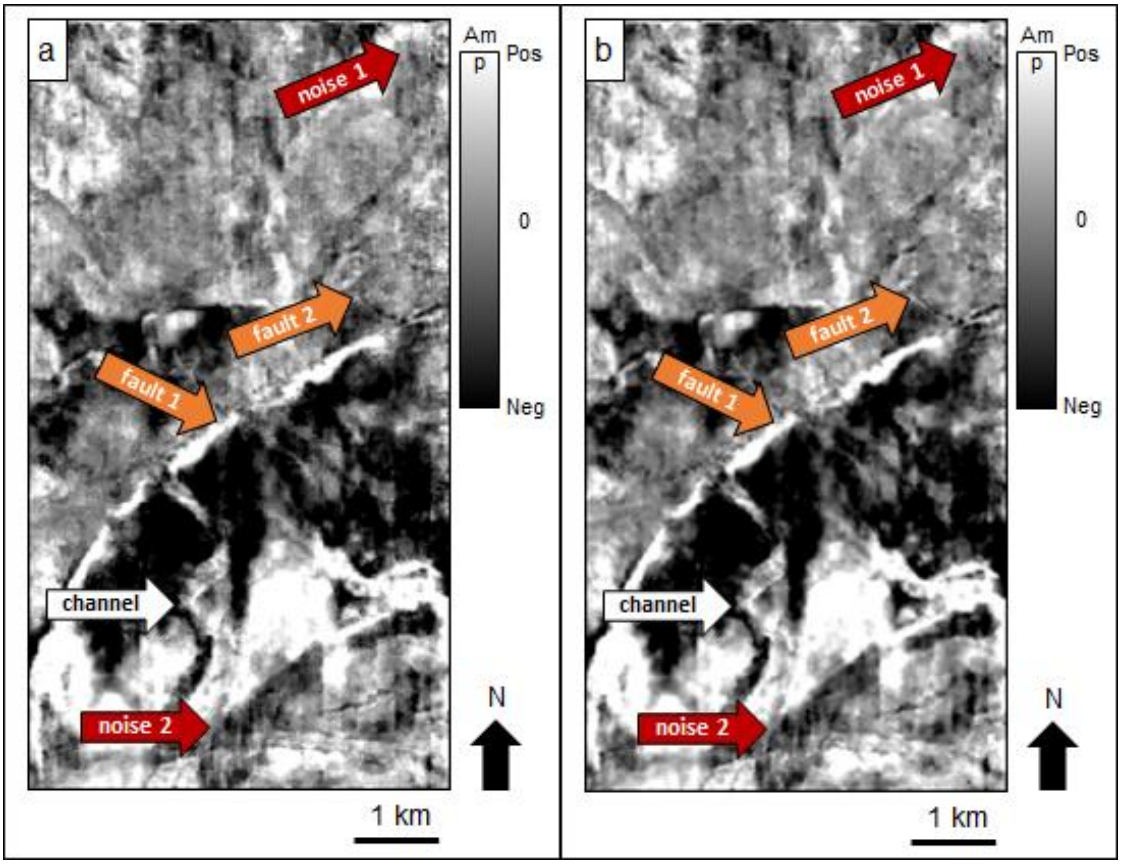

Figure 2.10. Time slices at t = 0.75s through the output (filtered) seismic amplitude using structure-oriented filtering based on (a) similarity and (b) statistical significance of coherence.

REFERENCES

Al-Dossary S., Y. E. Wang, and M. McFarlane, 2014, Estimating randomness using seismic disorder, Interpretation, Special section: Seismic attributes, SA93-SA97.

Blandford, R. R., 1974, An automatic event detector at the Tonto Forest seismic observatory: Geophysics, **39,** P633-P643.

Davogustto, O., and K. J. Marfurt, 2011, Removing acquisition footprint from legacy data volumes: SEG Technical Program Expended Abstracts 2011, 1025-1028.

Douze, E. J., and S. J. Laster, 1979, Statistics of semblance: Geophysics, **44**, 1999-2003.

Ha T., 2014, Seismic attribute illumination of tectonic deformation in Chicontepec basin, Mexico: The master thesis of University of Oklahoma.

Hoecker, C., and G. Fehmers, 2002, Fast structural interpretation with structure-oriented filtering: The Leading Edge, **21**, 238-243.

Kirlin, R. L., and W. J. Done, 1999, Covariance analysis for seismic signal processing: The Society of Exploration Geophysics, Tulsa, OK.

Lin, T., D. Chang, B. Zhang, J Guo, and K. J. Marfurt,2014, Seismic attributes estimation using a self-adaptive window: SEG Technical Program Expended Abstracts 2014, 1654-1658.

Lin, T., B. Zhang, S. Zhan, Z. Wan, D. Chang, and K. J. Marfurt, 2015, Geometric attribute estimation using data-adaptive windows: personal communication.

Marfurt, K. J., 2006: Robust estimates of reflector dip and azimuth: Geophysics, **71**, P29-P40.

Marfurt, K. J., R. L. Kirlin, S. L. Farmer, and M. S. Bahorich, 1998, 3-D seismic attributes using a semblance-based coherency algorithm: Geophysics, **63**, 1150-1165.

Neidell, N. S., and M. T. Taner, 1971, Semblance and other coherency measurements for multichannel data: Geophysics: **36**, 482-497.

Randen, T., E. Monsen, C. Signer, A. Abrahamsen, J. O. Hansen, T. Sceter, J. Schlaf, and L. Sonneland, 2000, Three-Dimensional texture attributes for seismic data analysis: SEG Technical Program Expended Abstracts 2000, 668-671.

Taner, M. T., and F. Koehler, 1969, Velocity spectra – digital computer derivation and application of velocity functions: Geophysics, **34**, 859-881.

APPENDIX

The Covariance Matrix, Semblance and KL-filter Estimates of Coherence

Taner and Koehler (1969) define the semblance, *s*, of a collection of *J* seismic traces u_j within a 2*K*+1 sample vertical analysis window to be the ratio of the energy of the average trace to the average energy of the individual traces (as shown in Figure 4.1). The traditional estimate of semblance is thus:

$$s(z) = \frac{\sum_{k=-K}^{+K} \alpha_k \left\{ \left[\sum_{j=1}^{J} \beta_j u_j(z+k\Delta z) \right]^2 + \left[\sum_{j=1}^{J} \beta_j u_j^H(z+k\Delta z) \right]^2 \right\}}{\sum_{k=-K}^{+K} \alpha_k \left\{ \sum_{j=1}^{J} \beta_j \left[u_j{}^2(z+k\Delta z) + u_j{}^{H^2}(z+k\Delta z) \right] \right\}}, \qquad (1)$$

where, $u_j(z)$ denotes the measured amplitude of the j^{th} trace at sample *z*, α_k are the weights applied to the k^{th} sample and β_j the weights applied to the j^{th} trace. Traditionally, β_j=1/*J* where the *J* traces fall within a user-defined elliptical or rectangular analysis window. Lin et al. (2015) show how one can generalize equation (1) for radially tapered analysis windows, where the radius and tapering of the analysis window are defined by some measure of the time- or time and space-varying spectrum. Generalization of equations requires one to first compute the covariance matrix, **C**,

$$C_{jl} = \sum_{k=-K}^{+K} \alpha_k \left\{ \sum_{j=1}^{J} \beta_j \left[u_j(z_j+k\Delta z) u_l(z_j+k\Delta z) + u_j^H(z_j+k\Delta z) u_l^H(z_j+k\Delta z) \right] \right\}. \qquad (2)$$

Along dipping horizon z_j, where we have augmented the data sample vectors u_j by its Hilbert transform, u_j^H to provide more robust estimates for small windows about zero crossings. We will use the same tapering windows described by Lin et al. (2015), although the subsequent description is appropriate for any tapering function. Specifically, we define:

$$a_k = \begin{cases} \frac{1}{2}\left[1 + cos\left(\frac{\pi k \Delta z}{Z}\right)\right] & k\Delta z < Z \\ 0 & k\Delta z \leq Z \end{cases}, \tag{3}$$

where:

$$Z = (K+1)\Delta z = \frac{\gamma}{\kappa_{ref}} + \Delta z\,, \tag{4}$$

where κ_{ref} is the reference wavenumber (a percentile, p, of the local wavenumber spectrum) and where γ represents a fraction of this reference window (e.g. 1.0 times the reference window). The final term Δz increases the computational window such that samples $\pm K$ will always have a non-zero value.

The radial analysis window will have weights:

$$\beta_j = \begin{cases} \frac{1}{2}\left[1 + cos\left(\frac{\pi r_j}{R}\right)\right] & r_j < R \\ 0 & r_j \leq R \end{cases}, \tag{5}$$

where:

$$r_j = \left(x_j^2 + y_j^2\right)^{1/2}, \text{ and} \tag{6}$$

$$R = \frac{\gamma}{\kappa_{ref}} + \text{MIN}(\Delta x, \Delta y)\,. \tag{7}$$

Using these weights, Lin et al. (2015) compute the semblance of a radially tapered analysis window to be:

$$c_s(z) = \frac{\mathbf{aTCa}}{\mathrm{Tr}(\mathbf{C})}, \tag{8}$$

where the mathematical trace Tr(**C**) of the covariance matrix, **C**, is defined as:

$$\mathrm{Tr}(\mathbf{C}) = \sum_{j=1}^{J} C_{jj}, \tag{9}$$

and where:

$$a_j = \left(\frac{\beta_j}{\sum_{l=1}^{J} \beta_l} \right)^{1/2}. \tag{10}$$

We will wish to apply our F-statistic estimate of the significance to not only semblance, but also to KL-filtered (energy ratio) coherence anomalies. This later estimate is (Lin et al., 2015):

$$c_{KL}(z) = \frac{\sum_{k=-K}^{+K} \alpha_k \left\{ \sum_{j=1}^{J} \beta_j \left[U_j{}^2(z_j + k\Delta z) + U_j^{H\,2}(z_j + k\Delta z) \right] \right\}}{\sum_{k=-K}^{+K} \alpha_k \left\{ \sum_{j=1}^{J} \beta_j \left[u_j(z_j + k\Delta z) + u_j^H(z_j + k\Delta z) \right]^2 \right\}}, \tag{11}$$

where $U_l(z_l)$ and $U_l^H(z_l)$ are the Karhunen-Loeve filtered versions of the original data.

Since they considered coherent energy to be signal and incoherent energy to be noise on common midpoint seismic gathers, Douze and Laster (1979) were able to estimate the signal to noise ratio from the numerator and denominator of the semblance computation:

$$s = \frac{\sum_{k=-K}^{+K}\left[\frac{1}{J}\sum_{j=1}^{J} u_j(t+k\Delta t)\right]^2}{\sum_{k=-K}^{+K}\frac{1}{J}\sum_{j=1}^{J}\left[u_j{}^2(t+k\Delta t)\right]} = \frac{P_S}{P_S + P_N}. \tag{12}$$

In this case, the signal to noise ratio P_S/P_N is simply:

$$\left(\frac{P_S}{P_N}\right)_s = \frac{\sum_{k=-K}^{+K}\left[\frac{1}{J}\sum_{j=1}^{J} u_j(t+k\Delta t)\right]^2}{\sum_{k=-K}^{+K}\frac{1}{J}\left\{\left[\sum_{j=1}^{J} u_j(t+k\Delta t)\right]^2 - \sum_{j=1}^{J}\left[u_j{}^2(t+k\Delta t)\right]\right\}}, \tag{13}$$

which varies between 0 and infinity.

For our attributes calculation, the signal to noise ratio for equation (11) is:

$$\left(\frac{P_S}{P_N}\right)_{KL} = \frac{\sum_{k=-K}^{+K}\alpha_k\left\{\sum_{j=1}^{J}\beta_j\left[U_j{}^2(z_j+k\Delta z) + U_j{}^{H\,2}(z_j+k\Delta z)\right]\right\}}{\sum_{k=-K}^{+K}\alpha_k\left\{\sum_{j=1}^{J}\beta_j\left[u_j{}^2(z_j+k\Delta z) + u_j{}^{H\,2}(z_j+k\Delta z)\right]^2 - \sum_{j=1}^{J}\beta_j\left[U_j{}^2(z_j+k\Delta z) + U_j{}^{H\,2}(z_j+k\Delta z)\right]\right\}}, \tag{14}$$

For seismic interpreters, high coherence indicates a high signal to noise ratio. However, low semblance or coherence has four interpretations:

1. A sharp discontinuity which may indicate the presence of a fault, channel edge, or erosional surface (i.e. the presence of planar geologic features),
2. A relatively diffuse low coherence pattern which may indicate the presence of karst collapse, hydrothermally-altered dolomite, and mass transport complexes (i.e. the presence of chaotic geologic features),
3. A relatively diffuse low coherence pattern that is associated with low reflectivity or inaccurate velocities and hence inaccurate imaging which may indicate the presence of salt diapirs, overpressured shales, and gas chimneys (i.e. an indicator rather than an image of the geology at a given voxel), and
4. A relatively diffusive low coherence pattern associated with random noise, operator aliasing, acquisition footprint, or overprinted multiples (i.e. the absence of geologic signal, and hence the presence of seismic noise).

While we will not be able to differentiate cases 3 and 4 described above, our more limited goal is to differentiate diffuse low coherence anomalies from high coherence reflectors and planar low coherence anomalies. One way to estimate such a signal-to-noise ratio is to use the disorder attribute.

Disorder

Al-Dossary (2014) introduces a "disorder" attribute that passes not only coherent reflectors but also vertically and horizontally oriented low coherence anomalies as signal and thus separates these two geologic patterns from diffuse low coherence patterns. His original algorithm cascades second derivatives in the *x*, *y*, and *z* directions on a window of the energy (or the power) of the data. This is equivalent to squaring the data and then filtering it with a 3x3x3 operator:

$$\mathbf{L} = \left\{ \begin{bmatrix} 1 & -2 & 1 \\ -2 & 4 & -2 \\ 1 & -2 & 1 \end{bmatrix}, \begin{bmatrix} -2 & 4 & -2 \\ 4 & -8 & 4 \\ -2 & 4 & -2 \end{bmatrix}, \begin{bmatrix} 1 & -2 & 1 \\ -2 & 4 & -2 \\ 1 & -2 & 1 \end{bmatrix} \right\}, \tag{15}$$

The original algorithm suffers from two main drawbacks: (1) it is sensitive to the local average amplitude, and (2) it gives rise to diagonal artifacts. To compensate for the local average amplitude sensitivity, Ha and Marfurt (2014) slightly modified the algorithm to compute disorder, *D*, by normalizing the attribute by the RMS magnitude of the windowed data:

$$D = \frac{\mathbf{L} \cdot \mathbf{e}}{\|\mathbf{L}\| \|\mathbf{e}\| + \varepsilon} , \tag{16}$$

where **L** is given by equation 15, **e** is a volume of amplitude energy, the dot indicates a triple inner product, ||**L**|| and ||**e**|| indicate the L_2 norm, or magnitude, of the operator and data, and ε is a small number to prevent division by zero. To minimize diagonal artifacts, we compute the standard deviation of this attribute along structural dip.

Estimation of Fault Plane Dip and Azimuth Using Eigenvector Analysis

Randen et al (2000) showed how one could estimate the dip and azimuth of a fault (or other planar) discontinuity using the eigenvectors of a coherence-weighted distance matrix, **G**, defined over a window of $M=J*(2K+1)$ data points within an analysis window by:

$$G_{ij} = \frac{\sum_{m=1}^{M} x_{im} x_{jm} \gamma_m}{\sum_{m=1}^{M} \gamma_m} \quad , \tag{17}$$

where $\gamma_m=1-c_m$ is the similarity, c_m is the coherence at the m^{th} data point, and x_{im} is the distance from the center of the analysis window along axis i of the m^{th} data point. Since we are interested in estimating anomalous behavior, we use γ_m where most values are close to 0.0, rather than coherence, c_m, which has values close to 1.0. The matrix **G** has three eigenvalues, λ_j, and eigenvectors, $\mathbf{v_j}$. By construction,

$$\lambda_1 \geq \lambda_2 \geq \lambda_3 . \tag{18}$$

The first eigenvalue, λ_1, represents the amount of variance defined by the first eigenvector, $\mathbf{v_1}$. Similarly, the second eigenvalue, λ_2, represents the amount of variance defined by the second eigenvector, $\mathbf{v_2}$. These first two eigenvalues and eigenvectors represent the amount of variance defined by $\mathbf{v_1}$ and $\mathbf{v_2}$. Following Kirlin and Done (1999), a truly chaotic pattern will have:

$$\lambda_1 = \lambda_2 = \lambda_3. \quad (19)$$

The third eigenvalue, λ_3, can thus serve as an estimate of noise-to-signal ratio if it is normalized. To be large, there are two conditions to be taken into consideration. First, there need to be some nonzero values of γ_m if any of the eigenvalues are to be non-zero. Second, the distribution of these finite values needs to be random rather than linear or planar, thereby representing either seismic or geologic noise as described by scenarios 3-4 above.

Statistical Significance of Coherence Estimates

With this background, we can now estimate the significance of a given semblance or energy ratio coherence estimate. Following Douze and Laster's (1979), we approximate the F-statistic with d_1 and d_2 degrees of freedom and non-centrally parameter ε (Blandford, 1974) as:

$$F_s(d_1, d_2, \varepsilon) = \frac{(J-1)\sum_{k=-K}^{+K} \alpha_k \left\{ \left[\sum_{j=1}^{J} \beta_j u_j(t+k\Delta t) \right]^2 + \left[\sum_{j=1}^{J} \beta_j u_j^H(t+k\Delta t) \right]^2 \right\}}{\sum_{k=-K}^{+K} \alpha_k \left\{ \sum_{j=1}^{J} \beta_j \left[u_j{}^2(t+k\Delta t) + u_j^{H\,2}(t+k\Delta t) \right] - \left[\sum_{j=1}^{J} \beta_j u_j(t+k\Delta t) \right]^2 + \left[\sum_{j=1}^{J} \beta_j u_j^H(t+k\Delta t) \right]^2 \right\}}, \quad (20)$$

and

$$F_c(d_1, d_2, \varepsilon)$$

$$= \frac{(J-1)\sum_{k=-K}^{+K} \alpha_k \left\{ \sum_{j=1}^{J} \left[U_j{}^2(t+k\Delta t) + U_j^{H\,2}(t+k\Delta t) \right] \right\}}{\sum_{k=-K}^{+K} \alpha_k \left\{ \sum_{j=1}^{J} \beta_j \left[u_j{}^2(t+k\Delta t) + u_j^{H\,2}(t+k\Delta t) \right] - \sum_{j=1}^{J} \left[U_j{}^2(t+k\Delta t) + U_j^{H\,2}(t+k\Delta t) \right] \right\}},$$

(21)

where:

$$d_1 = f_B \sum_{k=-K}^{+K} \alpha_k \Delta t, \tag{22a}$$

$$d_2 = d_1 \sum_{j=1}^{J} \beta_j \text{ , and} \tag{22b}$$

$$\varepsilon = J d_1 \left(\frac{S}{N} \right)^2. \tag{22c}$$

where f_B is the bandwidth of the signal in Hz, and *S/N* is the signal to noise ratio we obtain from equation (13) and (14).

CHAPTER 3

GEOMETRIC ATTRIBUTE ESTIMATION USING DATA-ADAPTIVE WINDOWS

Tengfei Lin[1], Bo Zhang[2], Kurt Marfurt[1], Deshuang Chang[3]

[1] University of Oklahoma, ConocoPhillips School of Geology and Geophysics,

[2] University of Alabama, Department of Geological Sciences,

[3]BGP Inc., China National Petroleum Company.

This paper was submitted to the AAPG-SEG journal *Interpretation*.

ABSTRACT

Geometric seismic attributes such as coherence are routinely used in seismic interpretation and reservoir characterization to describe faults, channels, and other geological features. Traditionally, we use a single user-defined analysis window of fixed size to calculate attributes for the entire seismic volume. In general, smaller windows produce sharper geological edges but they are more sensitive to noise. In contrast, larger windows reduce the effect of random noise, but might laterally smear faults and channel edges and vertically mix the stratigraphy. For data exhibiting a low signal-to-noise ratio, stratigraphic edges seen in coherence generally improve with increasing window size up to the dominant period of the data, while windows larger than the dominant period slightly improve the image at the expense of mixing shallower and deeper stratigraphy in the result. The vertical and lateral resolution of a 3D seismic survey changes with depth due to attenuation losses and velocity increase, such that a window size that provides optimal images in the shallower section is often too small for the deeper section. A common workaround to address this problem is to compute seismic attributes for a suite of fixed windows and then splice the results at the risk of reducing the vertical continuity of the final volume.

Our proposed solution is to define laterally and vertical smoothly varying analysis windows based on the spectral content of the data. The construction of such tapered windows requires a simple modification of the covariance matrix for

eigenstructure-based coherence and a less obvious, but also simple modification of semblance-based coherence. We demonstrate the values of our algorithm by applying it to a vintage 3D seismic survey acquired offshore Louisiana, USA.

LIST OF KEYWORDS

Seismic Attributes, Coherence, Spectral Decomposition, and Resolution.

INTRODUCTION

Geometric seismic attributes such as coherence measure changes in reflector shape and continuity (Chopra and Marfurt 2007) that can be tied to structural and depositional environments. While instantaneous and spectral attributes are computed trace by trace, geometric attributes are computed from a window of neighboring traces and samples. "Coherence" can be computed using cross-correlation (Bahorich and Farmer, 1995), semblance or variance (e.g., Marfurt et al., 1998; Marfurt, 2006; Pepper and Bejarano, 2005), Sobel filters (Luo et al., 1996; Barka, 2015), eigenvectors of the data covariance matrix (Gersztenkorn and Marfurt, 1999), eigenvectors of the gradient structure tensor (van Bemmel and Pepper, 2011), and prediction error filters (Bednar, 1998).

Most implementations of these algorithms use a fixed number of traces and samples for the entire volume to be analyzed. However, due to frequency losses in the overburden, as well as the increase of seismic velocity and decreasing range of incident angles with depth, the seismic data lose both temporal and lateral resolution with depth. Hence, a fixed analysis window optimized for the shallow section might provide suboptimal results in the deeper section.

A workaround is to approximate a time-variant algorithm by splicing the results of a suite of coherence computations run with different vertical and lateral

window dimensions. Unfortunately, the blended output generally lacks vertical continuity.

To address these problems, Barka (2015) defined the vertical size of a Sobel filter edge detector based on the frequency content. Lin et al. (2014a) showed how smoothed estimates of peak spectral frequency could help to define the data-adaptive vertical analysis windows to compute volumetric dip and coherence.

In this paper, we generalize Lin et al.'s (2014b) data adaptive workflow to define both the vertical and lateral size of the analysis window to be a function of the smoothed local spectral content, where the spectral magnitudes $m(t,f,x,y)$ are computed using spectral decomposition. We begin with a review of the sensitivity of the quality of coherence images to analysis window size. Next, we review the computation of energy ratio coherence based on the Karhunen-Loeve (KL) filter (Marfurt et al., 1998; Chopra and Marfurt, 2007) and show its relation to semblance. We then show how to construct the covariance matrix for vertically and radially tapered analysis windows, which in turn provide estimates of coherence. Given these definitions, we apply our modified algorithms to a 3D seismic volume and show the value of using data adaptive windows.

REVIEW – SENSITIVITY OF COHERENCE IMAGES TO WINDOW SIZE

Most geometric attributes including volumetric estimates of dip, coherence, curvature, amplitude gradients, and GLCM texture are computed within a 3D analysis window that shifts with each voxel analyzed. The lateral and vertical resolution of these attributes is limited by the temporal and spatial sampling intervals, spectral content of the data, and the signal-to-noise ratio. Lin et al. (2016) studied the sensitivity of coherence estimates to random noise using an F-statistic and found that the confidence of finding a coherent event increases with (1) the number of traces, and (2) the product of the bandwidth with vertical window size. Since the seismic bandwidth generally decreases with depth, their analysis suggests adaptation of the analysis window size to the spectral content of the seismic data to ensure consistent attribute image quality.

In general, larger analysis windows reduce random noise and "stack" vertically aligned discontinuities of interest, but will increase computational cost and may smear lateral discontinuities or mix vertical stratigraphy. High frequency data require smaller sampling intervals. Older seismic surveys were often sampled at 4 ms, while newer surveys are commonly sampled at 2 ms. Seismic data for tar sands, coal mining (e.g., Walton et al., 2000) or geotechnical purposes (e.g., Dana et al., 1999) are commonly sampled at 0.5 ms.

For this reason, many coherence algorithms define the analysis window by the number of vertical samples and lateral traces. Thus, common default 11-sample vertical windows for 4 ms, 2 ms and 0.5 ms sample intervals result in ±20 ms, ±10 ms, and ±2.5 ms, respectively.

Vertical Mixing of Stratigraphy

To understand the impact of the size of the analysis window on the resulting coherence image, one needs to examine the seismic reflectivity model:

$$d_k = \sum_{m=-M}^{M} \left(r_{k+m} w_m \right) + n_k , \qquad (1)$$

where

d_k is the measured seismic data at the k^{th} sample,

r_k is the reflectivity at the k^{th} sample,

w_m is a temporally limited seismic wavelet, where $M \leq m \leq M$, and

n_k is the noise at the k^{th} sample.

The seismic wavelet **w** mixes reflectivity from adjacent depths to the depth of interest. The amount of mixing is a function of the bandwidth of the data. For most seismic surveys, we lose higher frequencies with depth, while the lower frequencies remain, thereby decreasing the bandwidth. For this reason, a reasonable estimate of resolution is the half period (T_{min}, in two- way travel time) or quarter wavelength (λ_{min},

in depth-converted data) of the highest useable frequency in the spectrum, while a reasonable estimate of vertical mixing is the dominant period (T_{dom} in two-way travel time) or dominant wavenumber (λ_{dom} in depth converted data). These two numbers provide a means of estimating an optimum analysis window.

Lin et al.'s (2016) work shows that the confidence in coherence estimates for fixed signal-to-noise ratio increases with f_bT, where f_b is the bandwidth measured in Hertz, and T is the temporal analysis window measured in seconds. We therefore expect the quality of our images to improve with increasing window size up to $T=T_{min}$, improving slightly, but with the risk of more mixing, up to $T= T_{dom}$. For values $T> T_{dom}$, any improvement in the signal-to-noise ratio of the image at the target Horizon A3an be offset by increased mixing of geologic features from shallower and deeper events. For these reasons, we hypothesize that analysis windows that adapt to the bandwidth of the data will provide superior, better balanced images than those computed using a fixed window.

Stair-step Artifacts of Dipping Faults

While time slices through coherence volumes provide excellent images of the continuity and orientation of faults, the lateral location of these faults are often shifted from one manually picked on vertical slices through the seismic amplitude data by a human interpreter. Careful examination of vertical slices through the corresponding coherence volume shows the well-known and routinely encountered "stair-step" artifact (Figure 3.1). Eigenstructure-, semblance-, variance-, and gradient structure tensor based coherence as well as Sobel-filter estimates of discontinuities are dominated by the stronger amplitude events within the analysis window. Increasing the size of the vertical analysis window beyond the dominant period of a high-amplitude discontinuity undesirably propagates the discontinuity both shallower and deeper within the coherence image. For listric faults, these artifacts become worse than the annoying than stair step artifacts, such that the discontinuities of a given fault may appear more than once on time slice (Marfurt and Alves, 2015).

We evaluated two remedies to this problem, neither of which worked. First, we balanced the amplitude of each sample vector within the analysis window to have approximately the same contribution. Such balancing reduced, but did not eliminate the contribution of the stronger discontinuities within the analysis window. Second, we reduced the vertical size of the analysis window. As shown in Figure 3.1a, even a

window size of 1-sample results in a stair-step artifact, suggesting that the artifact is due to the seismic amplitude data and not to the size of the coherence window.

Reflectivity, Seismic Imaging, and the Seismic Wavelet

The stair-step artifact has perplexed the last author of this article since the inception of coherence some 20 years ago. Recent publications in diffraction imaging (e.g. Mosher, 2008) provide the insight into the cause of these artifacts. While the typical migration algorithm assumes that each subsurface image point is a point diffractor, those algorithms that explicitly include an obliquity factor actually assume each subsurface point is part of a specular reflector. In prestack migration, the obliquity factor is a function of the unit vector from the source to the image point, $\mathbf{p_s}$, the unit vector from the receiver group to the image point, $\mathbf{p_g}$, and the normal to the hypothesized reflector, **n** (Figure 3.2). In diffraction imaging, one computes **n,** defining the normal to the reflector dip, from a previous image of specular (or conventional) imaging. In this case, the obliquity factor, Ω, is

$$\Omega = \frac{\mathbf{p_s} + \mathbf{p_g}}{2} \cdot \mathbf{n}\,, \tag{2}$$

which geometrically is the cosine of the angle between the average of the angle of incidence and reflection and the normal. Examination of Figure 3.2 shows that for specular reflection, the angle of incidence equals the angle of reflection about the normal, such that $\Omega = 1$. Furthermore, migration ray pairs, $\mathbf{p_s}$ and $\mathbf{p_g}$, skewed to the left

of the specular angle will generally be accompanied by migration ray pairs skewed to the right. In most migration algorithms, the seismic image is built up point diffractor by point diffractor. The net result is that the seismic wavelet will be oriented perpendicular to the reflector, parallel to **n**.

Since we do not believe this phenomenon is well recognized by most interpreters, we generate a suite of synthetic shot gathers using a finite difference algorithm, prestack migrate the results to obtain images in both time and depth domain, and compute coherence (Figure 3.3). Note that the seismic wavelets near the fault edges are aligned perpendicular to the horizontal reflectors. Since these terminations occur at discrete layer boundaries, the result is a discrete stair step, with the vertical extent of the stair step defined by the size of the seismic wavelet.

ADAPTIVE WINDOWS

The above observations suggest that for a fixed signal-to-noise ratio that the ideal analysis window should be a function of the local seismic spectrum. Mathematical details of computing energy ratio and semblance based coherence within tapered windows are described by Lin et al., (2016) produced at chapter 2. Figure 3.4 is a cartoon showing how the input amplitude data are weighted both vertically and radially from the center. We will smooth our spectra to estimate λ_{dom} and λ_{min} defined above. Furthermore, we will assume our data have been depth converted, either through depth migration or through a simple velocity conversion. Finally, since we are as concerned about lateral resolution and mixing as well as vertical resolution and mixing, our analysis windows will vary both vertically and laterally, where "lateral" is defined as parallel to the local structural dip.

APPLICATION

We apply our data-adaptive coherence algorithm on a time-migrated data volume from the Gulf of Mexico, The 3D seismic data (Figure 3.5a) have been spectrally balanced and subjected to structure-oriented filtering to further improve the vertical and lateral resolution (Figure 3.5b).

Red arrows on the vertical slice of Figures 3.5a and b indicate four faults cutting from them shallower to the deeper section; the wavelength increases with depth as well. The frequency spectra in Figures 3.6a and b, respectively, ranges between 10 to 80 Hz, with a bandwidth that due to attenuation and poor imaging to range between 10~40 Hz. Based on Lin et al., (2016) F-statistical anomalies, one cannot define a image to generate coherence images with equal confidence.

Figures 3.7a-d show slices through energy ratio coherence using four different window sizes. Note higher volumes computed resolution in the shallower zone nearby Horizon A2, which allows for a relative small window size (Figure 3.7a). In Figure 3.7b and 3.7c, events shallower zone nearby Horizon A2 mix together due to the taller window (20 or 40 ms), making it harder to characterize faults and channel edges in the shallower section. In contrast, a larger window should be applied in the deeper section, to generate a more continuous, though lower resolution fault anomalies. The fault in the red dashed rectangular window shows the improvements of fault imaging

gradually in Figures 3.7b and c, despite the horizontal blur. Calculations using smoothly tapered data-adaptive windows provide a sharper and cleaner fault imaging in both shallower and deeper sections (Figure 3.7d).

Figure 3.8 indicates the zoomed in section of seismic profile of Figure 3.5b showing Horizon A1 and several normal faults. White arrows indicate two channels that fall on Horizon A1. Figure 3.9 shows a time-structure map of Horizon A1 along with a horizon slice through the coherence volume. Red lines in the profile pick normal faults, and the two channels are marked by the white arrows, which are crossed by Horizon A1.

By extracting seismic amplitude values along Horizon A1, which is located in the peak the seismic waveform (Figure 9b). Red arrows indicate several normal faults and two channels are marked by white arrows.

Energy ratio similarity is calculated in Figures 3.10a-d, using $\pm$4 ms, $\pm$20 ms, $\pm$40 ms and 5 traces, and data-adaptive (varying between $\pm$12 ms and 5 traces, and $\pm$100 ms and 13 traces) window size, resulting in fault and channel images with different resolution. Smaller windows ($\pm$4 ms) suffer from more random noise. Larger windows (($\pm$40 ms) suppress thin noise.

Figures 3.11-3.30 indicate the phantom horizons, which are 8 ms, 16 ms, 24 ms 32 ms and 40 ms above/below Horizon A1. The coherence are calculated by $\pm$4

ms, ±20 ms, ±40 ms and data-adaptive (±12~100 ms) window size. The channel indicated by white arrow 2 are detected in Figures 3.10a-d, and disappears in Figure 3.16a as it reaches the phantom 24 ms below Horizon A1 and 24 ms above Horizon A1. While it shows up again in Figure 3.12c, this is because the large window size (±40 ms) combines too much geological information together and smears the channel edges, making them hard to separate. The approximate frequency nearby Horizon A1 is 20 Hz, and its relevant window size in coherence algorithm is 25 ms, a little larger than the average window size applied in the while survey. Therefore, the coherence using data-adaptive window gives us perfect results, less random noise, sharper fault anomalies and reduced leakage.

Figures 3.31-3.51 indicate the Horizon A2 of the shallow zone, and its phantom horizons 8 ms, 16 ms, 24 ms, 32 ms and 40 ms above/below the Horizon A2. The red arrow shows a major fault. The data quality is low due to the footprint as well as the radon noise. A smaller window size should be applied because of the high frequency in the shallow zone. The energy ratio coherence along phantom horizons using constant window size of ±4 ms and 5 traces shows better imaging, this is because the too taller window size of ±20 ms and ± 40 ms mix too much geological together and the S/N of the shallow zone is relative low, generating lots of dark zones. This phenomenon is partly suppressed and improve the coherence values overall while keeping the geological information (fault) being easy to separate by the coherence using data-adaptive window.

Figures 3.53-3.74 indicate the Horizon A3 of the shallow zone, and its phantom horizons 8 ms, 16 ms, 24 ms, 32 ms and 40 ms above/below the Horizon A2. Red arrows show the major faults. For the coherence using constant window size, the geological can be imaged clearer, and mixed together at the same time. The application of the data-adaptive window perfectly suppresses the random nose, preserves the useful geological information belonging to the target horizon, and prevents the data leakage, to generate the perfect result from shallow to the deep section of the seismic data in coherence calculation.

CONCLUSIONS

The “optimum” window height for attributes such as coherence is a function of the dominant period in the window. In general, the analysis window used in geometric attribute calculation should be large enough to improve the signal-to-noise ratio of the estimate, yet small enough to avoid mixing the seismic signal of adjacent stratigraphy or discontinuities. In general, the computational cost of these attributes, as well as all coherence algorithms, increases linearly with the window height and with the square of the its radius. However, the reduction in interpretation time owing to the improved quality of the results compensates for the increased computational time.

Since the seismic amplitude response is the convolution of the reflectivity with the seismic wavelet, the “natural” way to define the analysis window should be a function of the effective wavelet within the area of interest. We define our window size to be a fraction of the p_{80} percentile of the balanced spectrum.

Attributes computed with a fixed user-defined window will generate good images within a given target zone. In the case of laterally variable changes in layer thickness, considerable improvement can be made by adaptively defining the vertical analysis window as a function of the frequency spectrum. Laterally abrupt jumps in window radius and height are minimized by including smooth tapers along the edges.

In this manner, while images at different depth may vary with data quality from high to low resolution, to significance of the anomalies will be similar.

ACKNOWLEDGEMENTS

We thank Schlumberger, for the use of the seismic data set in Westcam survey. Numerical models were generated using Tesseral's Tesseral 2D software. Seismic displays were generated used Schlumberger's Petrel software. We also thank the sponsors of Attribute-Assisted Seismic Processing and Interpretation Consortium (AASPI) for their guidance and financial support.

CHAPTER 3 FIGURES

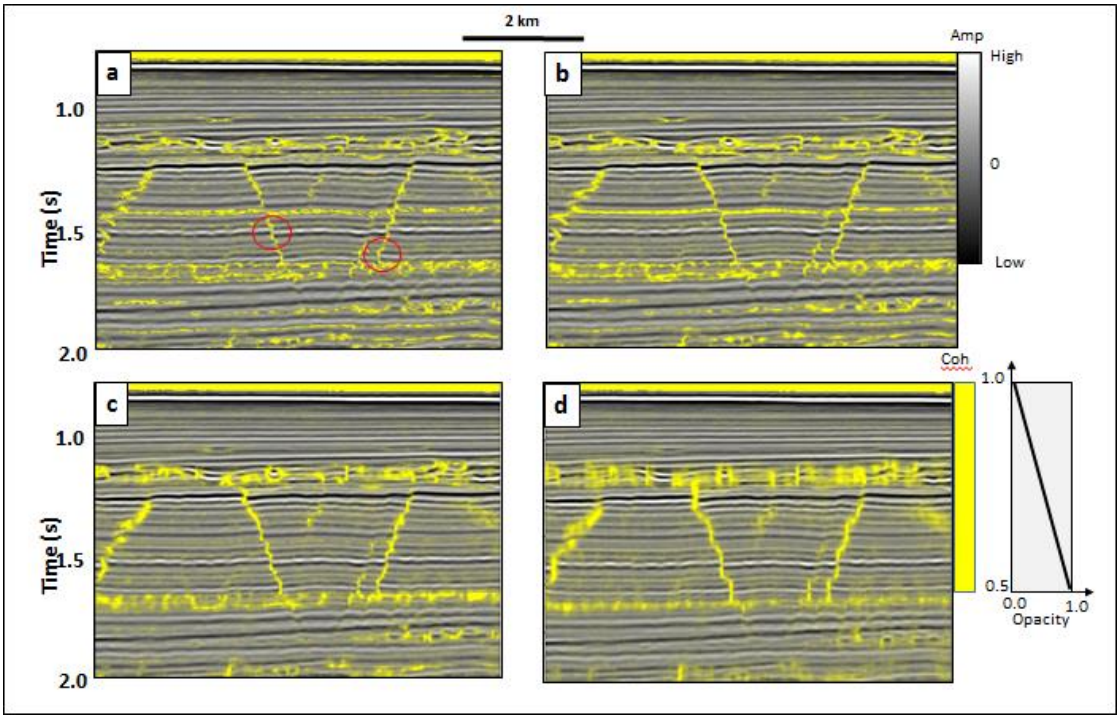

Figure 3.1. Vertical slices through a seismic amplitude volume co-rendered with coherence computed using a 5-trace by (a) ±0 ms, (b) ±4 ms, (c) ±20 ms, and (d) ±40 ms analysis window. Sample increment = 4 ms, bin size =12.5 m x 25 m. Note the stair-step artifacts in (a) indicated by the red circles, even for a vertical analysis window of a single sample. In this image, the stair step is due the vertical orientation of the seismic wavelet, perpendicular to the nearly horizontal reflector. (Data courtesy of NZPM).

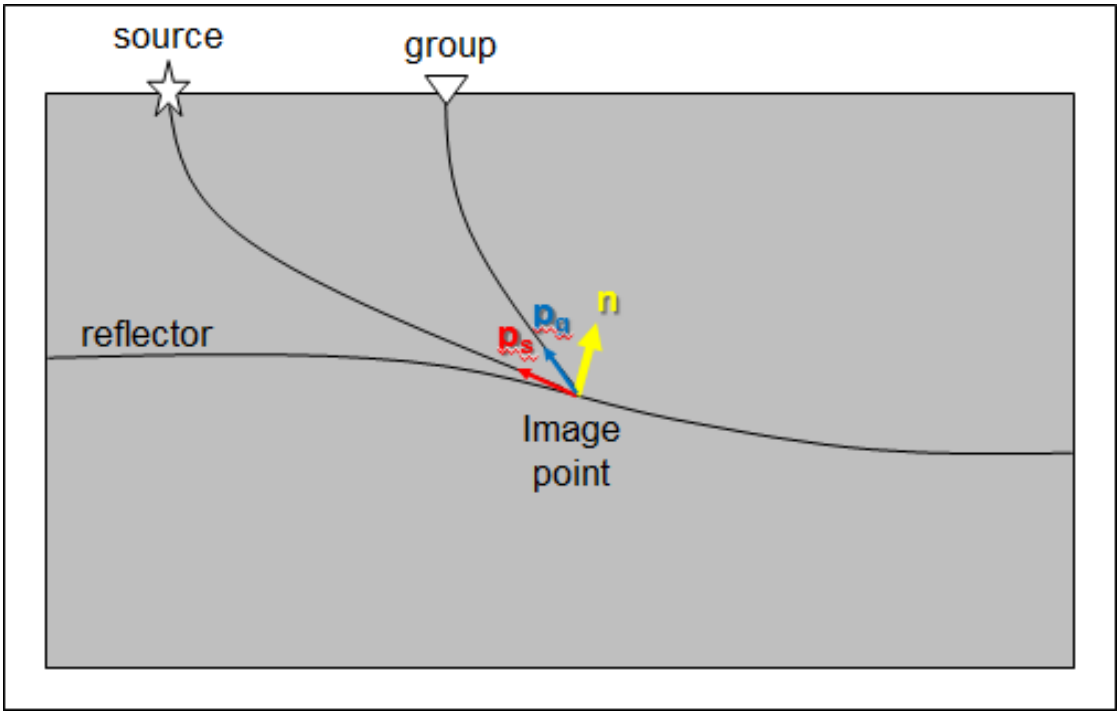

Figure 3.2. The geometry of seismic migration, using the notation of the diffraction imaging community. **n** defines the normal to the hypothesized reflector at the image point. If no hypothesis is made, most algorithms assume **n** to be vertical, while some eliminate the obliquity factor completely. $\mathbf{p}_s$ and $\mathbf{p}_g$ define unit vectors at the image point. The obliquity factor is the cosine of the angle between the yellow vector and the average of the blue and red vectors.

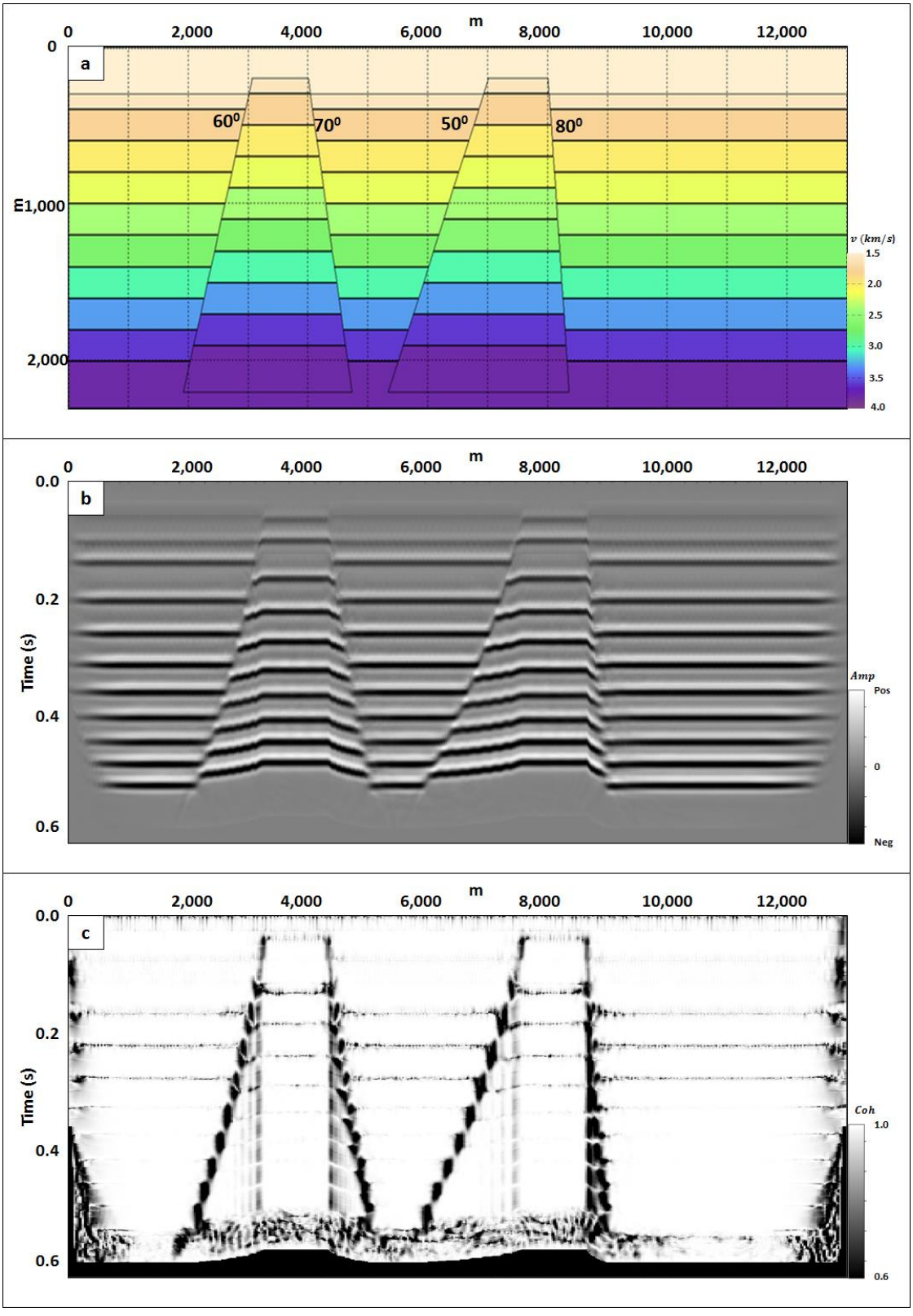
m
0
2,000
4,000
6,000
8,000
10,000
12,000
a
60⁰
70⁰
50⁰
80⁰
1,000
2,000
v (km/s)
1.5
2.0
2.5
3.0
3.5
4.0
b
0.0
0.2
0.4
0.6
Time (s)
Amp
Pos
0
Neg
c
Coh
1.0
0.6

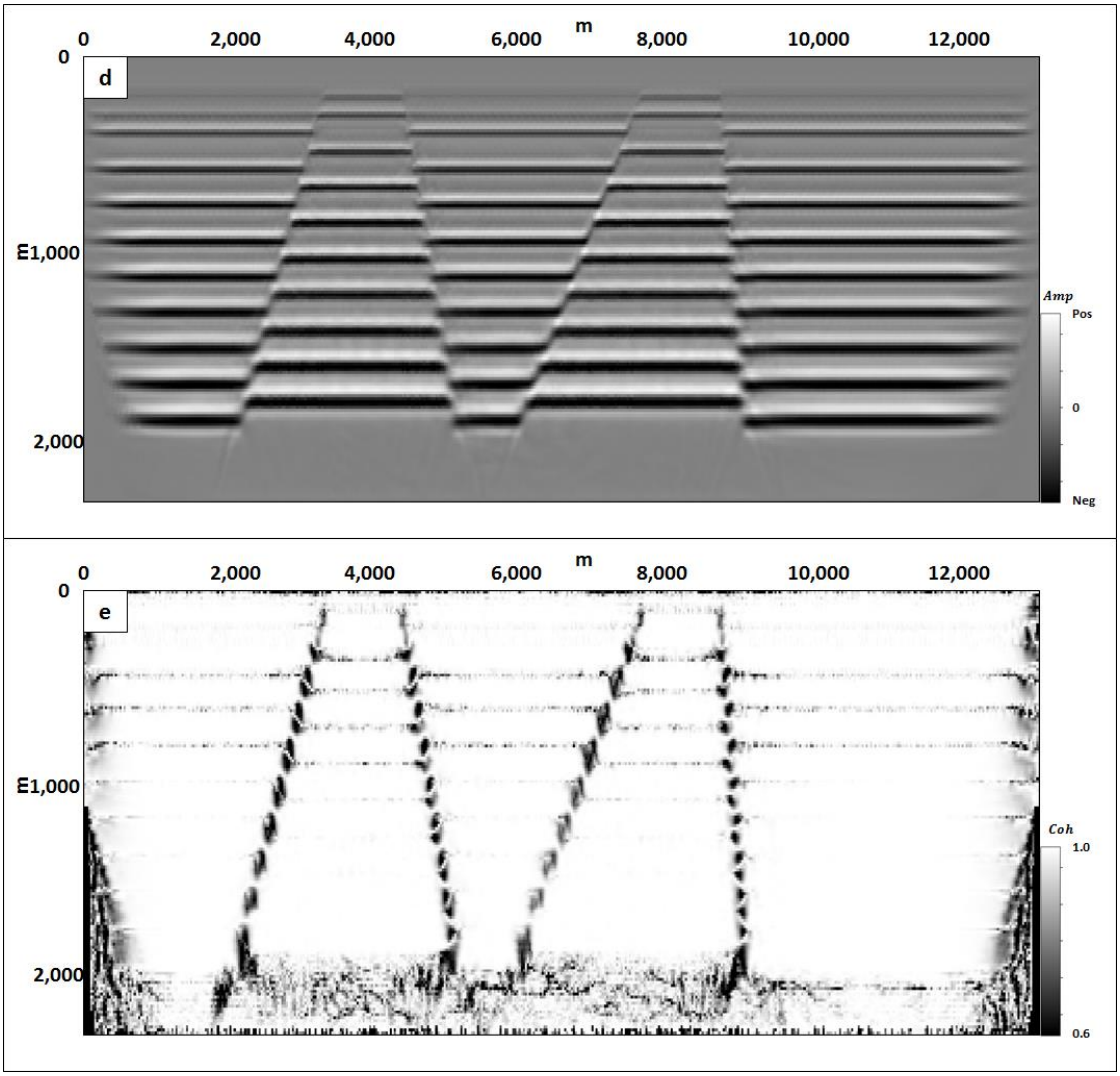
m
0
2,000
4,000
6,000
8,000
10,000
12,000
d
1,000
2,000
Amp
Pos
0
Neg
m
0
2,000
4,000
6,000
8,000
10,000
12,000
e
1,000
2,000
Coh
1.0
0.6

Figure 3.3. (a) A simple reflectivity model showing faults with dips of 500, 600, 700, and 800. Synthetics were generated using a 2D finite difference solution of the wave equation. (b) The resulting prestack time-migrated image. Note that the seismic wavelets are perpendicular to the reflector, including near the fault edges. The images suffer from fault shadows (Fagin, 1996). Fault plane reflectors were not imaged due to the finite migration aperture of 2000 m. (c) The coherence image computed from the seismic data (b) displayed in (a) using a vertical analysis window of 1 sample. (d) The resulting prestack depth-migrated image. (e) The coherence image computed from the seismic data (d) displayed in (a) using a vertical analysis window of one sample. Note the stair step artifacts are about the size of the seismic wavelet seen in (d). Depth migration has eliminated the fault shadows.

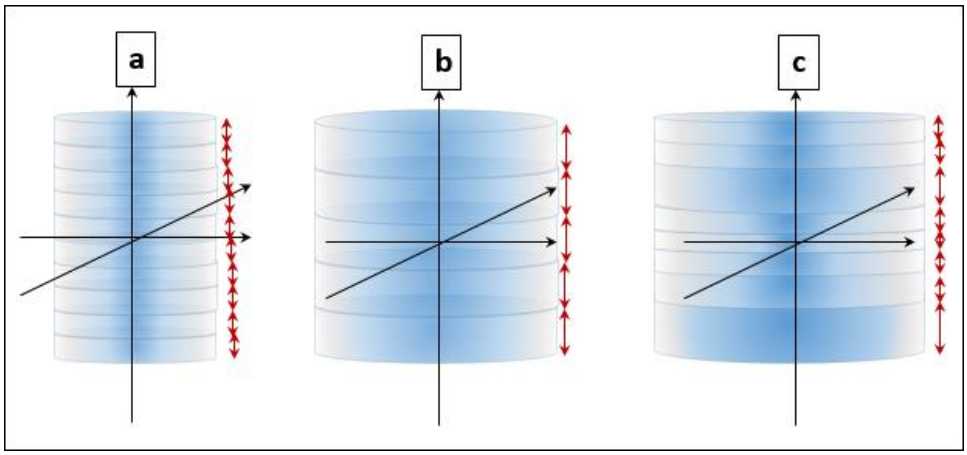

Figure 3.4. The diagram of the (a) fixed, small windows, (b) fixed, large window, and (c) the adaptive window tapered radially and vertically.

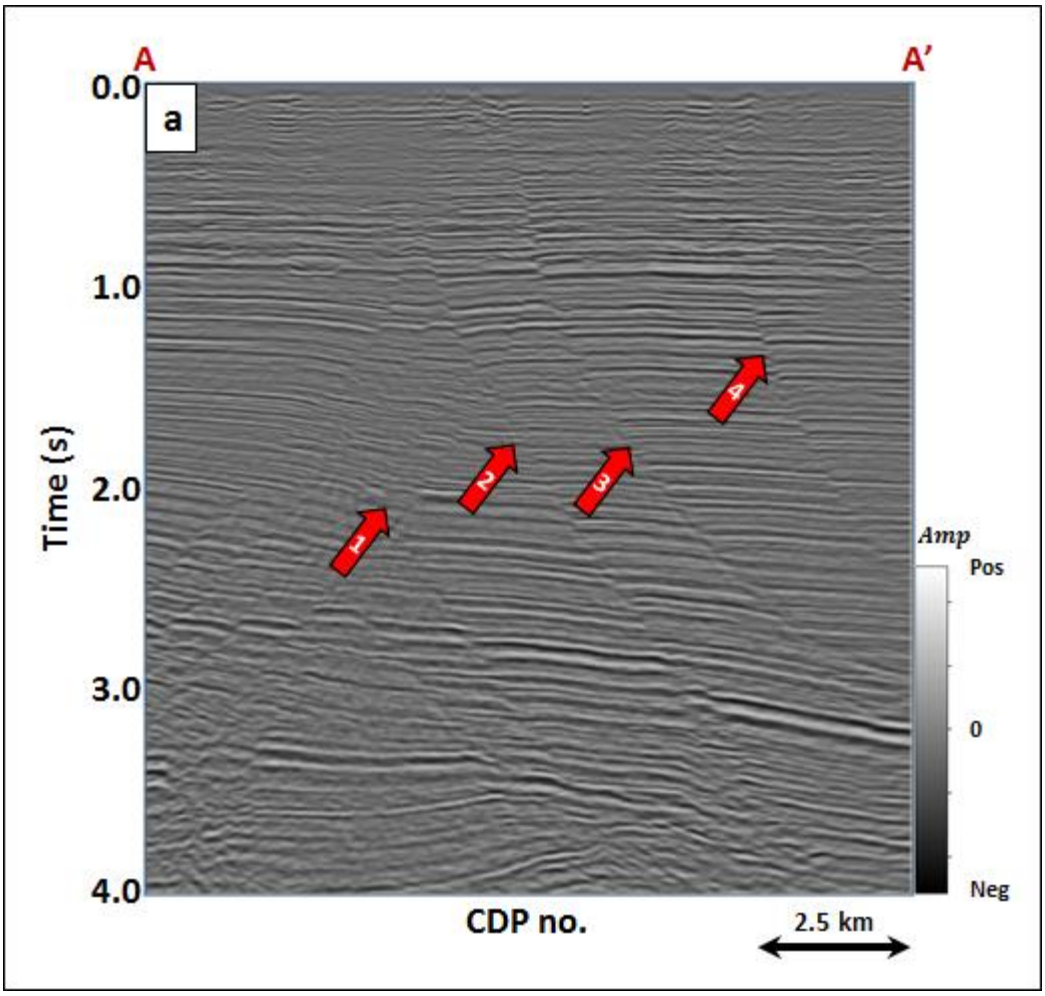
A
A'
a
0.0
1.0
2.0
3.0
4.0
Time (s)
1
2
3
4
Amp
Pos
0
Neg
CDP no.
2.5 km

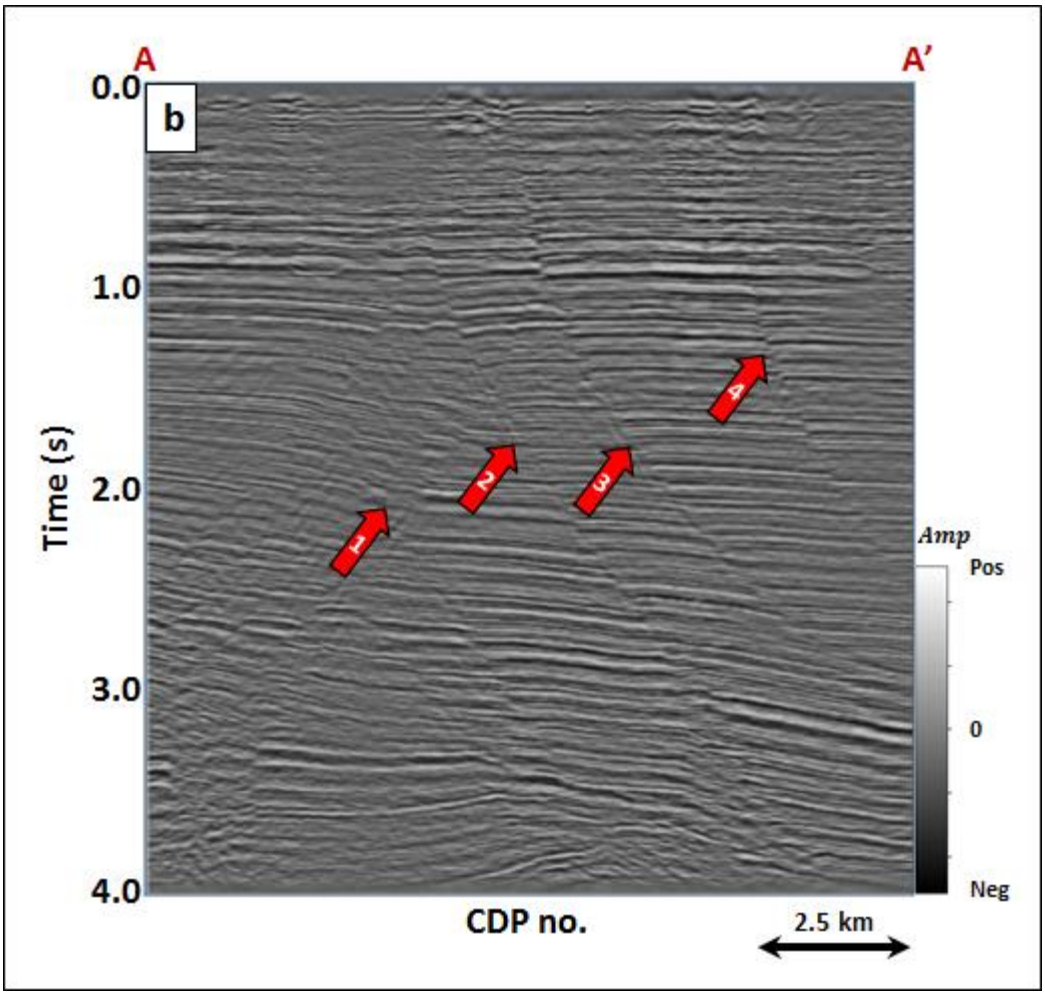
A
A'
b
0.0
1.0
2.0
3.0
4.0
Time (s)
1
2
3
4
Amp
Pos
0
Neg
CDP no.
2.5 km

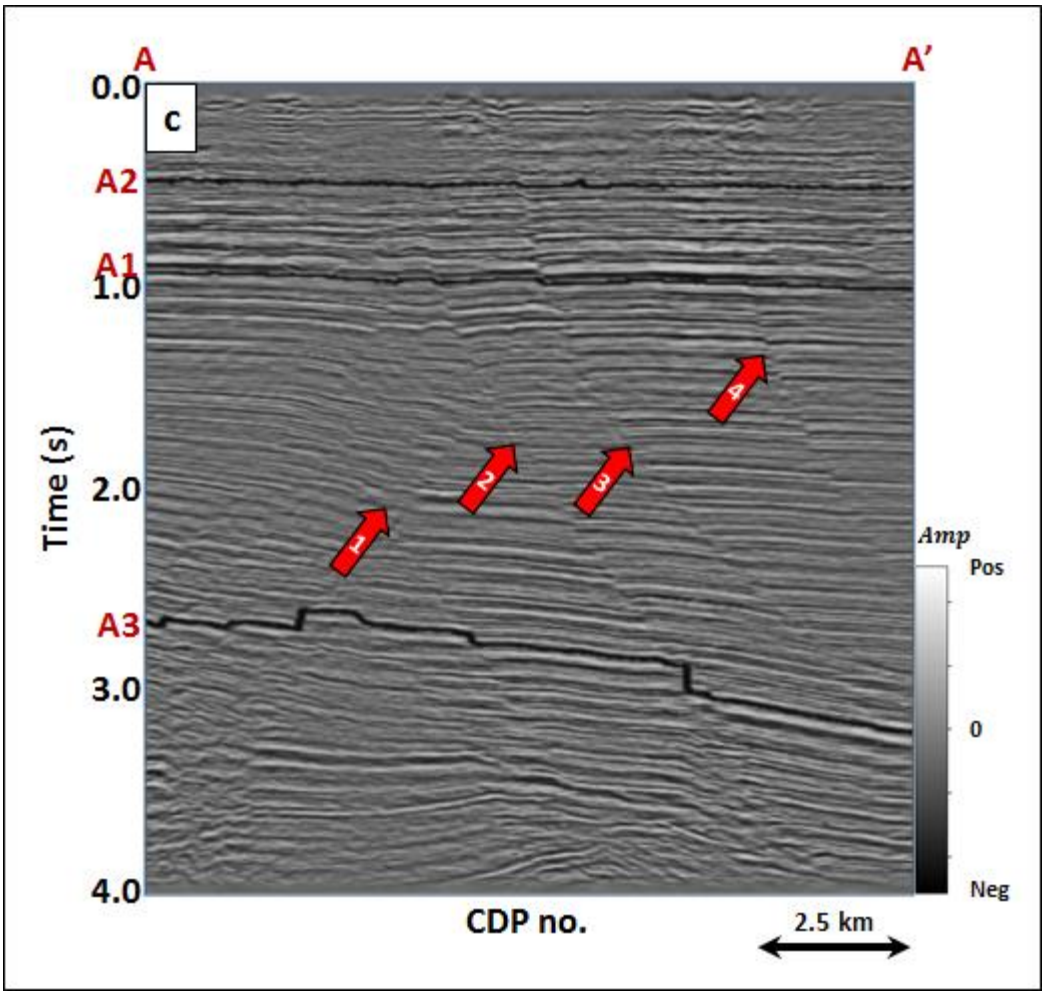

Figure 3.5. Vertical slice AA' through (a) origional seismic amplitude volume, and the seismic amplitude volume after (b) spectral balancing and (c) structural-oriented filtering. (sample interval: 4 ms).

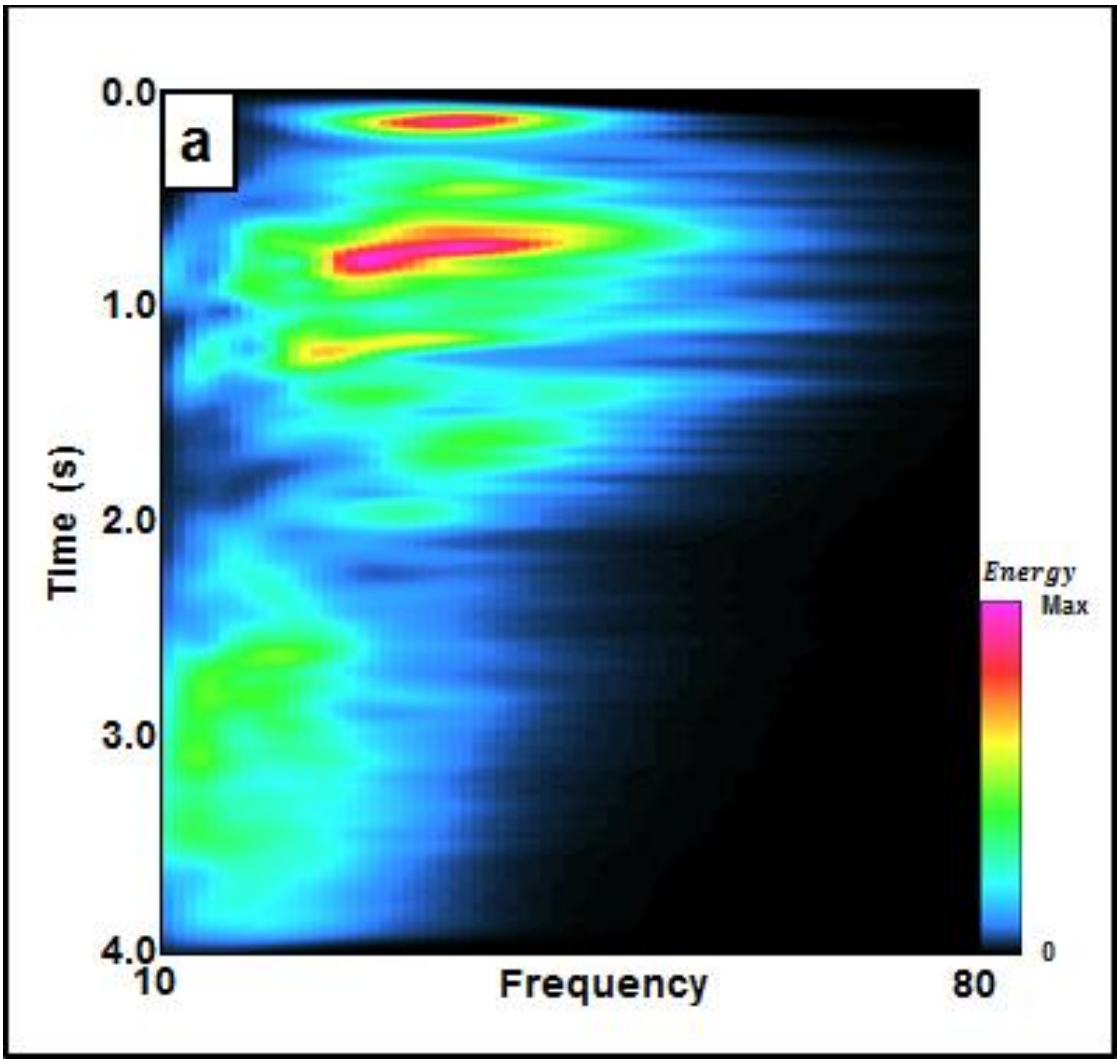
a
0.0
1.0
2.0
3.0
4.0
Time (s)
10
Frequency
80
Energy
Max
0

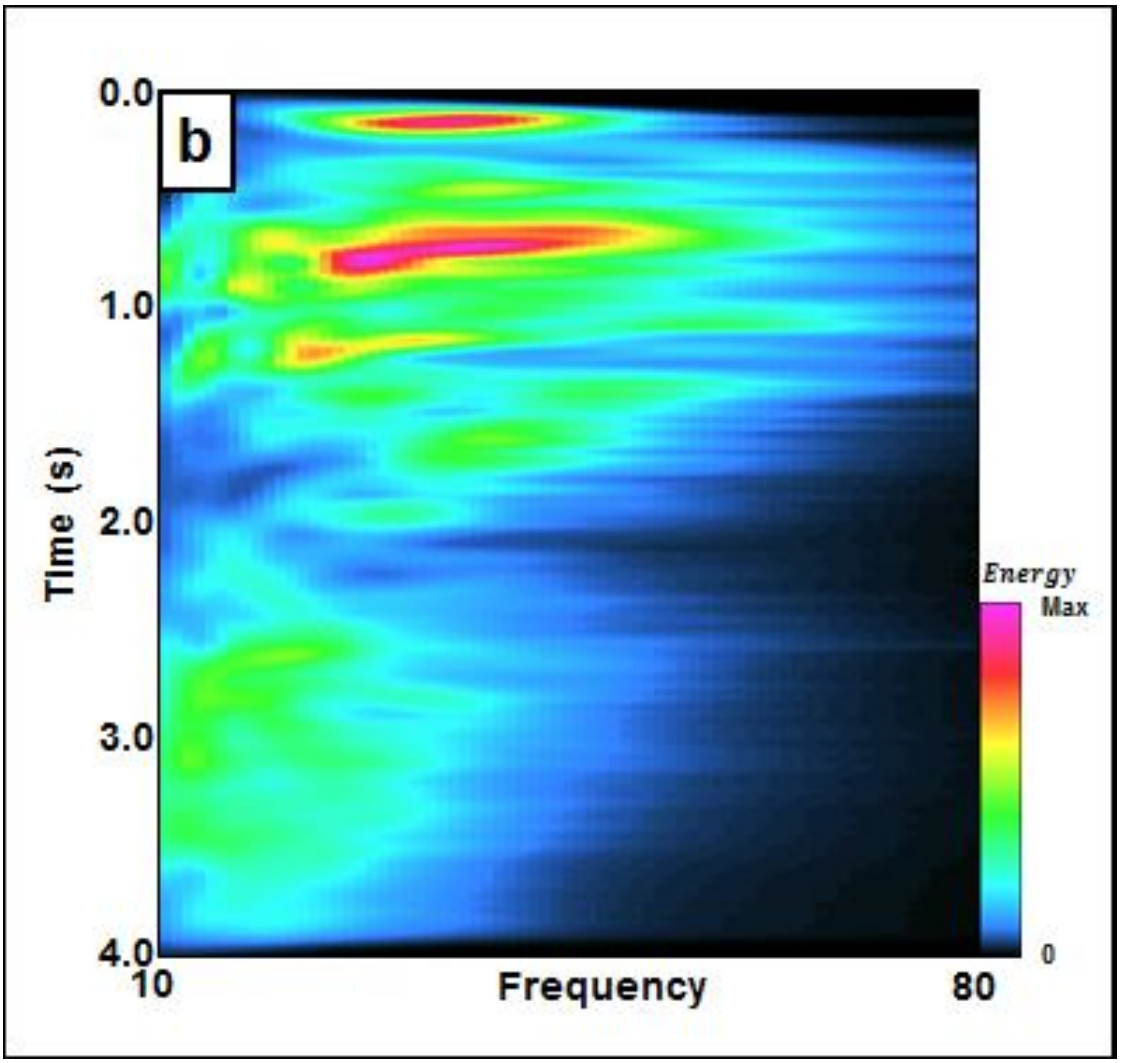

Figure 3.6. The frequency spectrum of seismic amplitude volume (a) and (b) after spectral balancing.

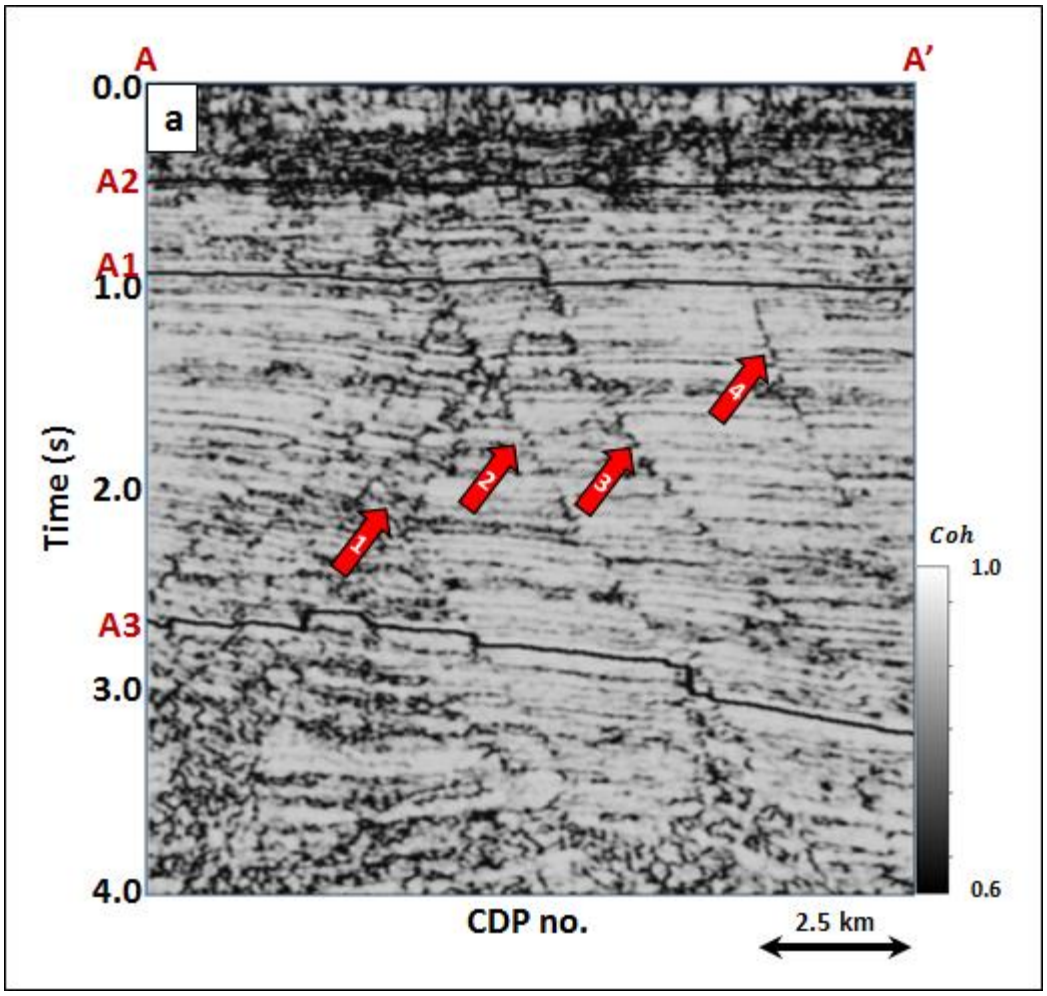
A
A'
a
0.0
A2
A1
1.0
2.0
A3
3.0
4.0
Time (s)
1
2
3
4
Coh
1.0
0.6
CDP no.
2.5 km

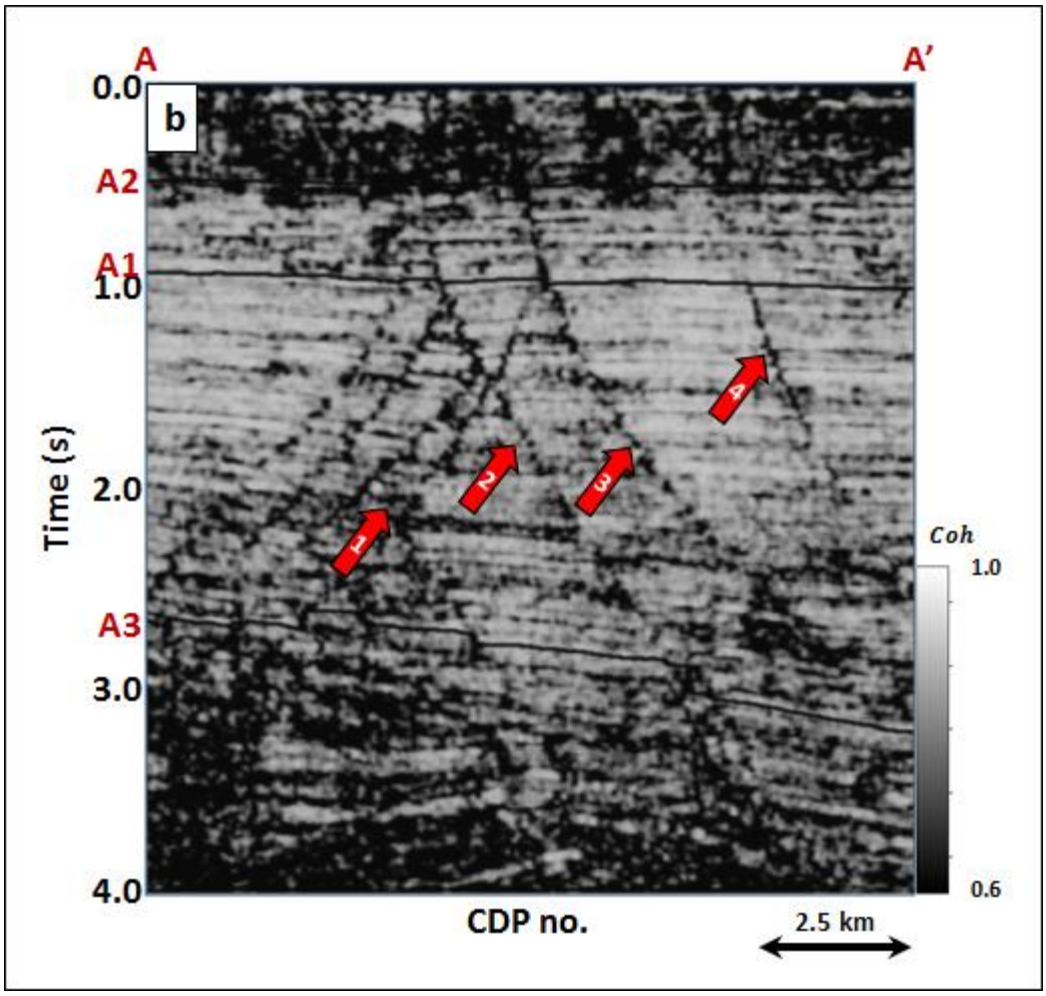
A
A'
b
0.0
A2
A1
1.0
2.0
A3
3.0
4.0
Time (s)
1
2
3
4
Coh
1.0
0.6
CDP no.
2.5 km

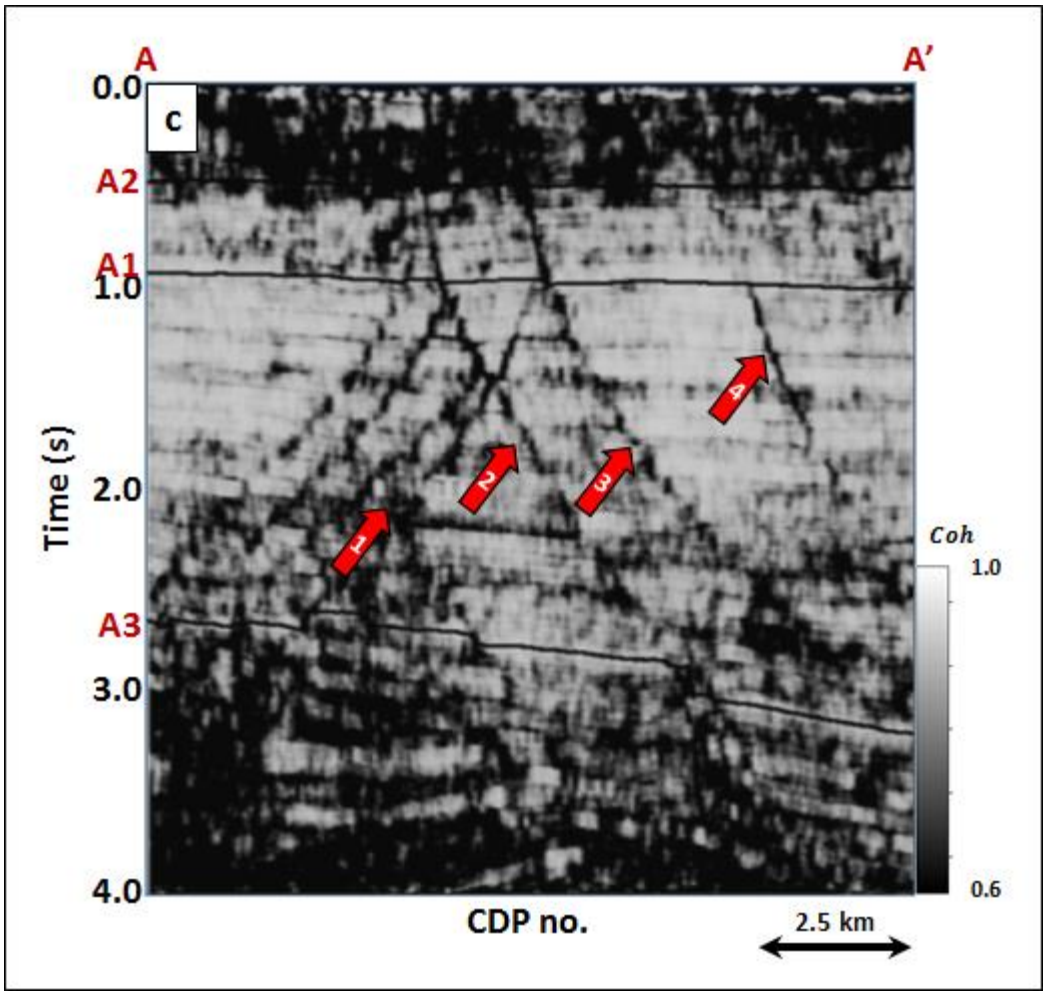
A
A'
0.0
c
A2
A1
1.0
Time (s)
2.0
A3
3.0
4.0
1
2
3
4
Coh
1.0
0.6
CDP no.
2.5 km

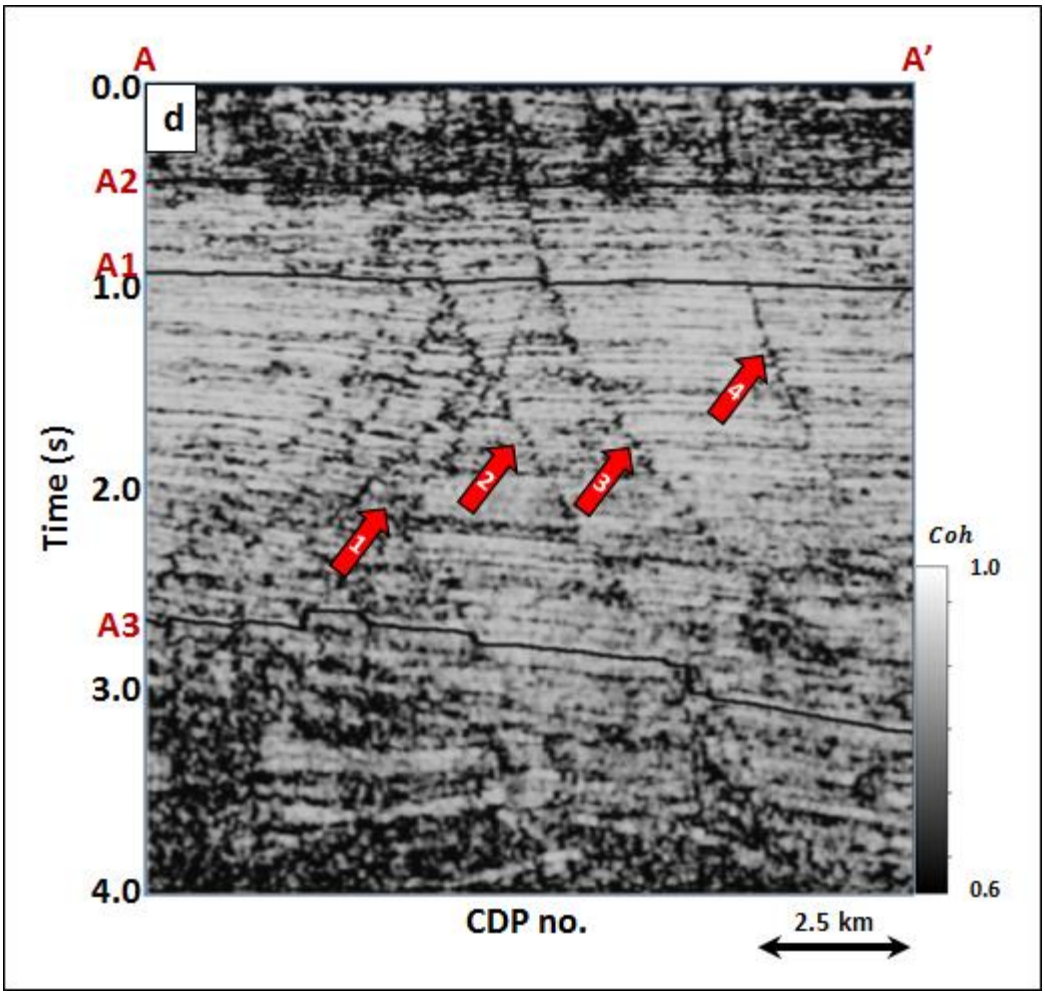

Figure 3.7. Vertical slice AA' through energy ratio coherence using a constant window size of (a) ±4 ms, (b) ±20 ms, (c) ±40 ms and (d) a data-adaptive window (±12~100 ms) of Figure 3.5c.

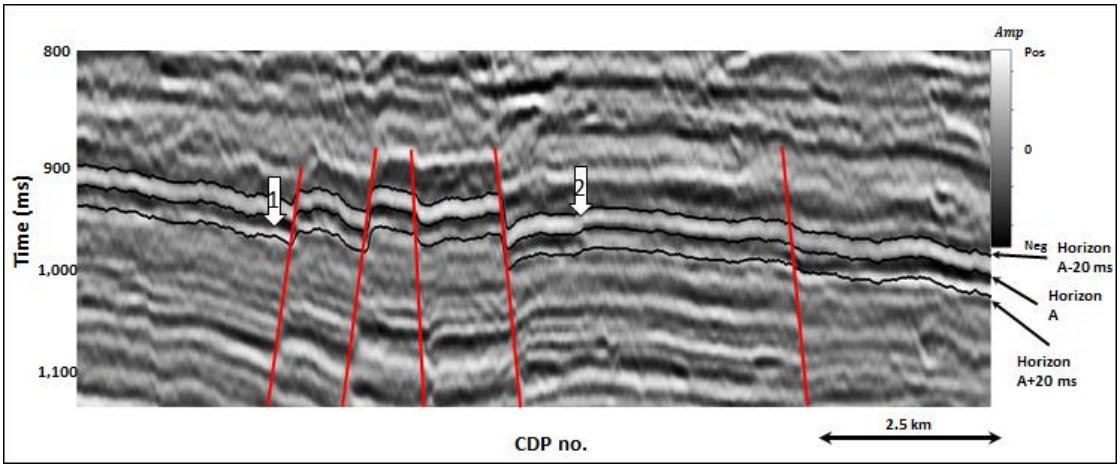

Figure 3.8. Zooned in section of seismic profile of Figure 3.5c (ranges 800~1150 ms).

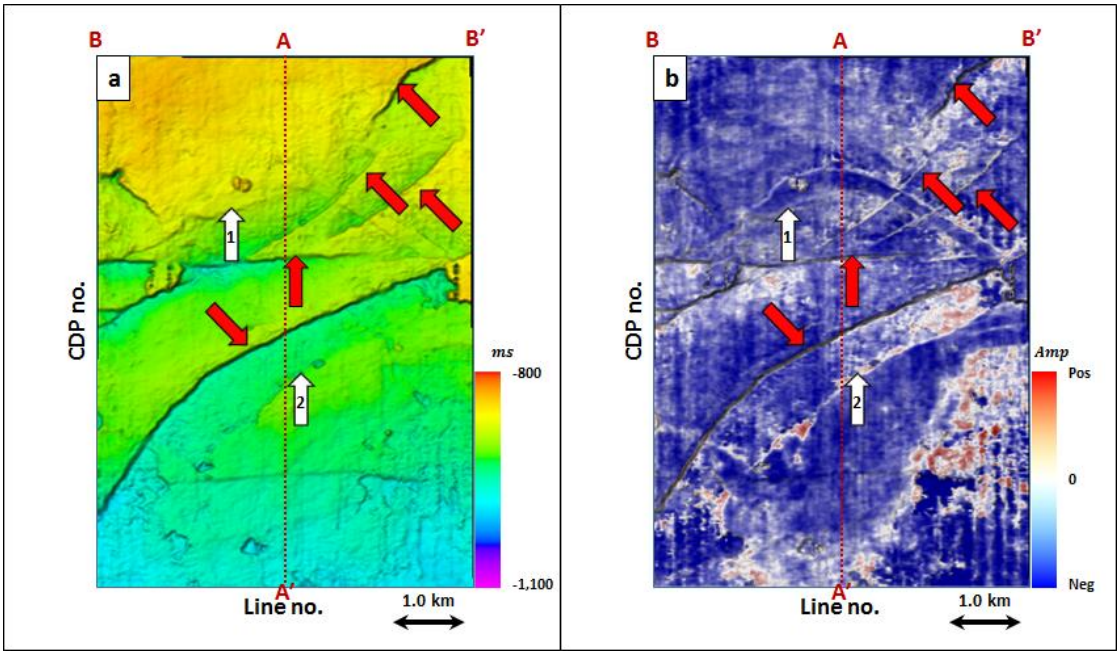

Figure 3.9. (a) Time-structure map of Horizon A1 and (b) a horizon slice through seismic amplitude. Horizon A1 was picked as a trough.

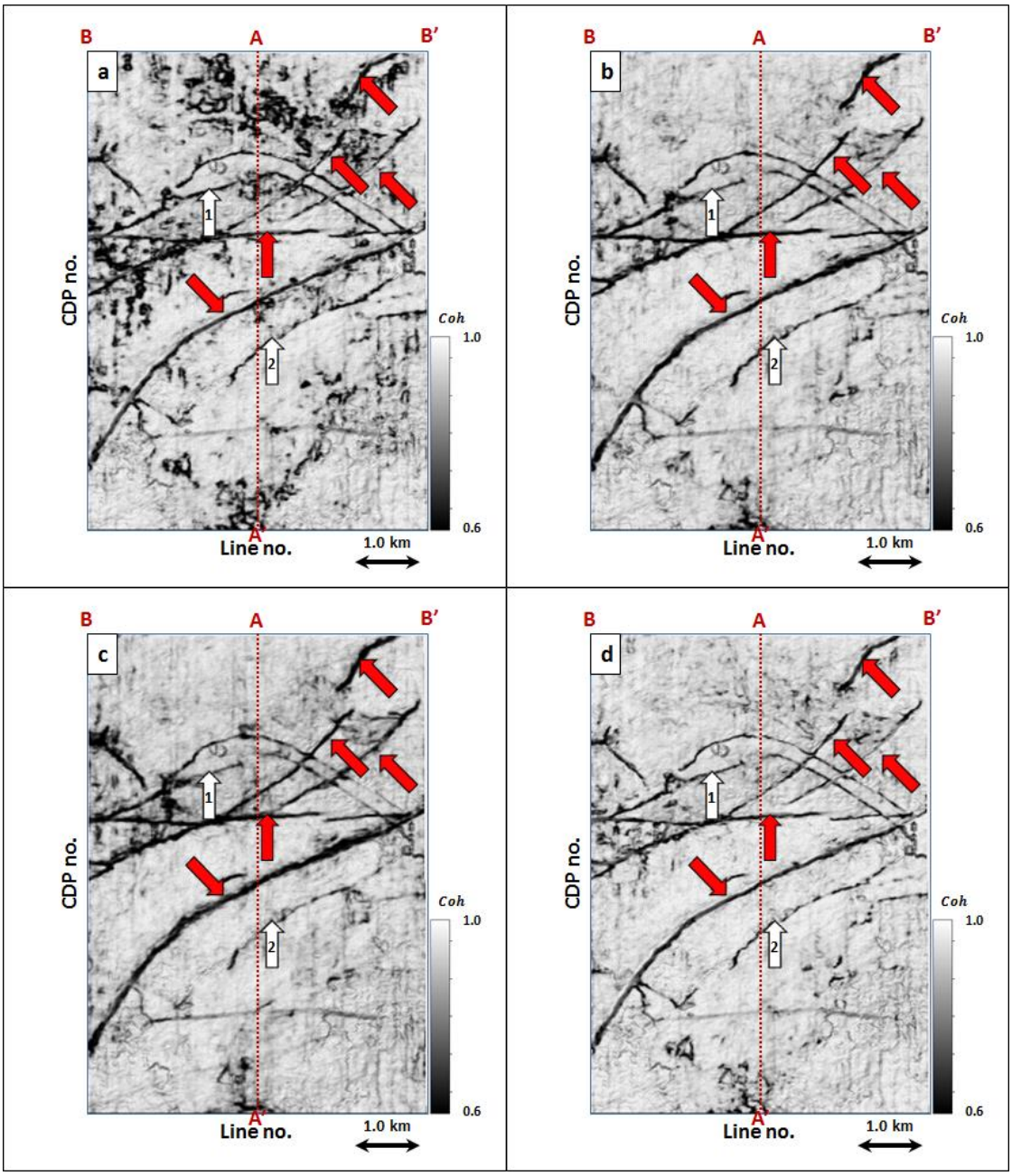

Figure 3.10. Energy ratio coherence along Horizon A1 using constant window size of (a) ±4 ms, (b) ±20 ms, (c) ±40 ms using 5 traces, and (d) a data-adaptive window varying between ±12 ms and 5 traces, and ±100 ms and 13 traces.

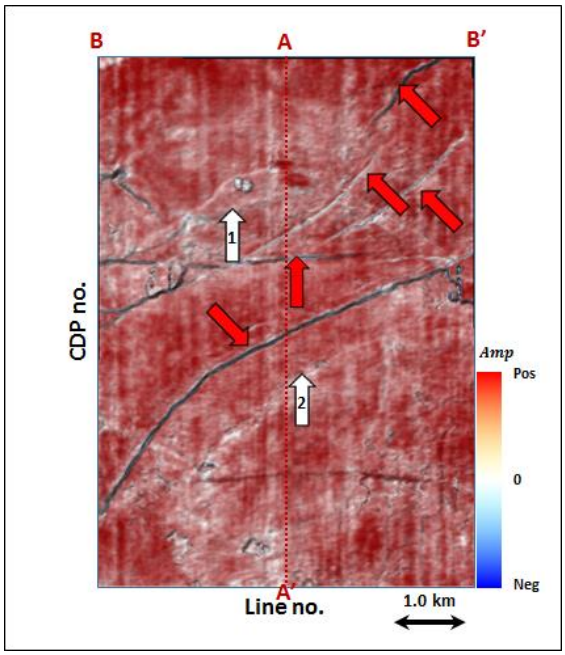

Figure 3.11. Phantom horizon 8 ms above Horizon A1 extracting along seismic amplitude data.

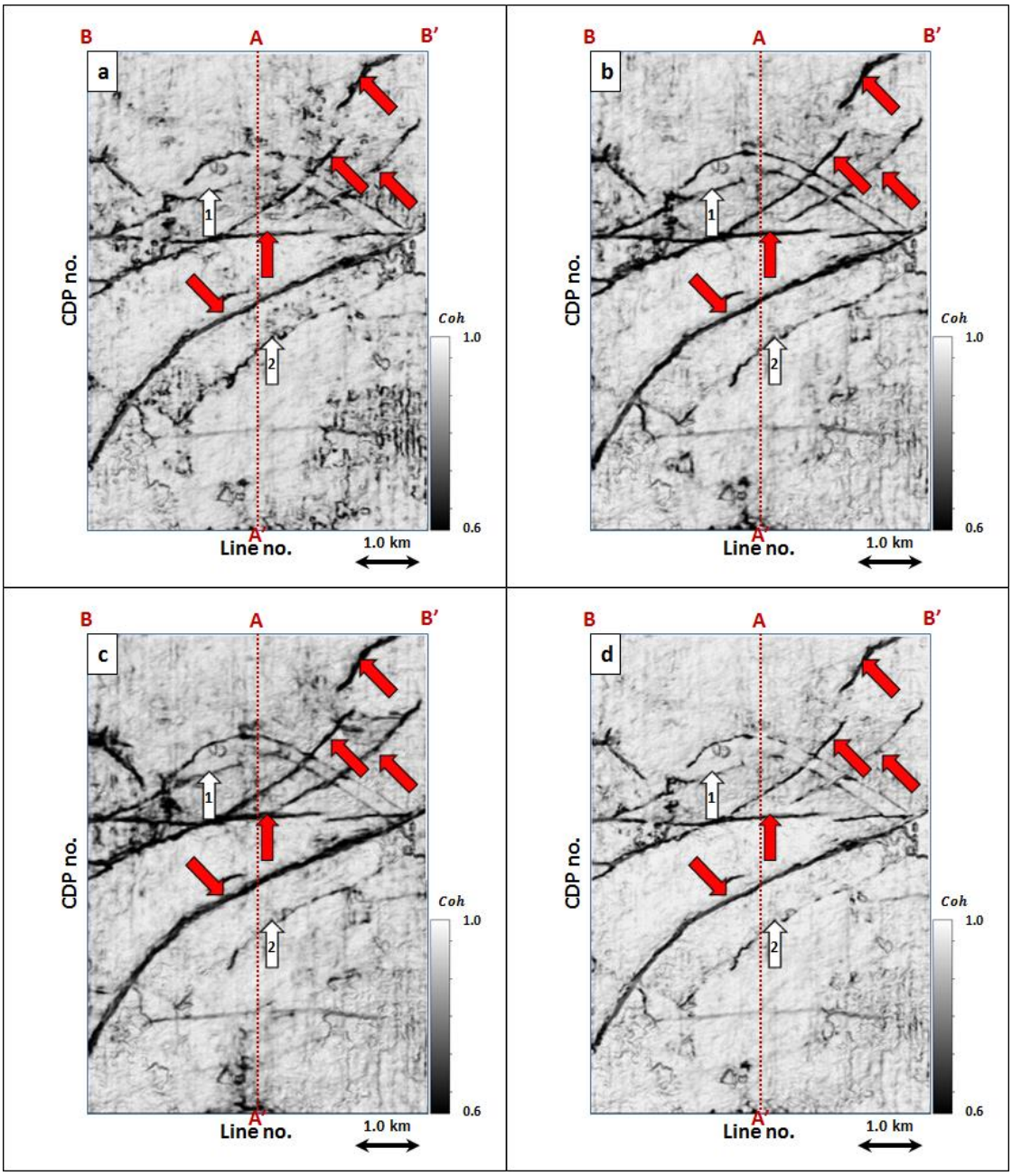

Figure 3.12. Energy ratio coherence along phantom horizon 8 ms above Horizon A1 using constant window size of (a) ±4 ms, (b) ±20 ms, (c) ±40 ms using 5 traces, and (d) a data-adaptive window varying between ±12 ms and 5 traces, and ±100 ms and 13 traces.

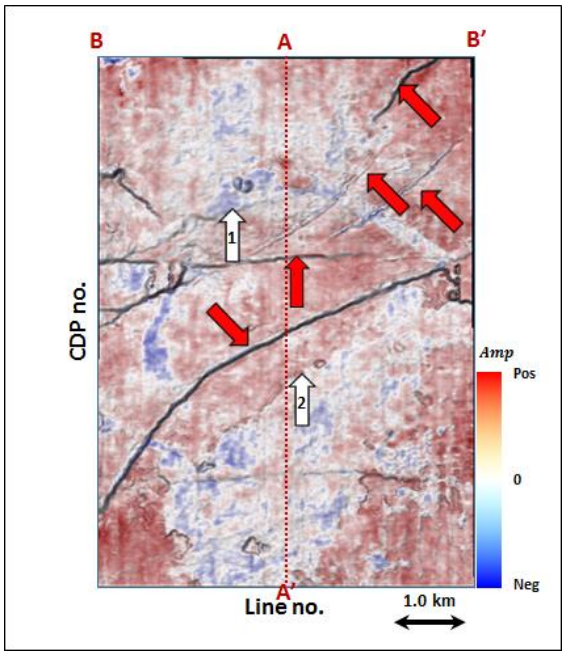

Figure 3.13. Phantom horizon 16 ms above Horizon A1 extracting along seismic amplitude data.

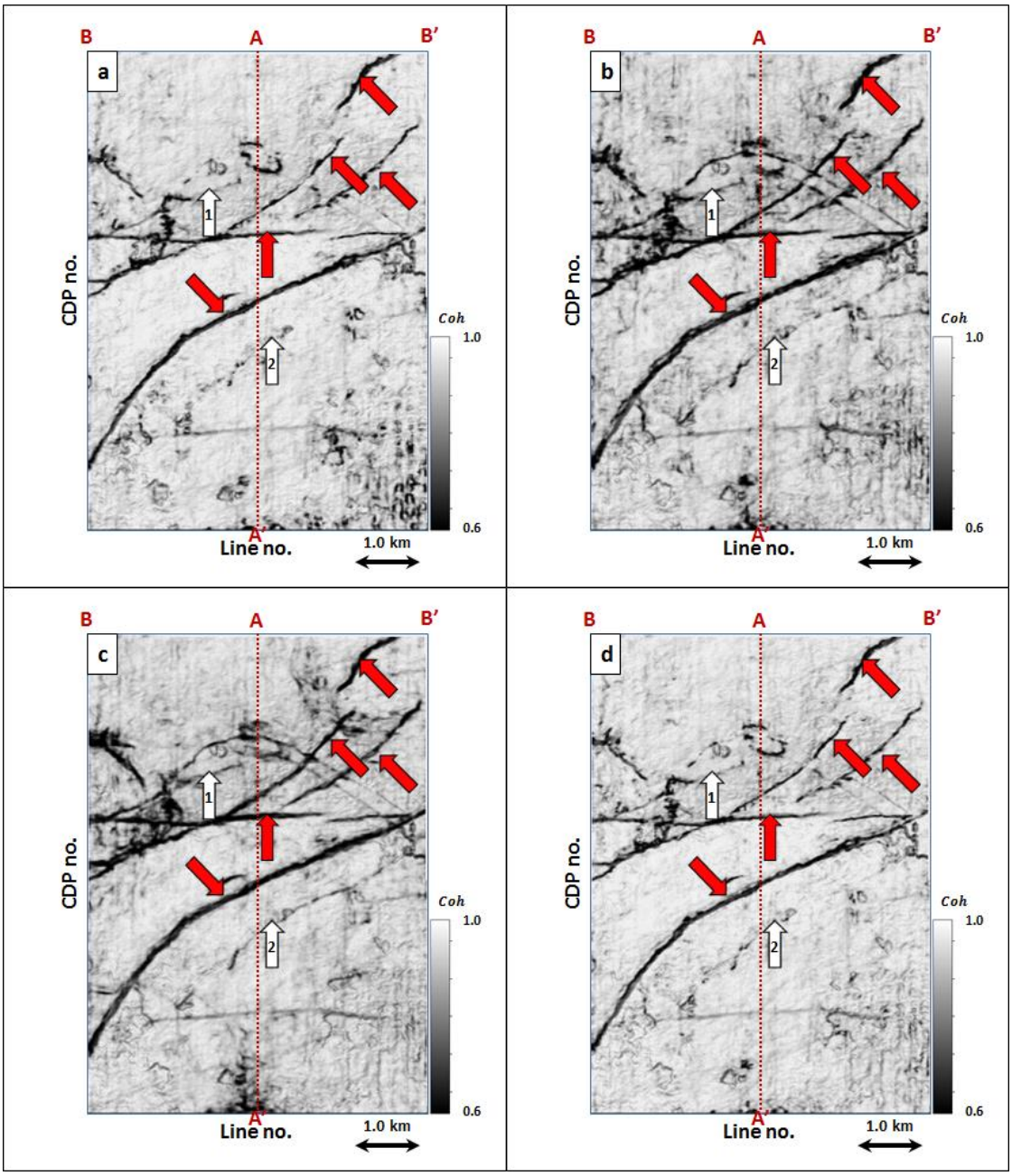

Figure 3.14. Energy ratio coherence along phantom horizon 16 ms above Horizon A1 using constant window size of (a) ±4 ms, (b) ±20 ms, (c) ±40 ms using 5 traces, and (d) a data-adaptive window varying between ±12 ms and 5 traces, and ±100 ms and 13 traces.

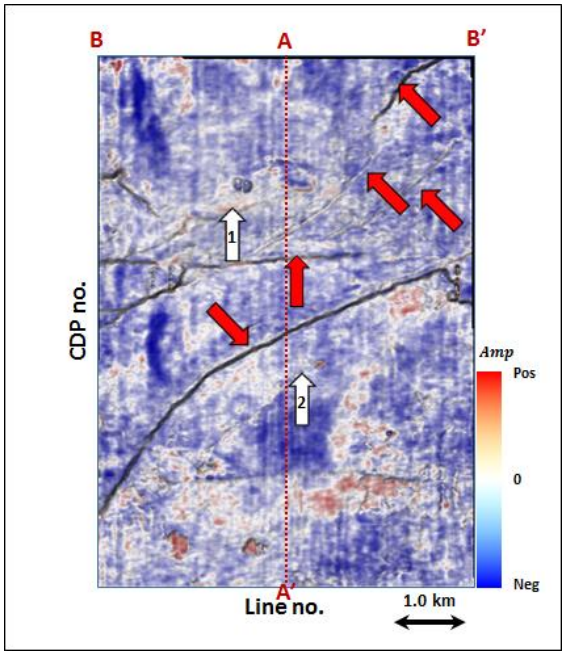

Figure 3.15. Phantom horizon 24 ms above Horizon A1 extracting along seismic amplitude data.

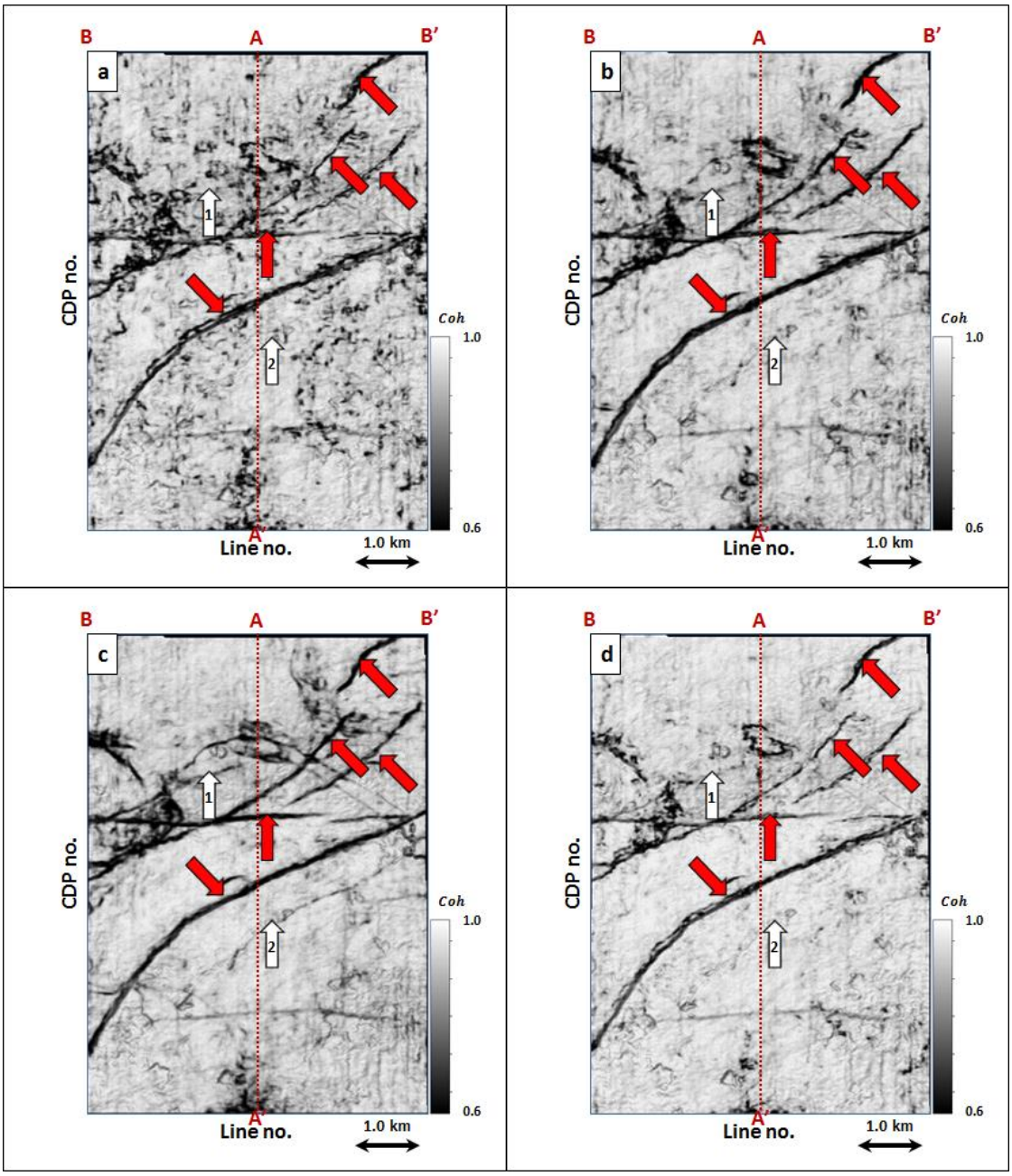

Figure 3.16. Energy ratio coherence along phantom horizon 24 ms above Horizon A1 using constant window size of (a) ±4 ms, (b) ±20 ms, (c) ±40 ms using 5 traces, and (d) a data-adaptive window varying between ±12 ms and 5 traces, and ±100 ms and 13 traces.

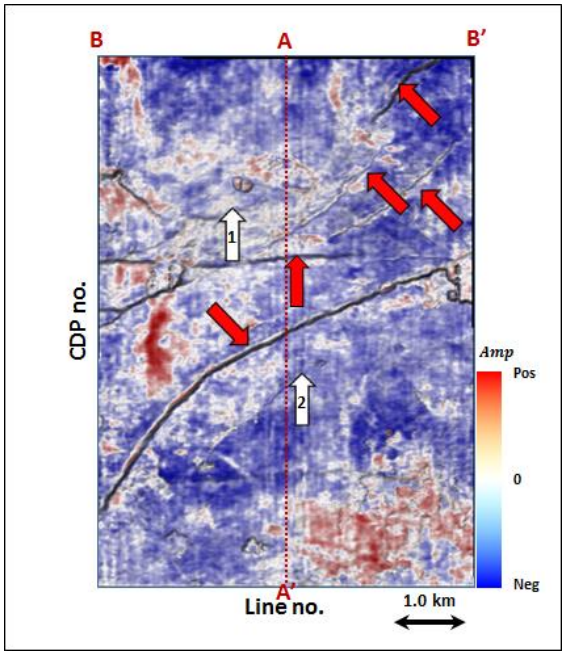

Figure 3.17. Phantom horizon 32 ms above Horizon A1 extracting along seismic amplitude data.

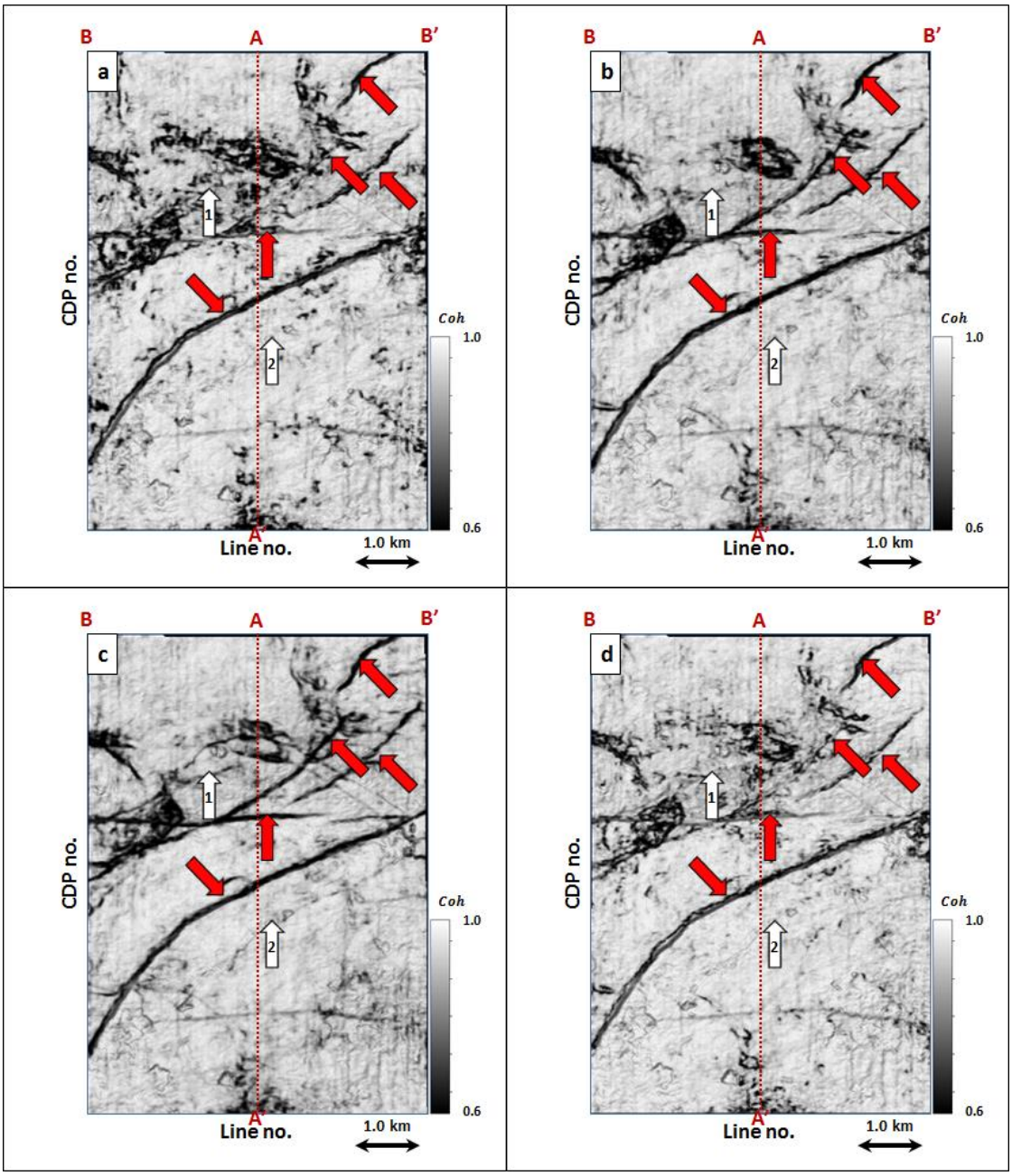

Figure 3.18. Energy ratio coherence along phantom horizon 32 ms above Horizon A1 using constant window size of (a) ±4 ms, (b) ±20 ms, (c) ±40 ms using 5 traces, and (d) a data-adaptive window varying between ±12 ms and 5 traces, and ±100 ms and 13 traces.

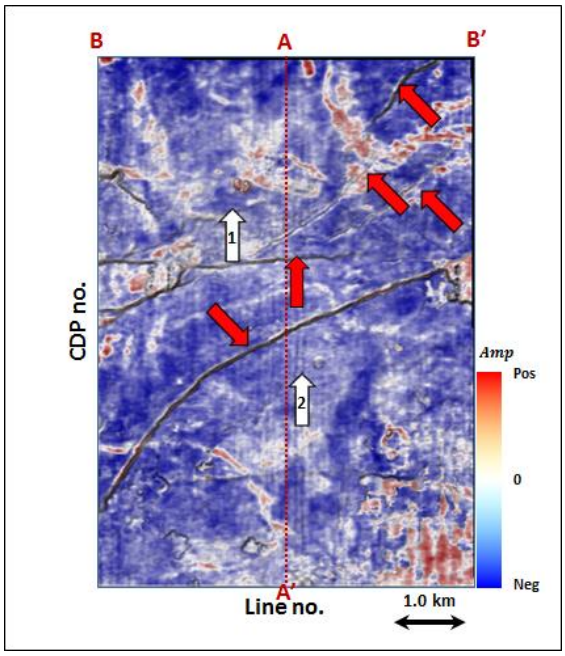

Figure 3.19. Phantom horizon 40 ms above Horizon A1 extracting along seismic amplitude data.

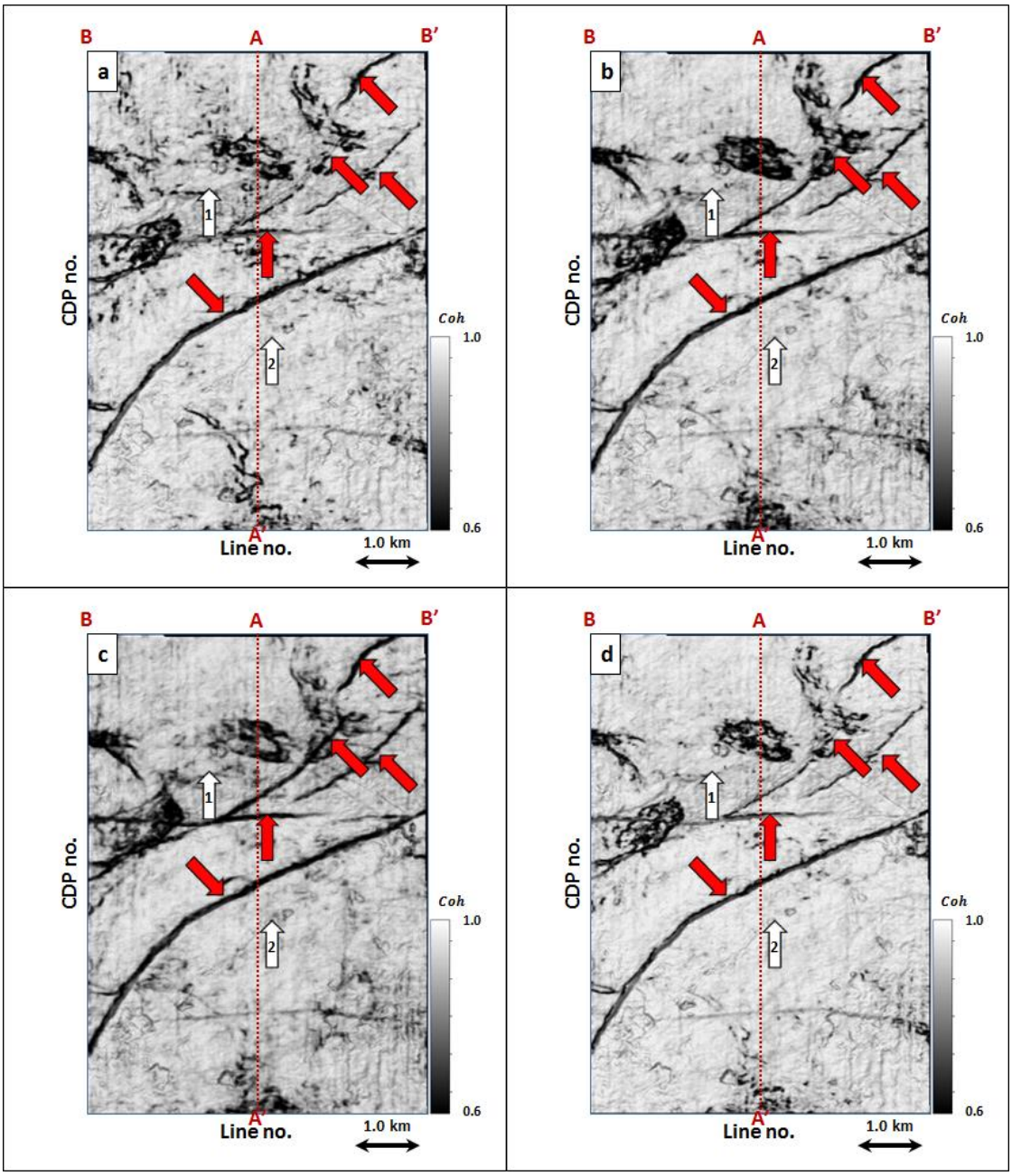

Figure 3.20. Energy ratio coherence along phantom horizon 40ms above Horizon A1 using constant window size of (a) ±4 ms, (b) ±20 ms, (c) ±40 ms using 5 traces, and (d) a data-adaptive window varying between ±12 ms and 5 traces, and ±100 ms and 13 traces.

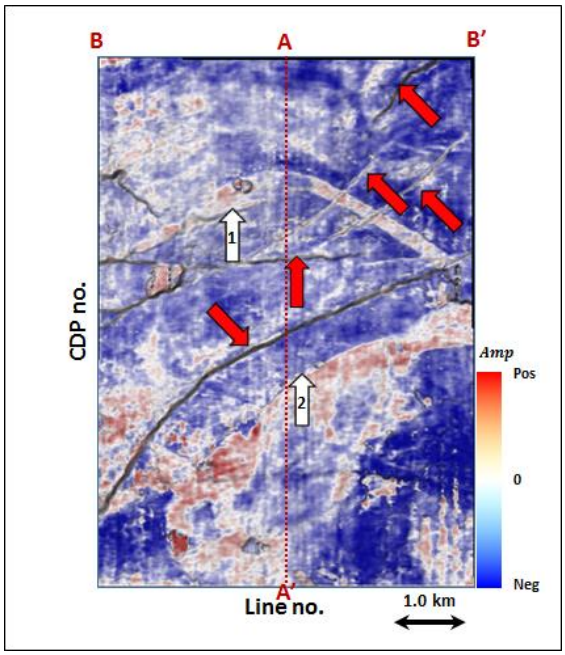

Figure 3.21. Phantom horizon 8 ms below Horizon A1 extracting along seismic amplitude data.

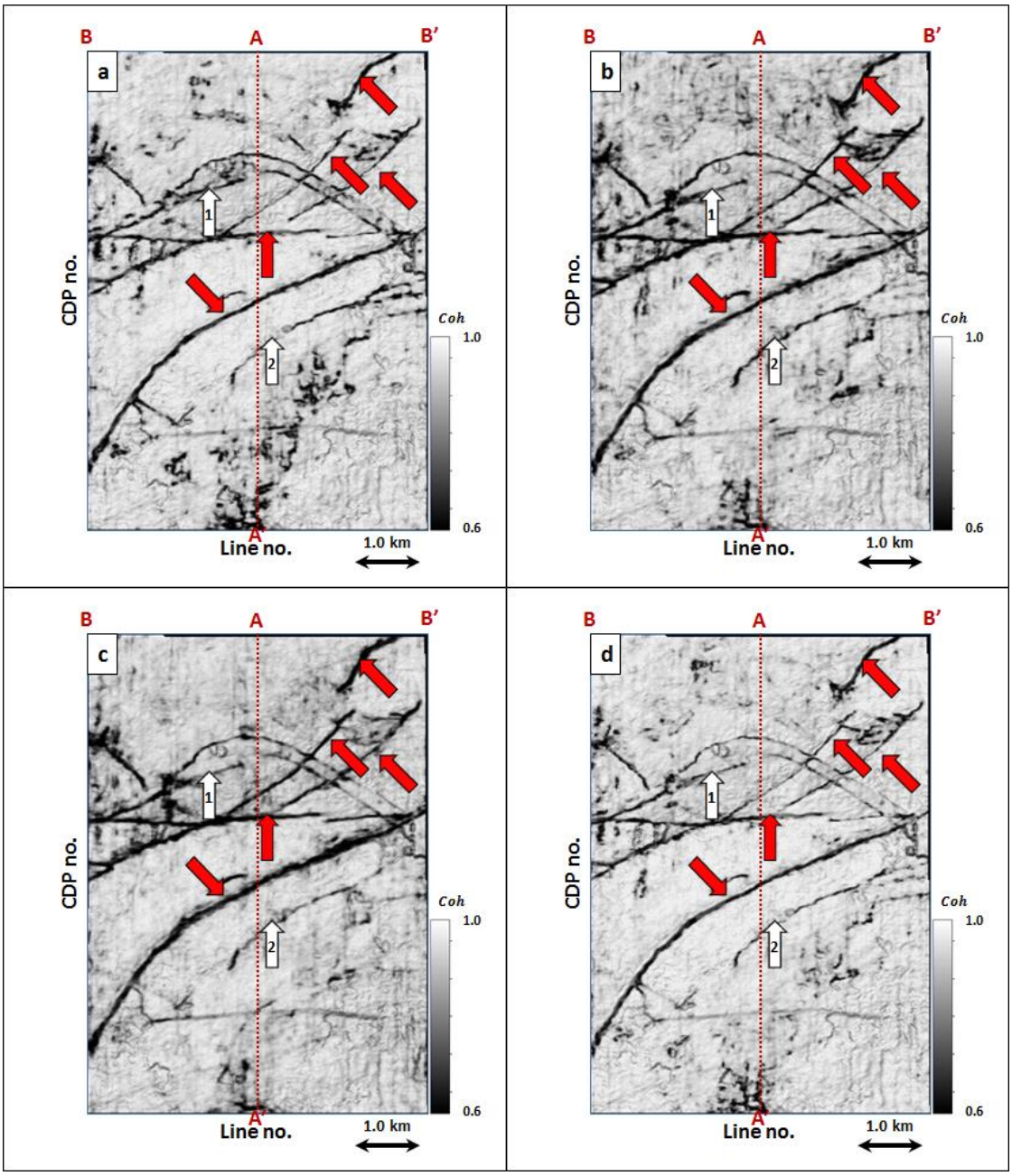

Figure 3.22. Energy ratio coherence along phantom horizon 8 ms below Horizon A1 using constant window size of (a) ±4 ms, (b) ±20 ms, (c) ±40 ms using 5 traces, and (d) a data-adaptive window varying between ±12 ms and 5 traces, and ±100 ms and 13 traces.

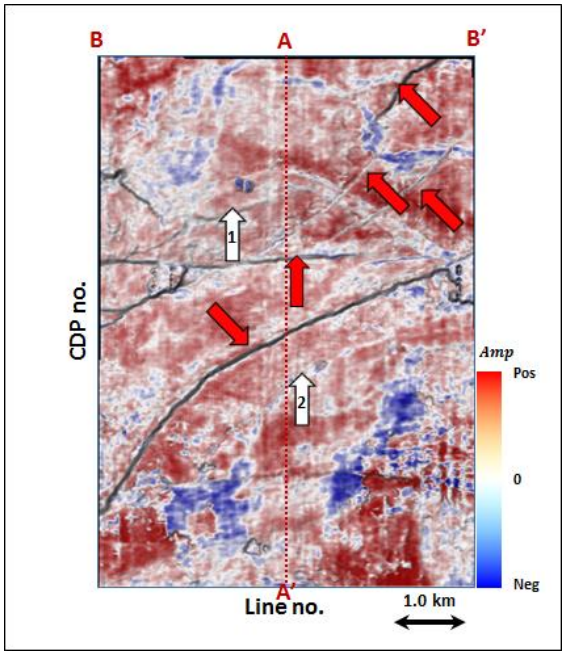

Figure 3.23. Phantom horizon 16 ms below Horizon A1 extracting along seismic amplitude data.

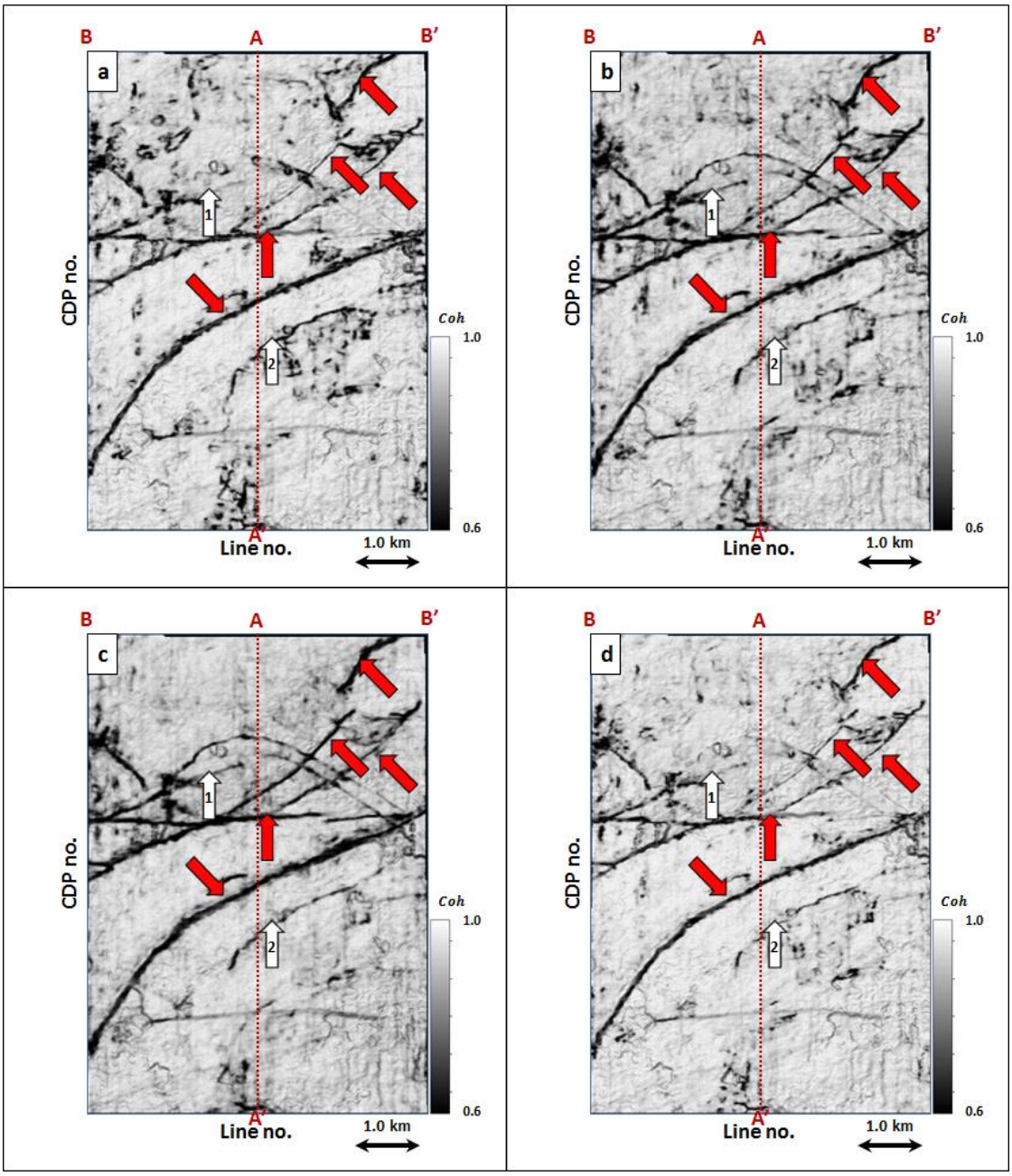

Figure 3.24. Energy ratio coherence along phantom horizon 16 ms below Horizon A1 using constant window size of (a) ±4 ms, (b) ±20 ms, (c) ±40 ms using 5 traces, and (d) a data-adaptive window varying between ±12 ms and 5 traces, and ±100 ms and 13 traces.

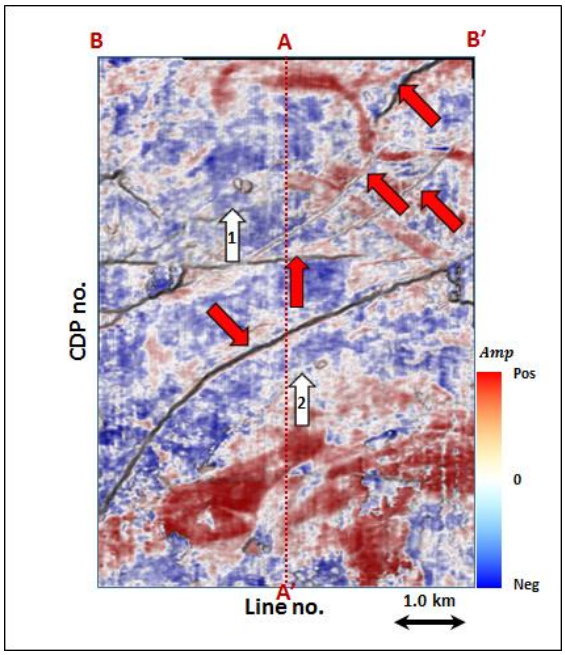

Figure 3.25. Phantom horizon 24 ms below Horizon A1 extracting along seismic amplitude data.

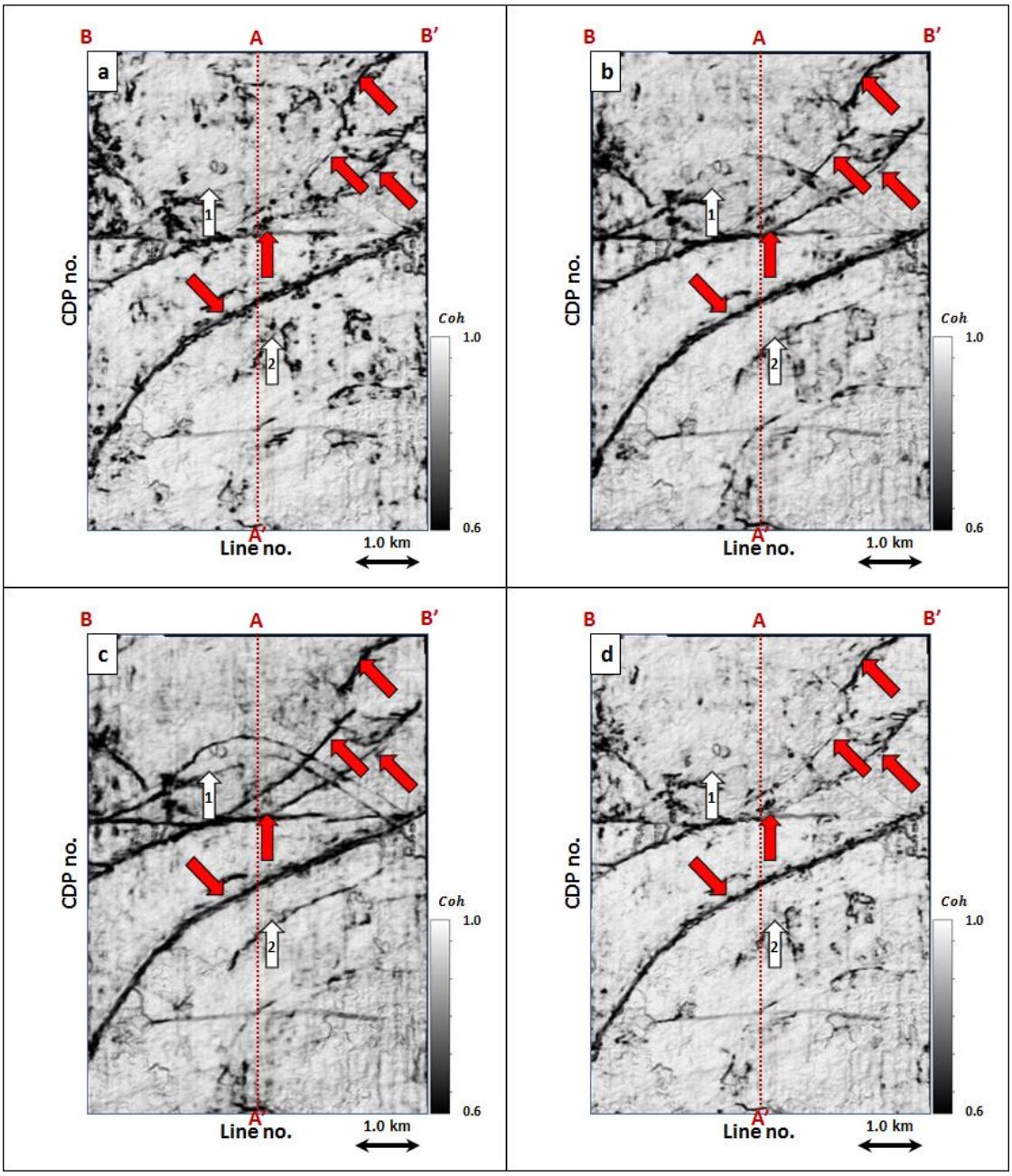

Figure 3.26. Energy ratio coherence along phantom horizon 24 ms below Horizon A1 using constant window size of (a) ±4 ms, (b) ±20 ms, (c) ±40 ms using 5 traces, and (d) a data-adaptive window varying between ±12 ms and 5 traces, and ±100 ms and 13 traces.

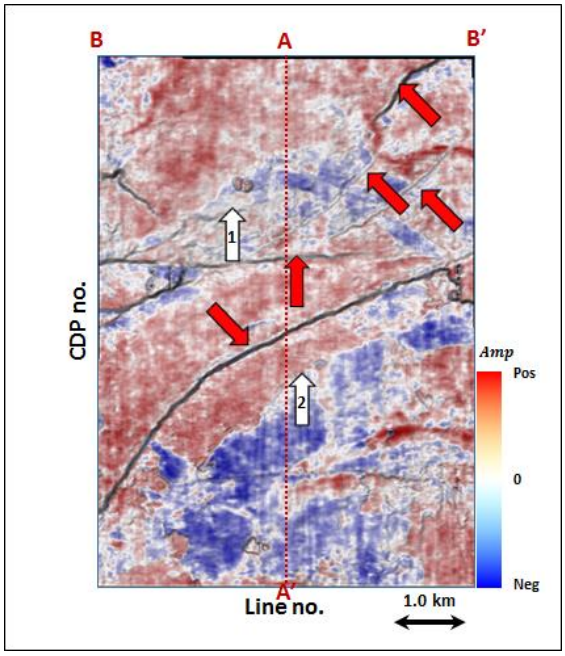

Figure 3.27. Phantom horizon 32 ms below Horizon A1 extracting along seismic amplitude data.

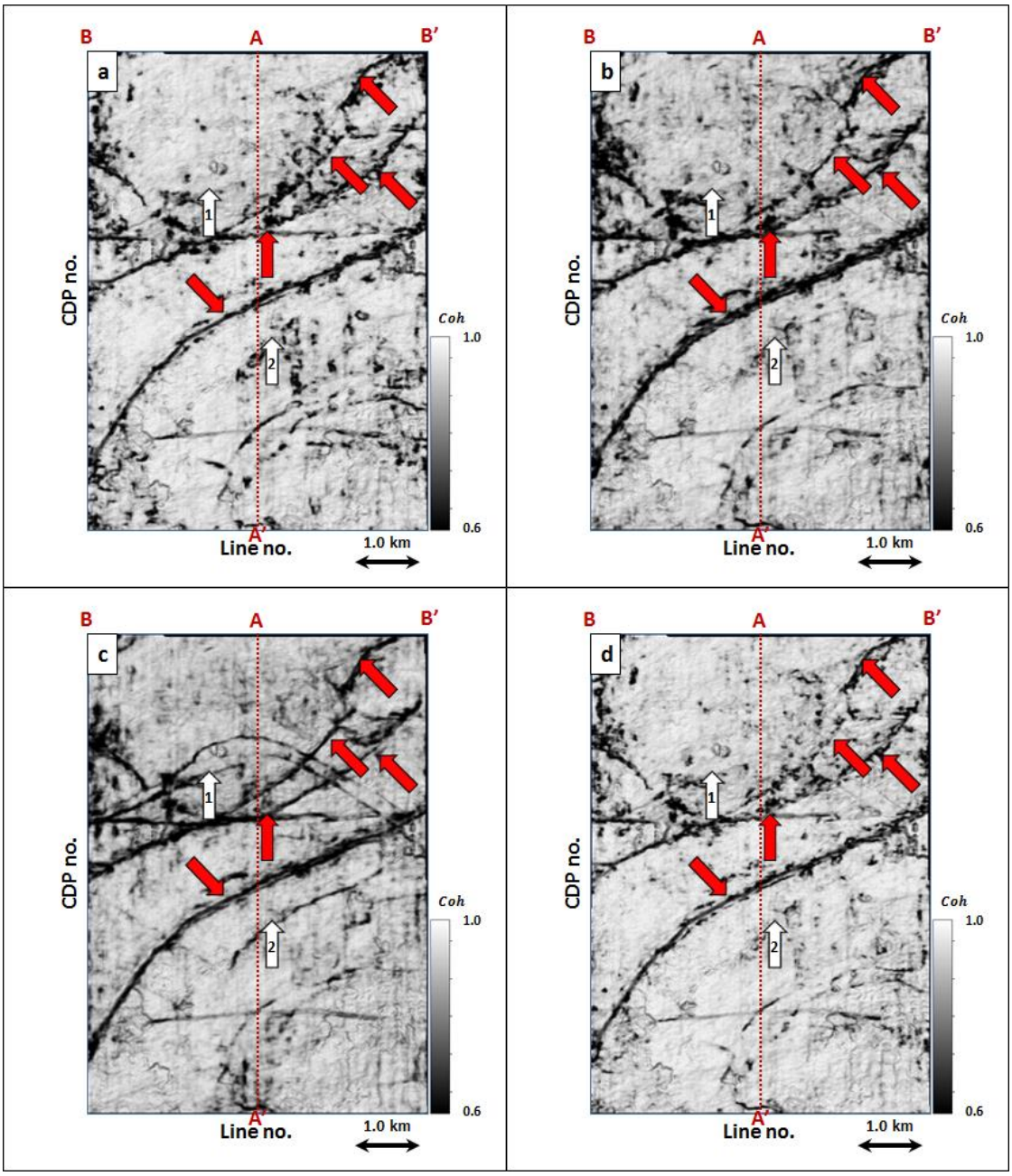

Figure 3.28. Energy ratio coherence along phantom horizon 32 ms below Horizon A1 using constant window size of (a) ±4 ms, (b) ±20 ms, (c) ±40 ms using 5 traces, and (d) a data-adaptive window varying between ±12 ms and 5 traces, and ±100 ms and 13 traces.

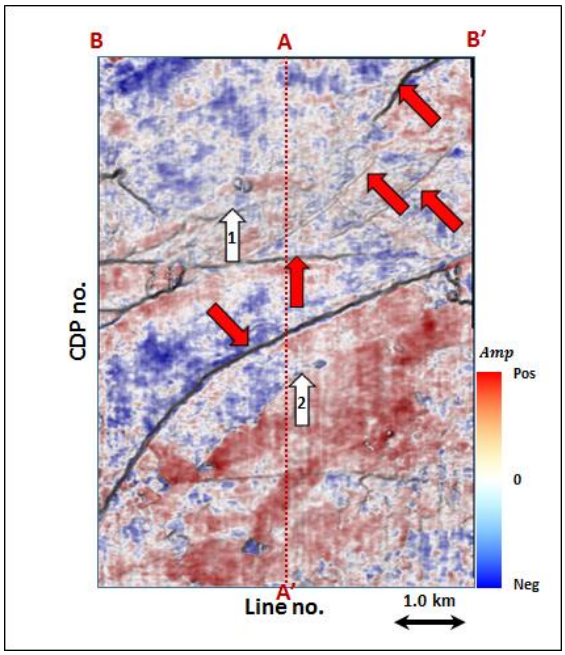

Figure 3.29. Phantom horizon 40 ms below Horizon A1 extracting along seismic amplitude data.

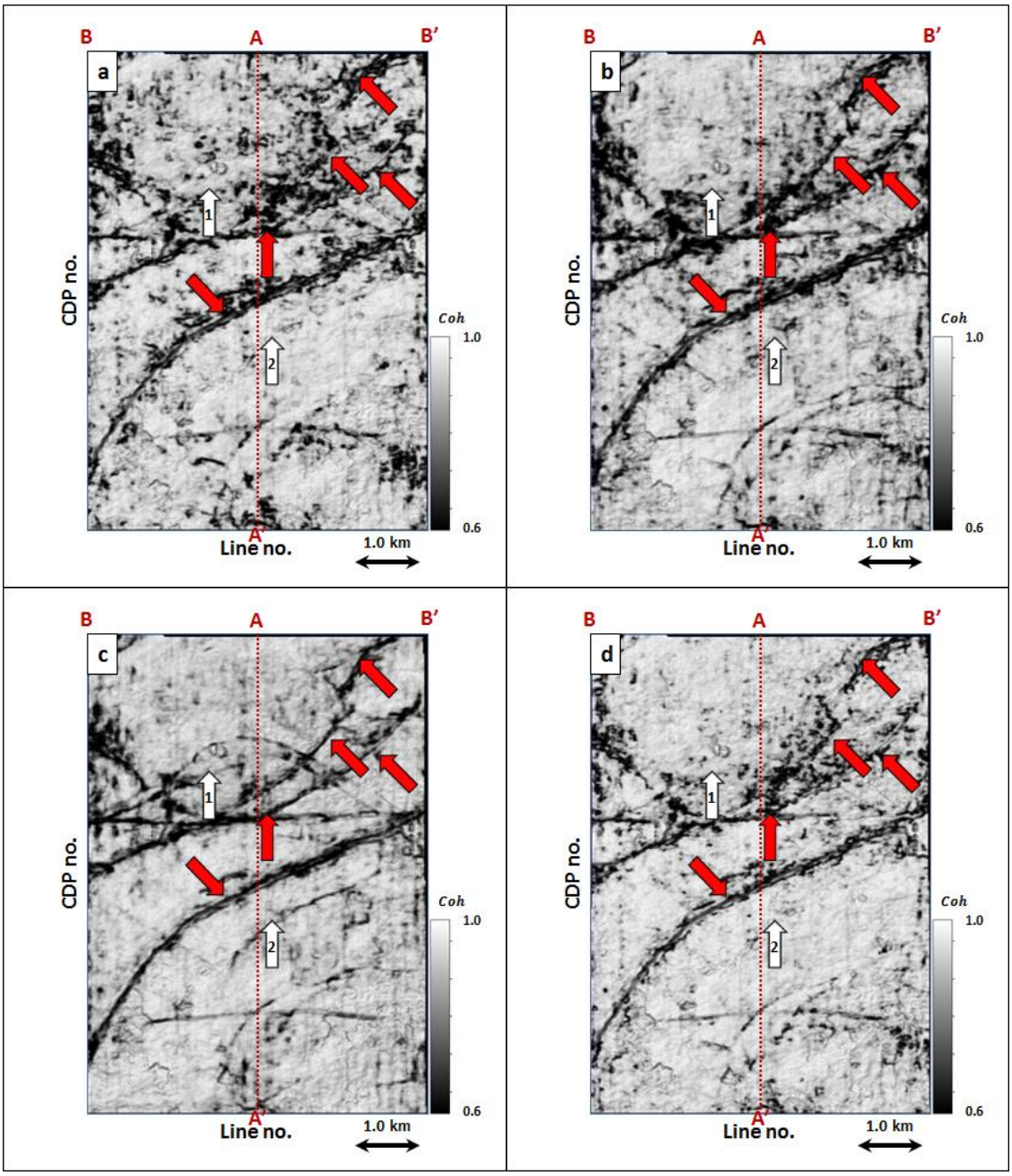

Figure 3.30. Energy ratio coherence along phantom horizon 40 ms below Horizon A1 using constant window size of (a) ±4 ms, (b) ±20 ms, (c) ±40 ms using 5 traces, and (d) a data-adaptive window varying between ±12 ms and 5 traces, and ±100 ms and 13 traces.

REFERENCES

Bahorich, M.S., and S. L. Farmer, 1995, 3-D seismic coherency for faults and stratigraphic features: The coherence cube: The Leading Edge, **14**, 1053-1058.

Barka D S., 2015, Sobel based edge detection algorithm with adaptive operator size applied to post-stack seismic data, Master thesis of University of Stavanger.

Bednar, B., 1998, Least-squares dip and coherency attributes: The Leading Edge, **17**, 777-778.

Chopra, S., and Marfurt, K. J., 2007, Seismic attributes for prospect identification and reservoir characterization. Geophysical Developments Series 11. SEG.

Dana, D., C. Zelt, and A. Levander. 1999, High-resolution seismic survey over a near-surface contamination site: 69th Annual International Meeting, SEG, Extended Abstracts, 579-583.

de Matos, D. C., and K. J. Marfurt, 2014, Complex wavelet transform spectral broadening: 84th Annual International Meeting, SEG, Extended Abstracts, 1465-1468.

Douze, E. J., and S. J. Laster, 1979, Statistics of semblance: Geophysics, **44**, 1999-2003.

Fagin, S., 1996, The fault shadow problem: Its nature and elimination: The Leading Edge, **17**, 1005-1013.

Gersztenkorn, A., and K. J. Marfurt, 1999, Eigenstructure based coherence computations as an aid to 3-D structural and stratigraphic mapping: Geophysics, **64**, 1468-1479.

Kirlin, R. L., and W. J. Done, 1999, Covariance analysis for seismic signal processing: Geophysical Developments Series, SEG**.**

Lin T., B. Zhang, S. Zhan, Z. Wan, F. Li, H. Zhou, and K. J. Marfurt, 2014a, Seismic attributes of time- vs. depth-migrated data using self-adaptive window: 84th Annual International Meeting, SEG, Extended Abstracts, 1659-1662.

Lin T., D. Chang, B. Zhang, J. Guo and K. J. Marfurt, 2014b, Seismic attributes estimation using a self-adaptive window: 84th Annual International Meeting, SEG, Extended Abstracts, 1654-1657.

Lin, T., T. Ha., K. J. Marfurt and K. Deal, 2016, Quantifying the significance of coherence anomalies: Interpretation, **4**, T205-T213.

Liu, J., and K. J. Marfurt, 2005, Matching pursuit decomposition using Morlet wavelets: 75th Annual International Meeting, SEG, Expanded Abstracts, 786-789.

Luo, Y., W. G. Higgs and W. S. Kowalik, 1996, Edge detection and stratigraphic analysis using 3D seismic data: 66th Annual International Meeting, SEG, Expanded Abstracts, 324 – 327.

Marfurt, K. J., 2006, Robust estimates of 3D reflector dip and azimuth: Geophysics, **71**, 29-40.

Marfurt, K. J., R. L. Kirlin, S. H. Farmer, and M. S. Bahorich, 1998, 3-D seismic attributes using a semblance-based coherency algorithm: Geophysics, **63**, 1150-1165.

Moser, T. J., and C. B. Howard, 2008, Diffraction imaging in depth: Geophysical Prospecting, **56**, 627-641.

Marfurt, K. J., and T. M. Alves, 2015, Pitfalls and limitations in seismic attribute interpretation of tectonic features, **3**(1), A5-A15

Neidell N. S., and M. T. Taner, 1971, Semblance and other coherency measures for multichannel data: Geophysics, **36**, 482-497.

Partyka, G., J. Gridley, and J. A. Lopez, 1999, Interpretational applications of spectral decomposition in reservoir characterization: The Leading Edge, **18**, 353-360.

Pepper, R., and G. Bejarano, 2005, Advances in seismic fault interpretation automation, AAPG Search and Discovery Article 40170, http://www.searchanddiscovery.com/documents/-2005/pepper/.

Puryear, C. I., O. N. Portniaguine, C. M. Cobos, and J. P. Castagna 2012, Constrained least-squares spectral analysis: Application to seismic data: Geophysics, **77**, V143-V167.

Van Bemmel, P. P., and R. E. F. Pepper, 2011, Seismic signal processing method and apparatus for generating a cube of variance values: US Patent, **8**, 055,026.

Walton, C., B. Evans, and M. Urosevic, 2000, Imaging coal seam structure using 3-D seismic methods: Exploration Geophysics, **31** (3), 509-514.

APPENDIX

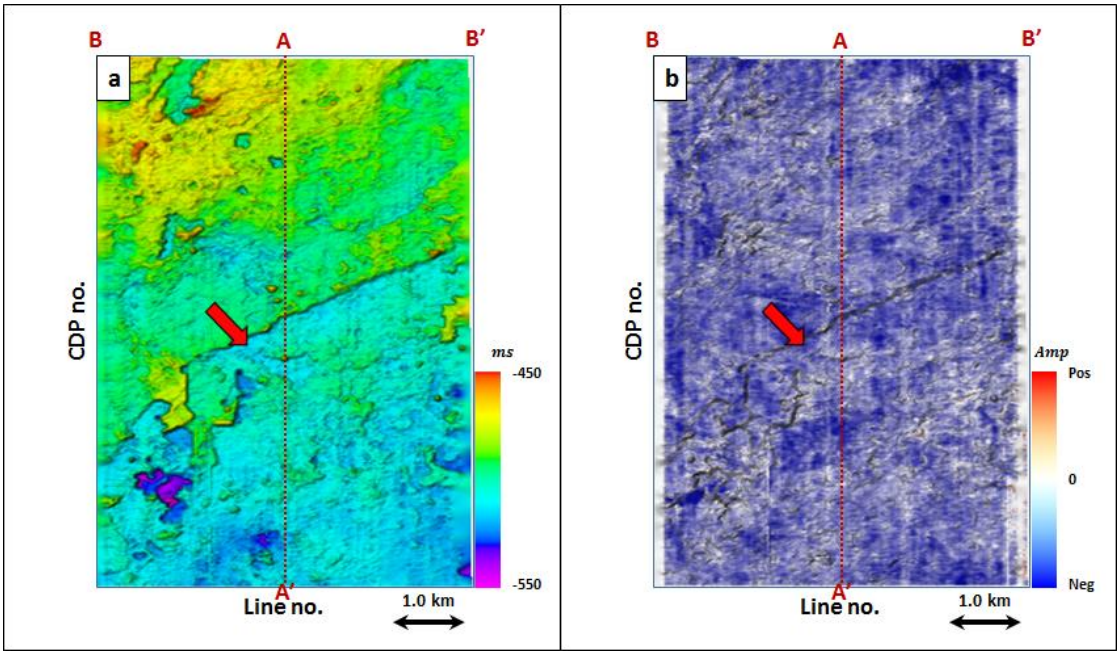

Figure 3.31. (a) Time-structure map of Horizon A2 and (b) a horizon slice through seismic amplitude. Horizon A2 was picked as a trough.

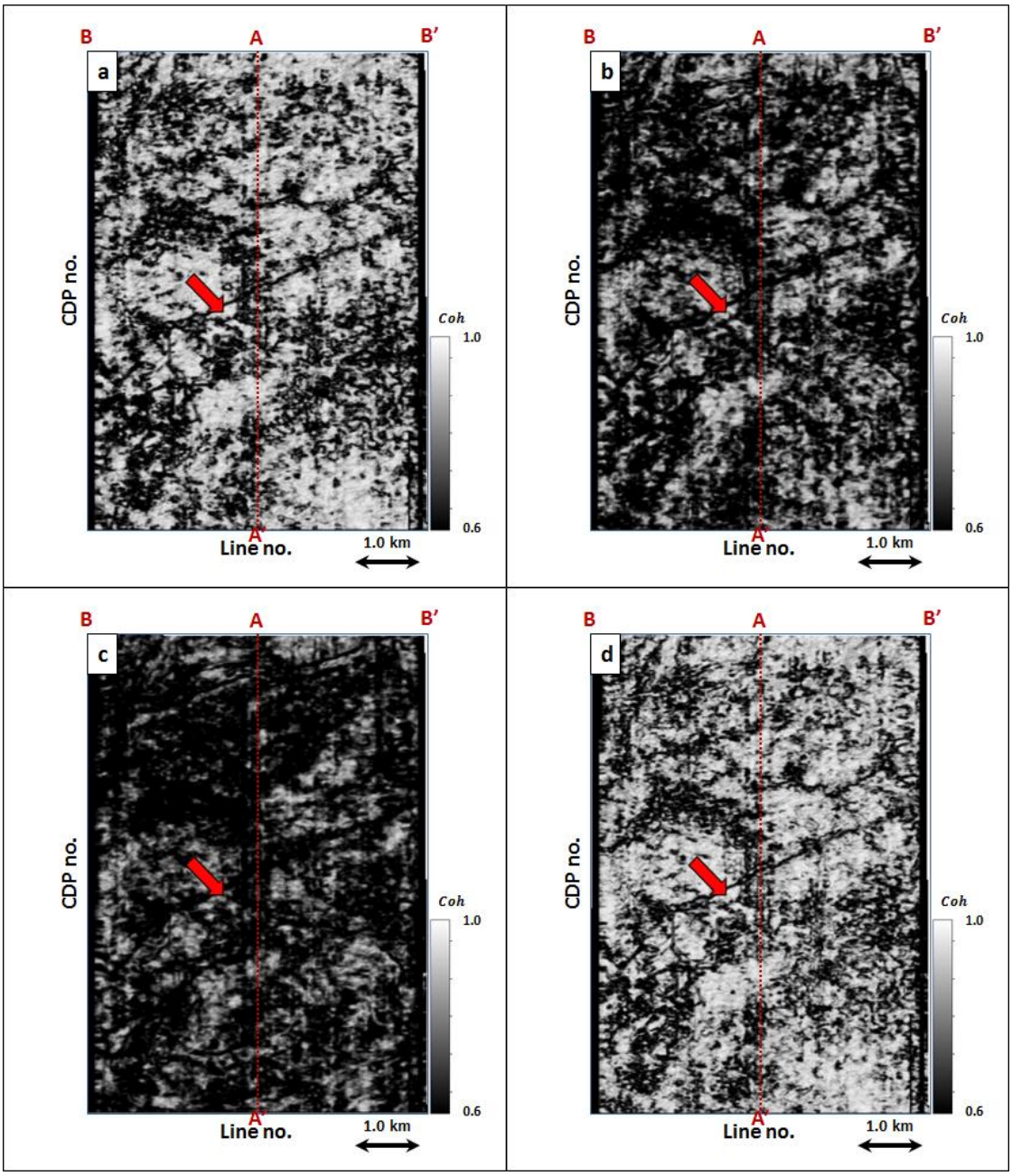

Figure 3.32. Energy ratio coherence along Horizon A2 using constant window size of (a) ±4 ms, (b) ±20 ms, (c) ±40 ms using 5 traces, and (d) a data-adaptive window varying between ±12 ms and 5 traces, and ±100 ms and 13 traces.

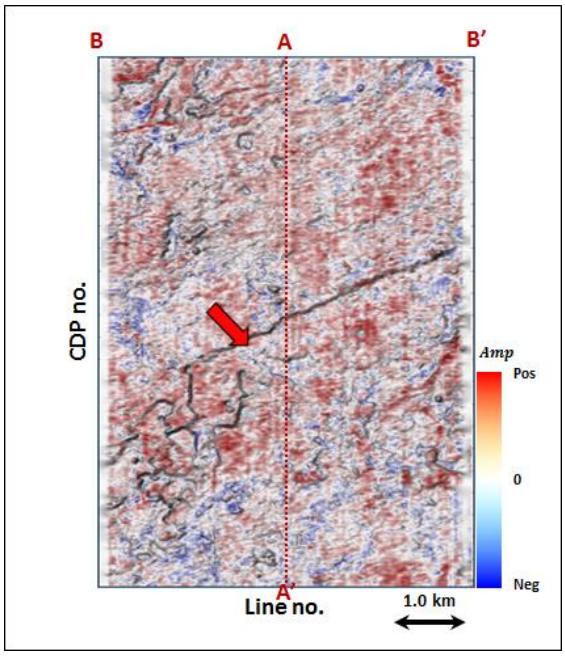

Figure 3.33. Phantom horizon 8 ms above Horizon A2 extracting along seismic amplitude data.

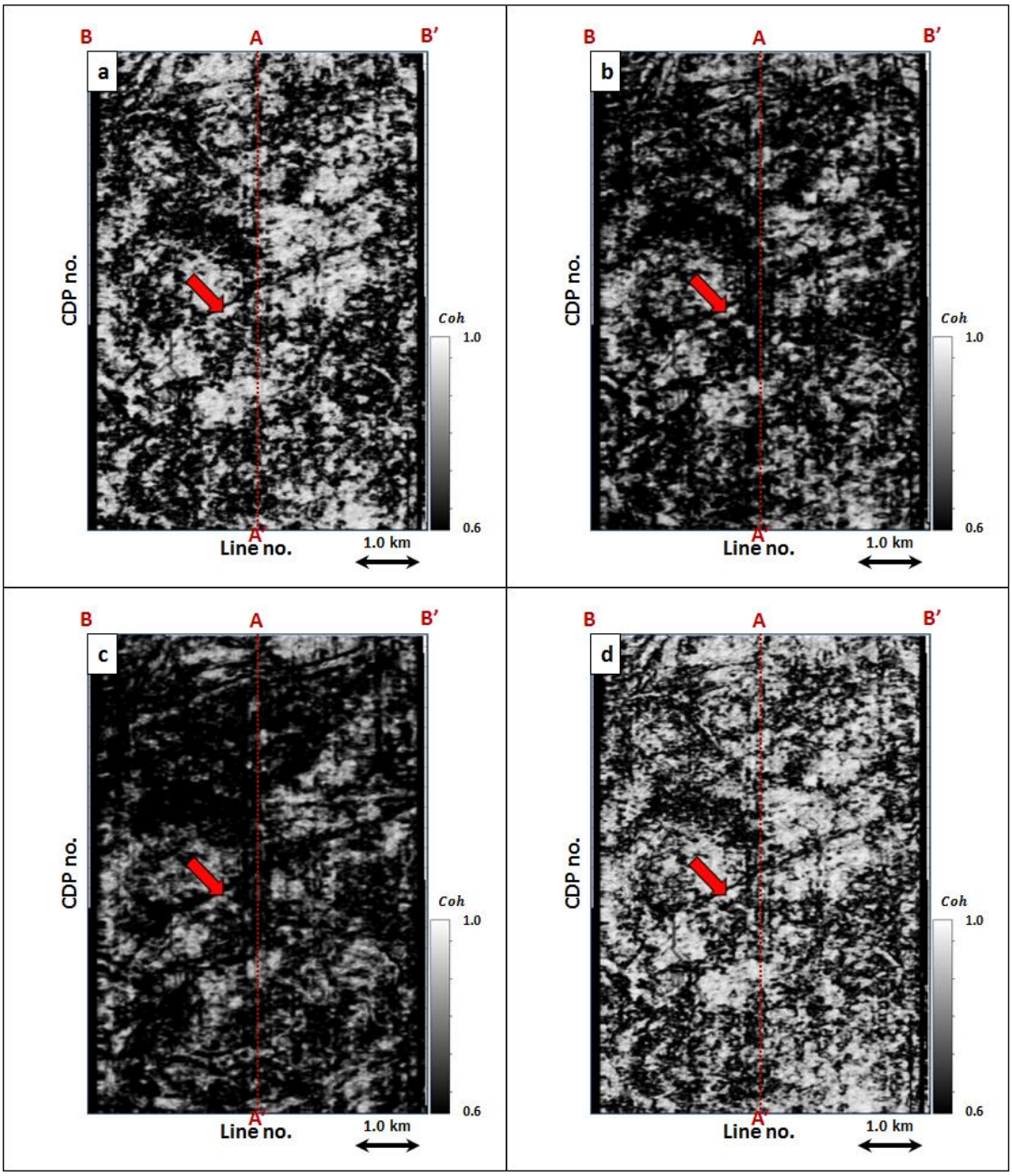

Figure 3.34. Energy ratio coherence along phantom horizon 8 ms above Horizon A2 using constant window size of (a) ±4 ms, (b) ±20 ms, (c) ±40 ms using 5 traces, and (d) a data-adaptive window varying between ±12 ms and 5 traces, and ±100 ms and 13 traces.

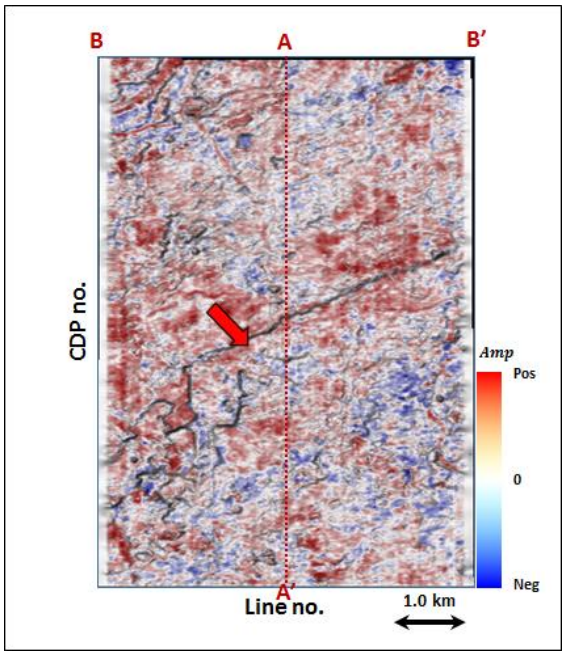

Figure 3.35. Phantom horizon 16 ms above Horizon A2 extracting along seismic amplitude data.

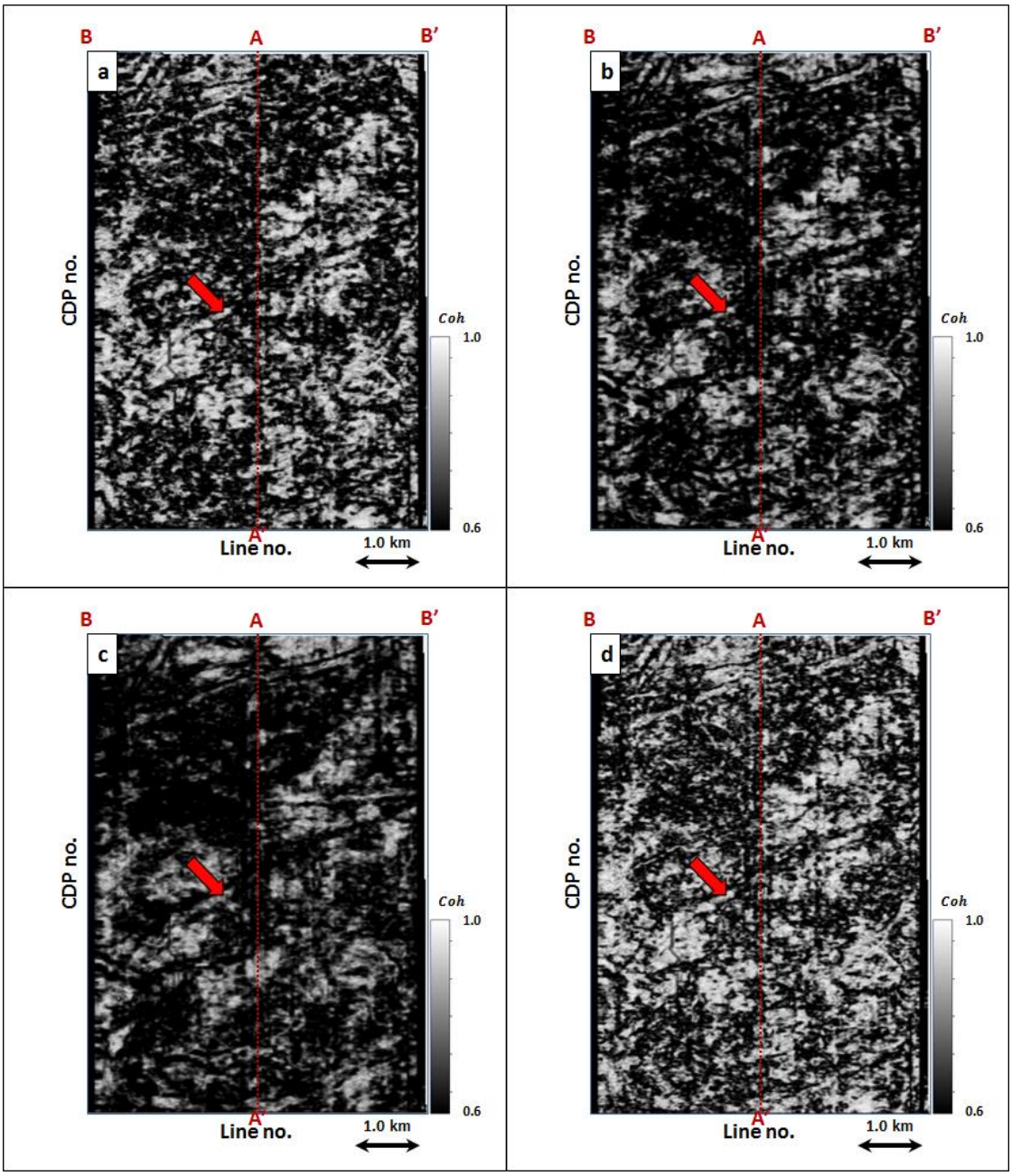

Figure 3.36. Energy ratio coherence along phantom horizon 16 ms above Horizon A2 using constant window size of (a) ±4 ms, (b) ±20 ms, (c) ±40 ms using 5 traces, and (d) a data-adaptive window varying between ±12 ms and 5 traces, and ±100 ms and 13 traces.

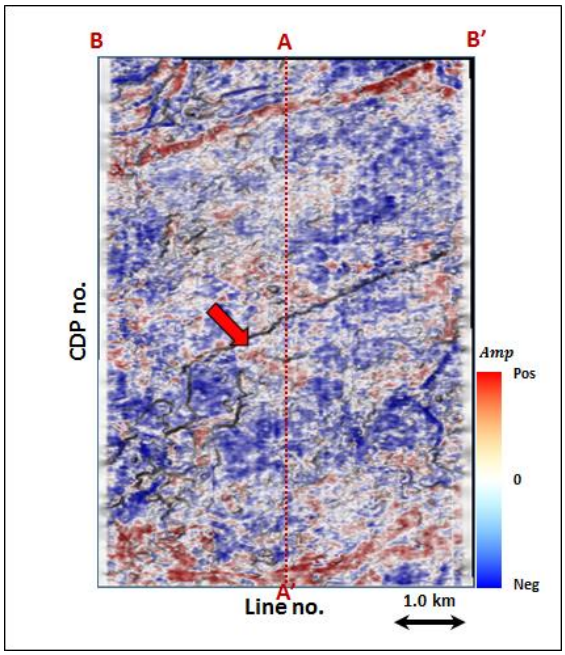

Figure 3.37. Phantom horizon 24 ms above Horizon A2 extracting along seismic amplitude data.

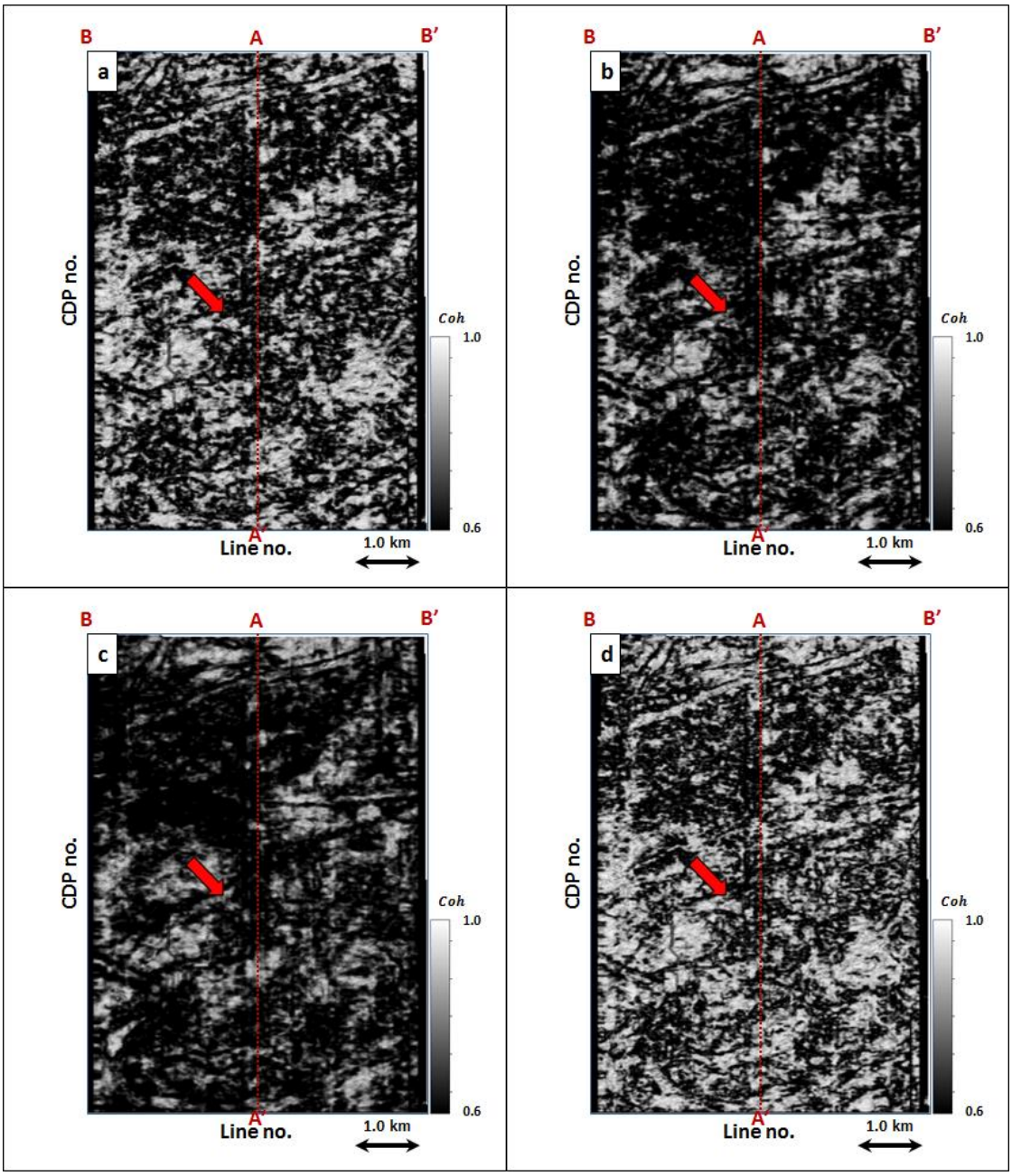

Figure 3.38. Energy ratio coherence along phantom horizon 24 ms above Horizon A2 using constant window size of (a) ±4 ms, (b) ±20 ms, (c) ±40 ms using 5 traces, and (d) a data-adaptive window varying between ±12 ms and 5 traces, and ±100 ms and 13 traces.

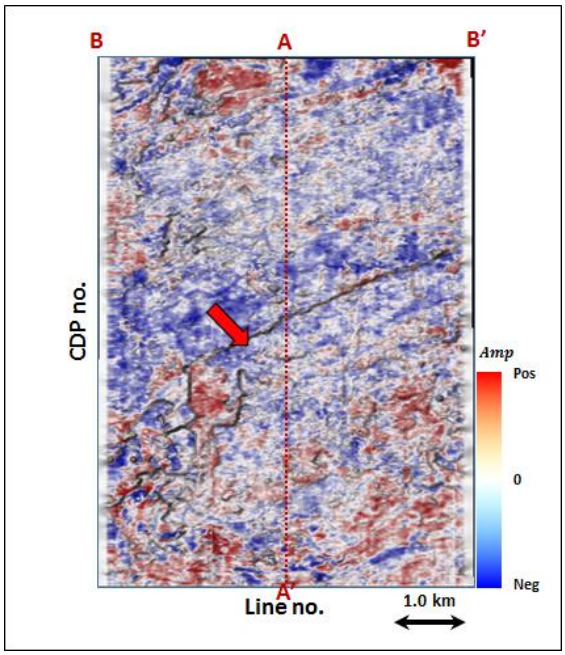

Figure 3.39. Phantom horizon 32 ms above Horizon A2 extracting along seismic amplitude data.

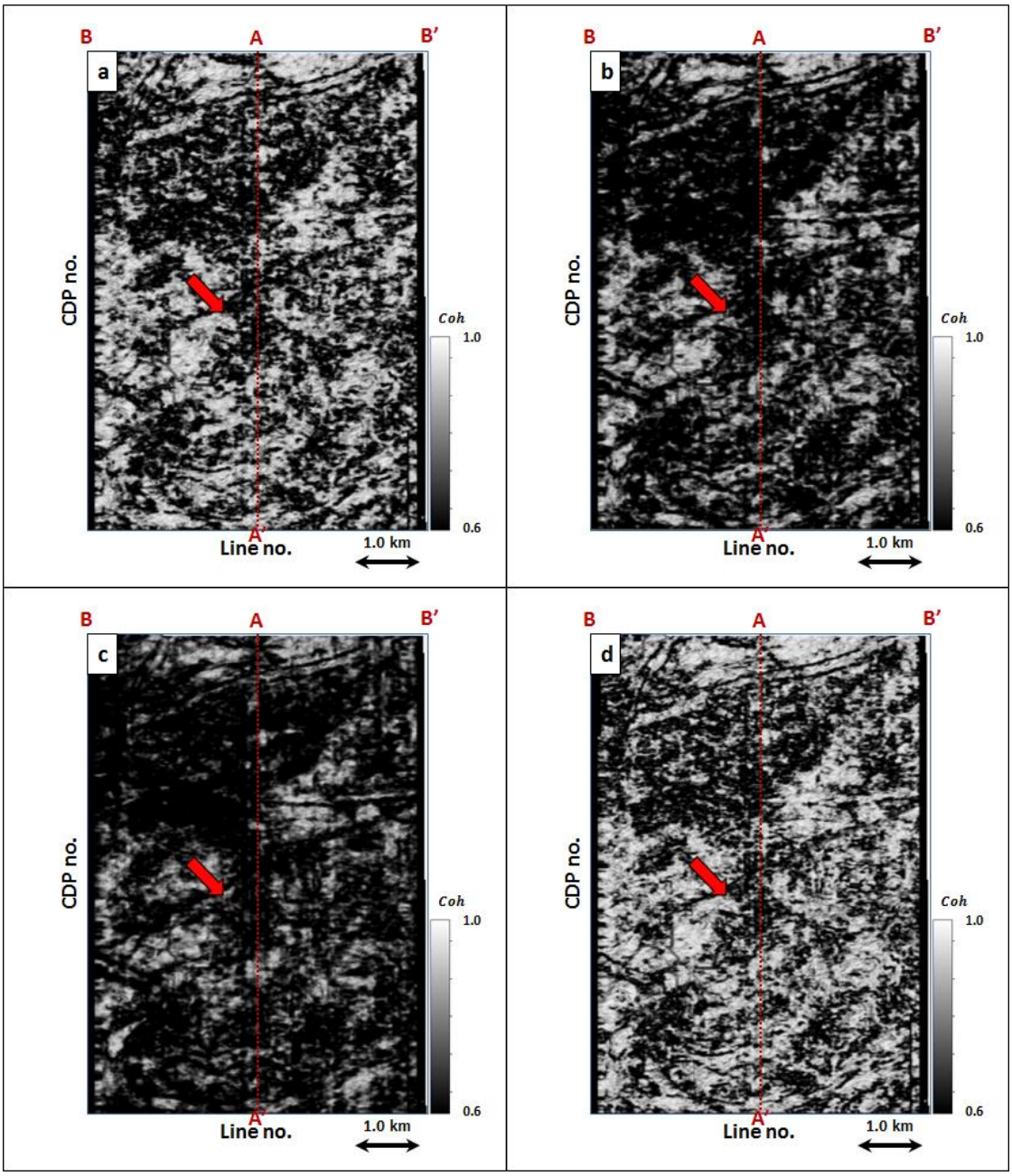

Figure 3.40. Energy ratio coherence along phantom horizon 32 ms above Horizon A2 using constant window size of (a) ±4 ms, (b) ±20 ms, (c) ±40 ms using 5 traces, and (d) a data-adaptive window varying between ±12 ms and 5 traces, and ±100 ms and 13 traces.

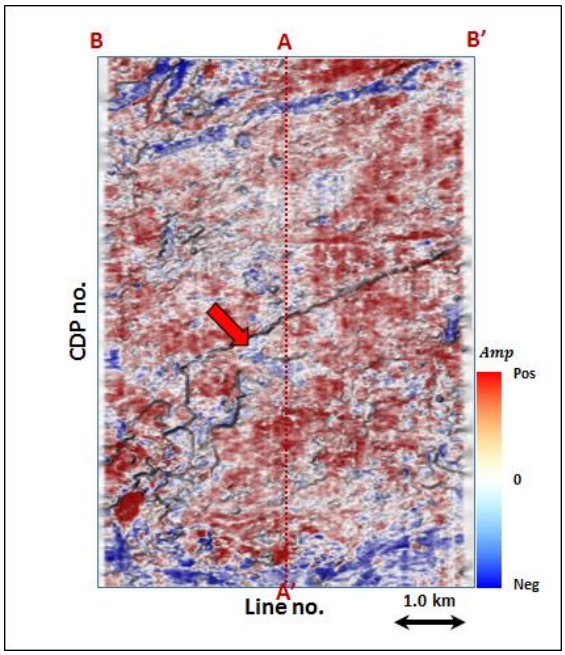

Figure 3.41. Phantom horizon 40 ms above Horizon A2 extracting along seismic amplitude data.

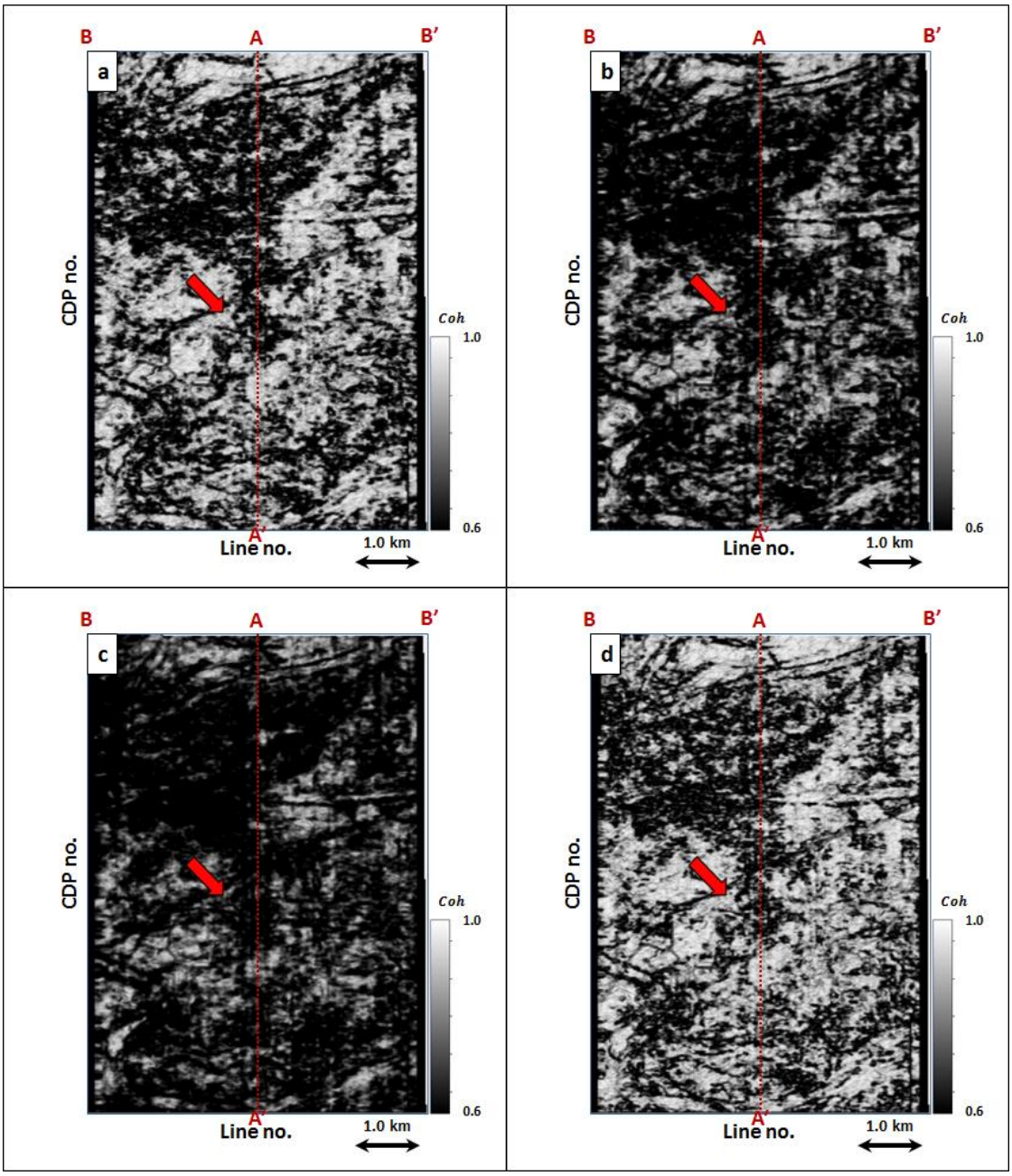

Figure 3.42. Energy ratio coherence along phantom horizon 40 ms above Horizon A2 using constant window size of (a) ±4 ms, (b) ±20 ms, (c) ±40 ms using 5 traces, and (d) a data-adaptive window varying between ±12 ms and 5 traces, and ±100 ms and 13 traces.

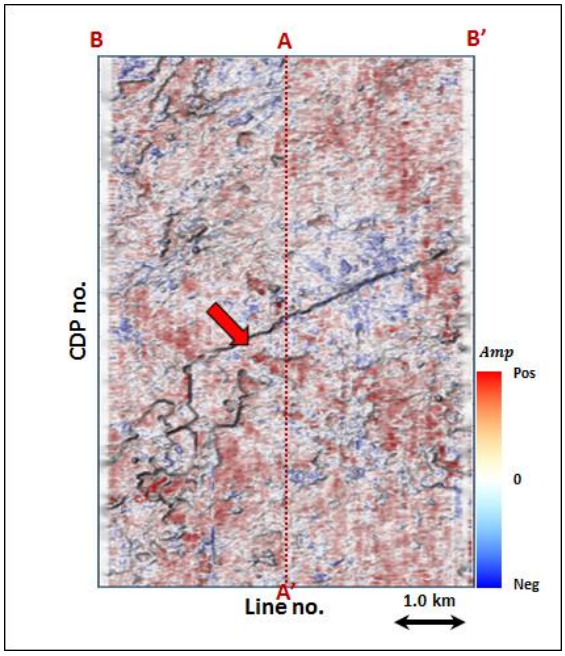

Figure 3.43. Phantom horizon 8 ms below Horizon A2 extracting along seismic amplitude data.

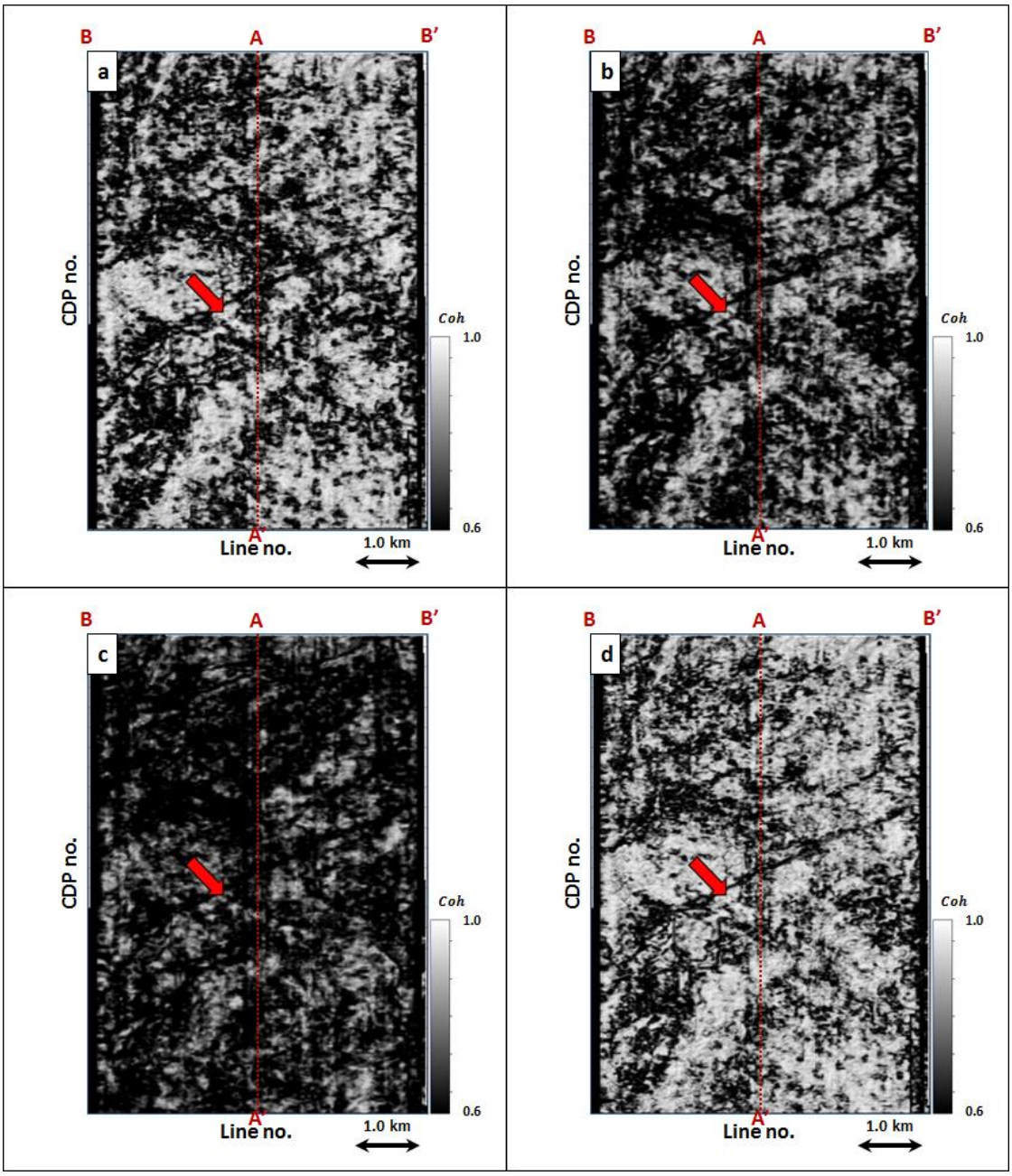

Figure 3.44. Energy ratio coherence along phantom horizon 8 ms below Horizon A2 using constant window size of (a) ±4 ms, (b) ±20 ms, (c) ±40 ms using 5 traces, and (d) a data-adaptive window varying between ±12 ms and 5 traces, and ±100 ms and 13 traces.

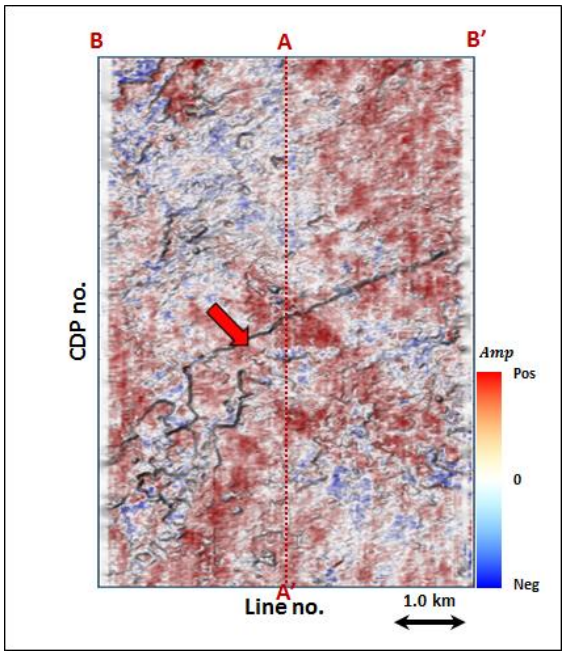

Figure 3.45. Phantom horizon 16 ms below Horizon A2 extracting along seismic amplitude data.

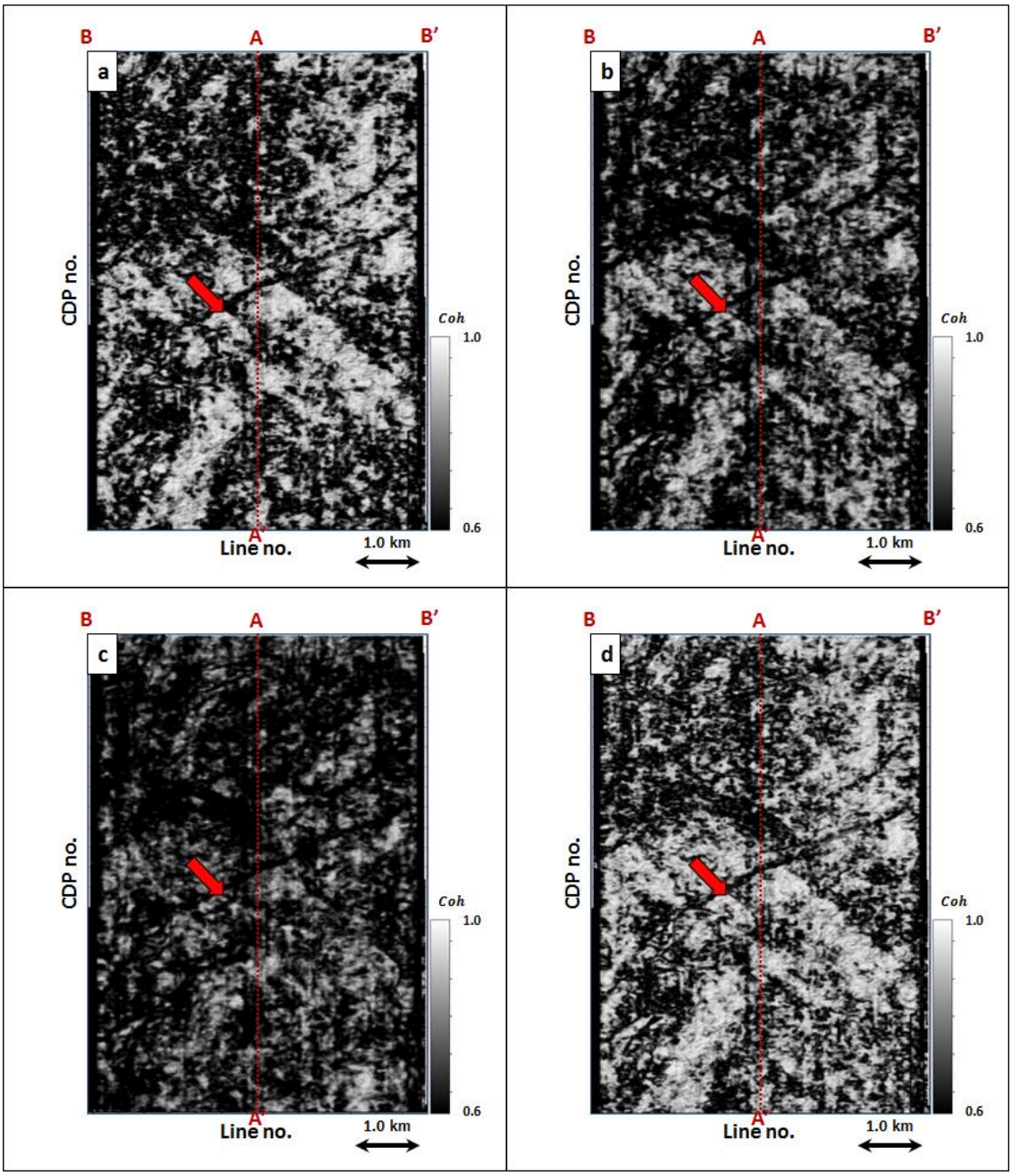

Figure 3.46. Energy ratio coherence along phantom horizon 16 ms below Horizon A2 using constant window size of (a) ±4 ms, (b) ±20 ms, (c) ±40 ms using 5 traces, and (d) a data-adaptive window varying between ±12 ms and 5 traces, and ±100 ms and 13 traces.

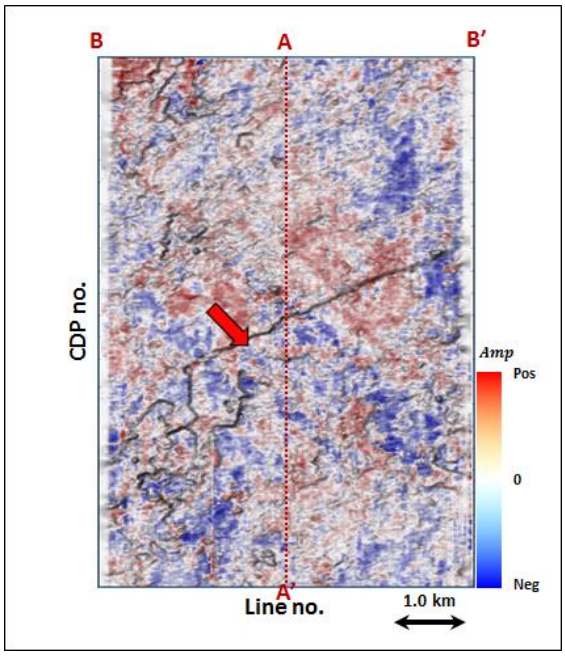

Figure 3.47. Phantom horizon 24 ms below Horizon A2 extracting along seismic amplitude data.

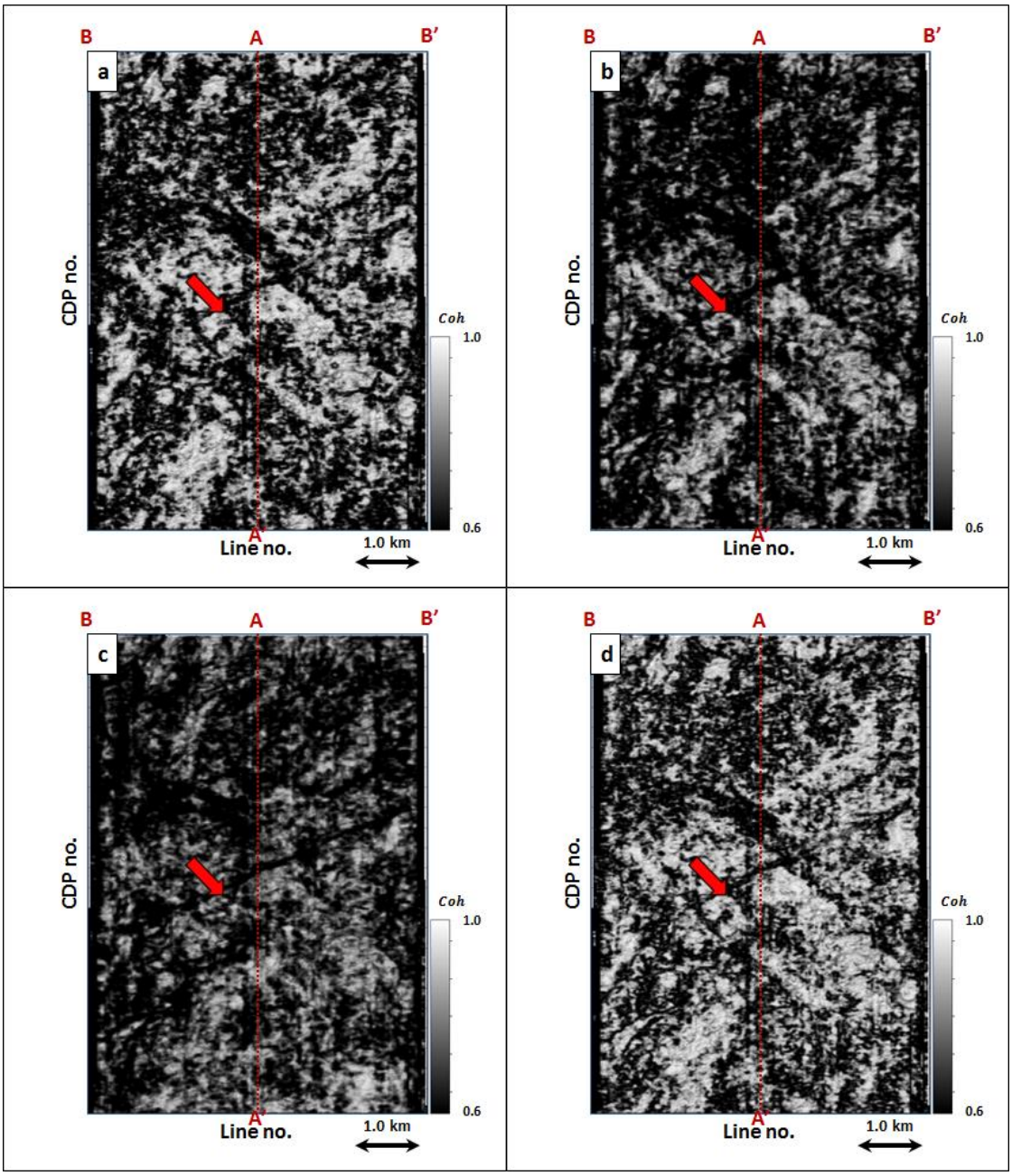

Figure 3.48. Energy ratio coherence along phantom horizon 24 ms below Horizon A2 using constant window size of (a) ±4 ms, (b) ±20 ms, (c) ±40 ms using 5 traces, and (d) a data-adaptive window varying between ±12 ms and 5 traces, and ±100 ms and 13 traces.

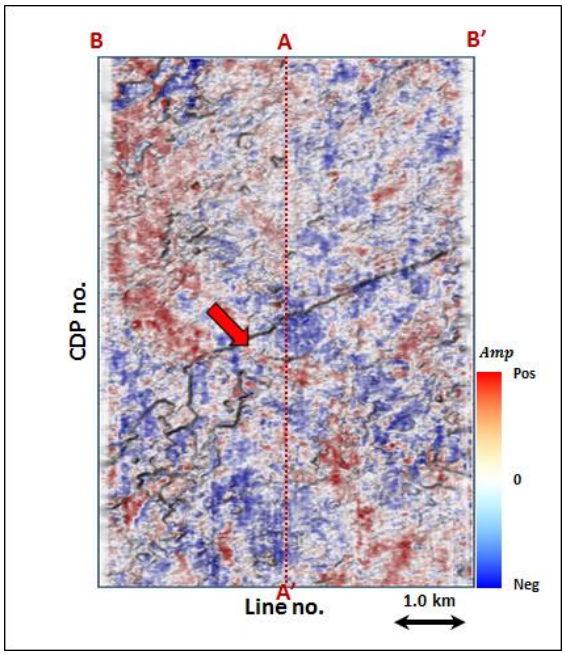

Figure 3.49. Phantom horizon 32 ms below Horizon A2 extracting along seismic amplitude data.

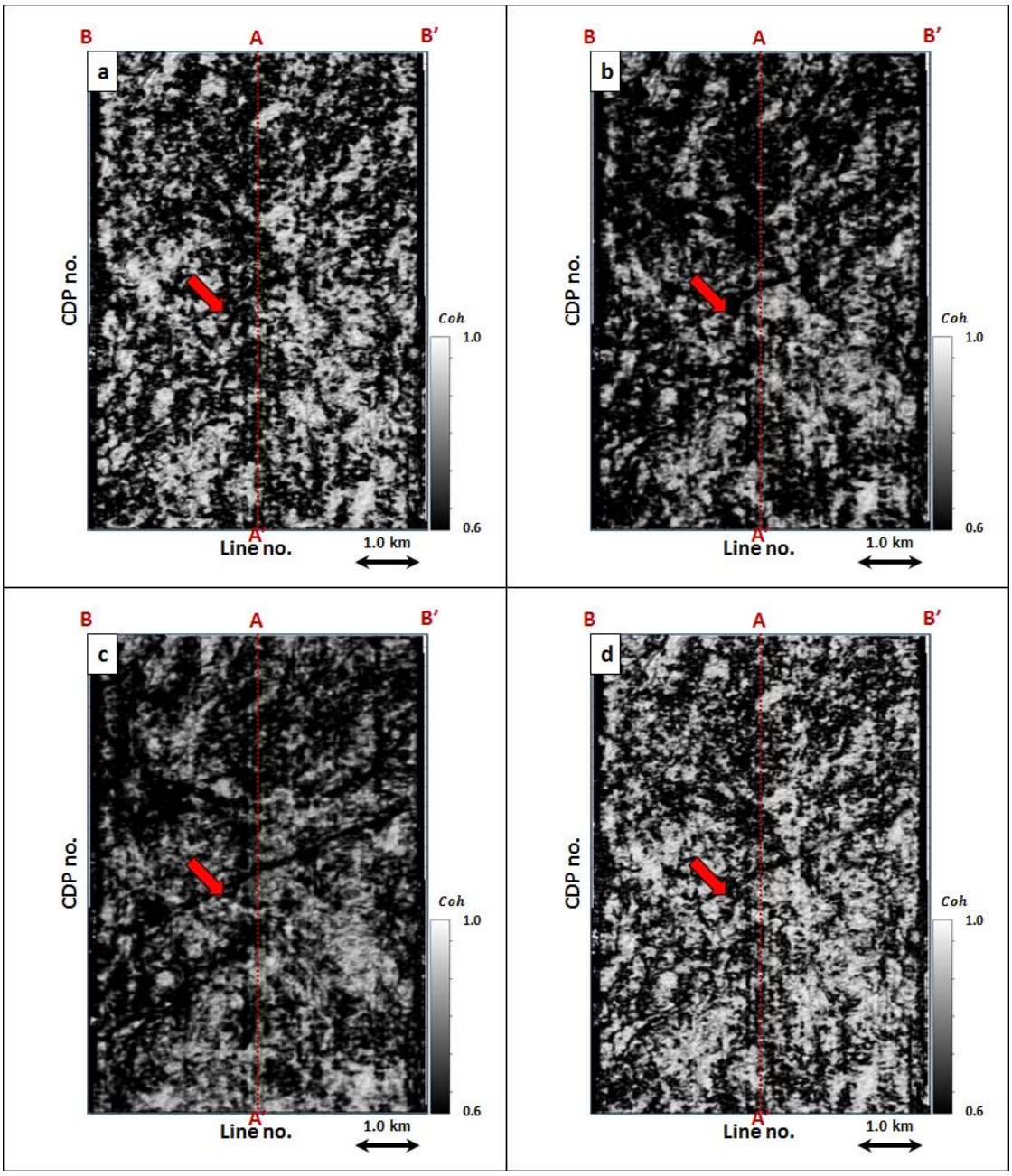

Figure 3.50. Energy ratio coherence along phantom horizon 32 ms below Horizon A2 using constant window size of (a) ±4 ms, (b) ±20 ms, (c) ±40 ms using 5 traces, and (d) a data-adaptive window varying between ±12 ms and 5 traces, and ±100 ms and 13 traces.

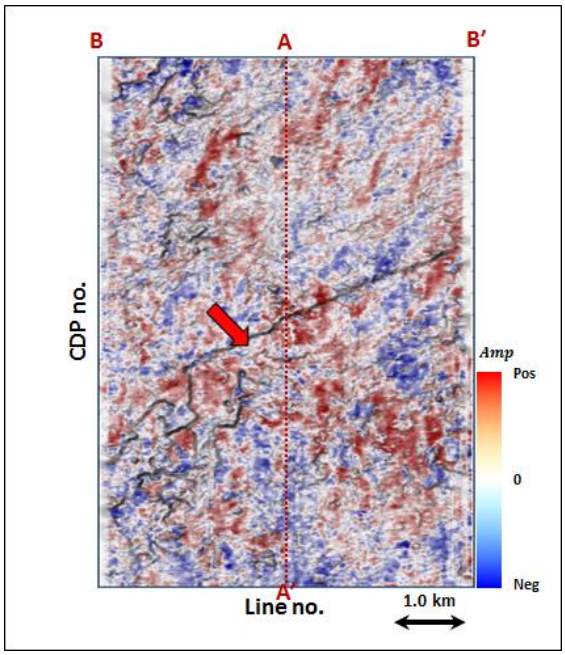

Figure 3.51. Phantom horizon 40 ms below Horizon A2 extracting along seismic amplitude data.

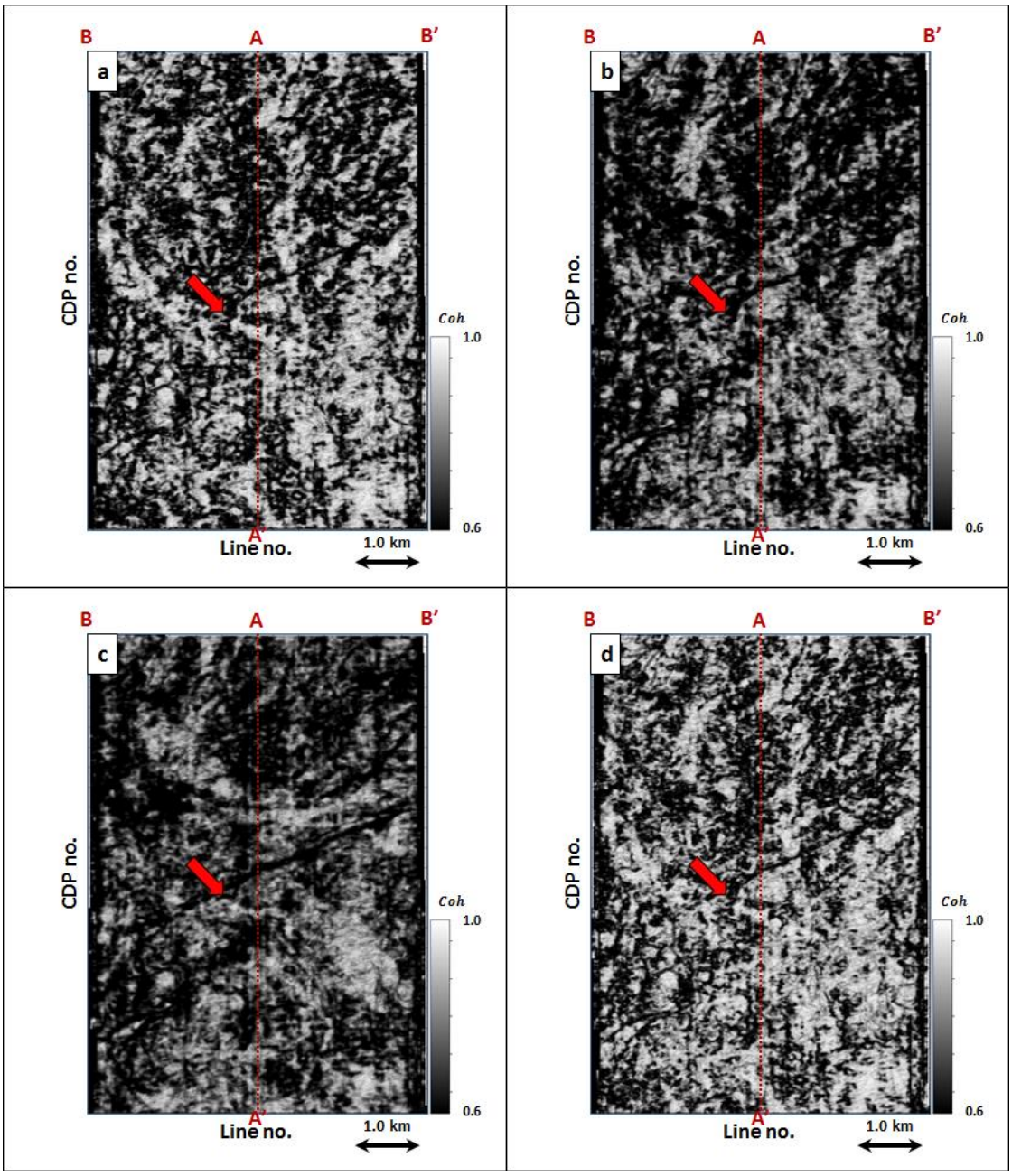

Figure 3.52. Energy ratio coherence along phantom horizon 40 ms below Horizon A2 using constant window size of (a) ±4 ms, (b) ±20 ms, (c) ±40 ms using 5 traces, and (d) a data-adaptive window varying between ±12 ms and 5 traces, and ±100 ms and 13 traces.

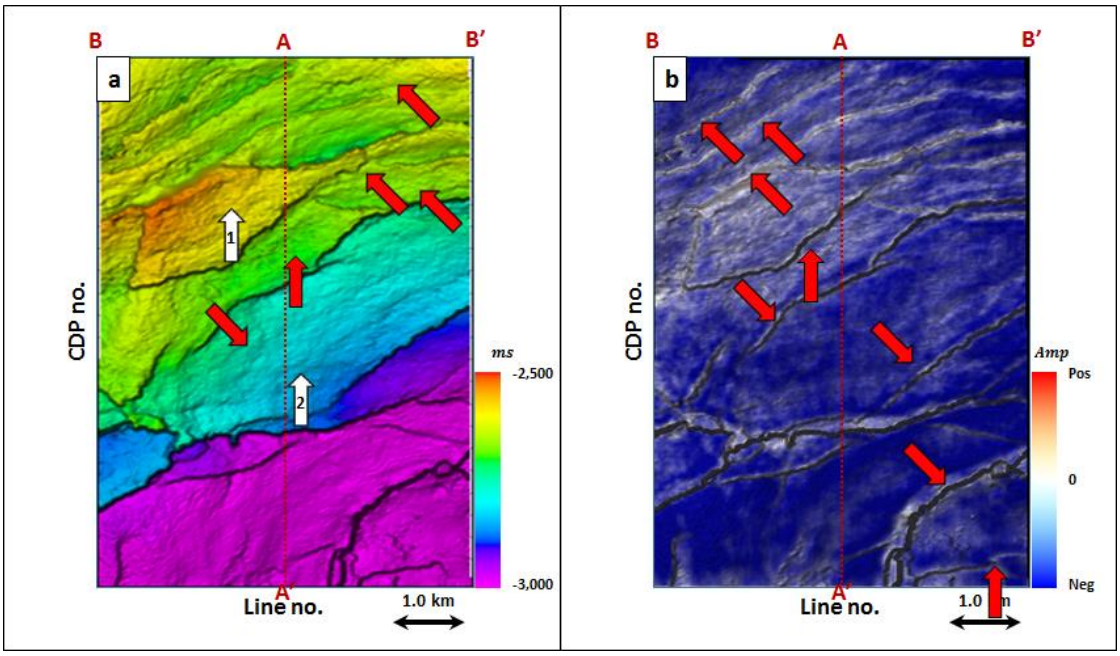

Figure 3.53. (a) Time-structure map of Horizon A3 and (b) a horizon slice through seismic amplitude. Horizon A1 was picked as a trough.

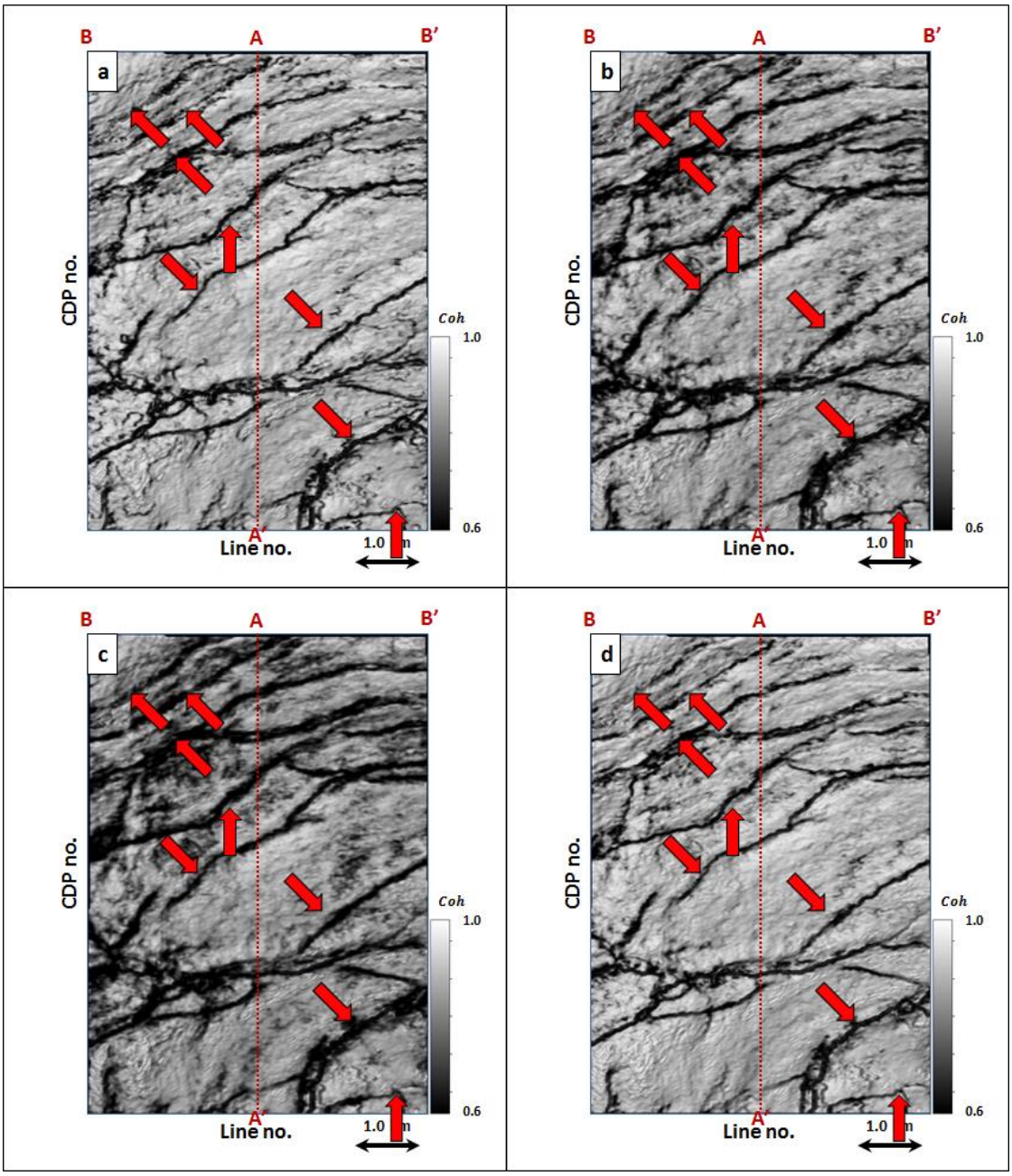

Figure 3.54. Energy ratio coherence along Horizon A1 using constant window size of (a) ±4 ms, (b) ±20 ms, (c) ±40 ms using 5 traces, and (d) a data-adaptive window varying between ±12 ms and 5 traces, and ±100 ms and 13 traces.

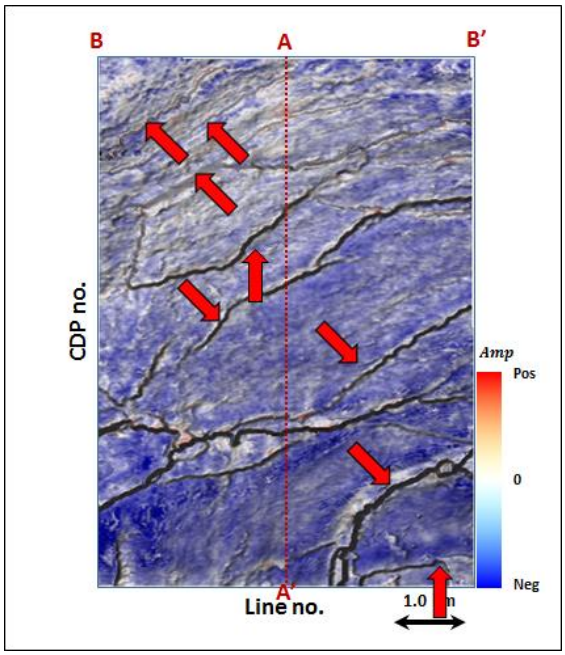

Figure 3.55. Phantom horizon 8 ms above Horizon A3 extracting along seismic amplitude data.

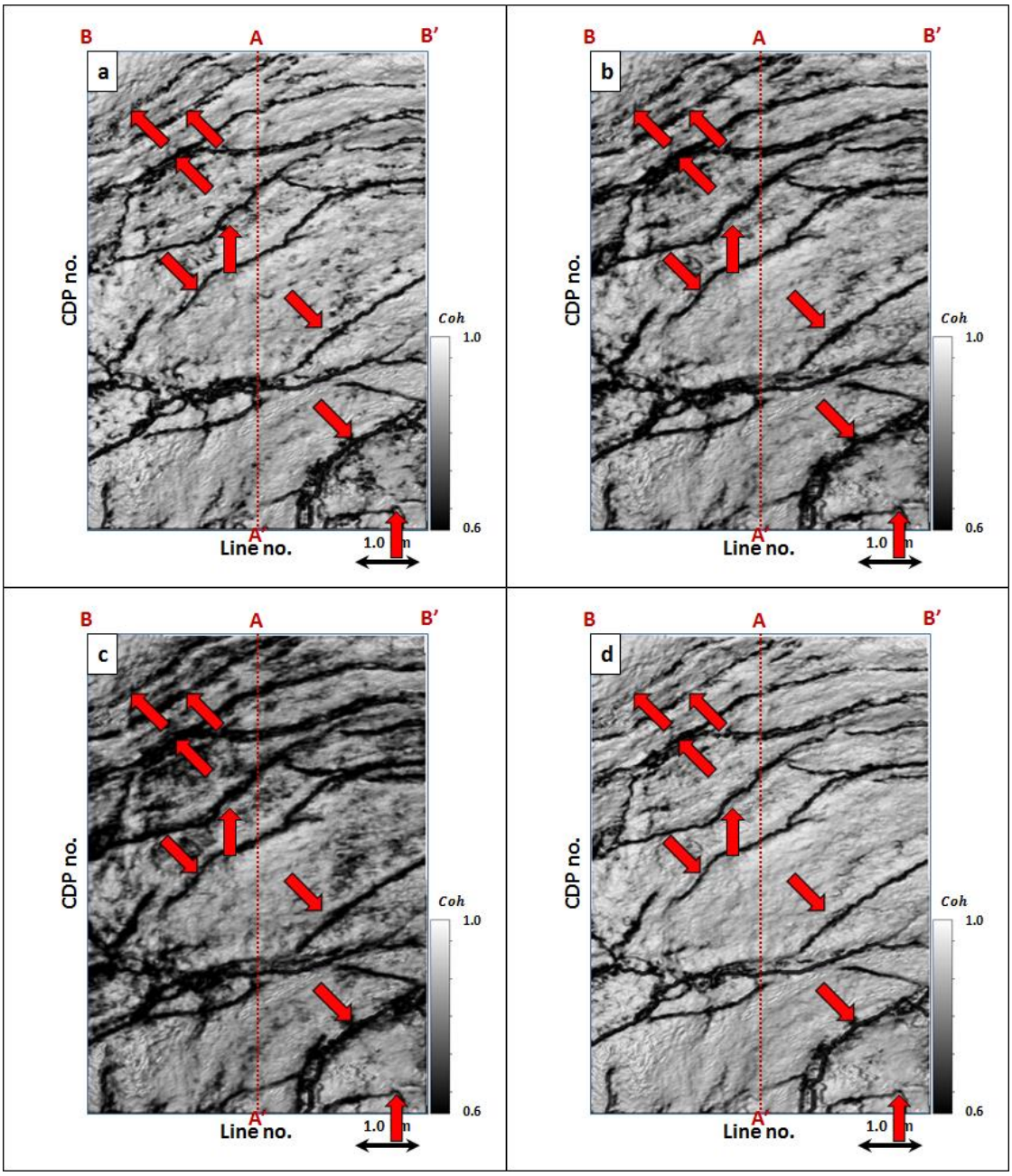

Figure 3.56. Energy ratio coherence along phantom horizon 8 ms above Horizon A2 using constant window size of (a) ±4 ms, (b) ±20 ms, (c) ±40 ms using 5 traces, and (d) a data-adaptive window varying between ±12 ms and 5 traces, and ±100 ms and 13 traces.

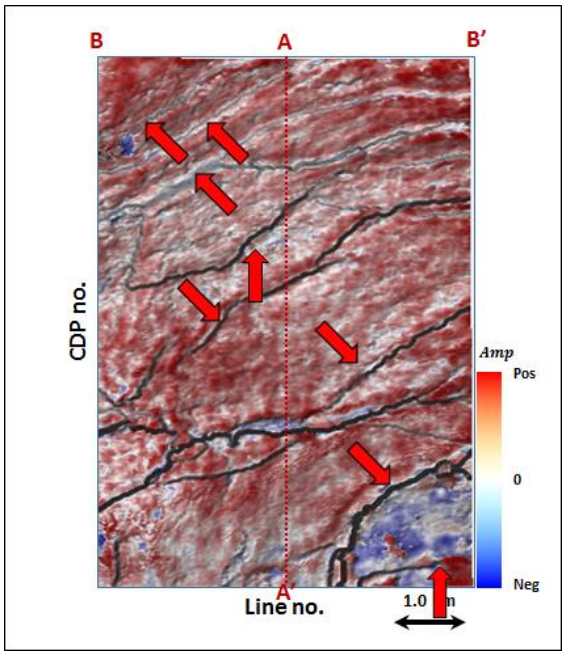

Figure 3.57. Phantom horizon 16 ms above Horizon A3 extracting along seismic amplitude data.

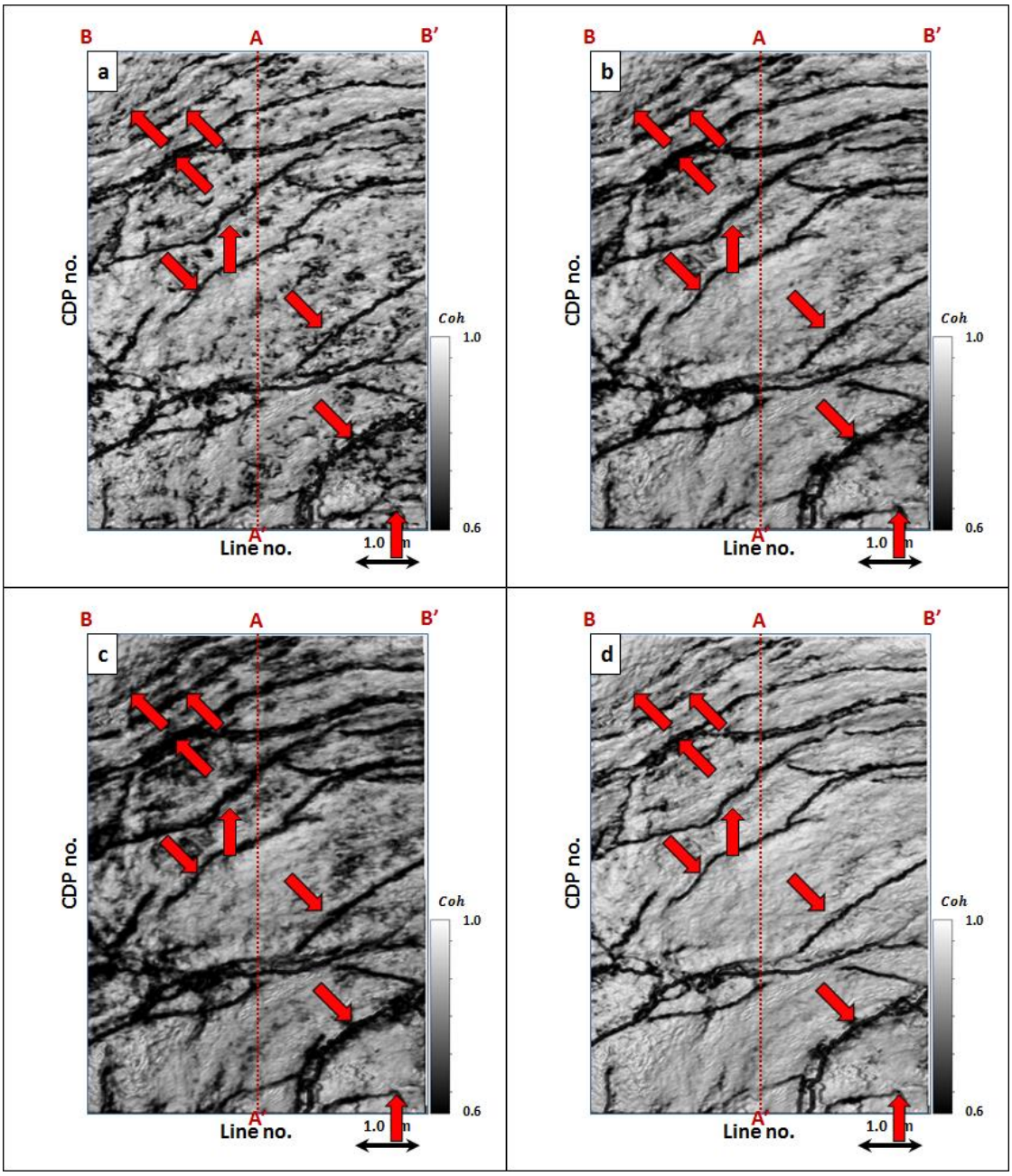

Figure 3.58. Energy ratio coherence along phantom horizon 16 ms above Horizon A3 using constant window size of (a) ±4 ms, (b) ±20 ms, (c) ±40 ms using 5 traces, and (d) a data-adaptive window varying between ±12 ms and 5 traces, and ±100 ms and 13 traces.

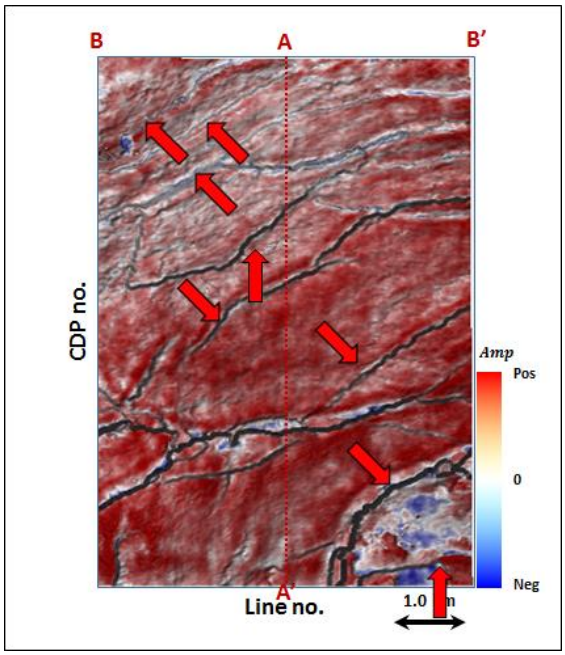

Figure 3.59. Phantom horizon 24 ms above Horizon A3 extracting along seismic amplitude data.

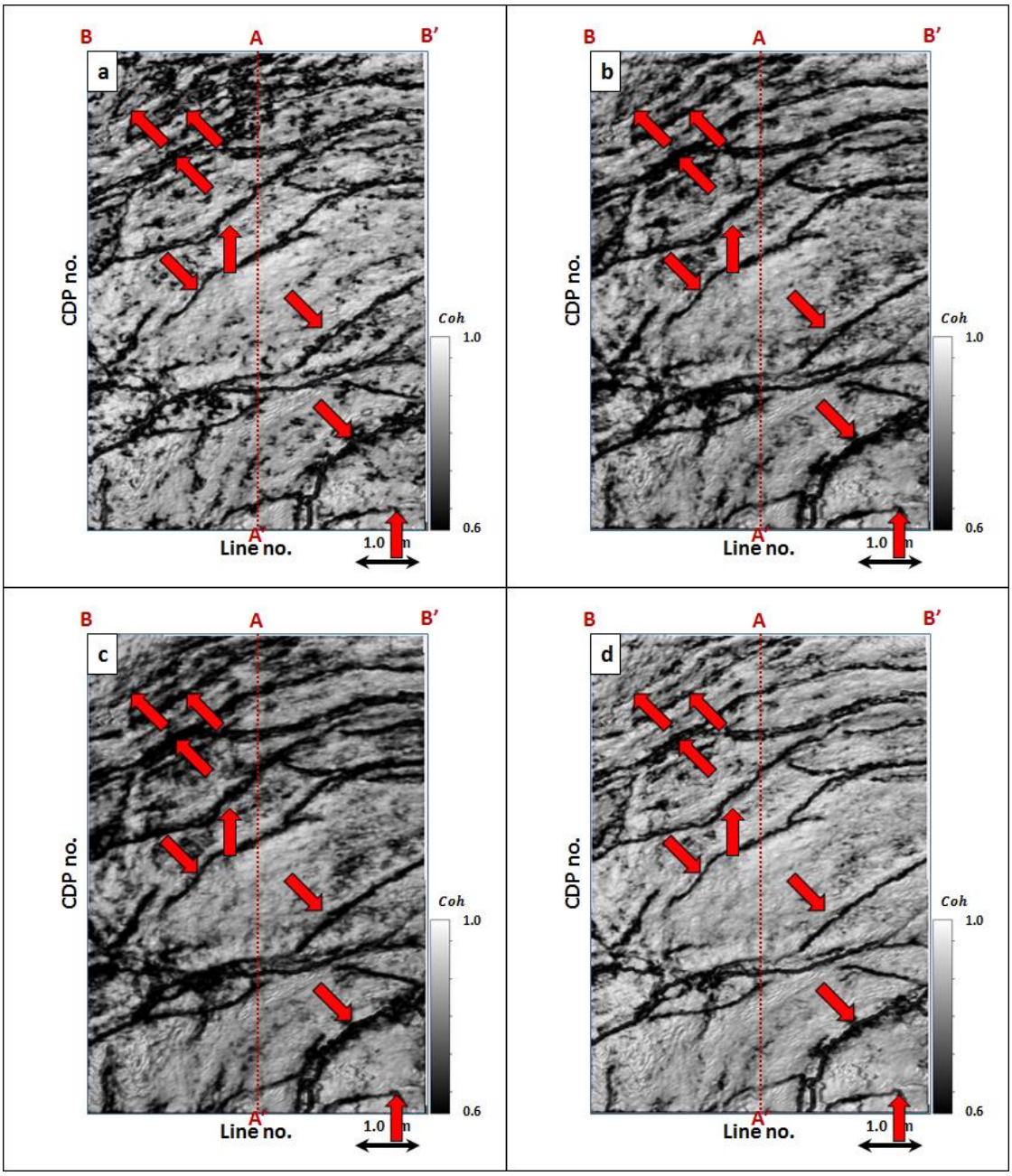

Figure 3.60. Energy ratio coherence along phantom horizon 24 ms above Horizon A3 using constant window size of (a) ±4 ms, (b) ±20 ms, (c) ±40 ms using 5 traces, and (d) a data-adaptive window varying between ±12 ms and 5 traces, and ±100 ms and 13 traces.

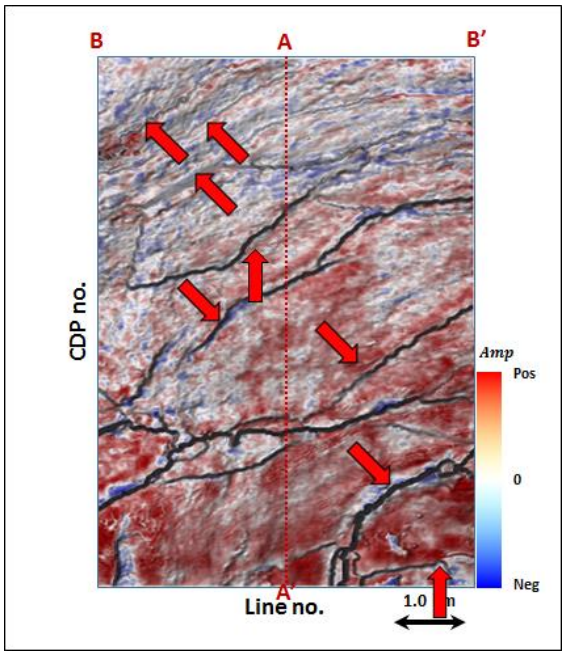

Figure 3.61. Phantom horizon 32 ms above Horizon A3 extracting along seismic amplitude data.

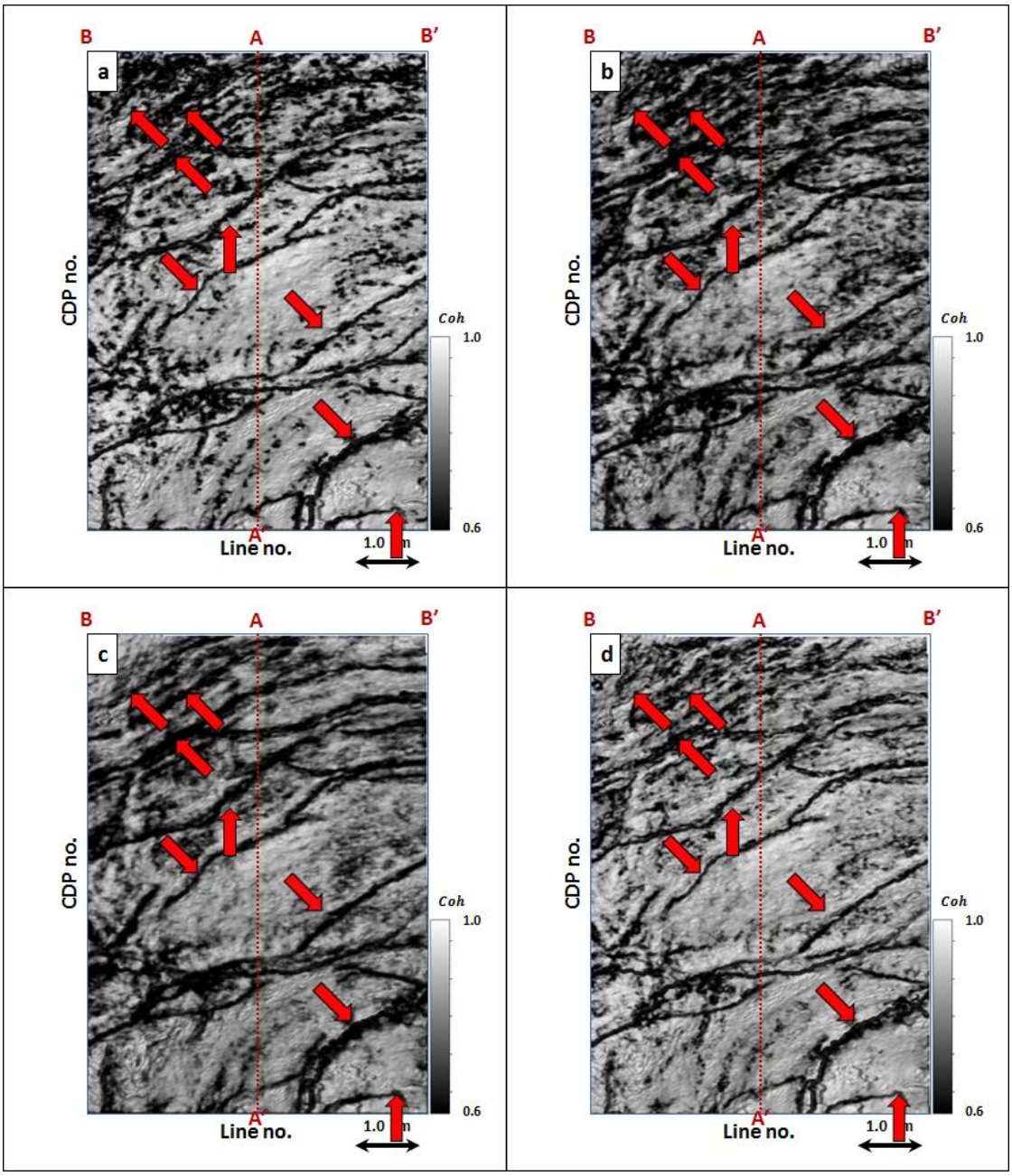

Figure 3.62. Energy ratio coherence along phantom horizon 32 ms above Horizon A3 using constant window size of (a) ±4 ms, (b) ±20 ms, (c) ±40 ms using 5 traces, and (d) a data-adaptive window varying between ±12 ms and 5 traces, and ±100 ms and 13 traces.

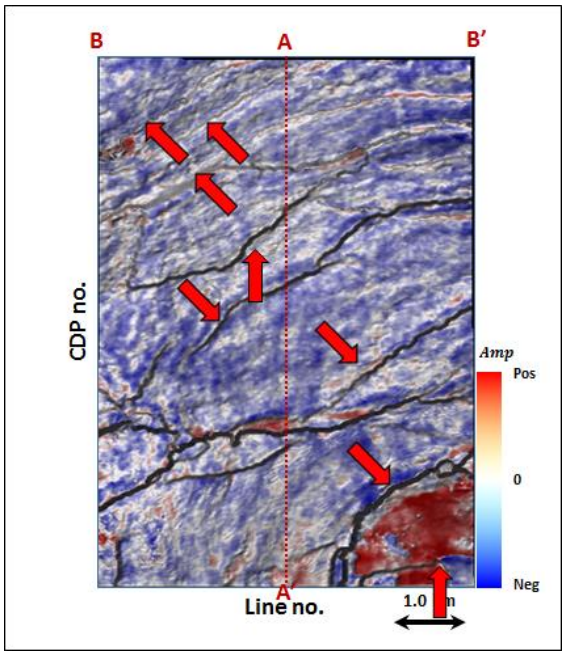

Figure 3.63. Phantom horizon 40 ms above Horizon A3 extracting along seismic amplitude data.

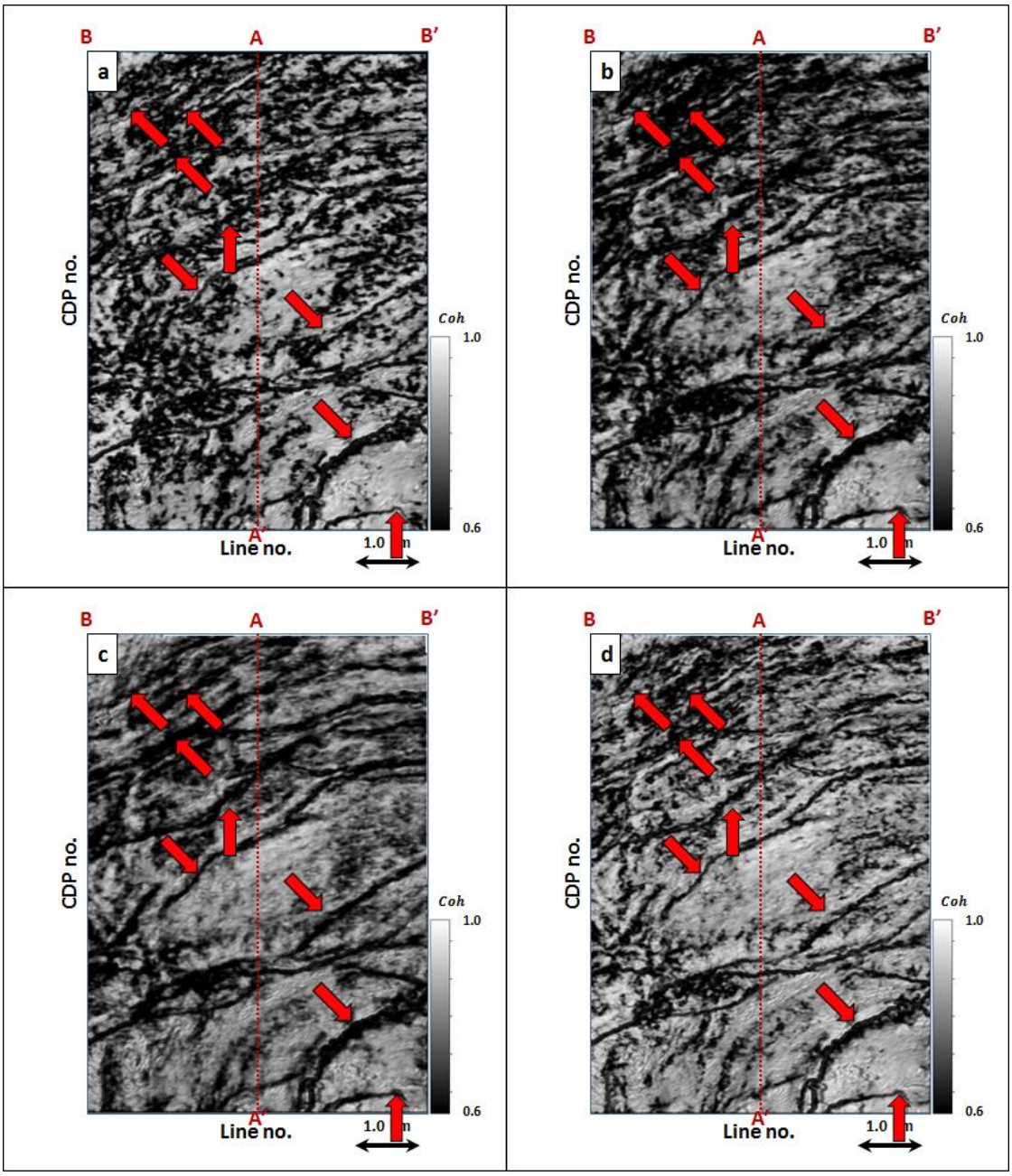

Figure 3.64. Energy ratio coherence along phantom horizon 40 ms above Horizon A3 using constant window size of (a) ±4 ms, (b) ±20 ms, (c) ±40 ms using 5 traces, and (d) a data-adaptive window varying between ±12 ms and 5 traces, and ±100 ms and 13 traces.

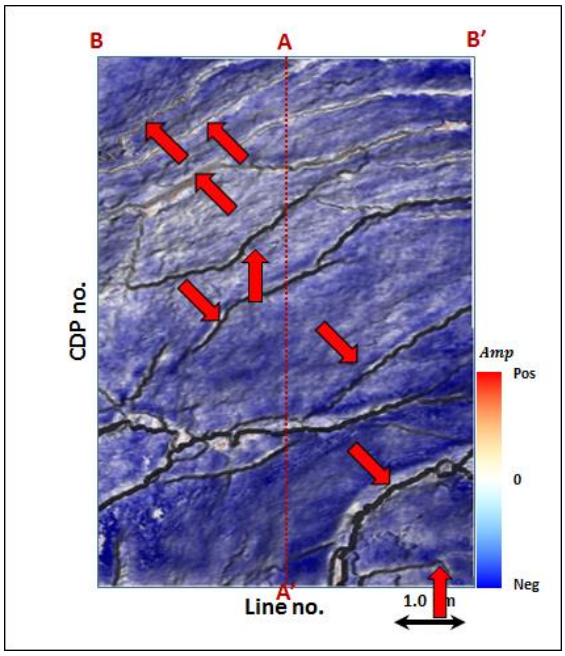

Figure 3.65. Phantom horizon 8 ms below Horizon A3 extracting along seismic amplitude data.

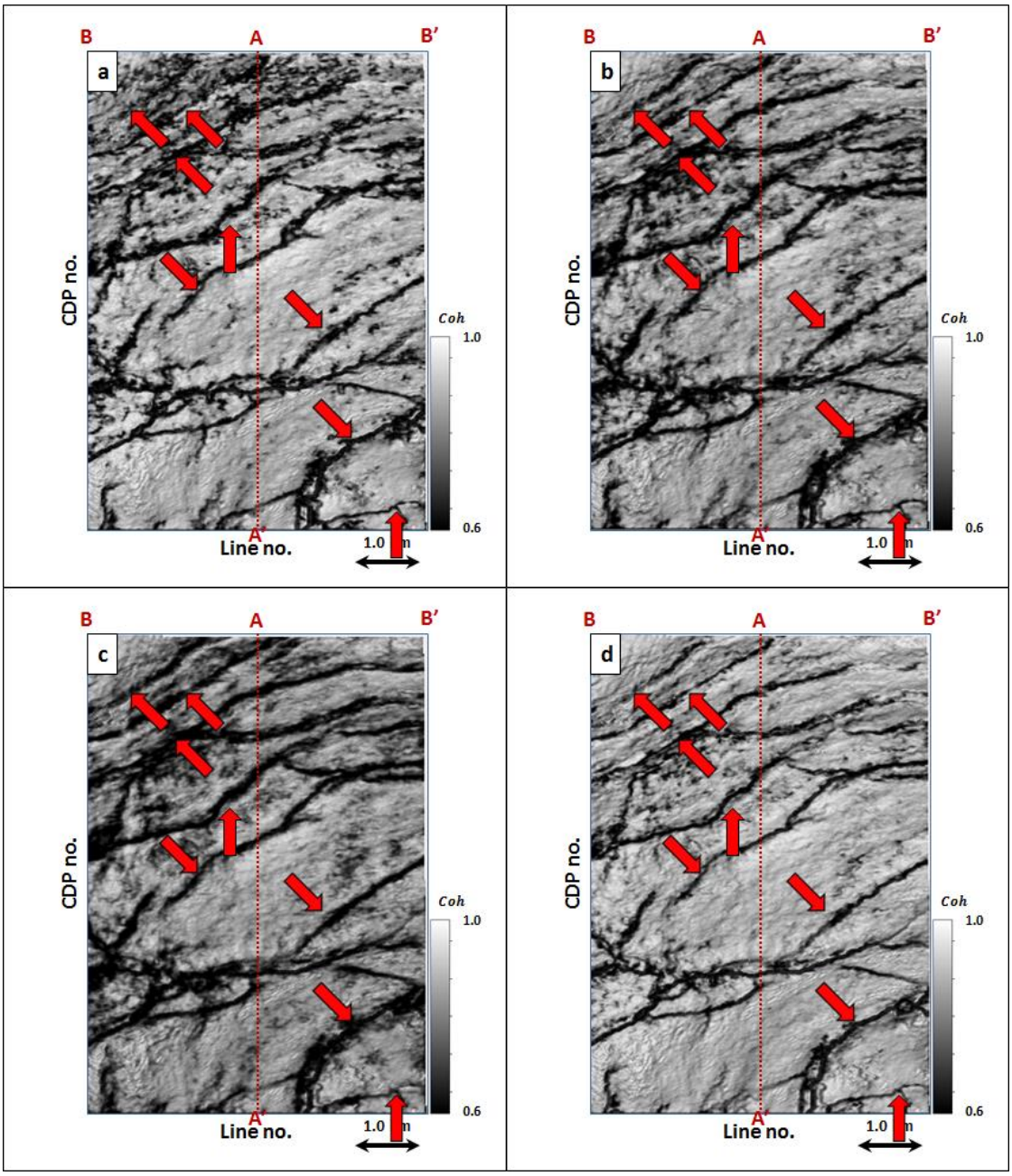

Figure 3.66. Energy ratio coherence along phantom horizon 8 ms below Horizon A3 using constant window size of (a) ±4 ms, (b) ±20 ms, (c) ±40 ms using 5 traces, and (d) a data-adaptive window varying between ±12 ms and 5 traces, and ±100 ms and 13 traces.

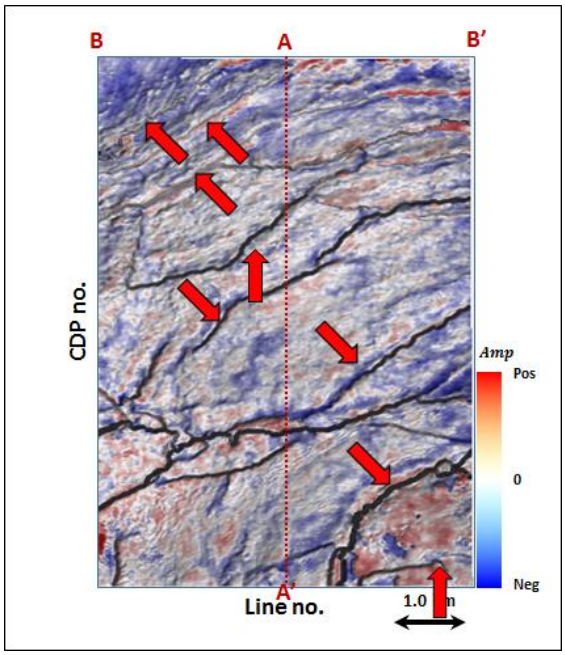

Figure 3.67. Phantom horizon 16 ms below Horizon A3 extracting along seismic amplitude data.

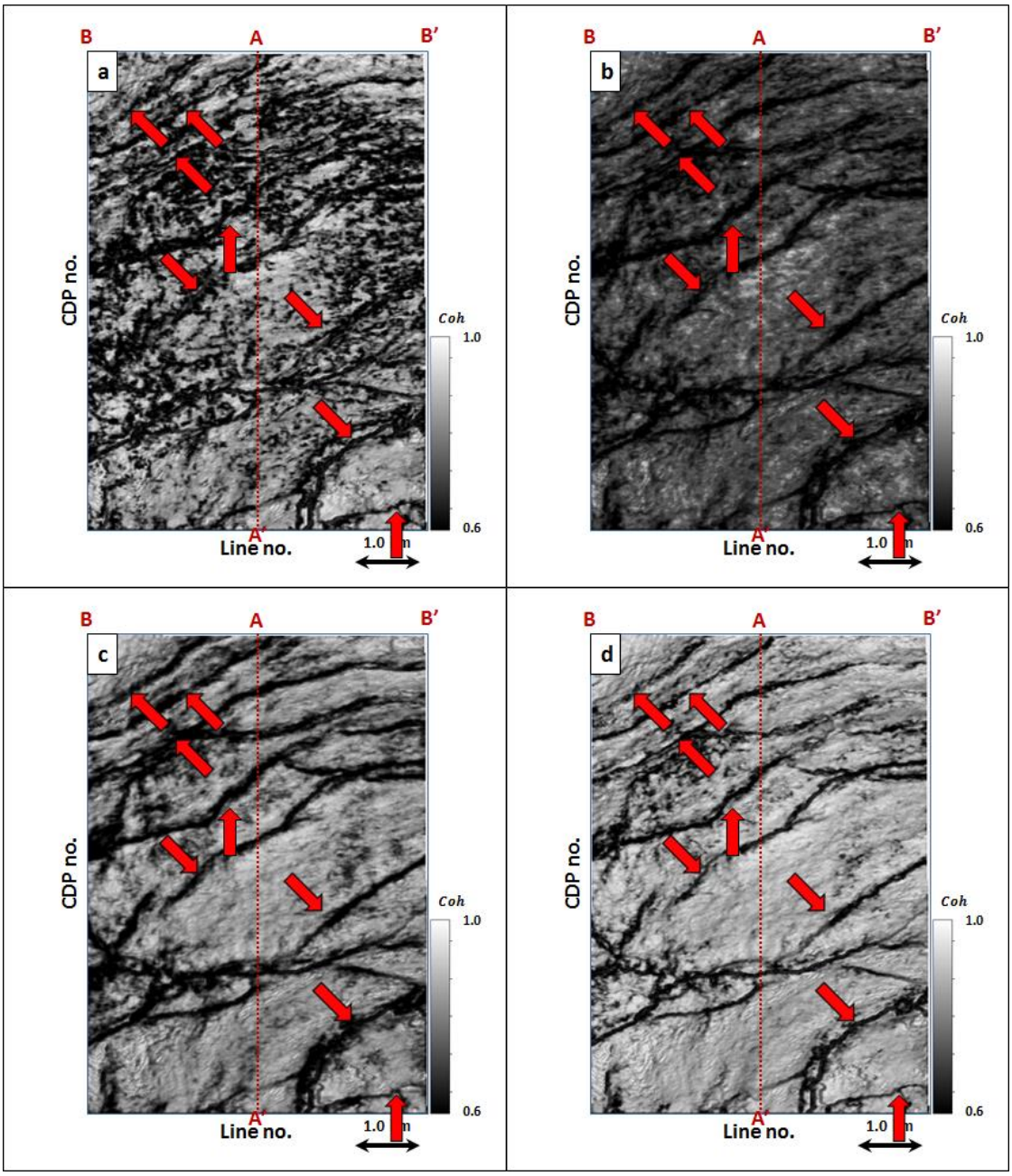

Figure 3.68. Energy ratio coherence along phantom horizon 16 ms below Horizon A3 using constant window size of (a) ±4 ms, (b) ±20 ms, (c) ±40 ms using 5 traces, and (d) a data-adaptive window varying between ±12 ms and 5 traces, and ±100 ms and 13 traces.

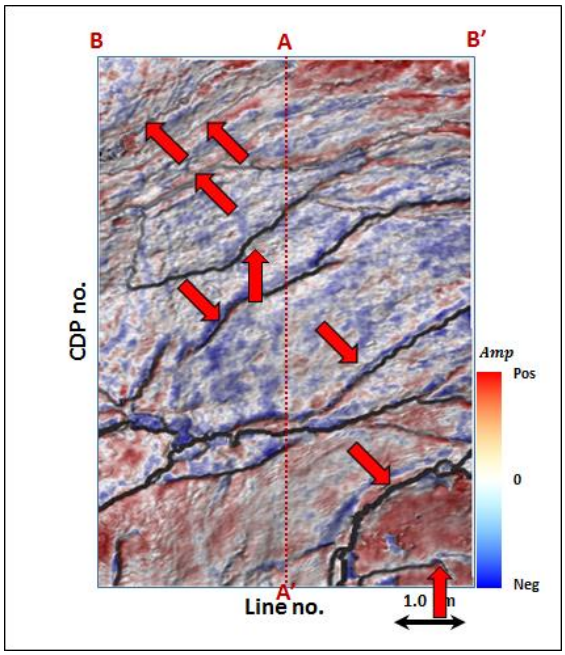

Figure 3.69. Phantom horizon 24 ms below Horizon A3 extracting along seismic amplitude data.

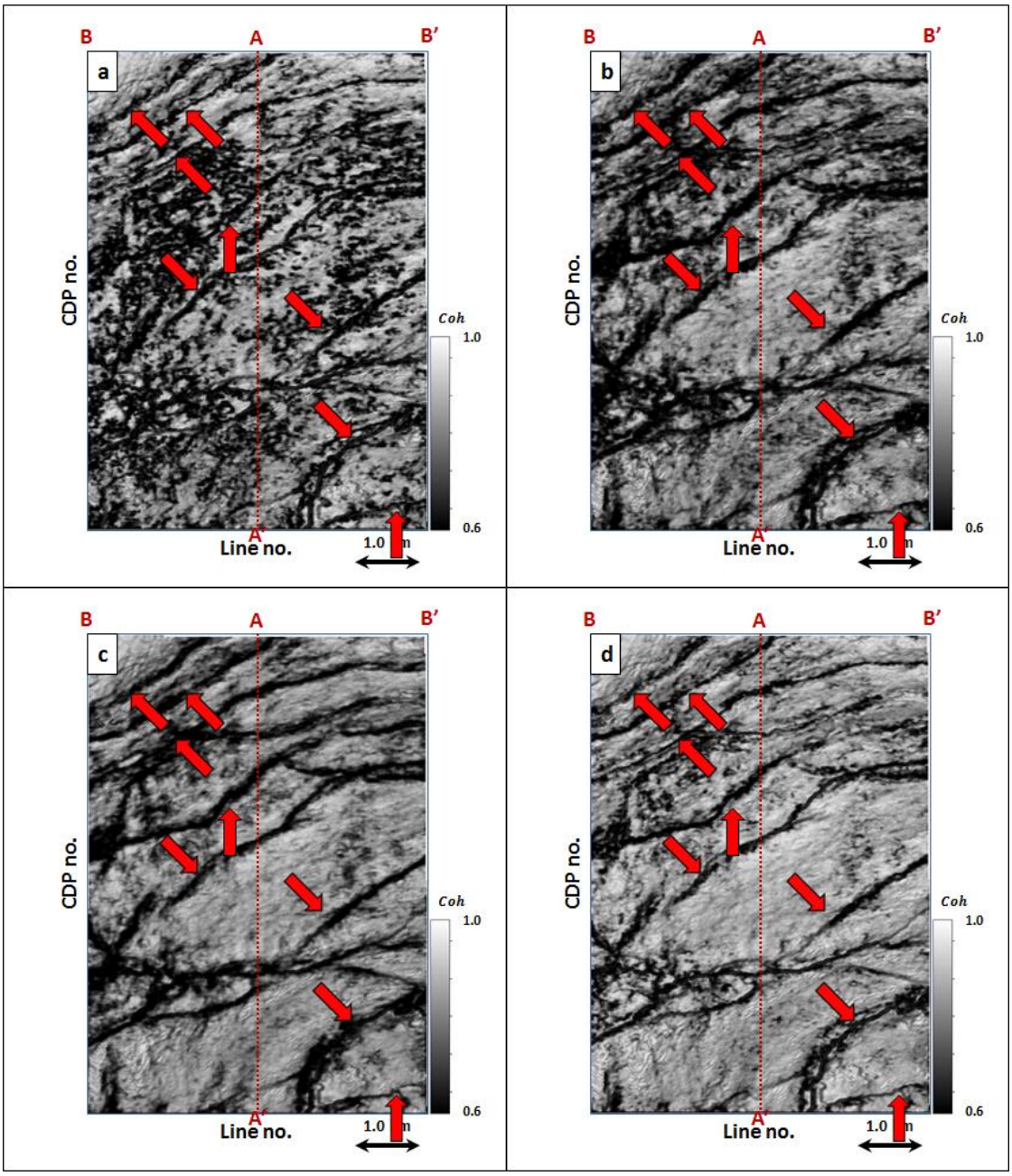

Figure 3.70. Energy ratio coherence along phantom horizon 24 ms below Horizon A3 using constant window size of (a) ±4 ms, (b) ±20 ms, (c) ±40 ms using 5 traces, and (d) a data-adaptive window varying between ±12 ms and 5 traces, and ±100 ms and 13 traces.

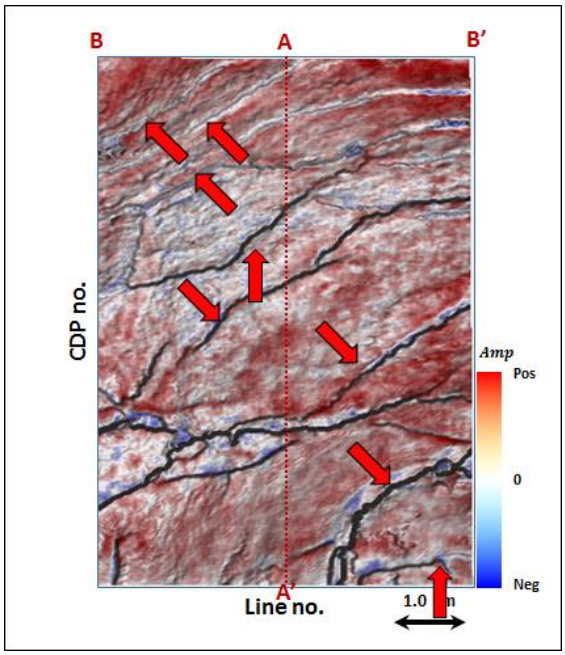

Figure 3.71. Phantom horizon 32 ms below Horizon A3 extracting along seismic amplitude data.

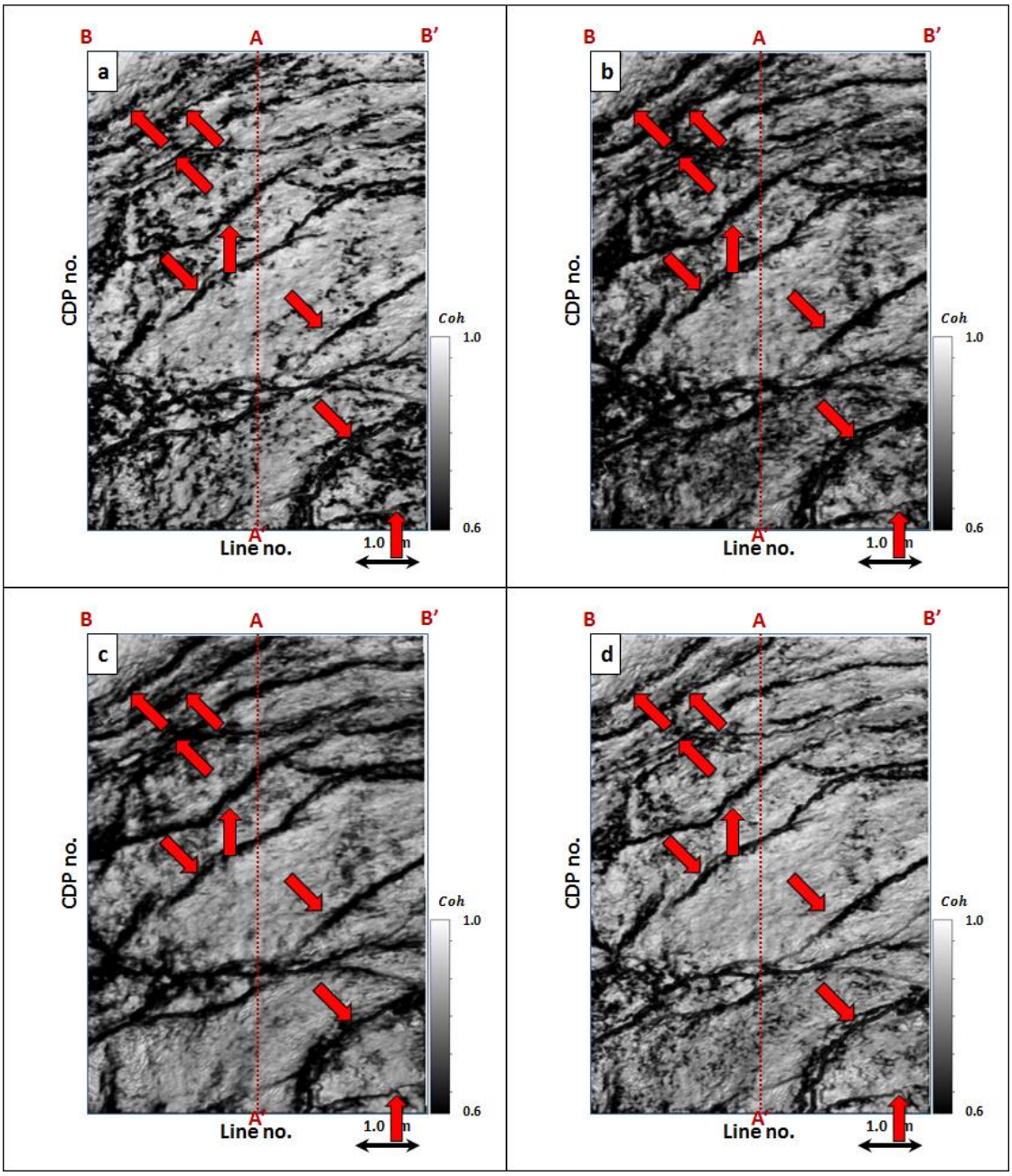

Figure 3.72. Energy ratio coherence along phantom horizon 32 ms below Horizon A3 using constant window size of (a) ±4 ms, (b) ±20 ms, (c) ±40 ms using 5 traces, and (d) a data-adaptive window varying between ±12 ms and 5 traces, and ±100 ms and 13 traces.

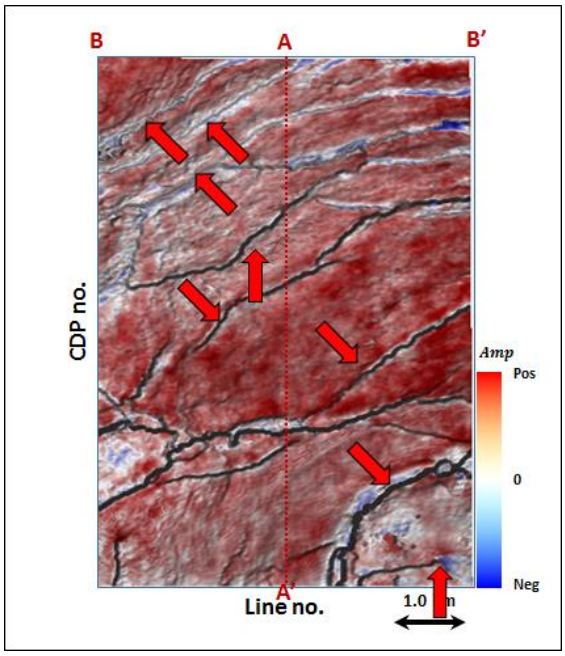

Figure 3.73. Phantom horizon 40 ms below Horizon A3 extracting along seismic amplitude data.

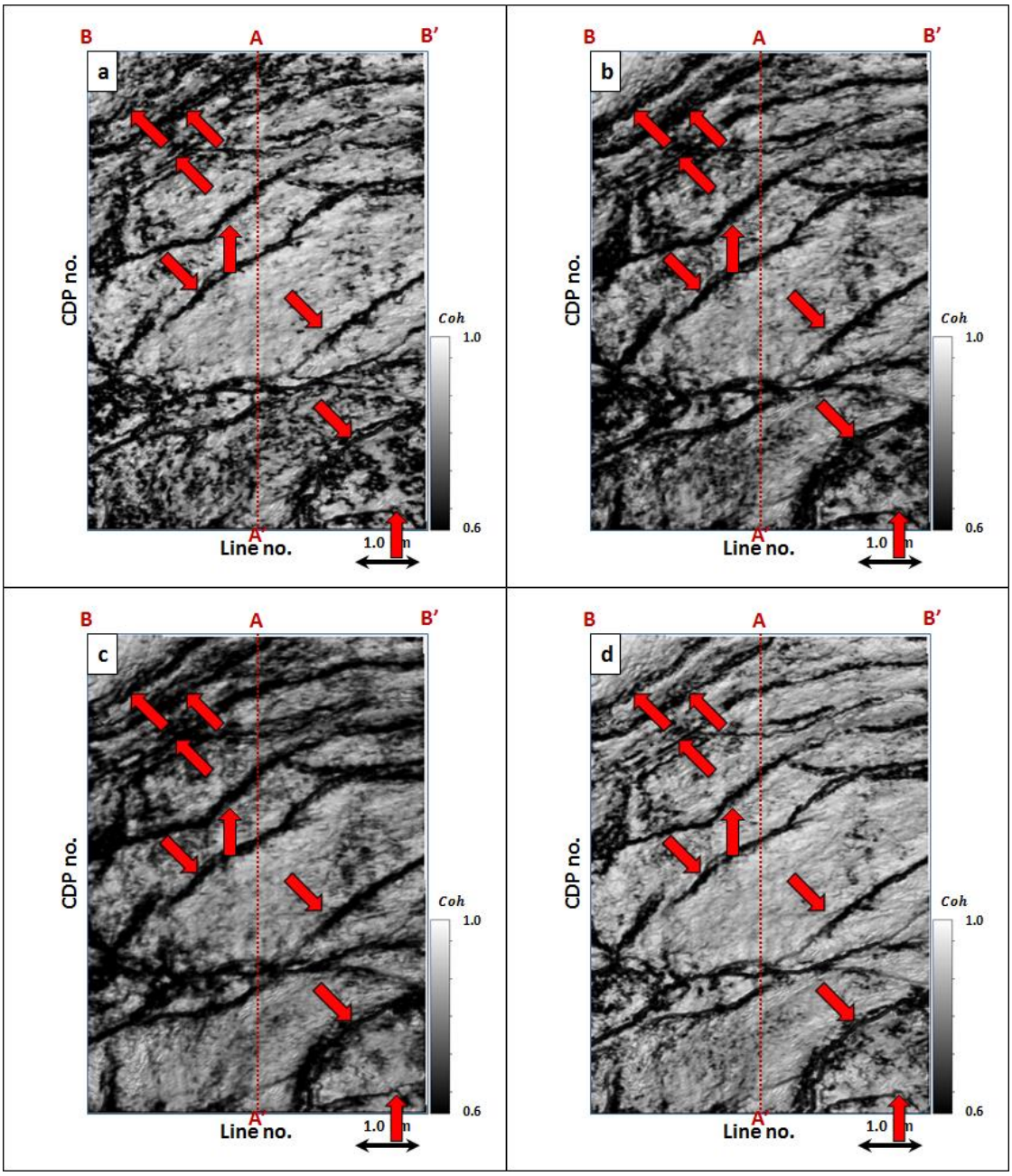

Figure 3.74. Energy ratio coherence along phantom horizon 40 ms below Horizon A3 using constant window size of (a) ±4 ms, (b) ±20 ms, (c) ±40 ms using 5 traces, and (d) a data-adaptive window varying between ±12 ms and 5 traces, and ±100 ms and 13 traces.

CHAPTER 4

ATTRIBUTE ARTIFACTS IN TIME- VS. DEPTH-MIGRATED DATA

Tengfei Lin[1], Bo Zhang[2], Kurt Marfurt[1]

[1] University of Oklahoma, ConocoPhillips School of Geology and Geophysics,

[2] University of Alabama, Department of Geological Sciences.

ABSTRACT

In general, depth migration is necessary in the presence of strong lateral velocity variation and avoids some of pitfalls that occur in time-migrated data. Fault shadows in time-migrated data give rise to discontinuity artifacts mapped by coherence. Depth migration eliminates velocity pull-up and push-down, and in general results in better focused image. Fault termination of reflectors may be misaligned, giving rise to “wormy” coherence anomalies. Channel and other stratigraphic features may be diffused making them hard to interpret. We illustrate these differences by analyzing seismic attributes computed from time- and depth-migrated seismic volumes from Bohai Bay Basin, China.

LIST OF KEYWORDS

Geometric attributes, depth-migrated data.

INTRODUCTION

Coherence algorithm measure lateral changes in seismic reflection amplitude, phase and frequency. (Bahorich and Farmer, 1995, 1996). Like other attributes, coherence is sensitive to noise.

In contrast to random noise, all coherence algorithms are sensitive to fault shadows seen in time-migrated data. Fagin (1991) uses forward ray trace modeling to illustrate the fault shadow problem. A more complete description of the "fault whisper" problem on prestack data is given by Hatchell (2000). Fault whisper is the phenomenon of transmission distortions, which are produced by velocity changes across buried faults and unconformities and related to the phenomenon known as fault shadows.

Depth-migrated data presents its own challenges. In time-migration the major impact of velocity is to focus or defocus reflectors and diffractors with some lateral movement. In depth-migration, these features are also moved both laterally and vertically. If the velocity model is inaccurate, depth-migrated data may be inferior to time-migrated data. Even if the data are properly imaged, the wavelet spectrum is no longer in Hertz, but in wavenumber that decreases with increasing velocity as depth increases.

SYNTHETIC MODELS

Figure 4.1 shows a fault model as well as its prestack time migration data (PSTM) seismic profile. The purple and green horizons indicate us two high velocity layers.

Looking in detail at these oscillations of PSTM seismic profile in Figure 4.2a, point A-H are the points located at the main fault of the model. The semi-transparent yellow zone indicates the fault shadow zone, where the reflectors are highly distorted compared to the original structural model. Pushdown from high velocity layer 1 occurs between point A and D; similarly, pushdown from high velocity layer 2 occurs between point E and H, which are pointed by red arrows. On the time-migrated section a near-vertical structural axis can be drawn which links the position of each of these anomalies for each underlying reflection. The pitfall is that these axes could be easily misinterpreted as conjugate faults, consistent with the normal fault. Another velocity pushdown and pull-up are caused by the slower (white arrow) and faster (black arrow) velocity objects, respectively. Fagin (1991) shows how one can predict these pushdown and pull-up phenomenon using simple zero-offset synthetics. The human interpreter sees a crest followed by a trough. Seismic attributes will see the same. On the depth-migrated section in Figure 4.2b, all of the artifacts are removed and give back the real structure of the fault model.

Figures 4.3a and b indicate the PSDM coherence profile computed from PSTM and PSDM seismic data, respectively. The horizon distortions (push down) marked by red arrows are imaged in coherence profile of PSTM seismic data, which is suppressed in Figure 4.3b. Another structural artifacts caused by differential objects indicated by white and black arrow are also removed. The 2D curvature profiles of PSTM in Figure 4.4a shows the conjugate curvature anomalies. Red and while arrows gives us push-down phenomenon distributing parallel negative curvatures inside and parallel positive curvatures outside; while the black arrow shows opposite pull-up phenomenon, with parallel positive curvatures inside and parallel negative curvatures outside.

APPLICATION

Geometric Attributes Computed from Prestack Time-Migrated Data

Figures 4.5 indicate us the seismic profile of PSTM amplitude volume. The survey is located in Hebei Province, which was acquired by BGP Inc., China National Petroleum Corporation.

F1 and F2 are two major faults, H1-H5 are horizons in the seismic profile. Seismic pitfalls (pull-up) are indicated by red arrows, which should be caused by the existence of high velocity zone between H3 and H5. The structural high zone seems unreasonable. This is because they are at upthrow, which means they should be structural low zone.

Coherence is an important aid in fault interpretation. Figure 4.6 indicates the vertical slice through coherence co-rendered with seismic amplitude for PSTM data. The grey curved solid line indicated by grey arrow can be interpreted as sub-fault splays to the main fault F2.

I co-render the most-positive curvature, most-negative curvature and seismic amplitude of time-migrated and depth-migrated data in Figure 4.7. The blue zone indicated by blue arrows for fault F2 and F3 indicates the syncline with most negative curvature, while the red zone indicated by red arrows for fault F2 and F3 indicates the

anticline with most positive curvature. Considering that F2 and F3 are normal faults, the parallel most positive- and negative- curvatures are unreasonable.

Geometric Attributes Computed from Prestack Depth-Migrated Data

Considering the pitfalls existed in seismic profile of the fault modal for PSTM in Figures 4.2-4.4, the prestack depth-migrated data (PSDM) shows its advantages in seismic attribute analysis, removing lot of artifacts caused by horizontal velocity variation.

Figure 4.8 indicates the seismic profile of PSDM amplitude volumes, which can accurately describe the structure compared to the Figure 4.5. The pull-up zone indicated by red arrow as well as the fault shadow zone in Figure 4.5 disappears in Figure 4.8. The fault shadow zone can be described as the sub-fault splays to the main fault F2 in Figure 4.6. Figure 4.9 indicates the vertical slice through coherence co-rendered with seismic amplitude for PSDM data, in which the sub-fault splays are removed. Figure 4.10 indicates vertical slice through most positive curvature co-rendered with most negative curvature (with long wavelet) and seismic amplitude along for PSTM. The parallel syncline and anticline indicated by blue and red arrows in Figure 4.7 disappear in Figure 4.10, which correct many structural pitfalls.

CONCLUSIONS

The seismic data from the Bohai Bay Basin in China are processed by PSTM as well as PSDM, separately, combining with seismic attributes to compare the seismic imaging quality. Several artifact sub-faults splays in coherence generate the fault-shadow zones under dipping main faults in PSTM data, but disappear in PSDM data. The curvature anomalies related to the lateral variations may be misinterpreted as real structures in PSTM data, which are removed in precise velocity PSDM data.

In the presence of strong lateral variations in velocity, PSDM is better for interpreting complex structures comparing PSTM, which fails to properly image the subsurface. First, fault shadows can give rise to a second (artificial) discontinuity coherence images computed from time-migrated data. Such artifacts are removed in accurate velocity depth-migrated data. Second, velocity pull-up and push down caused by the lateral changes in the overburden such as carbonate buildups and incised valleys will give rise to erroneous curvature anomalies in time-migrated data. These artifacts disappear in in properly depth-migrated data. Third, in complex structure time-migrated data may be poorly focused.

ACKNOWLEDGEMENTS

We thank BGP Inc., for the use of their Bohai Bay Basin data set. Numerical model was generated using Tesseral's Tesseral 2D software. Seismic displays were generated used Schlumberger's Petrel software. We also thank the sponsors of Attribute-Assisted Seismic Processing and Interpretation Consortium (AASPI) for their guidance and financial support.

CHAPTER 4 FIGURES

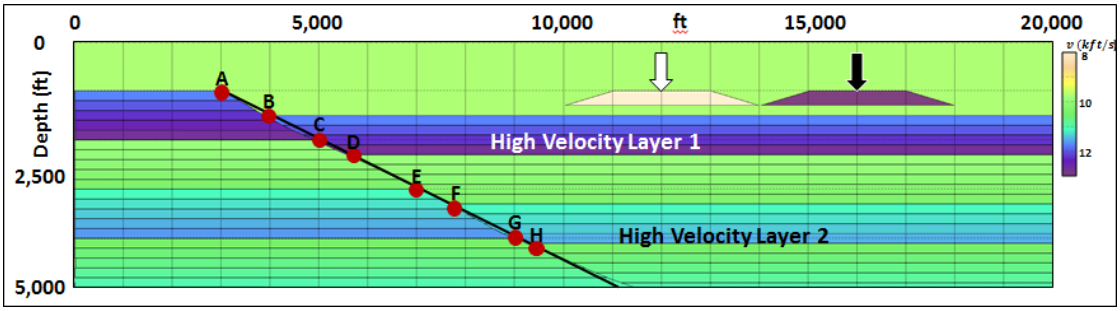

Figure 4.1. (a) The fault model with two high velocity layers.

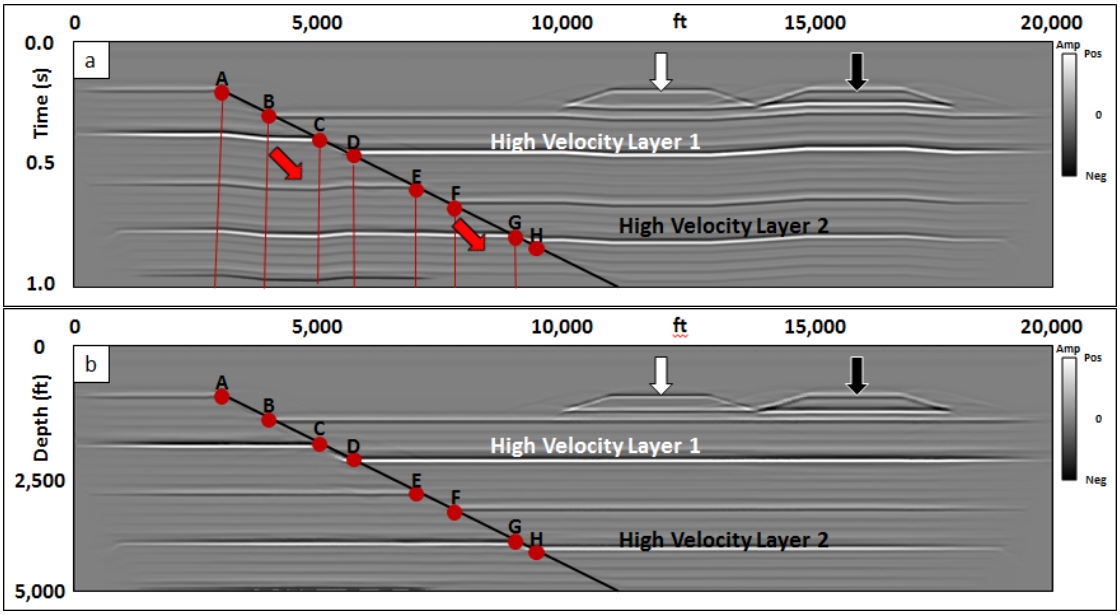

Figure 4.2. The (a) PSTM and (b) PSDM seismic profile of the fault model in Figure 4.1.

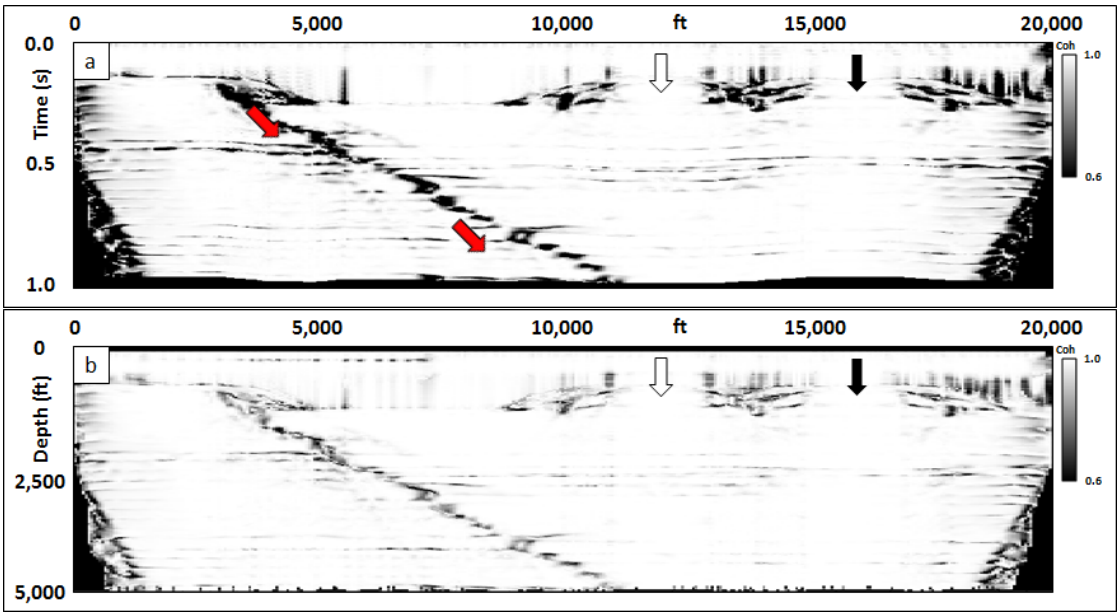

Figure 4.3. The (a) PSTM and (b) PSDM coherence profile computed from Figures 4.2a and b, respectively, of the fault model.

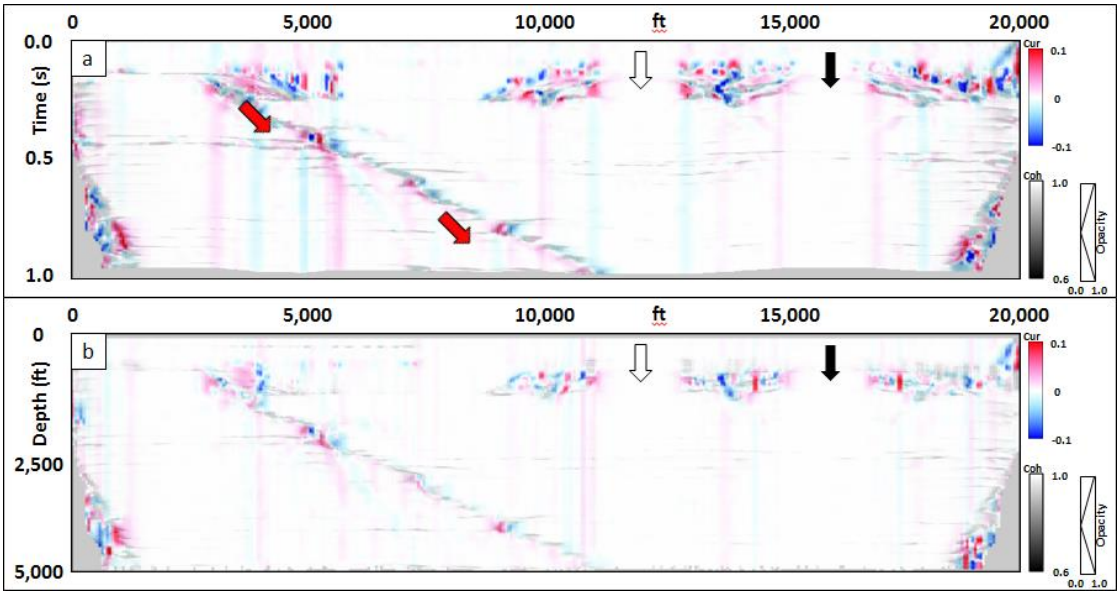

Figure 4.4. The (a) PSTM and (b) PSDM 2D curvature profile correnden with coherence computed from Figures 4.2a and b, respectively, of the fault model.

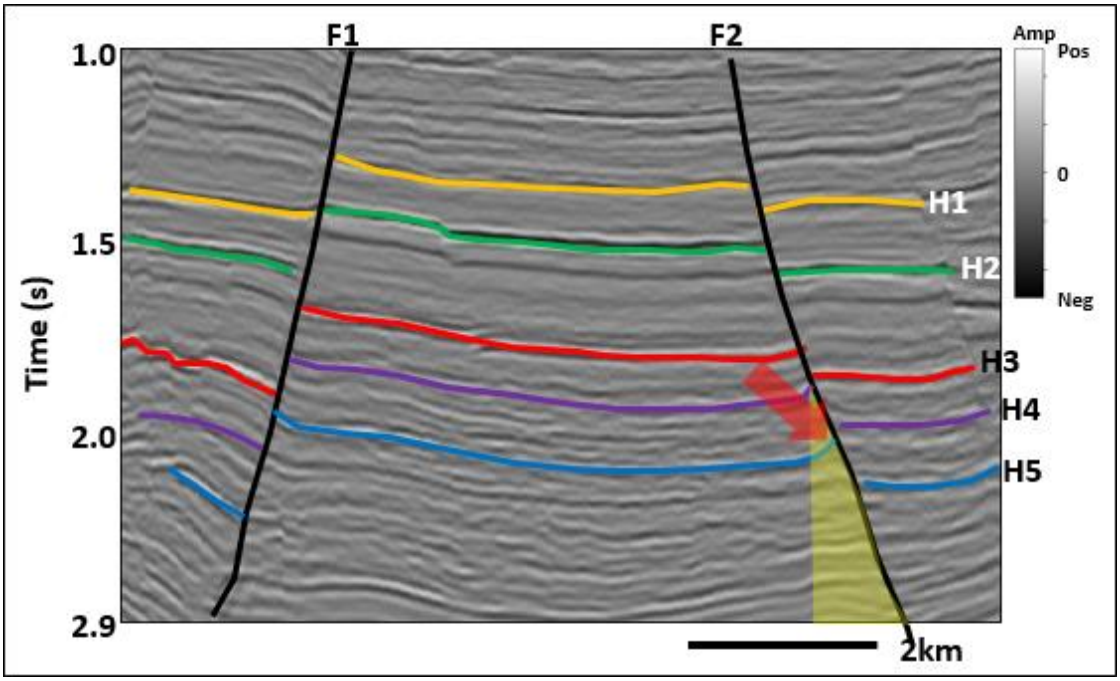

Figure 4.5. Seismic profile of PSTM amplitude volume.

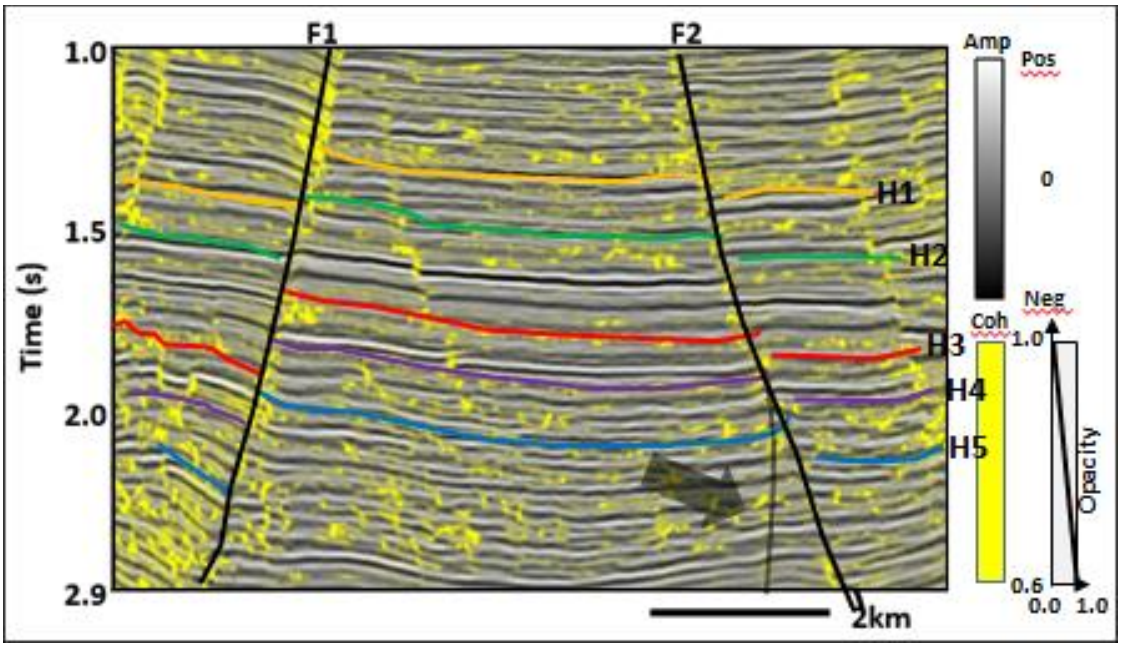

Figure 4.6. Vertical slice through coherence co-rendered with seismic amplitude for PSTM data.

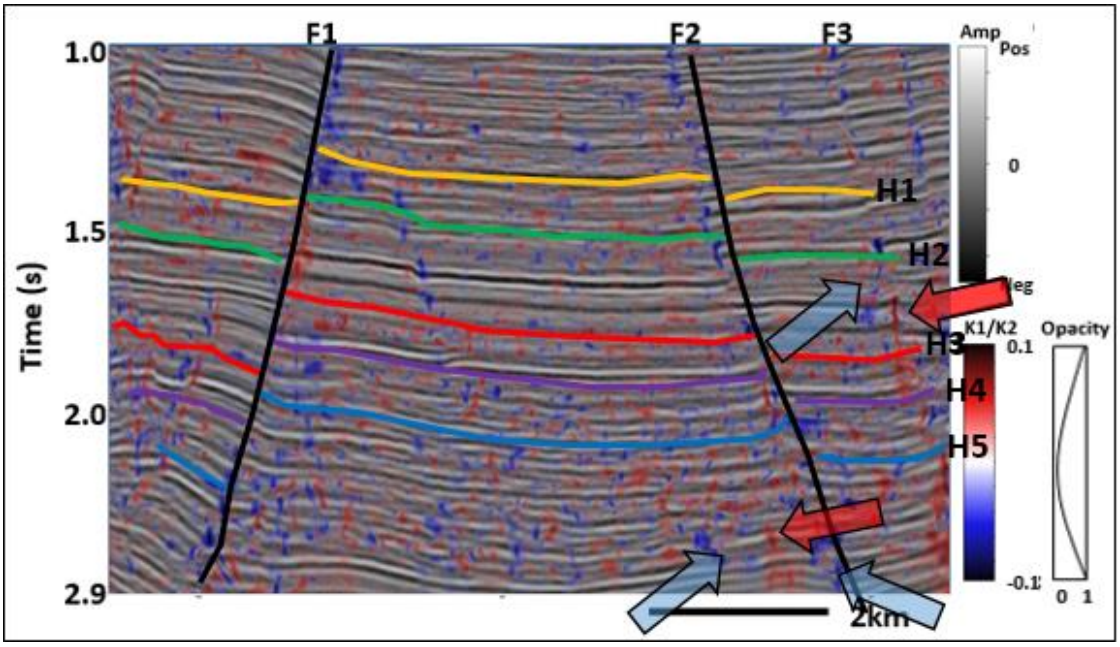

Figure 4.7. Vertical slice through most positive curvature co-rendered with most negative curvature (with long wavelet) and seismic amplitude along for PSTM data.

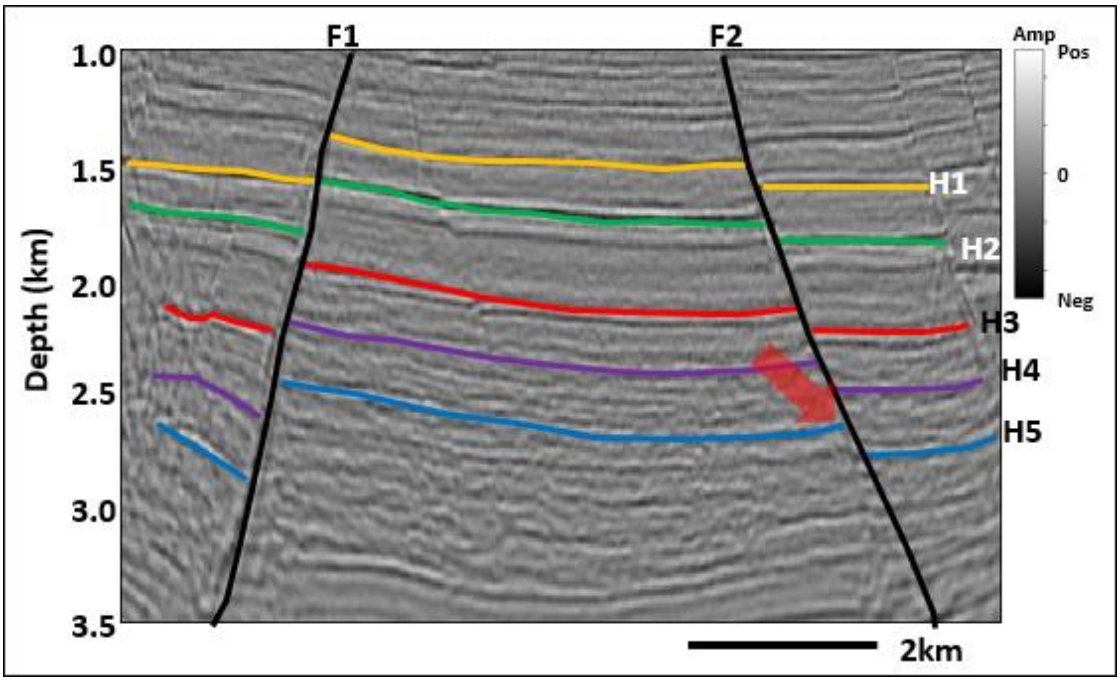

Figure 4.8. Seismic profile of PSDM amplitude volume.

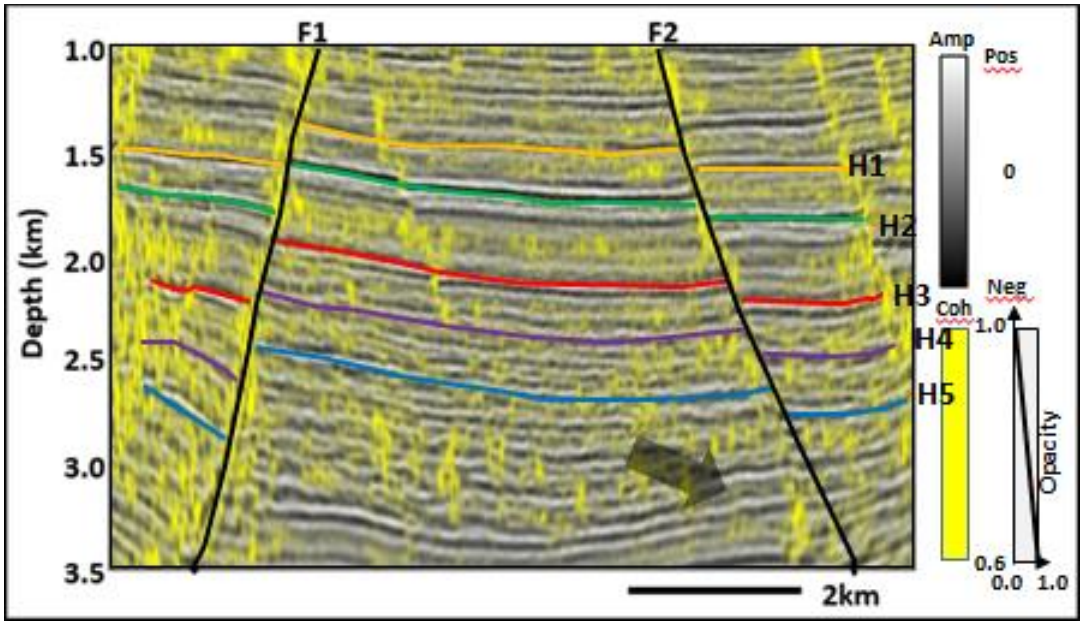

Figure 4.9. Vertical slice through coherence co-rendered with seismic amplitude for PSDM data.

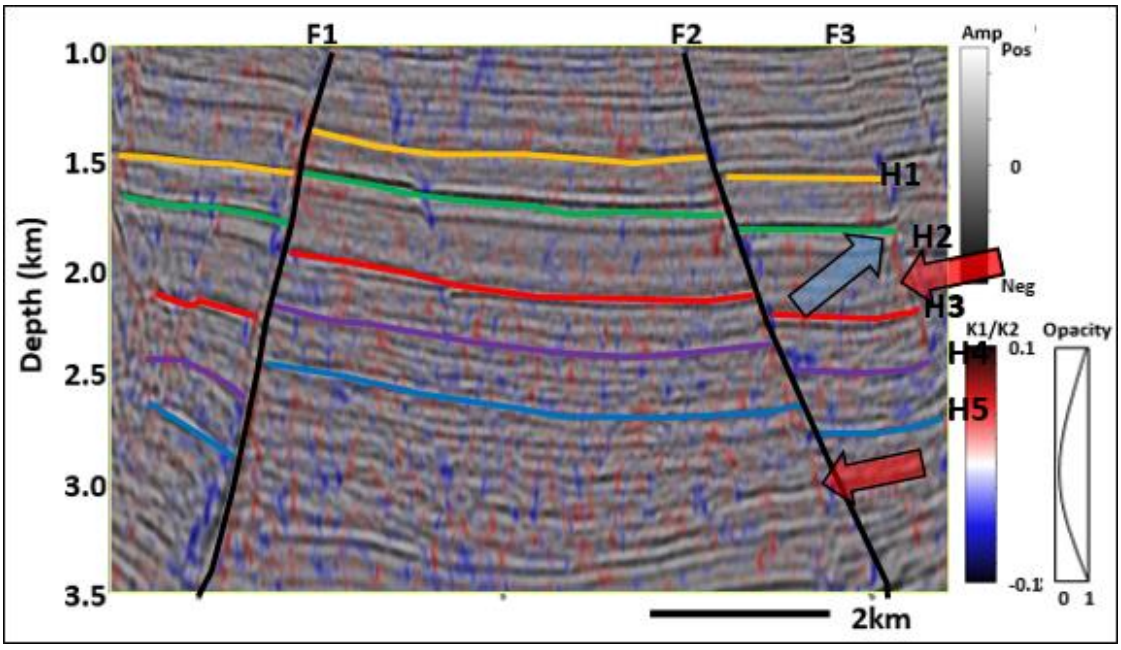

Figure 4.10. Vertical slice through most positive curvature co-rendered with most negative curvature (with long wavelet) and seismic amplitude along for PSDM data.

REFERENCES

Bahorich, M. S., and Farmer, S. L., 1995, 3-D seismic discontinuity for faults and stratigraphic features: The Leading Edge, **14**, 1053–1058.

Bahorich, M. S., and Farmer, S. L., 1996, Methods of seismic signal processing and exploration: U.S. Patent 5 563 949.

Fagin, S.W., 1991, Seismic modeling of geologic structures: Applications to exploration problems: Geophysical development series, 2. Society of Exploration Geophysics.

Hatchell P. J., 2000, Fault whispers: Transmission distortions on prestack seismic reflection data: Geophysics, **65**, 377 – 389.

CHAPTER 5

WAVELET-BASED RADON TRANSFORM

Tengfei Lin[1], Bo Zhang[2], Kurt Marfurt[1]

[1] University of Oklahoma, ConocoPhillips School of Geology and Geophysics,

[2] University of Alabama, Department of Geological Sciences.

ABSTRACT

Different approaches have been investigated and applied to the multiple attenuation problems. One of the most popular methods, the Radon transform, forms an industry standard workflow and is routinely used in seismic data conditioning. Because of cost, seismic data are often spatially undersampled and therefore aliased. “High resolution” Radon transform better on such aliased data. In this work, we generalize the high-resolution Radon transform to be to be wavelet based.

In this study, Radon transform techniques are reviewed and analyzed, and a new Radon transform algorithm, wavelet-based Radon transform using matching pursuit method is introduced. We compute Radon transform of the largest events for each trace, and then convert them to the tau-p domain. The multiples are then modeled and subtracted from the original reflections, till to reach the maximum iteration, which provides a power tool for multiple suppression.

LIST OF KEYWORDS

Radon Transform, Matching Pursuit Method.

INTRODUCTION

There are several computing de-multiple workflows: (1) deconvolution that predicts and then subtracts multiples from the measured seismic data, (2) separation of primary reflections and multiples in a transform domain, and (3) defining the multiple generators, modeling and then subtracting multiples from the measured seismic data. Parabolic Radon transform applied to NMO-corrected or migrated CMP gathers are routinely used in seismic data conditioning (Hampson, 1986; Russell et al. 1990a, 1990b), while linear Radon transform are used to suppress head waves and ground roll (Zhou and Greenhalgh, 1994). Surface related multiple estimation (SRME) is a more recent innovation application to common shot gathers prior to migration, which provides excellent results for the long period multiples generated from the earth surface. In general, SRME performs poorly on interbed multiples and converted waves, while Radon transform performs reasonably well.

Since Radon transform are applied to migrated gathers, they fit neatly into a quantitative interpretation toolbox, running well on modern desktop computers. Unfortunately, insufficient spatial sampling (aliasing) gives rise to artifacts that seriously prevent separating multiples and other noise from primary events of interest.

The least squares Radon transform (LSRT) in frequency-space domain was introduced (Thorson and Claerbout, 1985; Hampson, 1986; Yilmaz, 1989) to minimize the horizontal and oblique smearing seen using simple “projection” Radon transforms.

Later, Sacchi and Ulrych (1995) proposed a high resolution frequency domain Radon transform (HRFRT), which used a nonlinear sparse-spike constraint, to better separate the multiple from primary events. Not surprisingly, increasing the number of events diminishes the superiority of HRFRT, since the reflection spikes are no longer "sparse".

Semblance and other coherence measures are routinely used in seismic processing such as velocity spectra analysis, in seismic interpretation to estimate volumetric dip and to delineate geologic boundaries, and in poststack and prestack data conditioning such as edge-preserving structure-oriented filtering. The energy of coherent event, which traditionally ranges from 0 to 1, can be used as a weighting function (Stoffa et al. 1981; Yilmaz and Taner, 1994; Ng and Perz, 2004) to give a semblance-weighted Radon transform (SWRT).

The matching pursuit algorithm was first proposed for seismic analysis by Mallat and Zhang (1993) and has been widely applied to seismic signal processing (Wang and Pann, 1996; Zhang et al. 2012) and spectral analysis (Liu and Marfurt, 2005; Wang, 2006, 2010; Dao and Marfurt, 2013). Specifically, the algorithm asks "which Ricker wavelet with which moveout, best represents the seismic gather". After each estimate, that event is removed from the data, forming a residual. The algorithm will iterate until all events are described. My hypothesis is that the wavelet-based Radon transform using matching pursuit method will provide improved separation between primaries and multiples. After prototyping my algorithm, I apply it to a

marine data volume acquired by KIGAM in the Jeju Basin, Korea to verify its performance.

THEORETICAL ANALYSIS

The Radon Transform

2D Linear Radon Transform

The original 2D linear Radon transform (LRT) is the integral of seismic or other 2D data (such as photographs) over a suite of straight line trajectories in the time-space domain $d(t,x)$:

$$t(x) = t_0 + \frac{x}{v} = t_0 + p_L x \,, \tag{1}$$

where *v* is velocity and p_L=1/*v*, or slowness.

The data $d(t,x)$ are transformed to tau-p domain $u(\tau, p_L)$, where τ is defined as the intercept; and p_L the slope of the straight line:

$$u(\tau, p_L) = \int_{-\infty}^{\infty} d(t = \tau + p_L x, x)dx. \tag{2}$$

Consequently, a given constant slope, constant amplitude event in the time-space domain will be represented by a discrete point in the tau-p domain. Thus head waves and ground roll are often represented by focused energy points with constant values of τ and p. Primary hyperbolic reflections and multiple appear as ellipses in the (τ, p_L) domain.

The cartoon of Figure 5.1s shows common shot gather events corresponding to a horizontally layered model. The direct wave exhibits a constant velocity, v_D, and intercepts at t = 0 s at zero offset. Because this even can be represented by a single constant amplitude linear event, it maps to a dot in tau-p domain (Figure 5.1b). In this cartoon, Ground roll also exhibits linear moveout with lower velocity, which is also represented as a dot similar to direct wave but with larger $p=1/v_{GR}$ value. The primary reflection appears as a hyperbola with increasing slope (p) with offset. At critical angle, a linear head wave appears. The hyperbola maps to an ellipse while the head wave maps to a point $p=1/v_{HW}$. The multiple exhibits a similar pattern, but delayed in time since it arrives later.

The 2D Velocity Radon Transform, or Velocity Analysis

In seismology, a flat reflector results in a hyperbolic event in time-space domain with:

$$t(x) = \sqrt{t_0^2 + \frac{x^2}{v_{rms}^2}}, \tag{3}$$

where t_0 is the zero-offset two-way travel time of the event, v_{rms} is the relative RMS velocity, and x is the source-receiver offset.

The Velocity Radon transform (VRT) parameterizes the moveout curve with a hyperbola curvature, p_H,

$$u(\tau, p_H) = \int_{-\infty}^{\infty} d(t = \sqrt{\tau^2 + p_H x^2}, x)dx, \quad (4)$$

where $p_H = 1/v_{rms}^2$.

Figure 5.2 gives the diagram of 2D Velocity Radon Transform for a horizontally layered model. There are two sets of reflection, primary wave 1 and its multiple 1, and primary wave 2 and its multiple 2. Since they are hyperbolic events, all of them will be transformed to dots in tau-p domain. Primary wave 1 exhibits smaller velocity compared to primary wave 2, which means that primary wave 1 in tau-p domain has larger *p* value. The two multiples are characterized as the same *p* value as the relevant primary waves, respectively, with lower τ values. If we set a closed polygon marked by red dashed circle and remove them, the multiples will be removed in time-space domain. This is a main application of the Radon Transform.

2D Parabolic Radon Transform

After sorting to CMP gathers, reflection events are corrected by interactively picking velocity v_i (a stacking velocity), which defines a moveout curve:

$$t_i(x) = \sqrt{t_0^2 + \frac{x^2}{v_i^2}}. \quad (5)$$

If the true RMS velocity is v_{RMS}, the time difference, or residual moveout after NMO-correction is:

$$\Delta t(x) = \sqrt{t_0^2 + \frac{x^2}{v_{rms}^2}} - \sqrt{t_0^2 + \frac{x^2}{v_i^2}}. \quad (6)$$

The corrected event will appear at:

$$t_c(x) = t_0 + \sqrt{t_0^2 + \frac{x^2}{v_{rms}^2}} - \sqrt{t_0^2 + \frac{x^2}{v_i^2}}. \quad (7)$$

Applying a Taylor series to equation 6, one obtains:

$$t_c(x) = t_0 + \frac{x^2}{2t_0\, v_r^2} + \cdots, \quad (8)$$

where $\frac{1}{v_r^2} = \frac{1}{v_{rms}^2} - \frac{1}{v_i^2}$. Higher order terms in equation 7 are ignored if $\frac{x^2}{t_0^2 v_r^2}$<<1. With these observations, Hampson (1986) introduced the parabolic Radon transform (PRT):

$$u(\tau, p_P) = \int_{-\infty}^{\infty} d(t = \tau + p_P x^2, x)dx, \quad (9)$$

where $p_P = \frac{1}{2t_0\, v_r^2}$.

Ignoring anisotropy, primary reflections will be flattened if the interactive picking velocity v_i is correct ($v_i = v_{rms}$), while multiple reflections will be undercorrected parabola. Velocities that are too slow ($v_i < v_{rms}$) overcorrect hyperbolic events, while velocities that are too fast ($v_i > v_{rms}$) undercorrected hyperbolic events, both of which result in parabolic reflects.

Figure 5.3 shows a cartoon of a NMO-corrected (or time-migrated) CMP gathers and its parabolic Radon transform. The goal is to choose a velocity that provides a simple discrimination between faster primary and slower multiple events.

Least Squares Discrete Radon Transform

By combing equations 2, 4 and 9, the forward discrete Radon transform can be written as:

$$u(\tau, p) = \sum_x d(t = \tau + p\varphi(x), x). \quad (10)$$

In addition, the matrix form as:

$$\boldsymbol{u} = \boldsymbol{R^T d}, \quad (11)$$

where $\boldsymbol{T}$ indicates the matrix transpose. The reverse Radon transform from the tau-p domain to the time-space domain is:

$$d'(t, x) = \sum_p u(\tau = t - p\varphi(x), p), \quad (12)$$

as in form:

$$\boldsymbol{d'} = \boldsymbol{Ru}, \quad (13)$$

where $\boldsymbol{d'}$ is the modeled seismic data in time-space domain based on least squares method, $\boldsymbol{P}$ is the Radon transform operator, and $\boldsymbol{u}$ is the seismic data in tau-p domain.

Following Yilmaz (1989), the difference, $\boldsymbol{e}$, of the raw seismic data $d(t, x)$ and the modeled seismic data $d'(t, x)$ is:

$$\boldsymbol{e} = \boldsymbol{d} - \boldsymbol{Ru}, \quad (14)$$

where the cumulative squared error S can be written as:

$$S = \boldsymbol{e}^T \boldsymbol{e} = (\boldsymbol{d} - \boldsymbol{R}\boldsymbol{u})^{\boldsymbol{T}} (\boldsymbol{d} - \boldsymbol{R}\boldsymbol{u}). \quad (15)$$

By minimizing S, we obtain the least squares solution:

$$\boldsymbol{u} = (\boldsymbol{R}^T \boldsymbol{R})^{-\mathbf{1}} \boldsymbol{R}^T \boldsymbol{d}. \quad (16)$$

In order to keep the inversion of $\boldsymbol{R}^T \boldsymbol{R}$ stable, a minimum energy solution is often introduced to equation 16:

$$\boldsymbol{u} = (\boldsymbol{R}^T \boldsymbol{R} + \varepsilon \boldsymbol{I})^{-\mathbf{1}} \boldsymbol{R}^T \boldsymbol{d}, \quad (17)$$

where ε is an extreme small value, and $\boldsymbol{I}$ is identity matrix.

Artifacts of the Radon Transform

Aliasing

For seismic data, data aliasing is most commonly caused by coarse spatial sample. The Nyquist frequency, K_{ny}, of the seismic signal can be calculated by:

$$K_{ny} = \frac{2\pi}{2\Delta x}, \tag{18}$$

where Δx is the distance between traces.

If the sample rate, $\Delta x'$, is smaller than the Nyquist sample rate, Δx, the seismic signal can be reconstructed perfectly. In contrast, if $\Delta x' > \Delta x$, some of the original reflection signals will leak into the multiple domain, and treated as noise.

For the linear Radon transform, p is the slope of the linear reflection, which is related to both time and space axis. In order to avoid aliasing in the p axis in the tau-p domain, the sampling interval, Δp_L of p_L can be derived by (Turner, 1990):

$$\Delta p_L \leq \frac{1}{2(x_{max} - x_{min}) f_{max}}, \tag{20}$$

where x_{max} and x_{min} are the maximum and minimum offsets, respectively; and f_{max} is the maximum frequency of the signal in time-space domain.

For the velocity Radon transform, the sampling interval, Δp_H of p_H can be derived by:

$$\Delta p_H \leq \frac{1}{2(x_{max}^2 - x_{min}^2) f_{max}}, \tag{21}$$

For the parabolic Radon transform, the sampling interval, Δp_P of p_P can be derived by (Hugonnet and Canadas, 1995):

$$\Delta p_P \leq \frac{1}{2\sqrt{\left(x_{max}^2 - x_{min}^2 + z_{ref}^2\right) - z_{ref} f_{max}}}, \tag{22}$$

Transform Artifacts

Theoretically, a hyperbolic reflection in time-space domain should be transformed as a focused energy point in Radon domain. However, two artifacts after Radon transform can be detected: horizontal artifacts caused by near-offset truncation, and oblique artifacts caused by far-offset truncation (Kabir and Marfurt, 1999).

Figure 5.4a shows a CMP gathers with only one hyperbolic event in time-space domain. According to the velocity stack (Thorson and Claerbout, 1985), the hyperbolic event will be focused on an energy point shown in Figure 5.4b by green arrow. At the same time, both the near and far offset artifacts are also detected.

Each hyperbolic event can generate an energy point with two artifacts, while this phenomenon smears the energy distribution in Radon domain, making it hard to separate events, especially for the multiples' energy points from the primary energy points. Consequently, the conventional Radon transform's capability of attenuating multiples is greatly compromised.

Semblance-weighted Radon Transform

The transform artifacts have seriously weakened the function of Radon transform. While the energy still concentrates in the energy point rather than the artifacts. If we calculate the semblance in Radom domain:

$$S(\tau, p) = \frac{\sum_l [\sum_x d(t=\tau+p\varphi(x),x)]^2}{N_x \sum_l \sum_x d^2(t=\tau+p\varphi(x),x)}, \quad (23)$$

where l is the window size, and N_x is the number of seismic trace included in the semblance calculation.

For least squares discrete Radon transform, the semblance-weighted constraint in each iteration can be defined by an Ormsby filter:

$$w_S = \begin{cases} 0 & S \le s_1 or\ S \ge s_4 \\ 1 - 0.5 * (1 + cos(\pi(S - s_1)/(s_2 - s_1))) & s_1 \le S \le s_2 \\ 1 & s_2 \le S \le s_3 \\ 1 - 0.5 * (1 + cos(\pi(S - s_3)/(s_4 - s_3))) & s_3 \le S \le s_4 \end{cases}, \quad (24)$$

where s_1, s_2, s_3 and s_4 are corner values of the filter:

$$s_1 = \sigma_1 \gamma^n, \tag{24a}$$

$$s_2 = \sigma_2 \gamma^n, \tag{24b}$$

$$s_3 = 1.01, \tag{24c}$$

$$s_4 = 1.01, \tag{24d}$$

where σ_1 and σ_2 are the first and second points to pass high values of semblance, respectively, γ is the fractional values, and n is the number of iteration.

Orange arrows in time-space domain in Figure 5.5a are primary reflections, white arrows are multiples and the yellow arrow is the linear head wave reflection. The relevant focused energy is displayed in tau-p domain in Figure 5.5b, using least squares discrete velocity Radon transform. The multiples are close to the nearby primary reflections, while the existence of the near- and far-offset artifacts and aliasing (red arrows) makes them difficult to separate.

The semblance in Radon transform in Figure 5.6a can be calculated based on equation 23, and the semblance-weighted constraint is displayed in Figure 5.6. Figure 5.6c is the seismic profile in tau-p domain, using semblance-weighted least squares discrete velocity Radon transform, which is the product of Figure 5.5b and Figure 5.6b. The application of the semblance-weighted constraint effectively suppresses the transform artifacts and the aliasing of Figure 5.5b.

Wavelet-Based Radon Transform

Matching pursuit method has been widely used in spectral decomposition (Y. Wang, 2006, 2010), NMO correction (B. Zhang et al, 2013), and impedance estimation (Wen et al., 2015), all of which have inspired me to apply it to wavelet-based Radon transform.

Ricker wavelet or Morlet wavelet have been pre-computed at the beginning. We assume that a seismic trace can be decomposed into a suite of wavelets with certain amplitude, frequency and phase. The input seismic data, $d(t,x)$, is a common shot gather. By calculating the instantaneous envelope and frequency through Hilbert transform and setting a threshold, we can pick several envelope peaks above the threshold. For each picked peaks with known frequency, we can approximate its amplitude and phase using relevant wavelet using the least squares algorithm, to fit the instantaneous envelope. In this way, we can best describe the envelope peaks using the constructed wavelet with minimum error, and then convert each constructed wavelet using Radon transform. After that, we subtract the constructed wavelets of last picked peaks and loop the iteration. Once the residual energy reaches a user-defined value or a maximum number of iteration has reached, the wavelet Radon transform is perfectly executed for the final results.

In order to better illustrate the theory of wavelet-based Radon transform workflow in Figure 5.7, a seismic profile with only one live trace (the 100th trace) is introduced in Figure 5.8, which is plotted by wiggle in Figure 5.9a. White arrows indicate the reflections in the time-space domain. The different iteration residual traces are shown in Figures 5.9b-d, and the relevant reconstructed traces are shown in Figures 5.10 a-c. We can see that after third iteration, the residual trace is extremely small and can be considered below the noise level, and most of the useful signals are transformed to the tau-p domain. Each point in time-space domain is transformed as a straight line in tau-p domain.

Figure 5.11a indicates a seismic profile with five live traces in time-space domain, and five points on five seismic traces are shown by white arrows in Figure 5.11a and a focused energy point is generated by the five straight lines indicated by white arrows in Figure 5.11b. For the whole seismic profile in Figure 5.5a, the wavelet-based Radom transform is displayed in Figure 5.12. The aliasing is perfectly removed compared with Figure 5.5b. The multiples can be more easily separated from primary reflections as well, even though the transform artifacts are still obvious.

Generally, we need several steps to implement multiple suppression using wavelet-based Radon transform:

1. Data conditioning of CMP gathers (AASPI: sof_prestack);
2. Wavelet-based Radon transform (AASPI: anti_alias_drt_mp);

3. Pick polygons that include strong, coherent multiples, which are located at larger values of p (AASPI: aaspi_plot);
4. Reserve the data inside polygons and perform reverse Radon transform to simulate multiples (AASPI: anti_alias_drt_mp);
5. Subtract multiples of step 4 from CMP gathers to get filtered data (primaries) and loop to step 1.

SYNTHETIC ANALYSIS

In order to test the wavelet-based Radon transform, a layered horizontal model (Figure 5.13) with a high velocity interbed zone (Table 5.1) is created. The source and receiver spacing are defined as 50m and 10 m, respectively, and a 50 Hz Ricker wavelet is chosen in the model (Table 5.2). The existence of the high velocity interbed will generate interbed multiples indicated by white arrows in Figures 5.14a and b. The weight function is applied before the calculation of Radon transform.

Figures 5.14a and b indicate the seismic profile of the shot gather before and after NMO-correction, respectively of the layered horizontal model in Figure 5.13. Orange arrows give the primary reflections and multiples are shown by white arrows. The conventional velocity transform results of Figure 5.14a is shown in Figure 5.15a, the primary reflections (orange arrows) and multiples (white arrows) are concentrated on the energy points in Figure 5.15a. The black arrows indicate the aliasing artifacts. The wavelet-based velocity transform results in clearer imaging in tau-p domain and the aliasing is suppressed. Semi-transparent red shadows cover the multiples energy concentration, and are modeled using conventional and wavelet-based velocity transform as shown in Figure 5.16. The multiples are suppressed by subtracting the modeled ones (in Figure 5.16) from the original reflections in time-space domain (Figure 5.17). More multiples are suppressed by the application of the wavelet-based method, compared with the conventional velocity transform.

The NMO correction is applied and mute is applied in Figure 5.14b to avoid NMO stretching. The primary reflections have been flattened and the stretched zone has been muted, while the multiples exhibit parabolic events in the seismic gather due to the under-correction. The energy of the primary reflections (flatten events) will be transformed to the focused energy point near the p = 0, and the multiples will be focused on the relative large p value ($p \gg 0$). By eliminating aliasing, we define the sampling interval of p, Δp according to equations 21-23 for both conventional and wavelet-based Radon transform.

Figures 5.18a and b indicate the conventional and wavelet-based parabolic forward Radon transform of Figure 5.14b, respectively. The primary reflections are focused on the p values approaching zero, and the multiples are adjacent to the relevant primary waves and characterized as relative large p values. We can find some aliasing pointed by red arrows from the conventional Radon transform, while the result of the wavelet Radon transform is clearer and aliasing is almost smeared.

The semi-transparent red shadow zone depicts the distribution of the multiples. By reversing Radon transform to module multiples, we find the parabolic events are removed in Figure 5.20. The white arrows in Figure 5.20a indicate the residual multiples, which have been better suppressed in Figure 5.20b. The far-offset zone of the flattened primary reflections is scattered in Figure 5.16a, while they are converged better compared with the one in Figure 5.16b.

APPLICATION

Figure 5.21 indicates one CMP gather after muted NMO-correction. The survey is acquired in Jeju Basin, Korean. The marine seismic data always suffer from the multiples in the seismic processing workflow. NMO-correction has been applied and the primary reflections are almost flattened. While the multiples shown by white arrows behave under-corrected, which seriously damage the data quality.

Conventional and wavelet-based parabolic forward Radon transform are performed and shown in Figures 5.22a and b. White arrows indicate multiples being described as parabolic events in Figure 5.21, and are characterized by larger p values. The zoomed in sections of Figures 5.22a and b clearly prove the higher resolution and less aliasing (red arrows) in Figure 23b compared with the one in Figure 23a. The semi-transparent red shadow zone indicates the multiples zone, which is reserved and modeled in Figure 5.24. The filtered data in Figure 5.25 is created after the subtraction of modeled multiples; the seismic reflections are flattened batter in Figure 5.25b than that in Figure 5.25a.

CONCLUSIONS

Radon transform is an effective way to suppress multiple reflections in exploration seismology. Many methods have been developed to solve the resolution problem of Radon transform, and the matching pursuit algorithm, which has been well used in spectral decomposition, NMO correction, etc., is successfully applied to de-multiple processing.

The primary reflections are flattened by accurate velocity, while the multiples remain under correction due to lower velocity. The energy of the flattened reflections after NMO-correction will be focused on the p values approaching zero in tau-p domain, while the multiples are still characterized as the positive p values, which makes it possible to separate the multiples from the primary reflections.

The application of the wavelet-based Radon transform opens another door for multiple suppression, which more effectively removes the multiples compared with the conventional least squares discrete Radon transform.

ACKNOWLEDGEMENTS

We thank KIGAM for the use of their Jeju Basin data set. Numerical model was generated using Tesseral's Tesseral 2D software. Seismic displays were generated used Schlumberger's Petrel software. We also thank the sponsors of Attribute-Assisted Seismic Processing and Interpretation Consortium (AASPI) for their guidance and financial support.

CHAPTER 5 FIGURES

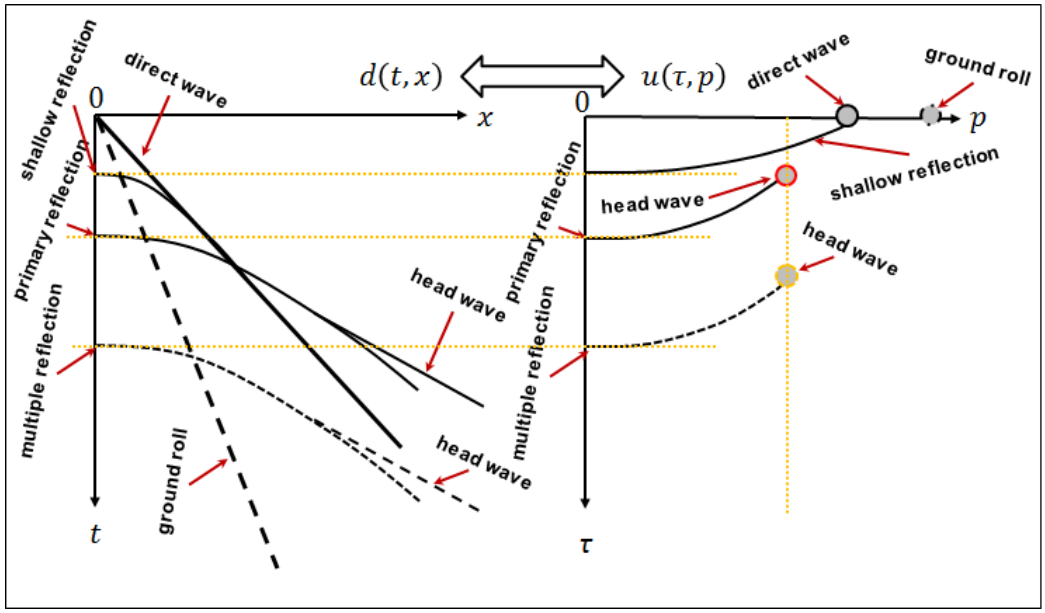

Figure 5.1. Cartoon of events in a seismic shot gather of a horizontally layered model and its resulting linear-moveout Radon transform. Note the ground roll have the slowest moveout (largest slowness p) followed by the direct p-wave.

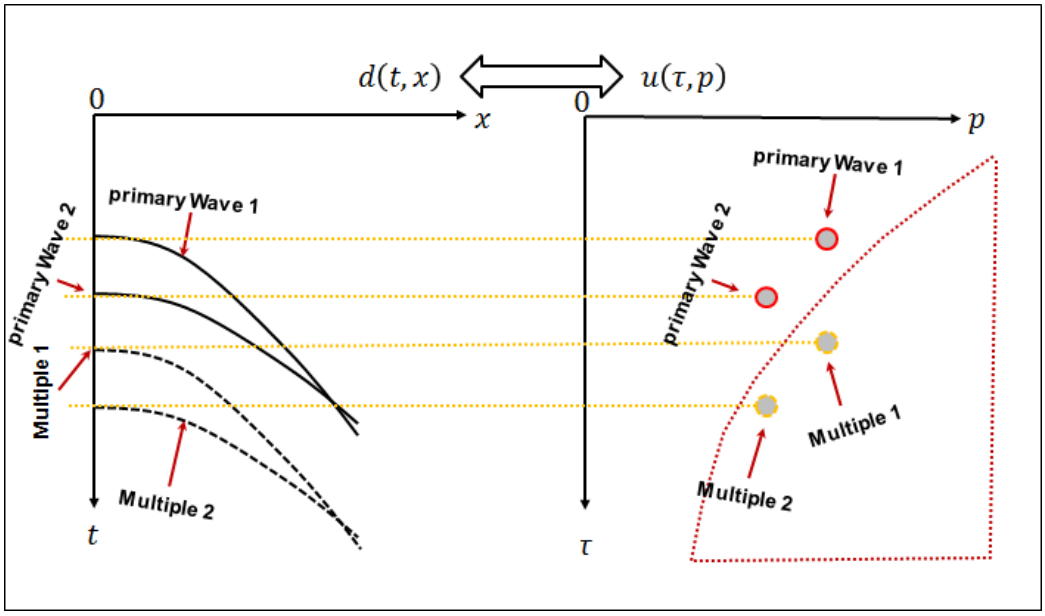

Figure 5.2. Cartoon of events in a seismic shot gather of a horizontally layered model and its resulting hyperbolic-moveout Radon Transform.

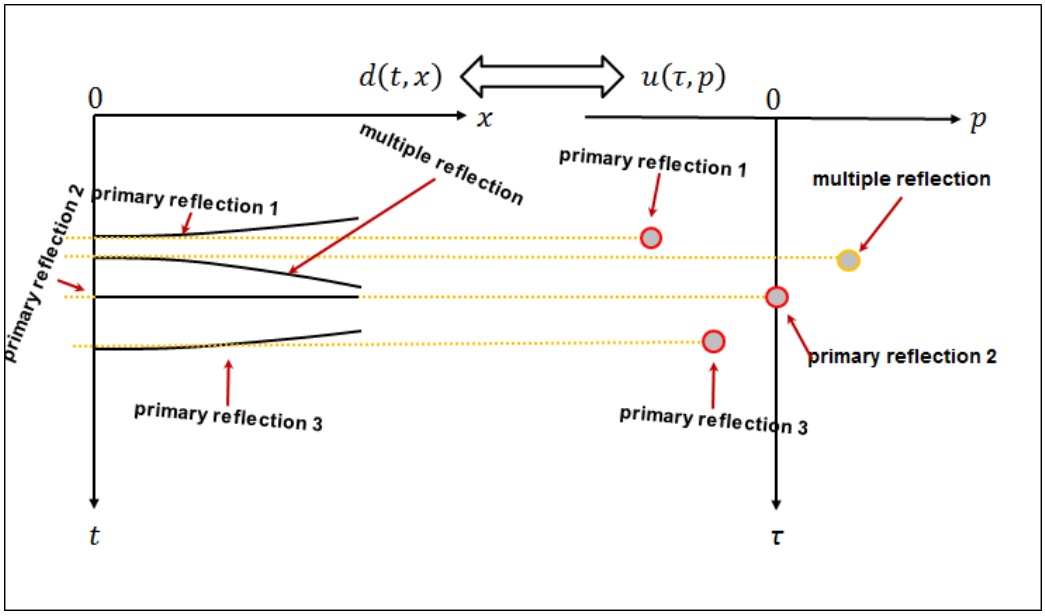

Figure 5.3. Cartoon of events in a seismic gather after NMO correction of a horizontally layered model and its resulting parabolic-moveout Radon Transform. In general, primary reflection events are flattened, or alternatively overcorrected, while multiple are undercorrected. The application of the parabolic NMO correction results in residual moveout that is approximately parabolic.

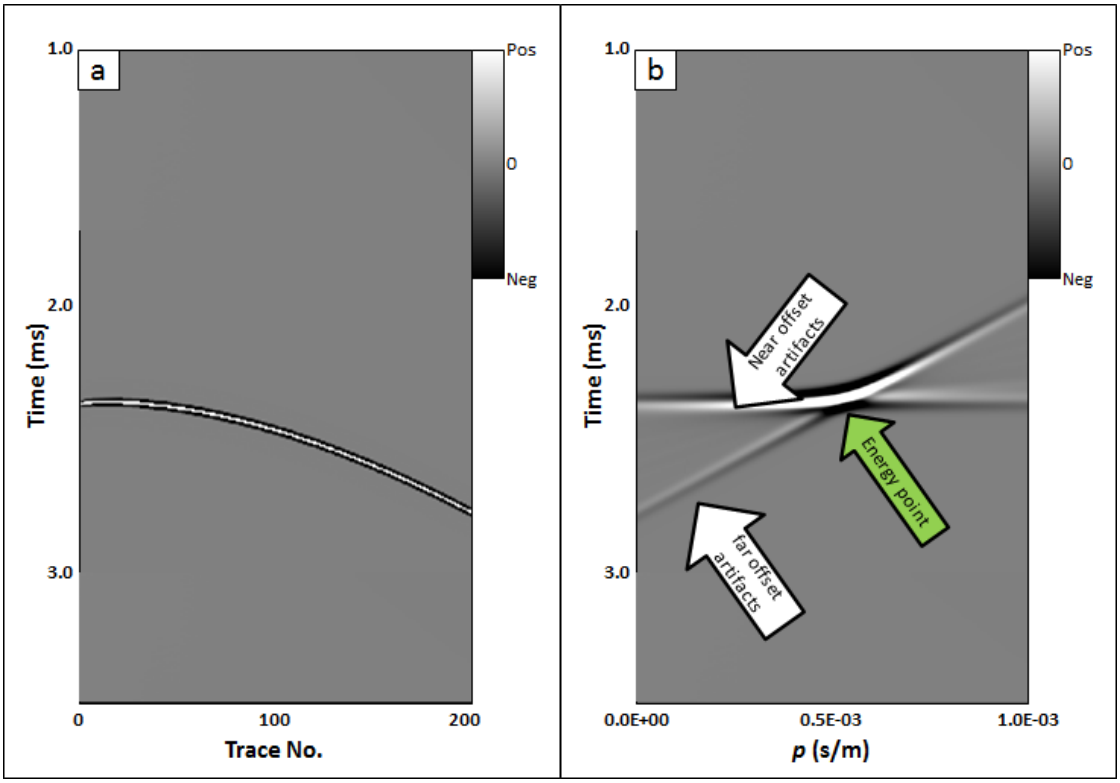

Figure 5.4. A seismic gather with a single hyperbolic event in (a) time-space domain and (b) tau-p domain using a least squares discrete velocity Radon transform. The green arrow indicates the focused energy of the hyperbolic event of Figure 5.4a; white arrows indicate near- and far-offset artifacts described by Kabir and Marfurt (1999).

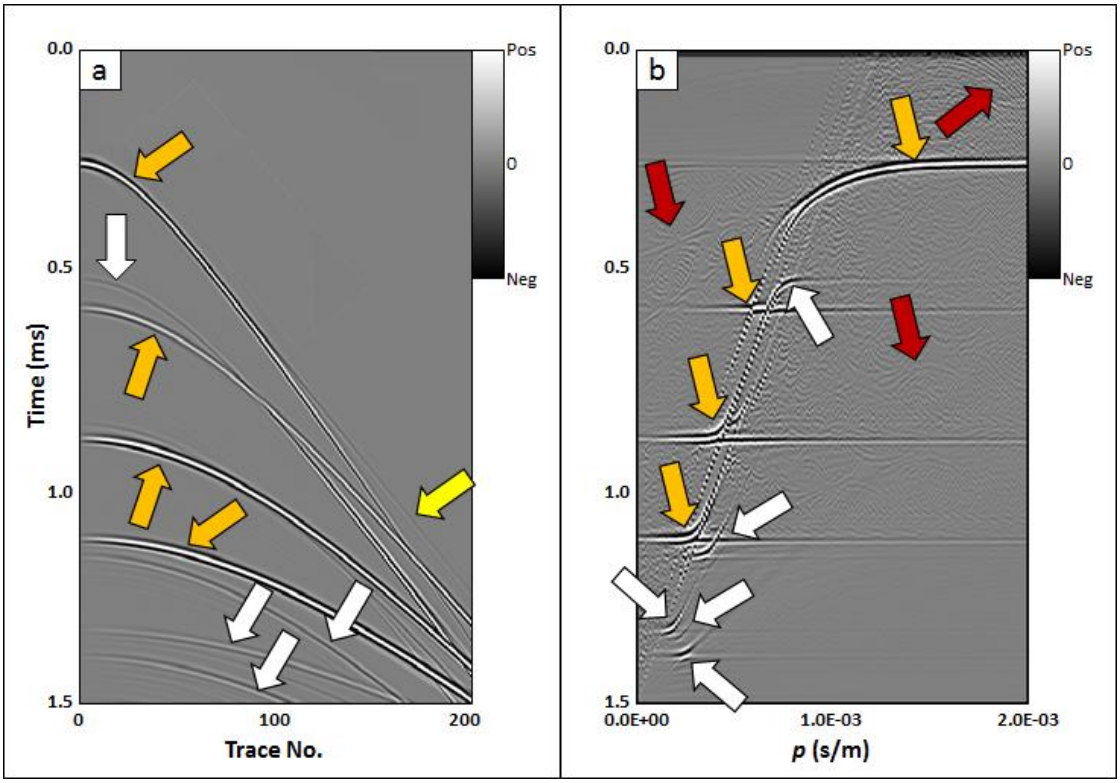

Figure 5.5. (a) A seismic gather and (b) its tau-p transform using a least squares discrete velocity Radon transform. Orange arrows indicate primary reflections, white arrows indicate multiples, and red arrows indicate aliasing artifacts.

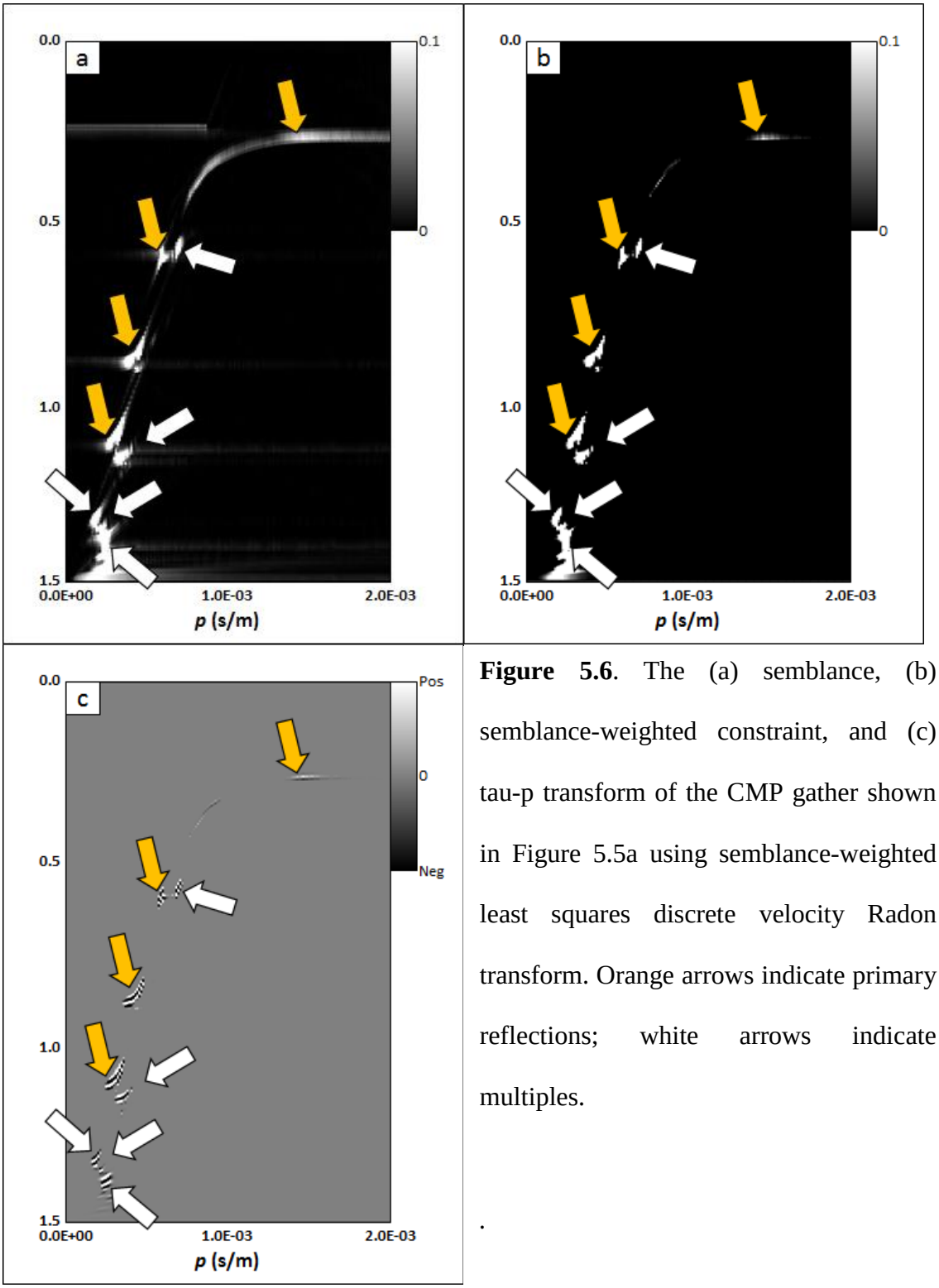

Figure 5.6. The (a) semblance, (b) semblance-weighted constraint, and (c) tau-p transform of the CMP gather shown in Figure 5.5a using semblance-weighted least squares discrete velocity Radon transform. Orange arrows indicate primary reflections; white arrows indicate multiples.

.

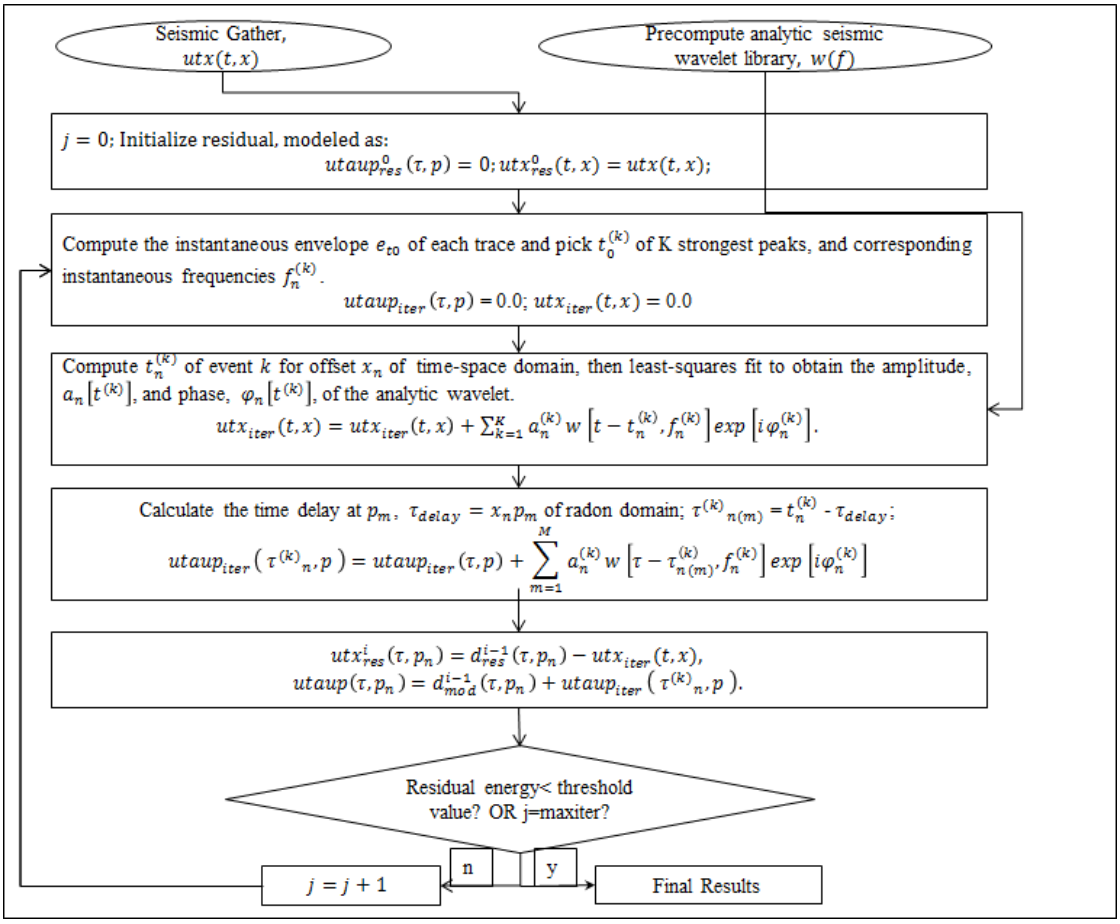

Figure 5.7. The flowchart for wavelet-based Radon transform.

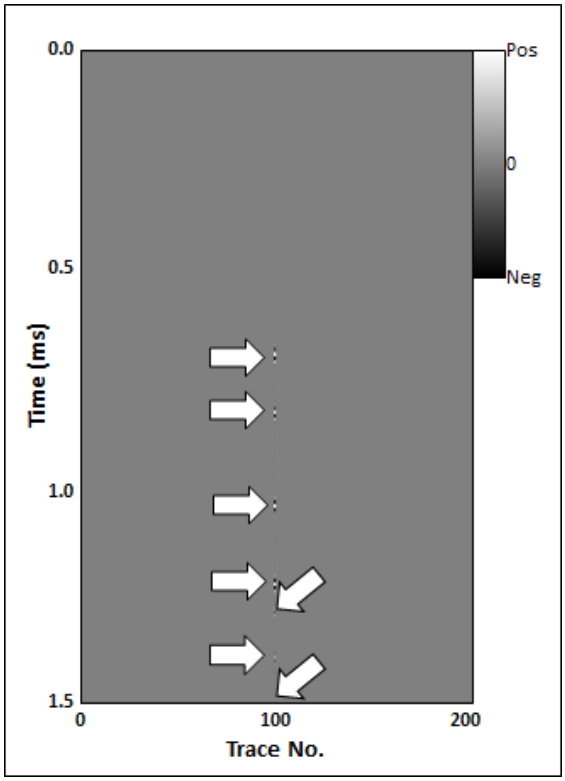

Figure 5.8. The seismic CMP gather shown in Figure 5.5a where only trace 100 is alive. White arrows indicate the reflections in the time-space domain.

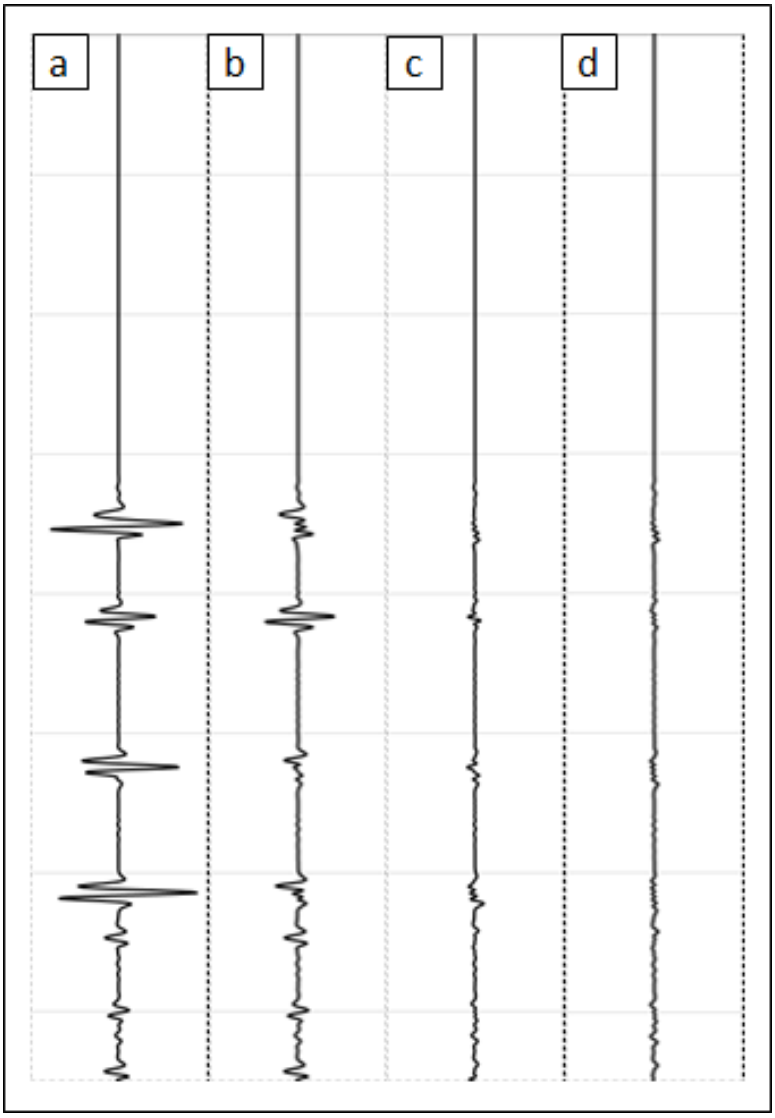

Figure 5.9. (a) Trace no. 100 from the gather shown in Figure 5.5a and (b-d) its Residual traces after 1, 2, and 3 matching pursuit iterations.

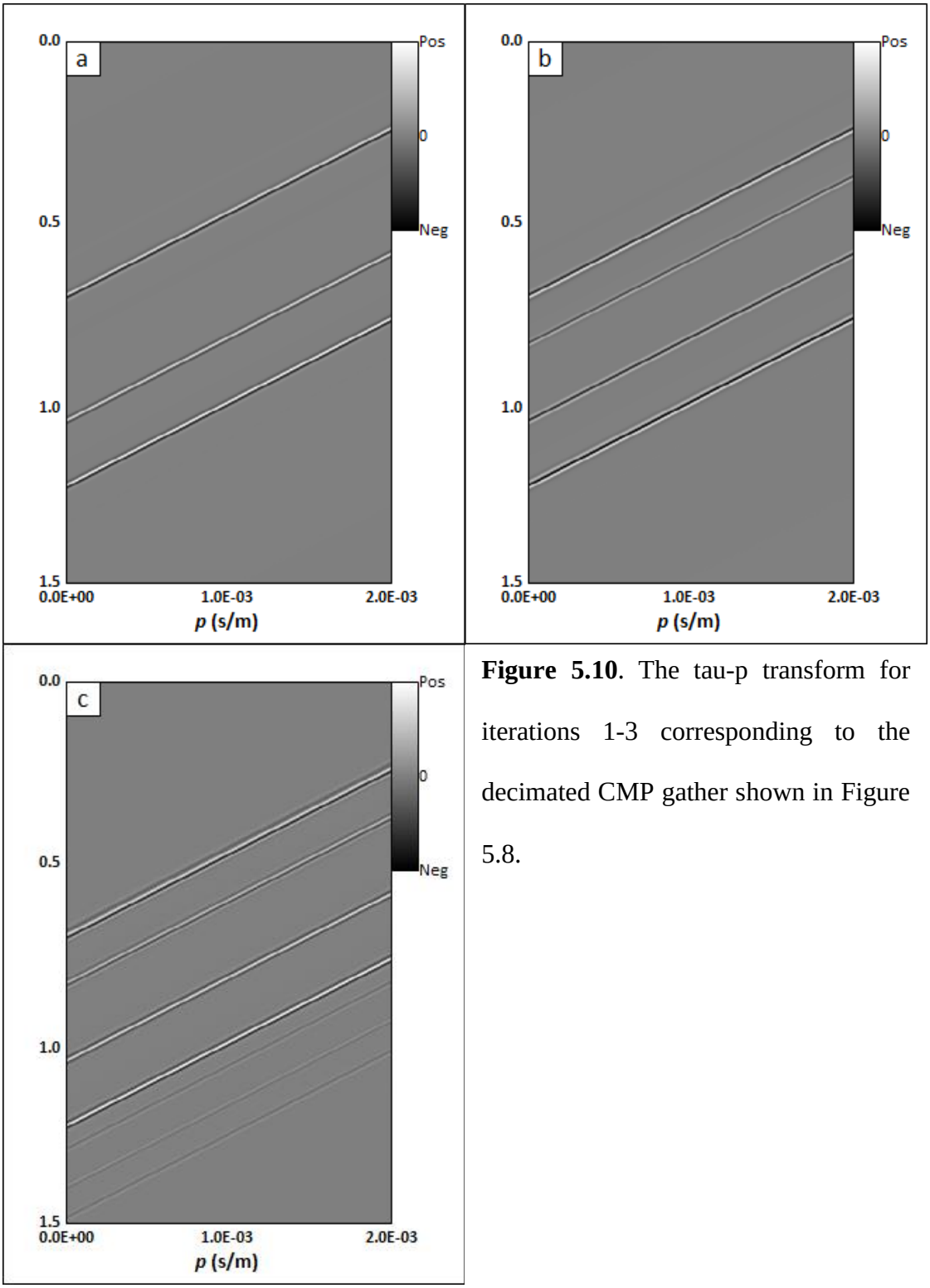

Figure 5.10. The tau-p transform for iterations 1-3 corresponding to the decimated CMP gather shown in Figure 5.8.

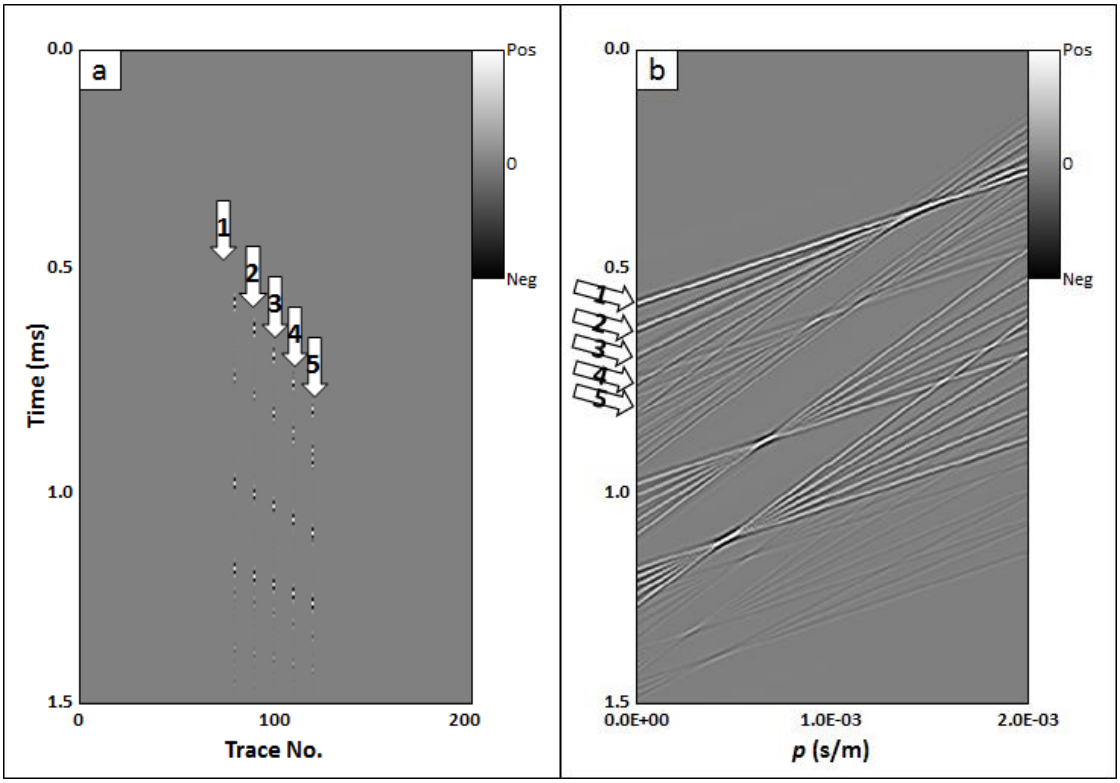

Figure 5.11. (a) The seismic CMP gathers of Figure 5.5a with five live traces, and (b) its tau-p transform. White arrows indicate five points on five seismic traces.

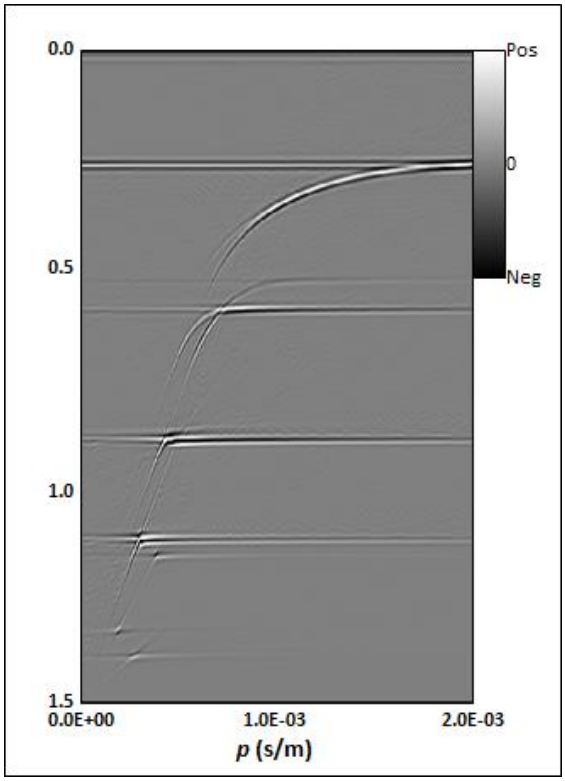

Figure 5.12. The tau-p transform of the CMP gather shown in Figure 5.5a constructed using a wavelet-based Radon transform. Note that the aliasing seen in figure 5.5b is reduced.

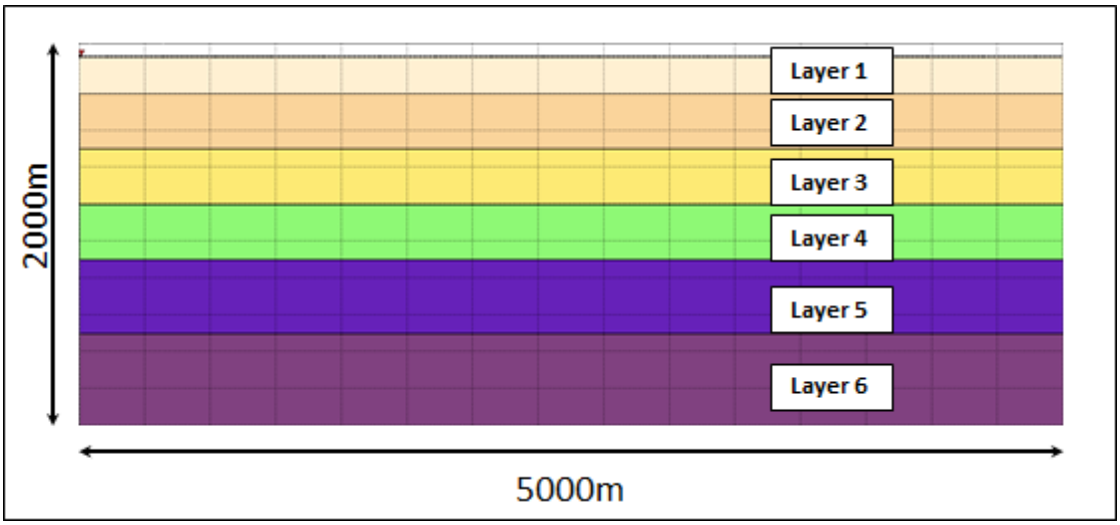

Figure 5.13. The diagram of the horizontally layered model.

Layer	1	2	3	4	5	6
V_P (m/s)	1500	2500	2000	2600	3800	4100
V_S (m/s)	700	1400	1000	1200	1900	2100
$\rho(\mathbf{g/cm^3})$	2.65	2.65	2.65	2.65	2.65	2.65
d (m)	200	500	800	1100	1480	Unlimited

Table 5.1. Elastic parameters of the horizontally layered model in Figure 5.13.

Wavelet	50Hz, Ricker
Source Spacing	50 m
Receiver Spacing	10 m
Sampling	2ms

Table 5.2. Geometry parameters of the horizontally layered model in Figure 5.13.

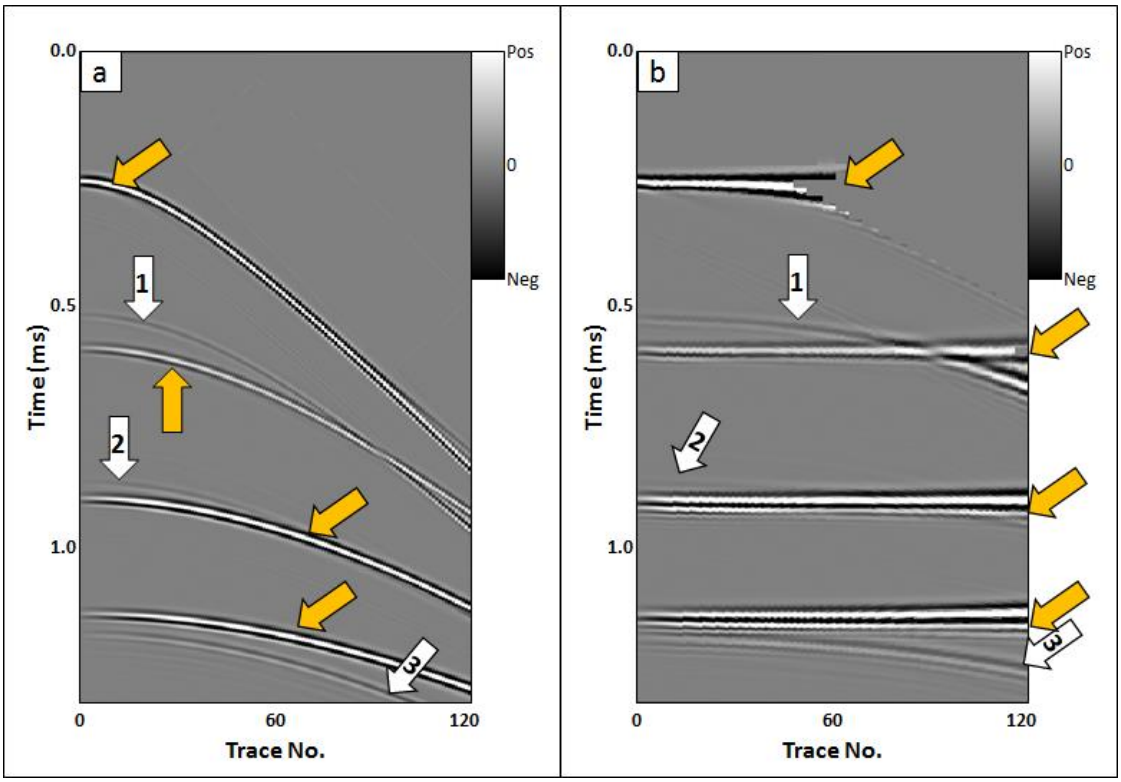

Figure 5.14. The CMP gather from Figure 5.13 (a) before and (b) after NMO-correction. The mute is applied in Figure 5.14b to avoid excessive NMO stretch. Orange arrows indicate primary reflections; white arrows multiples.

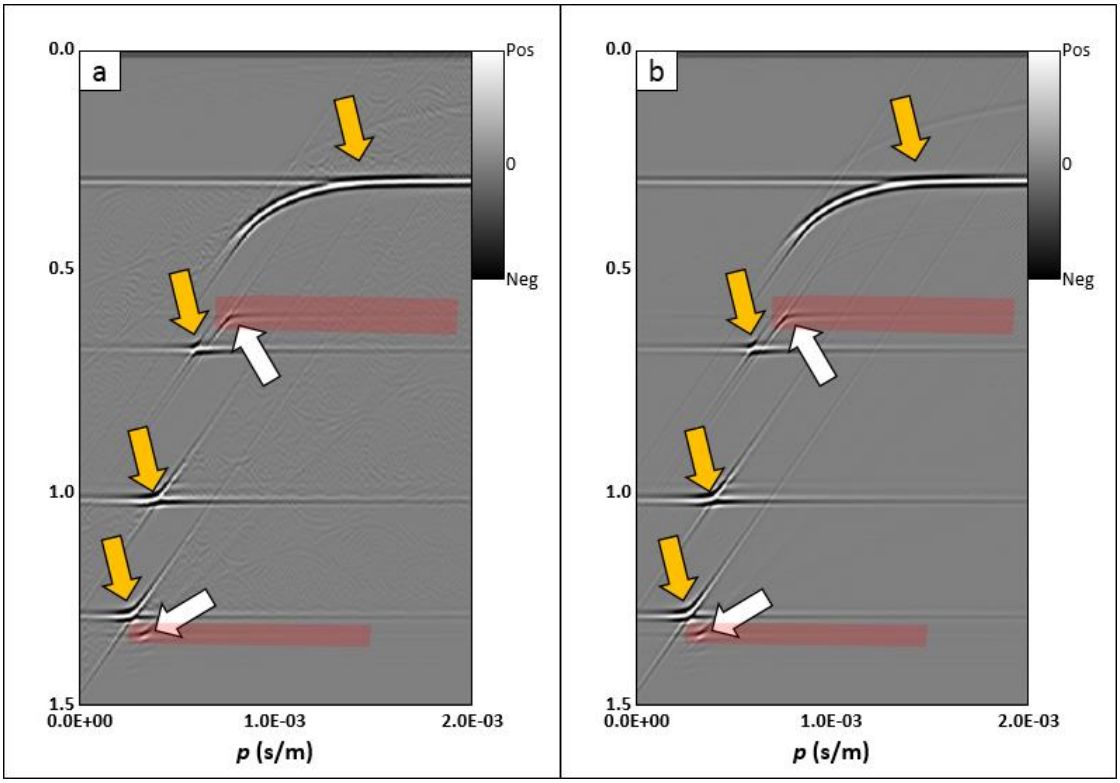

Figure 5.15. (a) Conventional and (b) wavelet-based forward velocity transform of the CMP gather shown in Figure 5.14a. Orange arrows indicate primary reflections, white arrows indicate multiples, the red polygon indicates the mute zone, and red arrows indicate the aliasing artifacts.

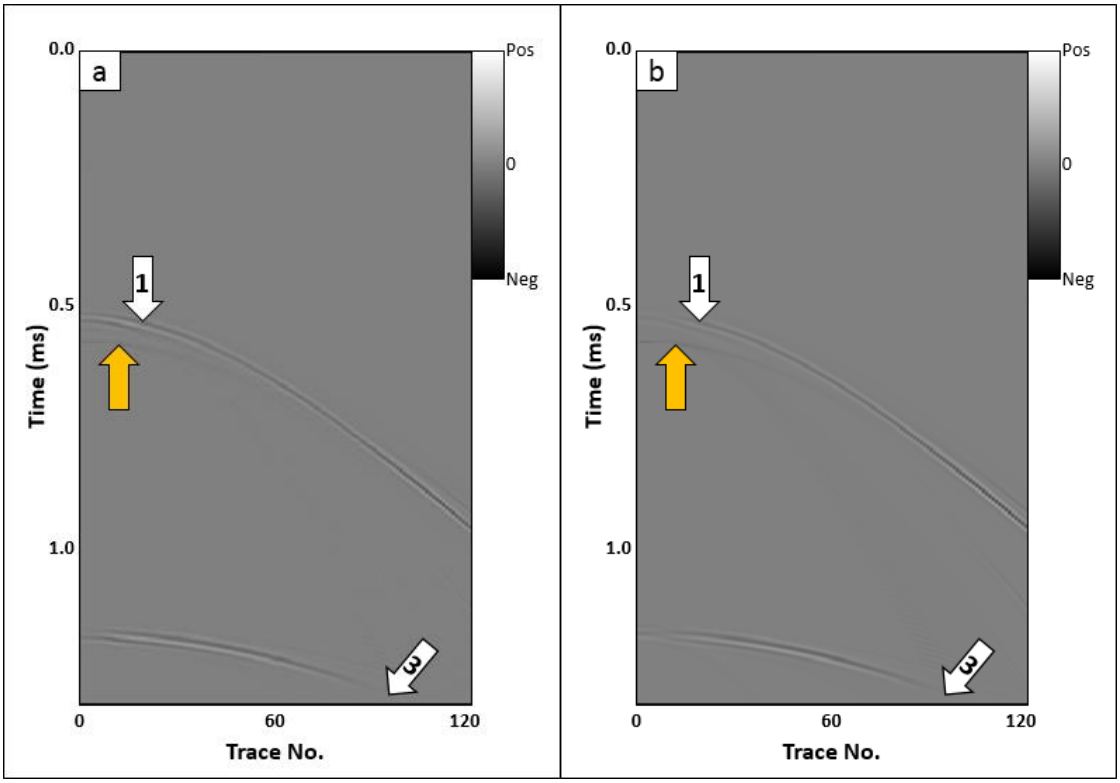

Figure 5.16. Modeled multiples using (a) Conventional and (b) wavelet-based velocity transform of the CMP gather shown in Figure 5.14a. Orange arrows indicate primary reflections, white arrows indicate multiples.

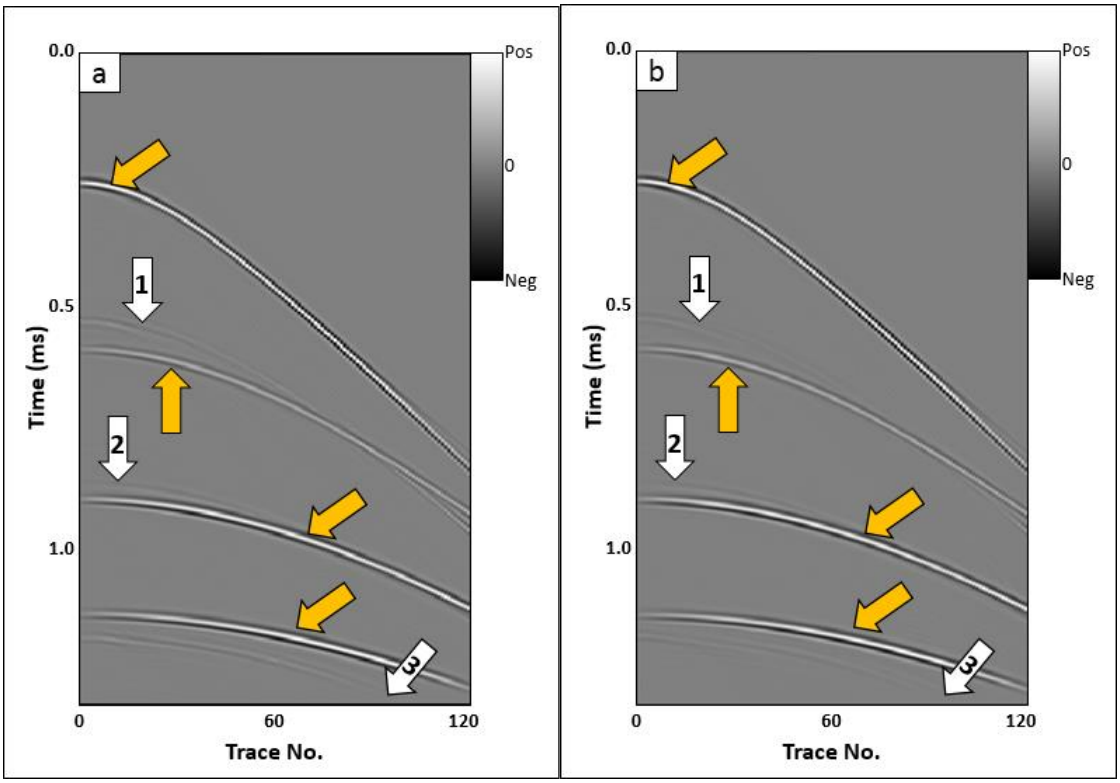

Figure 5.17. Filtered data using (a) Conventional and (b) wavelet-based velocity transform of the CMP gather shown in Figure 5.14a. Orange arrows indicate primary reflections, white arrows indicate multiples.

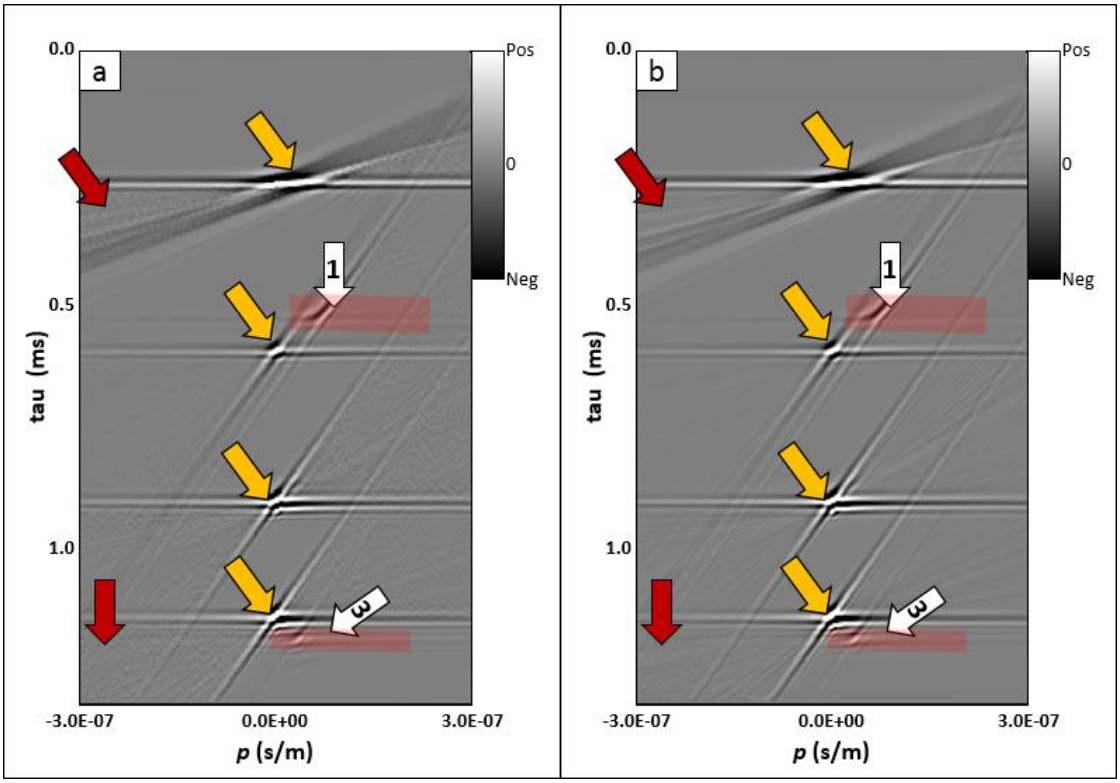

Figure 5.18. (a) Conventional and (b) wavelet-based parabolic forward Radon transform of the NMO-corrected gather shown in Figure 5.14b. Orange arrows indicate primary reflections, white arrows indicate multiples, the red polygon indicates the mute zone, and red arrows indicate the aliasing artifacts.

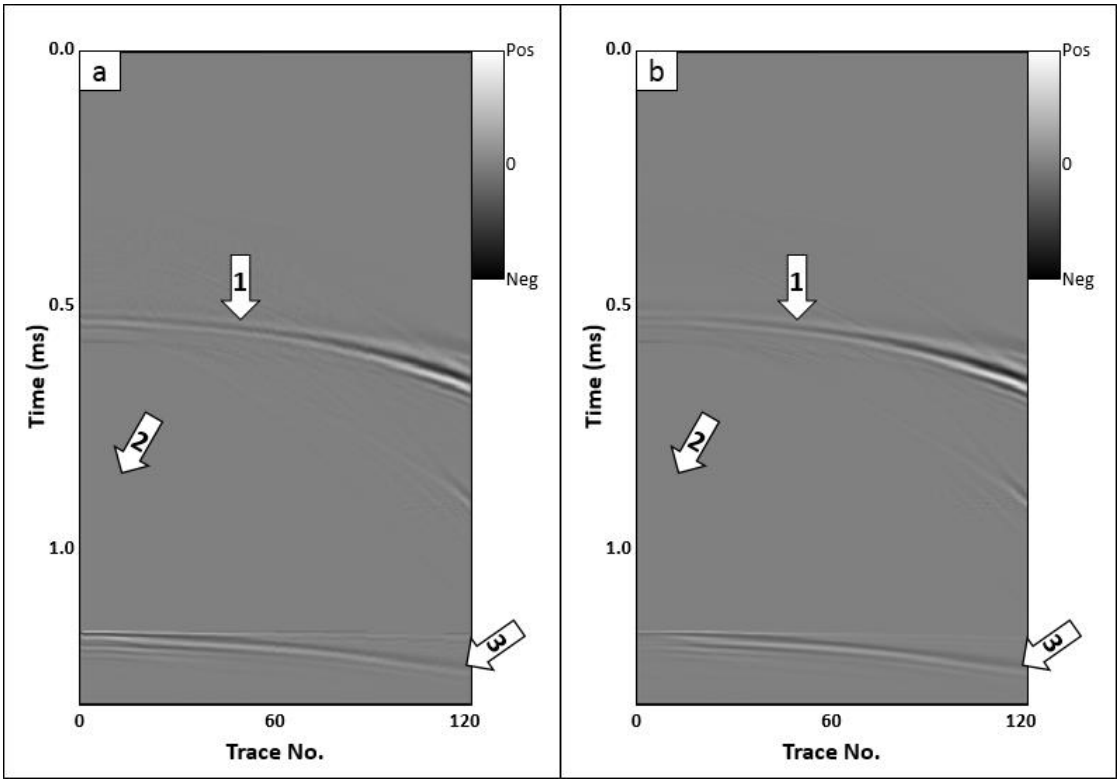

Figure 5.19. Modeled multiples using (a) Conventional and (b) wavelet-based parabolic transform of the NMO-corrected gather shown in Figure 5.14a. Orange arrows indicate primary reflections, white arrows indicate multiples.

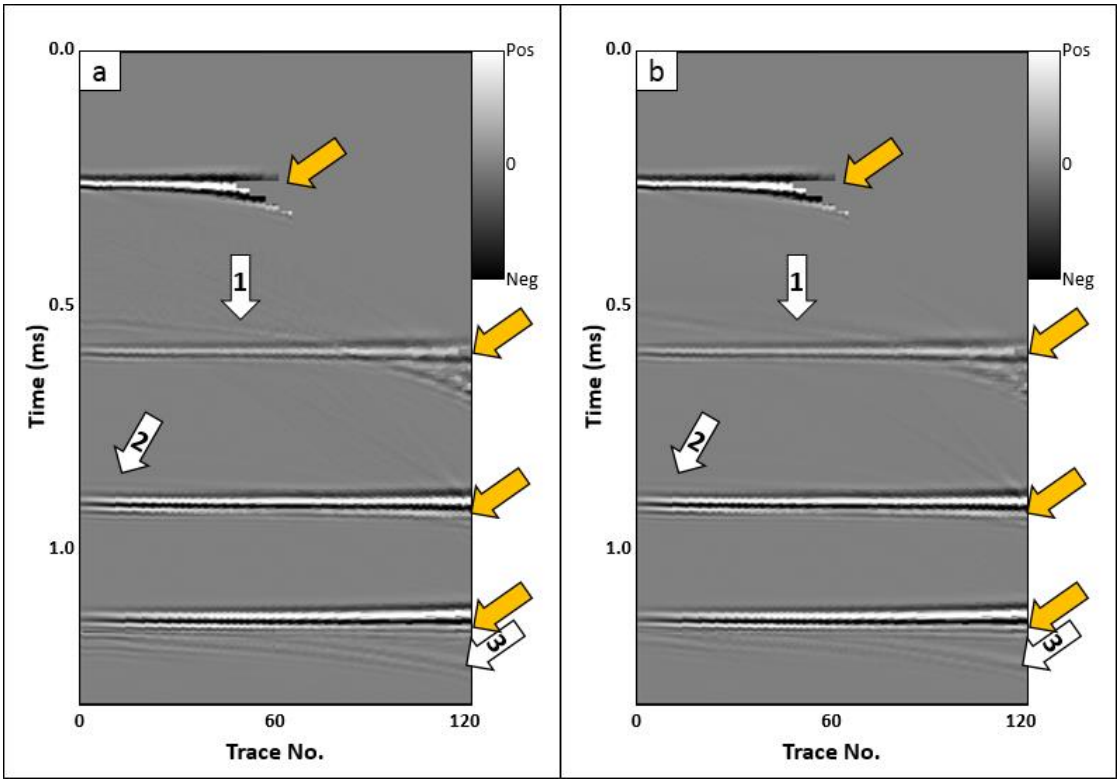

Figure 5.20. Filtered data using (a) Conventional and (b) wavelet-based parabolic transform of the NMO-corrected gather shown in Figure 5.14a. Orange arrows indicate primary reflections, white arrows indicate multiples.

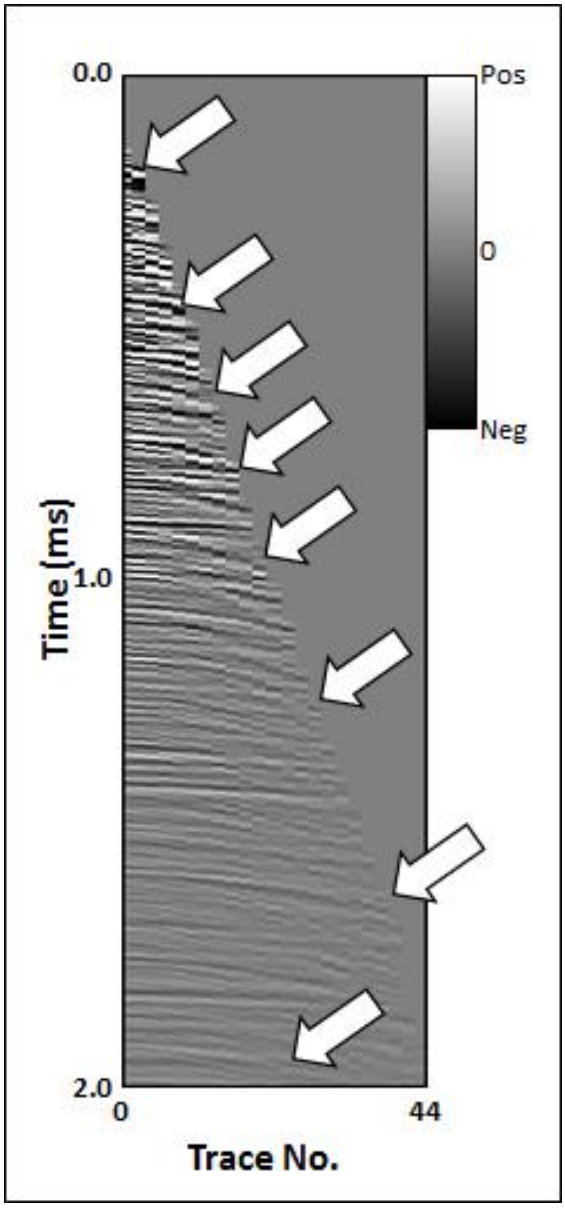

Figure 5.21. The CMP gather after NMO-correction. White arrows indicate multiples that appear described as hyperbolic events.

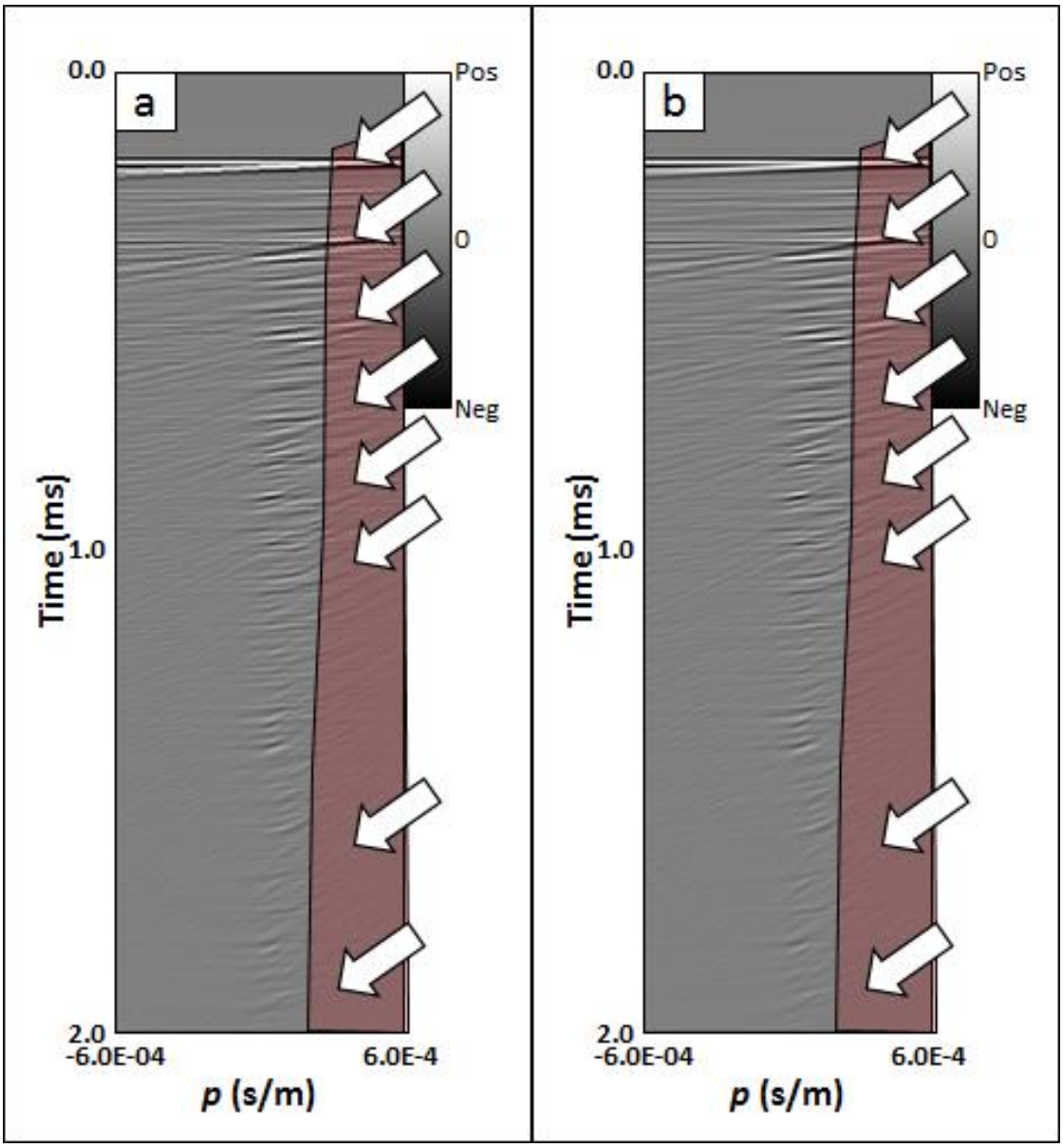

Figure 5.22. (a) Conventional and (b) wavelet-based parabolic forward Radon transform of Figure 5.21. White arrows indicate multiples being described as parabolic events.

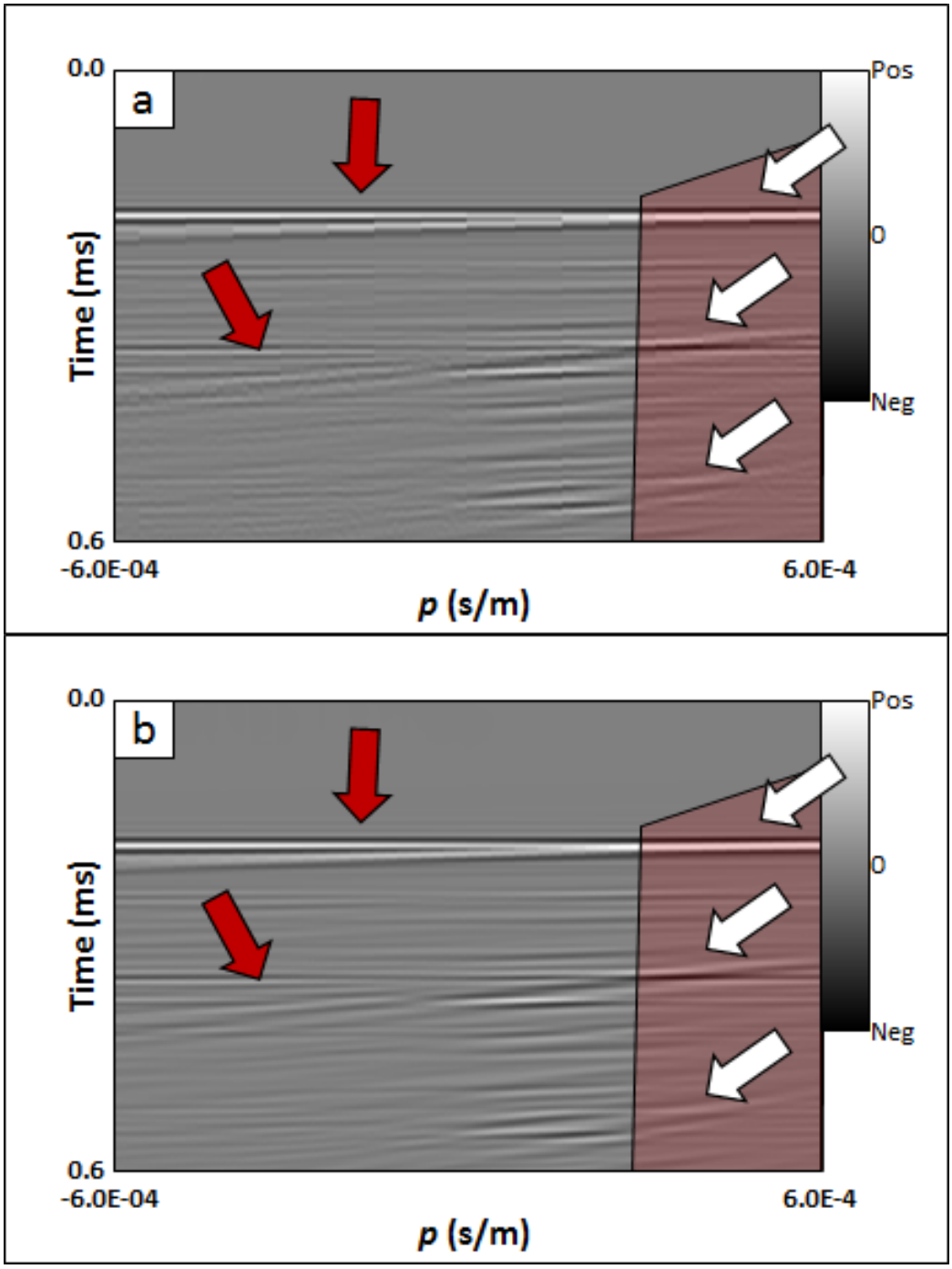

Figure 5.23. Zoomed in sections of (a) conventional and (b) wavelet-based parabolic forward Radon transform of Figure 5.21. White arrows indicate multiples being described as parabolic events, and the aliasing are shown by red arrows.

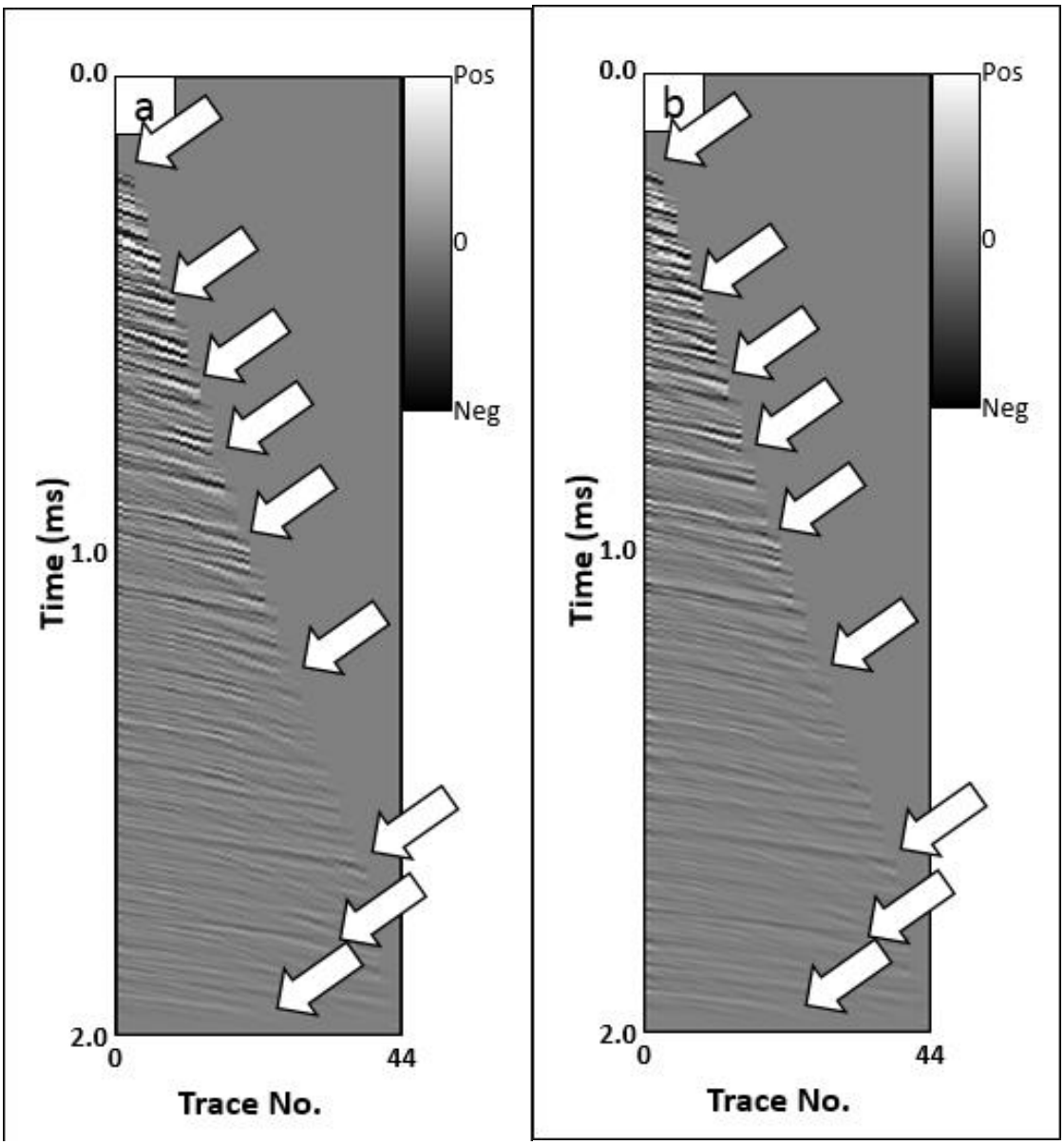

Figure 5.24. Modeled multiples using (a) Conventional and (b) wavelet-based parabolic transform of the NMO-corrected gather shown in Figure 5.21. White arrows indicate multiples.

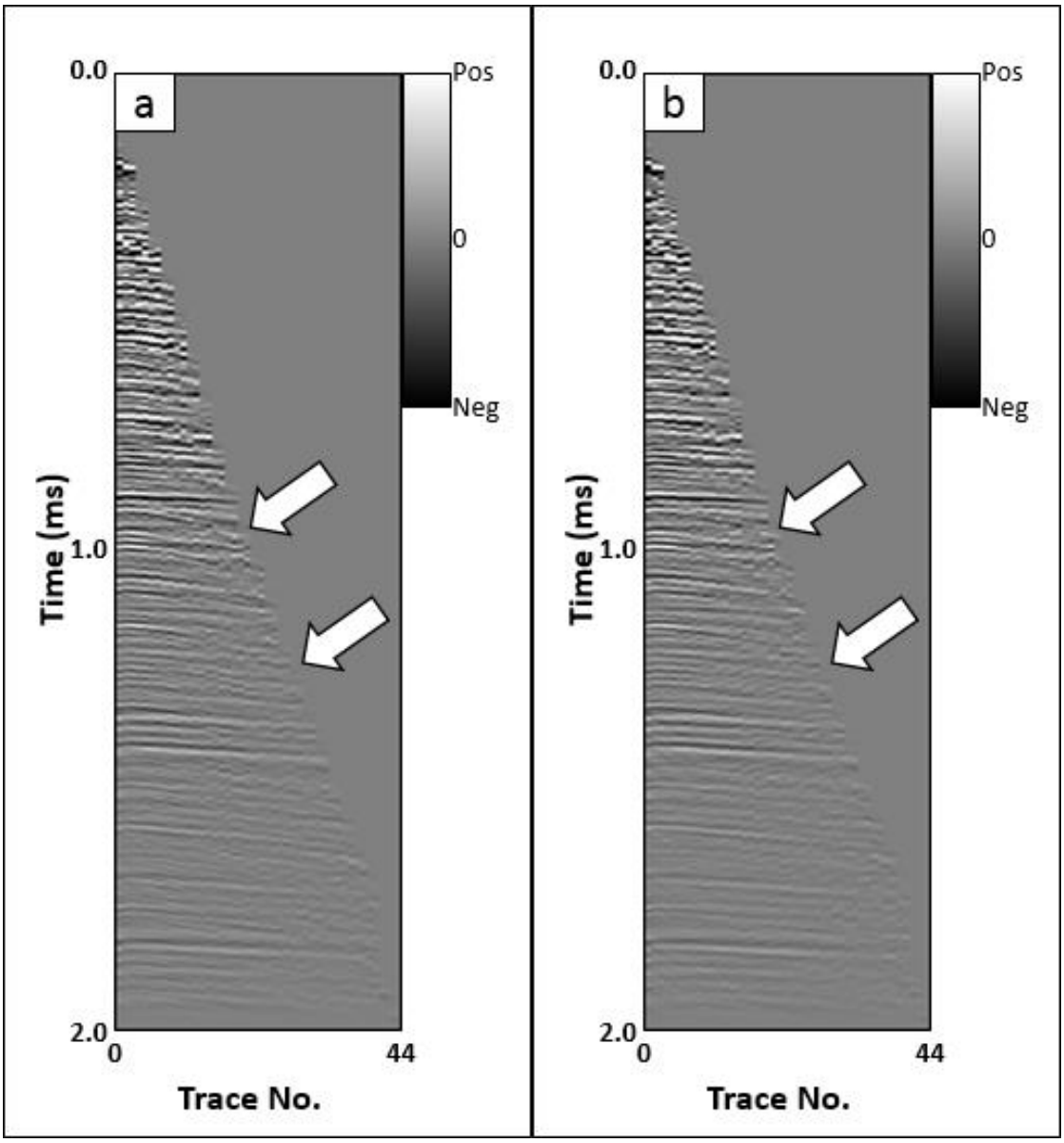

Figure 5.25. Filtered data using (a) Conventional and (b) wavelet-based parabolic transform of the NMO-corrected gather shown in Figure 5.21a. White arrows indicate residual multiples.

REFERENCES

Dao T., and K. J. Marfurt, 2013, Seismic data decomposition using singular points with a Matching Pursuit scheme: 83th Annual International Meeting, SEG, Expanded Abstracts, 4397-4401.

Hampson D., 1986, Inverse velocity stacking for multiple estimation: Journal of the Canadian Society of Exploration Geophysicists, **22** (1), 44-55.

Hugonnet P. and Canadas G. 1995. Aliasing in the parabolic Radon transform. 65th SEG meeting, Houston, USA, Expanded Abstracts, 1366-1369.

Liu J., and K. J. Marfurt, 2005, Matching Pursuit decomposition using Morlet wavelets: 75th Annual International Meeting, SEG, Expanded Abstracts, 786-789.

Mallat S. G., and Z. Zhang, 1993, Matching Pursuits with time-frequency dictionaries: IEEE Transactions on Signal Processing, **41**(12), 3397–3415.

Ng, M., and M. Perez, 2004, High resolution Radon transform in the t-x domain using "intelligent" prioritization of the Gauss-Seidel estimation sequence: 74th Annual International Meeting, SEG, Expanded Abstracts, 2160-2163.

Russell B., D. Hampson, and J. Chun, 1990a, Noise elimination and the Radon transform, part 1: The Leading Edge, **9**(10), 18-23.

Russell B., D. Hampson, and J. Chun, 1990b, Noise elimination and the Radon transform, part 2: The Leading Edge, **9**(11), 31-37.

Sacchi M. D, and T. J. Ulrych, 1995, High resolution velocity gathers and offset space reconstruction: Geophysics, **60**(4), 1169-1177.

Stoffa, P. L., P. Buhl, J. B. Diebold, and F. Wenzel, 1981, Direct mapping of seismic data to the domain of intercept time and ray parameter - A plane-wave decomposition: Geophysics, **46**(3), 255-267.

Turner, G., 1990, Aliasing in the tau-p transform and the removal of spatially aliased coherent noise: Geophysics, **55**, 1496-1503.

Thorson J. R., and J. F. Claerbout, 1985, Velocity-stack and slant-stack stochastic inversion: Geophysics, **50**(12), 2727-2741.

Wang B., and K. Pann, 1996, Kirchhoff migration of seismic data compressed by Matching Pursuit decomposition: 66th Annual International Meeting, SEG, Expanded Abstracts, 1642-1645.

Wang Y., 2006, Seismic time-frequency spectral decomposition by Matching Pursuit: Geophysics, **72**(1), 13-20.

Wang Y., 2010, Multichannel Matching Pursuit for seismic trace decomposition: Geophysics, **75**(4), 61-66.

Wen X., B. Zhang, W. Pennington, and Z. He, 2015, Relative P-impedance estimation using a dipole-based matching pursuit decomposition strategy: Interpretation, **3**(4), T197-T206.

Yilmaz O., 1989, Velocity stack processing: Geophysical Prospecting, **37**, 357-382.

Yilmaz O., and M. T. Taner, 1994, Discrete plane-wave decomposition by least mean square error method: Geophysics, **59**(6).

Zhang B., K. Zhang, S. Guo, and K. J. Marfurt, 2012, Nonstretching NMO correction of prestack time-migrated gathers using a Matching Pursuit algorithm: Geophysics, **78**(1), 9-18.

Zhou B., and S. A. Greenhalgh, 1994, Linear and parabolic τ-p transforms revised: Geophysics, **59**(7), 1133-1149.